Experimental and numerical study of soil-structure interaction subjected to cyclic-dynamic loading : application to offshore wind turbine monopile foundation

Hussein Bakri

École des Ponts ParisTech

THÈSE DE DOCTORAT

de l'École des Ponts ParisTech

Experimental and numerical study of soil-structure interaction subjected to cyclic-dynamic loading: Application to offshore wind turbine monopile foundation

École doctorale N°531, Sciences, Ingénierie et Environnment (SIE)

Spécialité : Géotechnique

Thèse préparée au laboratoire Navier UMR 8205

Soutenue le 8 Décembre 2021, par

Hussein BAKRI

Composition du jury:

Fabrice, Emeriault Professeur, Grenoble INP	*Rapporteur*
Panagiotis, Kotronis Professeur, Ecole Centrale de Nantes	*Rapporteur*
Luc, Thorel Directeur de recherche, Université Gustave Eiffel	*Examinateur (Président)*
Christelle, Abadie University Lecturer, University of Cambridge	*Examinateur*
Gwendal, Cumunel Chargé de recherche, Ecole des Ponts ParisTech	*Examinateur*
Laura, Kerner Chercheuse, Université Gustave Eiffel	*Examinateur*
Jean-Michel, Pereira Professeur, Ecole des Ponts ParisTech	*Directeur de thèse*
Jean-Claude, Dupla Chargé de recherche, Ecole des Ponts ParisTech	*Co-directeur de thèse*
Emmanuel, Bourgeois Chercheur, Université Gustave Eiffel	*Invité*
Bassel, Seif-El-Dine Professeur associé, Université Libanaise	*Invité*

École des Ponts
ParisTech

Thèse

soumise pour l'obtention du grade de
Docteur de l'École des ponts ParisTech
Ecole Doctorale Sciences, Ingénierie et Environnement (SIE)

par

Hussein BAKRI

Experimental and numerical study of soil-structure interaction subjected to cyclic-dynamic loading: Application to offshore wind turbine monopile foundation

---

Spécialité : *Géotechnique*

Thèse préparée au laboratoire Navier

Soutenue le 8 Décembre 2021 devant un jury composé de :

Fabrice Emeriault	Grenoble INP	Rapporteur
Panagiotis Kotronis	Ecole Centrale de Nantes	Rapporteur
Luc Thorel	Université Gustave Eiffel	Examinateur
Christelle Abadie	University of Cambridge	Examinateur
Gwendal Cumunel	Ecole des Ponts ParisTech	Examinateur
Laura Kerner	Université Gustave Eiffel	Examinateur
Jean-Michel Pereira	Ecole des Ponts ParisTech	Directeur de thèse
Jean-Claude Dupla	Ecole des Ponts ParisTech	Co-directeur de thèse
Emmanuel Bourgeois	Université Gustave Eiffel	Invité
Bassel Seif-El-Dine	Université Libanaise	Invité

Thèse préparée par

Hussein BAKRI

Spécialité : *Géotechnique*

Thèse préparée au laboratoire Navier

Thèse encadrée par :

Jean-Michel Pereira	Ecole des Ponts ParisTech
Jean-Claude Dupla	Ecole des Ponts ParisTech
Gwendal Cumunel	Ecole des Ponts ParisTech
Laura Kerner	Université Gustave Eiffel
Emmanuel Bourgeois	Université Gustave Eiffel
Bassel Seif-El-Dine	Université Libanaise
Layal Jradi	Université Libanaise

Acknowledgements/Remerciements

Ce travail de thèse est réalisé au sein de l'équipe géotechnique du laboratoire Navier – Ecole des Ponts ParisTech. Ce travail est en codirection avec l'Université Libanaise à Beyrouth.

Je tiens à remercier profondément M. Jean-Michel Pereira, mon directeur de thèse, professeur à l'ENPC, pour avoir supervisé ces trois années de recherche. J'apprécie beaucoup son soutien et sa patience. Sa contribution scientifique avait toujours un apport important qui m'encourage et améliore mes travaux.

Je tiens également à exprimer mes sincères remerciements à M. Jean-Claude Dupla, co-directeur de thèse et chercheur à l'ENPC, qui était toujours prêt pour toute aide et tout soutien. Je veux lui remercier encore pour sa confiance en moi durant la thèse et pour me donner la chance de continuer en post-doc après la thèse.

Mes vifs remerciements vont également à mon encadrant de thèse M. Gwendal Cumunel, chercheur à l'ENPC, pour son aide et ses conseils surtout dans la partie expérimentale. Grâce à lui, je suis bien convaincu que chaque problème doit avoir une solution. De même, je remercie vivement mon encadrante Mme. Laura Kerner, ingénieur/chercheuse à l'Université Gustave Eiffel, pour être toujours prête pour toute aide. De plus, je tiens à remercier chaleureusement mon encadrant, M. Emmanuel Bourgeois, chercheur à l'Université Gustave Eiffel, qui m'a appris énormément de choses dans la partie numérique et qui était toujours à côté de moi.

Je tiens particulièrement à remercier mes encadrants M. Bassel Seif El Dine, professeur associé à l'Université Libanaise à Beyrouth, et Mme Layal Jradi, docteur à l'Université Libanaise à Beyrouth, qui ont eu confiance en moi et m'ont accordé cette thèse. Je veux les remercier également pour leur soutien, leurs conseils, et leur suivi de la thèse. Je tiens à remercier chaleureusement M. Fabrice Emeriault, professeur à l'INP – Grenoble, et M. Panagiotis Kotronis, professeur à l'Ecole Centrale des Nantes, de m'avoir fait l'honneur d'accepter le rôle de rapporteur de ce mémoire.

Je remercie également M. Luc Thorel, directeur de recherche à l'Université Gustave Eiffel, d'avoir présidé mon jury de thèse ; et Mme. Christelle Abadie, University Lecturer à

l'University of Cambridge, d'avoir accepté de participé à mon jury de thèse et pour l'intérêt qu'ils ont porté à mon travail, pour leur soutien et leurs remarques pertinentes.

Je tiens à remercier l'équipe technique du laboratoire Navier – Géotechnique, qui ont été toujours à mon service. En particulier, je remercie le chef de l'équipe M. Emmanuel De Laure qui je suis toujours impressionner par son enthousiasme et sa curiosité scientifique. Je remercie Mme Marine Le Maire et M. Xavier Boulay, qui s'occupaient surtout des systèmes d'acquisitions et des outils de mesures. Je remercie également M. Baptiste Chabot et M. Loic Lesueur, pour leurs aides au niveau du développement et montage de mes manips expérimentales. Finalement, Je tiens à remercier Mme Sabrina Chartier, assistante administrative de l'équipe Géotechnique, pour sa gestion impeccable.

Je tiens à remercier l'ensemble de l'équipe géotechnique du laboratoire Navier, qui assure une ambiance très formidable pour travailler avec plein de plaisir. Je remercie du fond de mon cœur mes amis les doctorants. J'ai vraiment passé trois années inoubliable grâce à vous.

Je tiens à remercier mes amis libanais en France qui ont été toujours à côté de moi, et que je les considère comme une partie de ma famille. Je veux remercier particulièrement ceux qui ont venu de loin pour suivre la soutenance et ceux qui m'ont préparé un pot magnifique.

Finalement, je tiens à remercier ma famille. Mes parents, mes frères, et ma sœur, je vous remercie pour votre soutien infini, vous étiez loin de mes yeux, toujours près de mon cœur ! Un remerciement particulier pour ma grand-mère, qui a sacrifié sa vie pour notre bonheur. Pour mon amie, ma collègue, et ma copine durant ces trois années et toute ma vie, May, merci pour ton soutien, ta patience, et ton amour qui m'encourage toujours. Je ne peux dire que L'Ecole des Ponts m'a donné beaucoup plus qu'une thèse !

Abstract

Offshore wind turbines form one of the principal solutions adopted to ensure the cleanliness, sustainability, and renewability of energy sources. Therefore, this field is growing exponentially, manifested by the increase of the dimensions and capacities of these structures. Besides, the environmental loading acting on these structures equally increases, imposing particular attention on the design of the foundation system. Due to economic and practical reasons, monopile foundations are commonly adopted. The form of these monopiles depends on wind turbines growth, moving to a smaller length-to-diameter ratio and then to more rigid behavior. The behavior of this kind of monopiles under lateral cyclic loading still involves some knowledge gaps. Recently, several physical models have been developed to fulfill this purpose, leading to propose a conservative design method. Due to the problem complexity (soil-structure interaction, dynamic aspect, soil liquefaction, scouring,...) and despite the progress achieved in this field, conflicting findings are still encountered, depending on the considered approach to the problem.

In the framework of this thesis, two reasonable sets of monopile dimensions are proposed in a way to obtain different factors of rigidity (semi-rigid and perfectly rigid monopiles). The aim is to examine the cyclic behavior of each monopile foundation and then evaluate their performance as a foundation of *"DTU 10 MW RWT"* in relatively deep waters. An accurate set of scaling laws under laboratory gravity is proposed and adopted in the development of representative scale models. The challenge is to respect the combination of (i) the soil non-linearity, (ii) the soil-structure interaction, and (iii) the dynamic response of the system. The obtained scale model should not only simulate the qualitative behavior of the system but also be able to offer quantitative insight into this behavior. Finite element simulations using *Cesar–LCPC 3D* are carried out to verify the dynamic similarity between the scale models and the prototype for the first mode of vibration.

Conscious of the difficulties and limitations underlying the 1g physical modeling, a part of this study is dedicated to the investigation of sand behavior at different stress levels (triaxial tests program). This study aims to determine the parameters of stress-dilatancy relation for Fontainebleau (*NE34*) sand, permitting the determination of the sand state required to simulate the prototype sand state at the laboratory scale. Besides, specific procedures are

followed to ensure the tests repeatability at corresponding low-stress levels (development of monopile guidance and driving system). Cyclic strain-controlled tests are performed, showing tests repeatability and, therefore, the validity of the testing procedure. Then, cyclic tests with different excitation frequencies are performed, highlighting the dynamic aspect of the system response. The analysis of a typical test shows the capability of the proposed scale model to fulfill some knowledge gaps. This part ends with the recommendation of a cyclic tests program, aiming at tackling some ambiguous points to assist in the scientific debate in this domain.

On another side, a constitutive model is developed to simulate the sand behavior at different stress levels. This model is based on *Hoek-Brown* failure criteria and a suitable hardening function. This model is calibrated against the experimental findings of monotonic, strain-controlled, triaxial tests. Then, this model is implemented in *Cesar–LCPC 3D* finite element program and validated against a parametric study of monotonic laterally loaded rigid monopile. A good agreement is obtained between the numerical and experimental findings. This parametric study aims to discuss and evaluate the performance of failure criteria proposed for rigid monopile foundations. This discussion ends with the suggestion of a new failure criterion and the recommendation to adopt tilt criteria (e.g. failure defined for a tilt of $2°$ at the sand surface) instead of displacement criteria (e.g. failure defined for a displacement of $0.1D$ at the sand surface) in case of rigid monopiles.

Keywords: Offshore wind turbines; Monopile; Cyclic loading; Physical modeling; Scaling laws; Low stress; Constitutive law; Failure criteria; Finite element analysis.

Résumé

Les éoliennes offshores sont une des solutions principales adoptées pour assurer la propreté et la durabilité des sources d'énergie. Ce domaine connaît donc une croissance exponentielle, comme le montre l'augmentation des dimensions et des capacités de ces structures. En outre, les chargements agissant sur ces structures augmentent également, imposant une attention particulière à la conception des fondations. Pour des raisons économiques et pratiques, les fondations monopieux sont couramment adoptées. La forme de ces monopieux dépend de la croissance des dimensions des éoliennes, évoluant vers un élancement plus petit et un comportement plus rigide. Le comportement de ce type de monopieux sous chargements latéraux cycliques forme actuellement un débat scientifique. Récemment, plusieurs modèles réduits ont été développés pour répondre à cet objectif, conduisant à proposer une méthode de conception conservatrice. En raison de la complexité du problème (interaction sol-structure, aspect dynamique, liquéfaction du sol, affouillement,...) et malgré les progrès réalisés dans ce domaine, des résultats contradictoires sont encore rencontrés, dépendant de l'approche considérée du problème.

Dans le cadre de cette thèse, deux monopieux ayant des dimensions raisonnables sont proposés de manière à obtenir différents facteurs de rigidité (monopieu semi-rigide et un autre parfaitement rigide). Le but est d'examiner le comportement cyclique de chaque type de fondation et ensuite d'évaluer leur performance en tant qu'une fondation du *"DTU 10 MW RWT*" dans des eaux relativement profondes. Un ensemble précis de lois d 'échelle sous gravité de laboratoire est proposé et adopté dans le développement de modèles réduits représentatifs. Le défi est de respecter la combinaison de (i) la non-linéarité du sol, (ii) l'interaction sol-structure, et (iii) la réponse dynamique du système. Les modèles réduits obtenus doivent non seulement simuler le comportement qualitatif du système mais aussi être capable d'offrir un aperçu quantitatif de ce comportement. Des simulations par éléments finis en utilisant *Cesar-LCPC 3D* sont effectuées pour vérifier la similitude dynamique entre les modèles réduits et le prototype pour le premier mode de vibration.

Conscients des difficultés et des limites de la modélisation physique à 1g, une partie de cette étude est consacrée à l'investigation du comportement du sable à différents niveaux de contrainte (programme d'essais triaxiaux). Cette étude vise à déterminer les paramètres

de la relation contrainte-dilatation pour le sable de Fontainebleau *(NE34)*, permettant de déterminer l'état du sable nécessaire pour simuler le sable du prototype à l'échelle du laboratoire. En outre, des procédures spécifiques sont suivies pour assurer la répétabilité des essais à des niveaux de contraintes faibles (développement d'un système de guidage et du battage des monopieux). Des essais cycliques avec déformation contrôlé sont effectués, montrant la répétabilité des essais et, par conséquent, la validité de la procédure d'essai. Ensuite, des essais cycliques en variant la fréquence d'excitation sont réalisés, mettant en évidence l'aspect dynamique du problème. L'analyse d'un essai typique montre la capacité du modèle réduit proposé à clarifier certaines lacunes dans les connaissances. Cette partie se termine par la recommandation d'un programme d'essais cycliques, visant à aborder certains points ambigus afin de contribuer au débat scientifique dans ce domaine.

D'autre part, une loi de comportement est développée pour simuler la réponse du sable à différents niveaux de contrainte. Ce modèle est basé sur le critère de rupture de *Hoek-Brown* et une fonction d'écrouissage convenable. Ce modèle est calibré par rapport aux résultats expérimentaux d'essais triaxiaux monotones à déformation-contrôlée. Ensuite, ce modèle est implémenté dans le programme d'éléments finis *Cesar-LCPC 3D* et validé par une étude paramétrique sur un monopieu rigide sous chargement latéral. Un bon accord est obtenu entre les résultats numériques et expérimentaux. Cette étude paramétrique a pour but de discuter et d'évaluer la performance des critères de rupture proposés pour les fondations monopieux rigides. Cette discussion arrive à la suggestion d'un nouveau critère de rupture et la recommandation d'adopter des critères basés sur l'angle de rotation (par exemple, rupture définie pour une inclinaison de $2°$ à la surface du sable) au lieu de critères basés sur le déplacement (par exemple, la rupture définie pour un déplacement de $0,1D$ à la surface du sable) dans le cas des monopieux rigides.

Mots-clefs: Eoliennes offshores; monopieu; Chargements cycliques; Lois d'échelle; Faible contrainte; Loi de comportement; Critère de rupture; Analyse des éléments finis.

Contents

1 Introduction

Global warming, climate change, sustainability of energy sources are the main challenges to which governments are faced in the current decade. Wind energy is one of the efficient solutions that can be adopted to solve these issues. Last year, the European Union (EU) increased its greenhouse gas emissions reduction target for 2030 from 40% to 55% (Wind Europe, 2020). Currently, the wind energy ensures 16.6% of the electricity demand in Europe (Figure 1.1). The EU commission raises the renewable energy target from 32% to 40% by 2030, which requires 451 *GW* of wind power capacity from 180 *GW* today (Wind Europe, 2020). France aims to reach 34 *GW* of wind energy by 2028, up from 18 *GW* today. In parallel, the *USA* administration announces a plan to deploy 30 *GW* of offshore wind energy by 2030, after the installation of seven major offshore wind farms on the east and west coasts and in the Gulf of Mexico (TheGuardian, 2021).

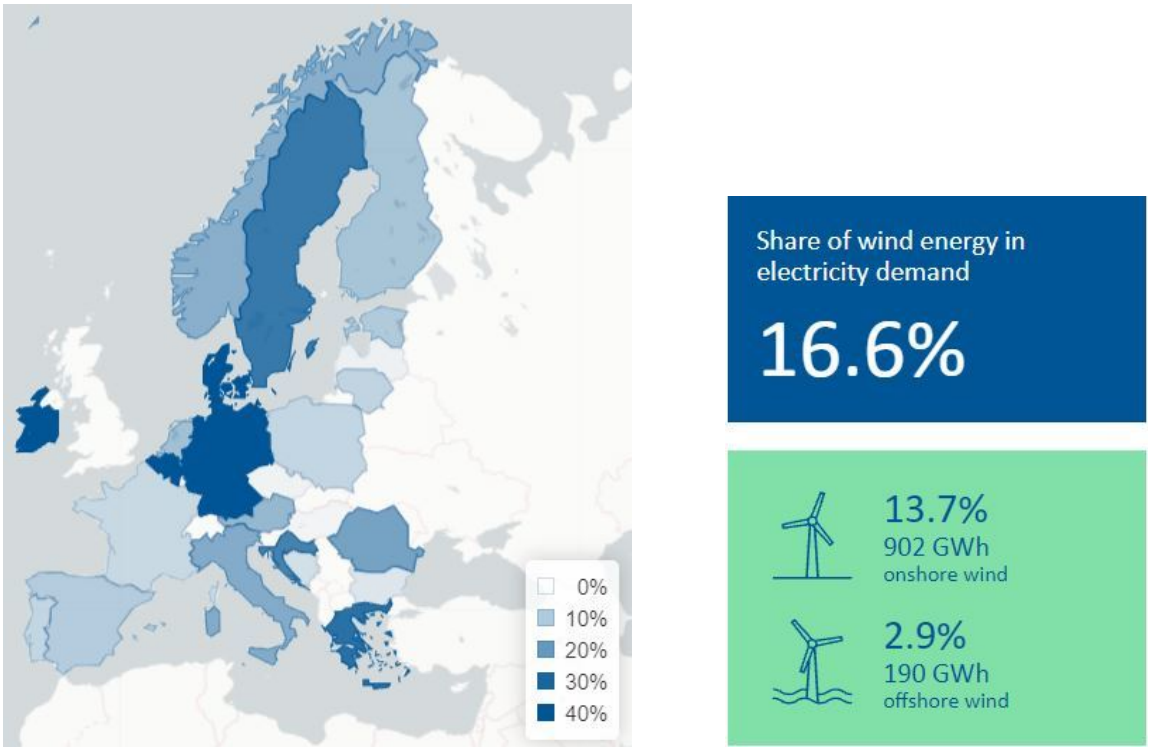

(a) (b)

Fig. 1.1.: Wind energy contribution in the European Union (Wind Europe, 2020)

All these numbers show the exponential growth of the wind turbines sector. Despite their current contribution to 17.5% of the global wind energy production, offshore development

for these structures is considered as a solution to the significant increase in their dimensions and the associated operating noise. Figure 1.2 show the evolution of the installed and cumulative capacity of offshore turbines in the last decade. According to the publications of the Offshore Renewables Energy Strategy (ORES), the EU's ambition is to build 300 *GW* of offshore wind capacity by 2050 (Wind Europe, 2020). In terms of cumulative installations, the North Sea gathers 79% of all offshore wind capacity in Europe (Wind Europe, 2020). The average rated capacity of turbines installed in 2020 was 8.2 *MW*, from 3 *MW* in 2010 (Wind Europe, 2020). The installation of these turbines goes into deep water, where the average water depth of offshore wind farms under construction in 2020 is 36 *m* (Wind Europe, 2020).

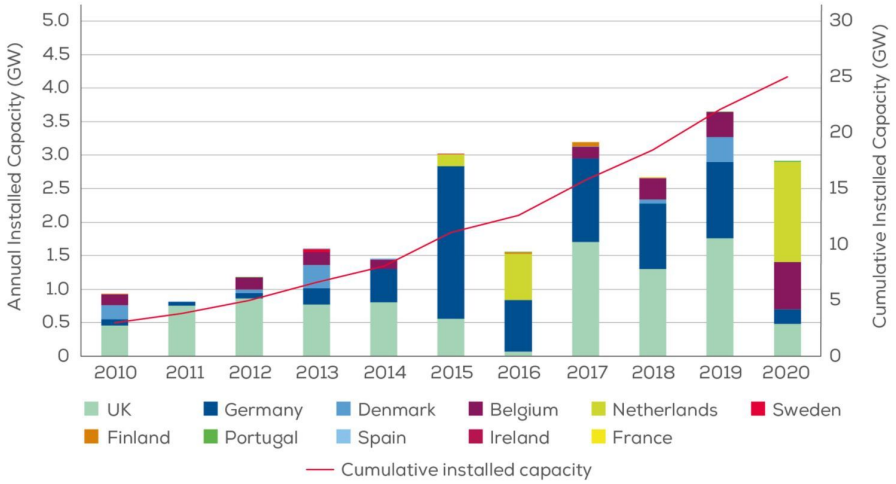

Fig. 1.2.: Evolution of the offshore turbines capacity installed between 2010 and 2020, and the evolution of the cumulative installed capacity

Many foundations are adopted to support the offshore turbine's structure, while the monopiles are still the most common by a percentage exceeding 81% of the cumulative turbines installed (Figure 1.3).

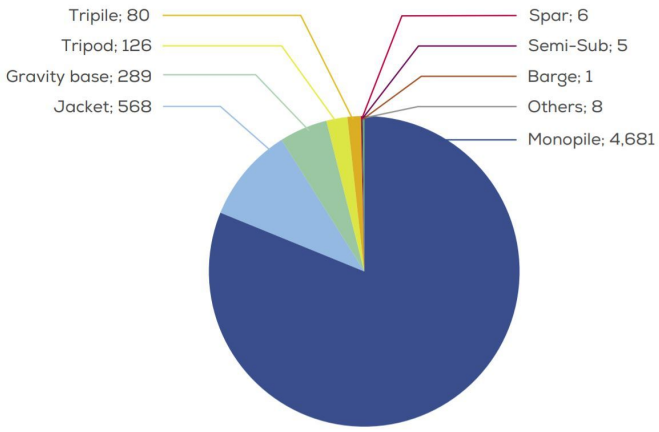

Fig. 1.3.: Repartition of foundation types adopted for offshore turbines installed (Wind Europe, 2020)

Therefore, some research projects are launched to enrich the knowledge and ensure the design tools of monopile foundations e.g. *Solcyp* (Puech and Garnier, 2017); *PISA* (Byrne et al., 2017); and *Solcyp+* (Dupla et al., 2019) projects. While, the increase in the dimensions of the offshore wind turbines has some significant implications:

- An increase in the amplitude of the wind load (one-way) acting on the structure. Besides, the increase in the substructure diameter and the water depth leads to higher contribution of the wave load (two-way), which affects the characteristics of the cyclic loading (Arany et al., 2017, Jalbi et al., 2019).

- The increase in the structure dimensions imposes a change in the monopiles diameter and length to diameter ratio. Indeed, the current monopiles have diameters up to $8\ m$, with a length to diameter ratio ranging between 3 and 6 (Sorenson et al., 2017, Schroeder et al., 2015), while the diameter of the next generation of offshore wind turbines is expected to exceed $10\ m$ (Richards, 2019). This kind of monopiles is characterized by a rigid behavior, depending mainly on its length to diameter ratio (Peralta and Achmus, 2010, Dietrich, 1982; Figure 1.4a).

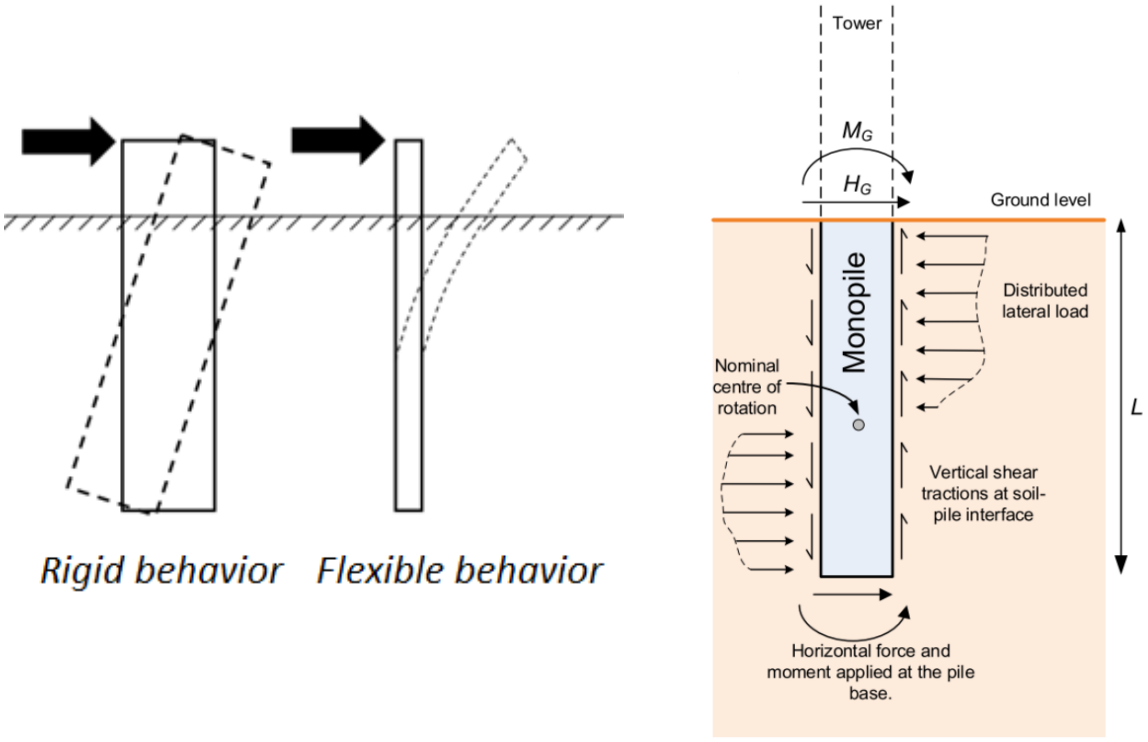

Fig. 1.4.: (a) Different monopile behaviors, and (b) schematic of the soil reaction components acting on a rigid monopile (from Byrne et al., 2017)

According to Byrne et al., 2017, some components of the soil reaction, which are neglected in the conventional design methods based on flexible monopiles, become relevant, and

ignoring them considerably affects the findings. Figure 1.4b shows the four components of the soil reaction opposing to lateral loading: distributed lateral load, vertical shear traction at the soil-pile interface, and horizontal force and moment at the monopile base. The knowledge tools required to design rigid monopiles are relatively limited compared with flexible monopiles.

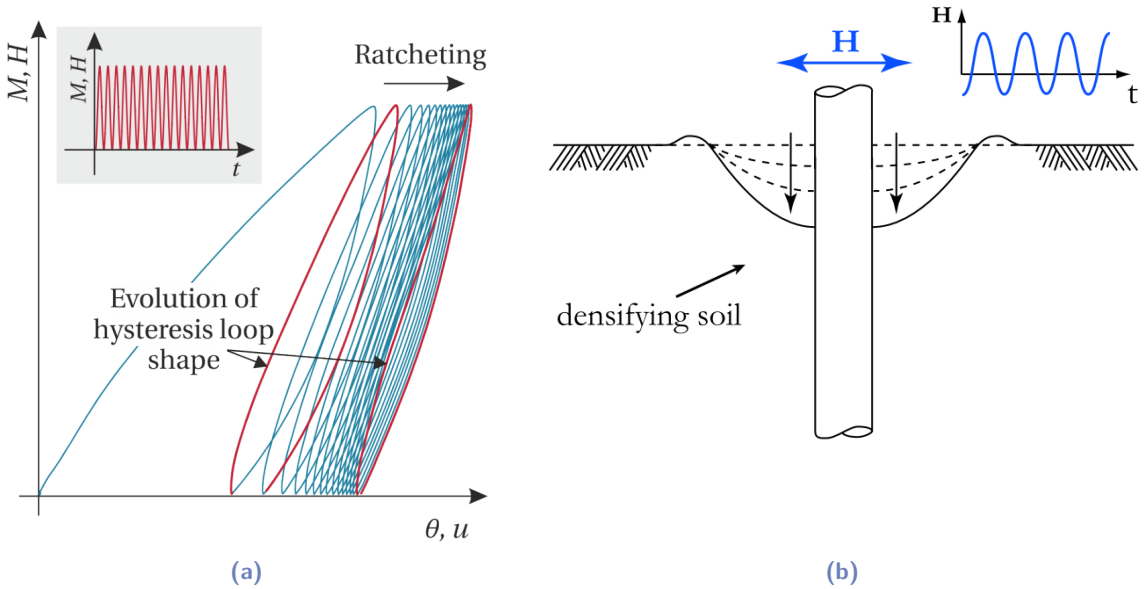

Fig. 1.5.: Phenomena underlying the cyclic response of rigid monopiles (a) from Richards, 2019 (b) from Cuéllar, 2011

On another hand, the offshore wind turbines are subjected to a high number of loading cycles, and the main phenomena underlying the cyclic response of rigid monopiles are the following: (i) displacement and rotation accumulation (ratcheting), (ii) evolution of the hysteresis loop shape manifested by an increase in the soil stiffness and a decrease in the soil damping in case of sand materials (Figure 1.5a), (iii) subsidence cone formation caused by the sand densification around the monopile (Figure 1.5b). The key features of these phenomena and their evolution depending on loading characteristics and foundation properties still involve knowledge gaps and form a scientific debate.

- The offshore wind turbines are considered as dynamically sensitive structures DNV-OS-J101, 2014. The design of these structures should ensure that the natural frequencies avoid any resonance phenomena with: (i) wind loading frequencies, (ii) wave loading frequencies, (iii) rotor frequencies *1P*, and blade-passing frequencies *3P* (Figure 1.6). As an essential step of the foundation design, the first natural frequency should be carefully regarded due to its proximity to the excitation frequencies and its dependence on the foundation properties. Structures supported by monopile foundations are typically designed as soft-stiff structures, where the natural frequency of the first mode should be in the narrow band between the *1P* and *3P* excitation frequencies. Generally, the first

natural frequency at the installation of the offshore wind turbine tends to decrease with the growth of their dimensions (Arany et al., 2017), challenging the satisfaction of the lower band of the dynamic design criterion. Besides, the cyclic response of the monopile to external loads can affect the evolution of the natural frequency during the turbine exploitation. The coupling of many phenomena (e.g. subsidence cone formation due to densification, soil stiffness evolution, hydrodynamic scouring, see e.g. Yu et al., 2015, Liang et al., 2020, Prendergast et al., 2015) controls the evolution of the first natural frequency, which makes the prediction of the trend of this evolution a difficult task.

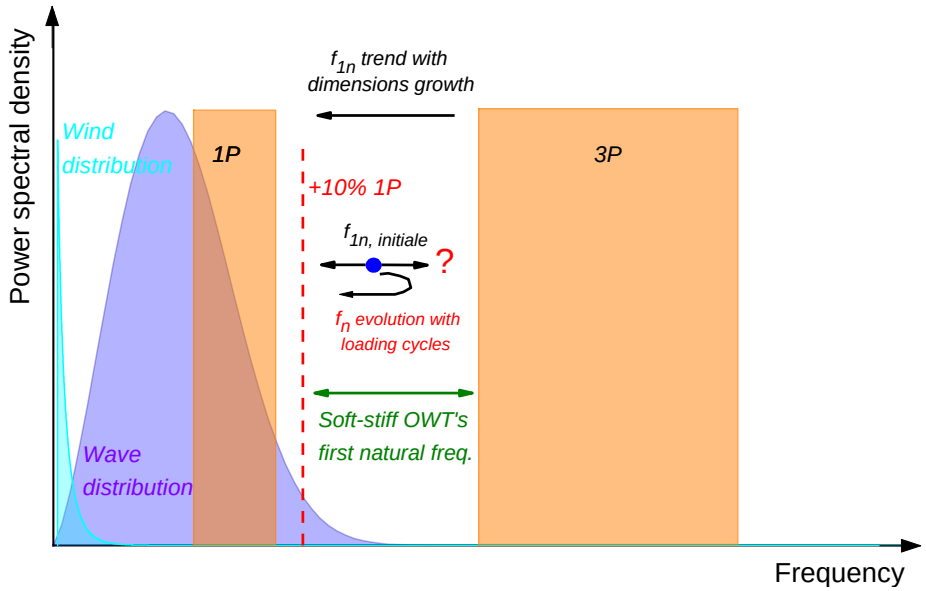

Fig. 1.6.: Typical frequency spectrum for loads acting on an offshore wind turbine

Aiming to enhance the understanding of the cyclic behavior of an offshore wind turbine supported by a rigid monopile, the first objective of this thesis is the development of a representative 1g scale model considering the complex aspects of the problem: (i) soil-monopile interaction, (ii) soil non-linearity, and (iii) structure dynamic sensitivity. This scale model is at the basis of a cautious experimental program capable of fulfilling some knowledge gaps in this scientific field. The second objective is to validate a dynamic *3D FEM Cesar-LCPC* model to be used in (i) the verification of the dynamic similarity between the scale model and the prototype for the first mode of vibration, and (ii) the understanding of the evolution of the system first natural frequency based on parametric studies. The third objective is to develop a sand constitutive model accounting for relatively low-stress levels, and able to capture the main features of the sand response during triaxial compression. Using this newly developed constitutive model, the validation of *3D FEM* models based on experimental findings provides a numerical design tool for rigid monopiles.

After the presentation of the motivations, challenges, and objectives of this study, in addition to this introductory chapter, this manuscript is organized into seven chapters:

- Chapter 2 presents the background of this study, as methods adopted to estimate the environmental loads acting on offshore wind turbines, to design rigid monopiles, and to develop representative scale models. Then, it finishes with the proposition of a new set of scaling laws and the development of 1g scale models representing a reference offshore wind turbine "DTU 10 MW RWT".

- Chapter 3 presents an experimental campaign to determine the *NE34* sand parameters at different stress levels.

- Chapter 4 starts with a literature review of 1g and centrifuge scale models and their findings. Then, the different experimental procedures applied on this study are presented, and their capability and repeatability are proven. Besides, a dynamic *FEM* model is presented and used to validate the dynamic similarity between the scale models and the prototype for the first mode of vibration.

- Chapter 5 presents some inspirations on the cyclic response of offshore wind turbines based on a limited experimental test program and a numerical parametric study. This chapter ends with the proposition of a large cyclic experimental program aiming to fulfill some knowledge gaps in this domain.

- Chapter 6 presents a new constitutive model able to capture the main features of the sand response during triaxial compression. A method of calibration is also presented and applied on the findings of Chapter 3 for *NE34* sand.

- Chapter 7 illustrates the findings of an experimental parametric study tackling the monotonic response of rigid monopiles. These findings are used (i) to propose a new failure criterion for rigid monopiles and (ii) to show the performance of the new sand constitutive law to simulate the monotonic response at the laboratory scale (low-stress levels).

- Chapter 8 discusses the major findings of this work and the possible perspectives for future studies.

Aiming to clarify the links between the different parts of this study, a graphical outline of the thesis manuscript is presented in Figure 1.7, and commented below:

As the main scope of this study is to understand the cyclic response of offshore wind turbine, the first target is to ensure a representative 1g scale model. To avoid the limitations of previous works, a new set of scaling laws is presented in Chapter 2. As part of this scaling methodology, some parameters for *NE34* sand, controlling its behavior at different stress levels, are required. Therefore, an experimental campaign (mainly on the triaxial device) is

conducted and presented in Chapter 3. Besides, the obtained scale model should be able to simulate the first vibration mode of the offshore wind turbine. Its performance is shown in Chapter 4, using a dynamic *FEM* model. On another side, a new sand constitutive model, adapted for different stress levels, is developed and presented in Chapter 6. The capability of a static *FEM* model, informed by this constitutive model, to simulate the monotonic response of rigid monopiles is shown in Chapter 7. The static *FEM* model constitutes (i) a numerical design tool of rigid monopiles, and (ii) can be useful on the judgment of the experimental results obtained at the laboratory scale and their transition to the prototype scale.

Once representative scaling is achieved, experimental procedures should be applied to determine the monotonic and cyclic responses. The cyclic loading applied is characterized by its magnitude as the percentage of the monopile ultimate capacity. This characterization depends on the failure criterion adopted to define the ultimate capacity. The limited performance of conventional failure criteria to ensure equivalent evaluation of ultimate capacities for different monopile properties is discussed in Chapter 7, which affects the generalization of obtained results. Therefore, based on a parametric study of a laterally loaded rigid monopile, a new failure criterion is proposed and validated as a solution to this limitation (also in Chapter 7).

After a limited cyclic test program, some inspirations on the offshore wind turbine behavior are presented in Chapter 5. This work is supported by a numerical parametric study due to the limited number of tests performed.

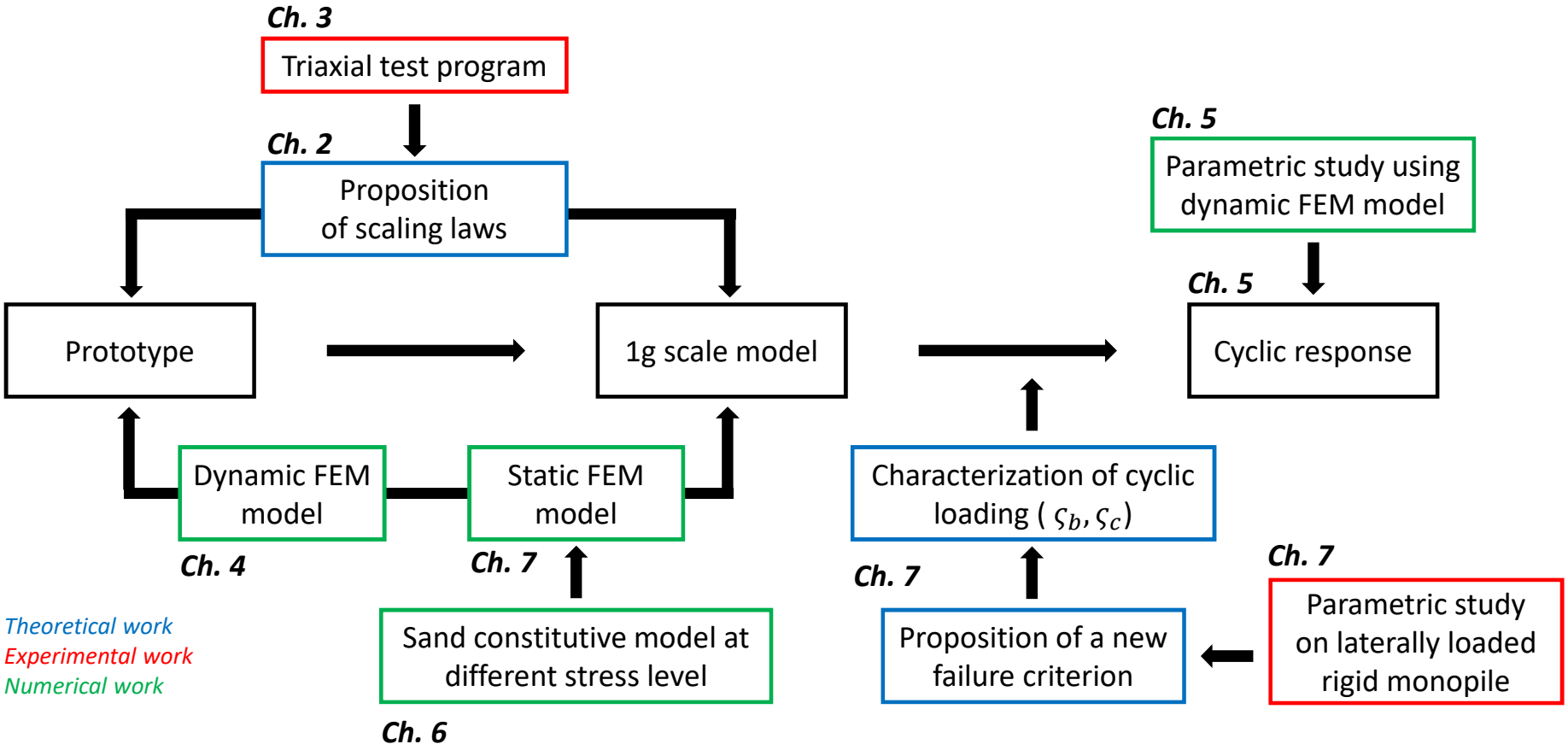

Fig. 1.7.: Thesis structure

2 Prototype design and 1g-scale model development

This chapter aims to develop a scale model able to simulate the aspects affecting the foundation design of an offshore wind turbine. Reproducing these aspects would improve the understanding of the long-term effect of environmental and operational loading on the stability of offshore wind turbines. The specific form of these structures and their location in adverse environmental conditions make them dynamically sensitive, which adds a dynamic component to the problem, as seen in Chapter 1. Most of works in this domain disregard the dynamic similarity between the scale model and the prototype, satisfied by the similarity of the qualitative behavior of monopile foundation subjected to lateral cyclic loading. The challenge is to respect the combination of (i) the soil non-linearity, (ii) the soil-structure interaction, and (iii) the dynamic response of the system. The obtained scale model should not only simulate the qualitative behavior of the system but also be able to offer a quantitative insight into this behavior.

The development of two representatives scale models is presented. First, a literature review presents some key points of the study: (i) methodology to estimate and simplify the environmental loading, (ii) relevant available design methodologies, and (iii) relevant scaling laws adopted for 1-g physical modeling. Then, an overview of 10 *MW* reference offshore wind turbine is introduced, followed by the proposition of two types of monopiles foundations. These foundation-structure systems proposed are considered the prototypes of the two scale models, which are developed in the section following the proposition and application of adequate static/dynamic scaling laws.

2.1 Overview and background

2.1.1 Estimation of loads acting on an offshore wind turbine

The offshore wind turbines are subjected to a large set of loads. These loads can be divided into a few principal categories:

- Permanent loads: self-weight of the structure.

- Variable loads: loads due to the installation, boats impact, ...

- Environmental loads: the effect of wind, waves, currents, earthquakes, tidal, snow, and ice.

- Operational loads: vibrations caused by rotor motion and blades passing.

Due to the specific form of these structures and the foundations adopted, the critical loading in their design is the lateral loading. Operational loads are characterized by relatively small amplitudes and high frequencies, restricting the natural frequency of the structure as seen in Chapter 1. Environmental loads are dominant in terms of amplitude. They have a primordial effect on ultimate and service limit states. The estimation of these loads is the first step to evaluate the stability of an offshore wind turbine. The Figure 2.1 shows a schematic diagram of main loads acting on an offshore wind turbine.

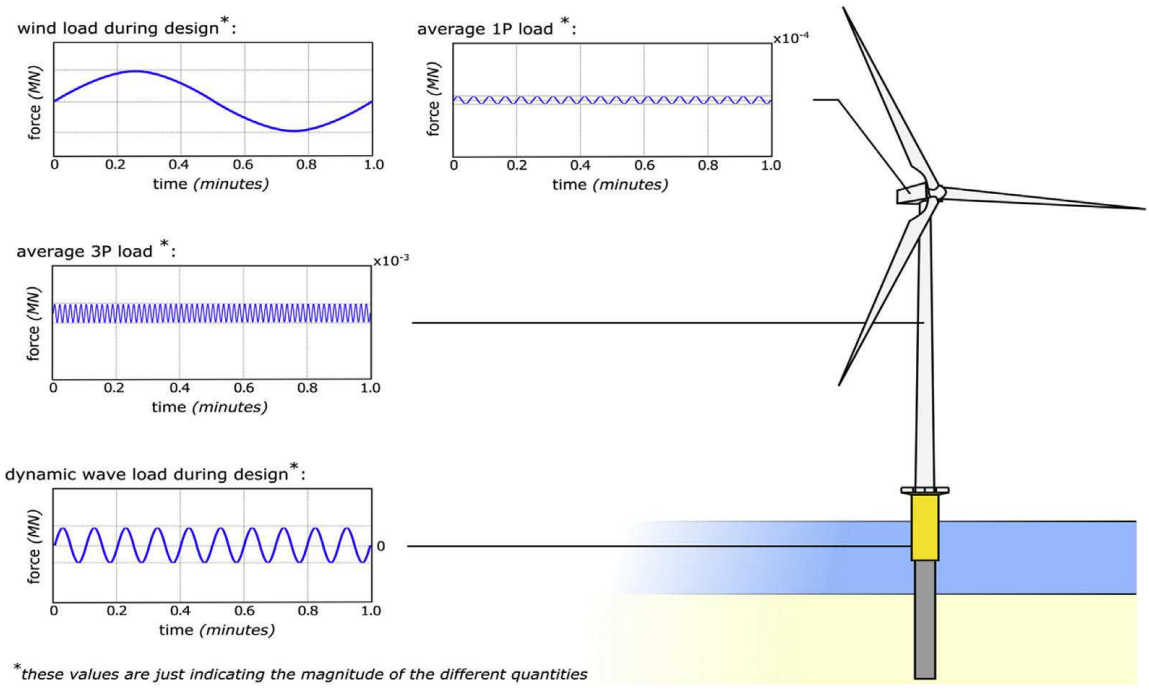

Fig. 2.1.: Schematic of loads acting on an offshore wind turbine after Bhattacharya et al., 2017

Environmental conditions

The principal sources of environmental loads acting on an offshore wind turbine are wind and waves. The characteristics of winds and waves are irregular and vary considerably over time and space. Hence the estimation of environmental loads starts with a methodology to represent the significant state of sea condition.

- Wind conditions:

  The wind speed varies over space, time, and direction. Due to the wind shear phenomena, the wind speed increases with height. Furthermore, the realistic wind speed varies around its mean value due to the effect of turbulence (Figure 2.2a). Two main models are proposed to fit the relation between mean wind speed and elevation:

  - Logarithmic profile

$$V_w(z) = V_{ref}\frac{\ln(z/z_0)}{\ln(z_{ref}/z_0)} \tag{2.1}$$

  - Power-law profile

$$V_w(z) = V_{ref}\left(\frac{z}{z_{ref}}\right)^{\alpha} \tag{2.2}$$

  Where V_w is the wind speed at an elevation equal to z. The surface roughness length z_0 corresponds to the elevation above sea or ground level where wind speed is equal to zero. The surface roughness length z_0 and power law coefficient α depend on the nature of the studied field (city, forest, calm sea, ...). DNV-OS-J101, 2014 recommends values of $z_0 = 0.05\ m$ and $\alpha = 0.12$ for offshore applications in a calm sea. Figure 2.2b represents the two models corresponding to a reference height z_{ref} of $120\ m$ and mean wind speed V_{ref} at this height equal to $15\ m/s$.

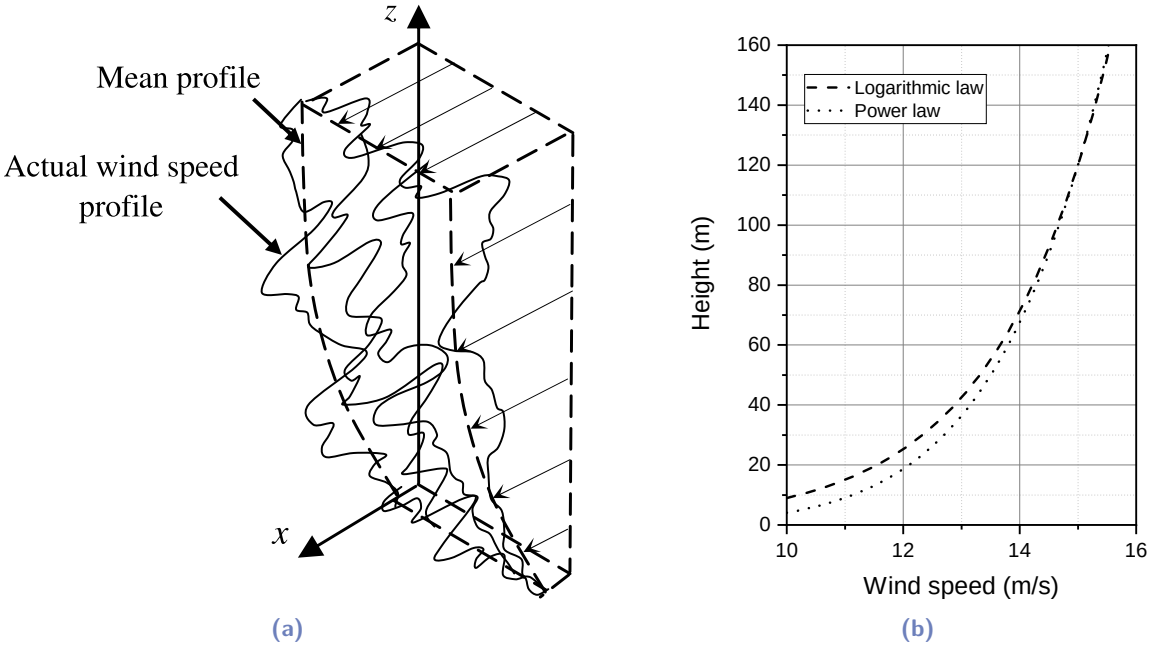

Fig. 2.2.: (a) Realistic profile of wind speed (Van der Tempel, 2006); (b) Empirical profile laws of wind speed

The wind climate is represented by 10-minutes mean wind speed U_{10} and the standard deviation of the wind speed σ_U (considered as wind turbulence). In the short term, during 10 minutes for example, defined parameters U_{10} and σ_U are assumed to be constant. The turbulence of wind (σ_U) can be represented in a spectral form, which shows the distribution of the wind speed energy with various frequencies. The Diederich et al. (1957) and Kaimal et al. (1972) spectra are the most commonly used models, which depend on the mean wind speed, turbulence intensity, and length scale. Besides, another wind-speed spectrum is constructed by Van der Hoven (1957) based on long- and short-term records. These spectra are presented in the Figure 2.3. For more details, refer to Wind Energy Handbook (Burton et al., 2011).

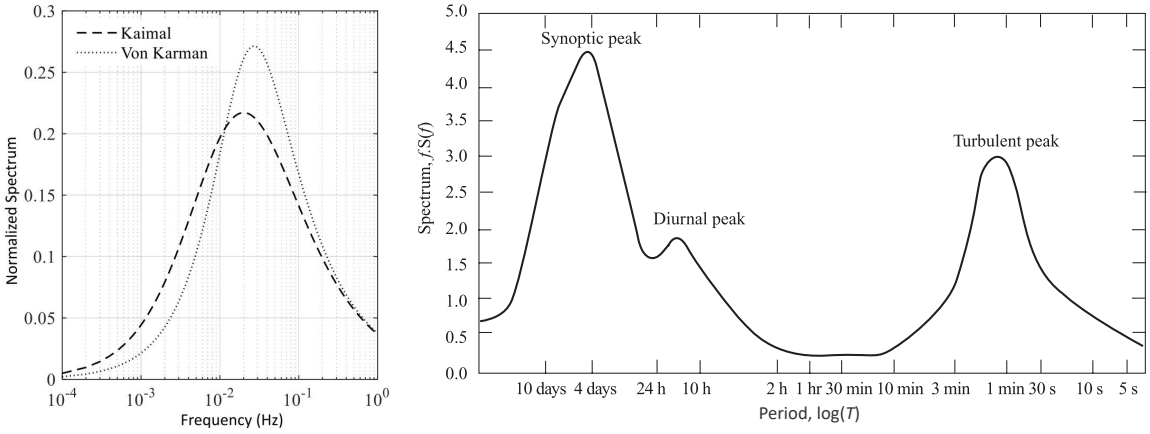

Fig. 2.3.: (a) Normalized wind-speed spectrum of Kaimal and von Karman; (b) Wind spectrum Farm Brookhaven based on work by Van der Hoven (1957)

Due to the long lifetime of an offshore wind turbine, the wind climate parameters used as a basis for the design should be representative of the long-term wind conditions. The DNV-OS-J101, 2014 recommends that these studies should cover a long period of time, preferably 10 years or more. Statistical methods are adopted to determine the wind parameters. In general, a Weibull distribution well represents the arbitrary 10-minute mean wind speed U_{10} at a given height z. The corresponding cumulative distribution function (CDF) can be written in the following form:

$$F_{U_{10}}(u) = 1 - e^{-(\frac{u}{A})^k} \tag{2.3}$$

Where the scale parameter A and the shape parameter k depend on the site and the height.

From this function, the annual maximum 10-minute mean wind speed can be approximated by the following expression:

$$F_{U_{10,max},1year}(u) = (F_{U_{10}}(u))^N \tag{2.4}$$

where N is the number of 10-minute intervals during 1 year, and it is equal to 52595.

From the obtained function, the 10-minute mean wind speed with return period T_R in unit of years can be determined. It corresponds to $(1 - 1/T_R)$ quantile in the distribution of the annual maximum 10-minute mean wind speed. In other terms, it is the 10-minute mean wind speed whose probability of exceedance in one year is $1/T_R$. It is denoted U_{10,T_R} and obtained by applying the following equation:

$$U_{10,T_R} = F^{-1}_{U_{10,max},1year}(1 - 1/T_R) \tag{2.5}$$

This methodology permits the determination of the 50-year 10-minute mean wind speed $U_{10,50}$ and the 100-year 10-minute mean wind speed $U_{10,100}$, which correspond respectively to the quantiles 0.98 and 0.99 in the cumulative distribution of the annual maximum 10-minute mean wind speed. These speeds are typically used in wind turbine design for extreme sea states. Practically, the arranged formulation to obtain 10-minute mean wind speed with return period T_R becomes:

$$U_{10,T_R} = A\Big(- \ln\Big(1 - (1 - 1/T_R)^{1/N}\Big)\Big)^{1/k} \tag{2.6}$$

- Wave conditions:

  Waves are irregular and random in shape, height, length, and speed of propagation (DNV GL, 2014). Hence, the wave conditions should be described by a stochastic method applying wave spectra. Similar to wind climate, the determination of wave parameters and the consideration of long-term wave conditions require statistical methods which cover a sufficiently long period of time, preferably 10 years or more (according to DNV GL, 2014).

  The wave climate is represented by the significant wave height H_S and the spectral peak period T_P. H_S is defined as the average height (trough to crest) of the highest one-third waves over a defined period (generally 3 hours). In the short term, for 3 hours for example, defined parameters H_S and T_P are assumed to be constant. The irregular sea states should be described by a wave spectrum, which shows the power spectral density function of the vertical sea surface displacement. The Pierson-Moskowitz (PM)

spectrum and JONSWAP spectrum are the most commonly used models (Pierson and Moskowitz, 1964; Hasselmann et al., 1973). The JONSWAP spectrum extends the PM spectrum, which is originally proposed for fully developed seas. Both spectra describe "wind sea" conditions, where waves depend on the local wind. These spectra are presented in the Figure 2.4a, which shows that the peak of wave frequency is about 0.15 *Hz*. The Figure 2.4b is based on the PM spectrum and permits the determination of the wave parameters according to mean wind speed at a level of 10 *m*.

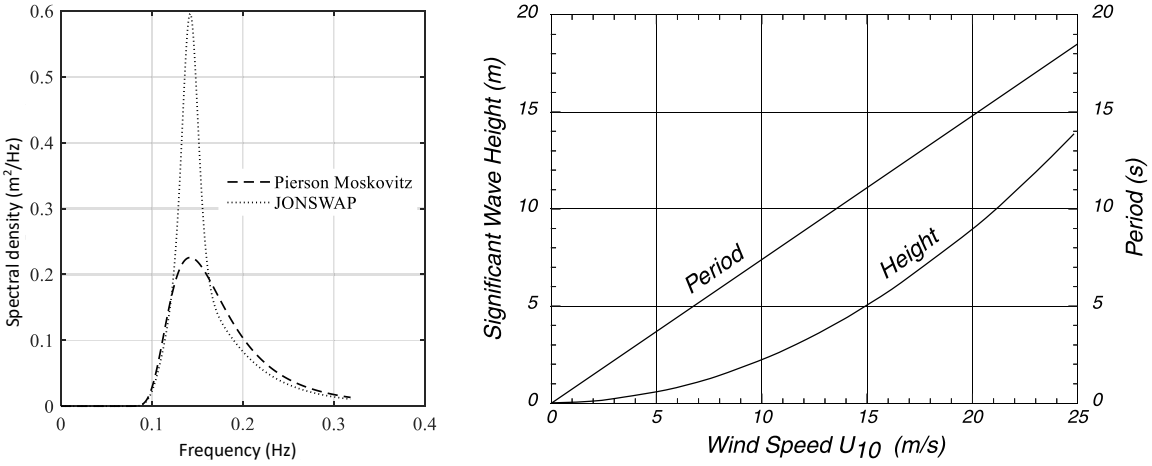

(a) (b)

Fig. 2.4.: (a) PM and JONSWAP spectra for H_S=1.5 *m* and T_P= 5 *s*; (b) H_S and T_P of a fully developed sea calculated from the PM spectrum.

As for wind climate, a Weibull distribution is adopted. It permits to obtain representative parameters of long-term wave conditions. The significant wave height H_S replaces the 10-minutes mean wind speed U_{10} in the three previous equations (2.4, 2.5, and 2.6), and N becomes equal to 2922 (number of 3-hours intervals in one year).

The maximum wave height H_{max} in a sea state should be estimated to check the offshore wind turbine stability during extreme scenarios. Empirical relations are proposed in DNV GL AS, 2016 to estimate the mean and the mode of the highest wave in the record of waves during a sea state. It is common to use the highest wave mode (rather than the mean), which is assumed to be given by the following equation:

$$H_{max,mode} = \left(\sqrt{\frac{1}{2}\ln N}\right) H_S \tag{2.7}$$

where N is the number of cycles during a sea state. For a sea state of duration $T_S = 3$ hours, N is assumed to be about 1000. Practically, the ratio between maximum and significant wave height should be taken greater than 1.86.

Some essential wave parameters are defined to represent the long-term wave characteristics. This set of parameters forms the load scenarios used in the design of an offshore wind turbine. Usually, it is impossible to obtain the entirety of these parameters. Some correlations are proposed to estimate the missing parameters based on the other parameters:

- The ratio between the 50- and 1-year significant wave heights $H_{S,50}/H_{S,1}$ is approximately equal to 1.25.

- In the southern and central parts of the North Sea, experience shows that the ratio between the 100- and 50-year significant wave heights $H_{S,100}/H_{S,50}$ is approximately equal to 1.04 or 1.05.

- The wave periods T is assumed to be within the range given by:

$$11.1\sqrt{\frac{H_S}{g}} < T < 14.3\sqrt{\frac{H_S}{g}} \tag{2.8}$$

This section aims to provide a general view of the methodology adopted to evaluate the short and long-term environmental conditions and then determine the design parameters. For deeper studies, more details are available in the following references: DNV-OS-J101, 2014, Van der Tempel, 2006, Stewart, 1987, Burton et al., 2011, and IEC-61400-1, 2005.

Calculation method of environmental loading

After identifying the parameters essential to the design, calculation methods should be applied to estimate loads acting on an offshore wind turbine. The relevant methodology to determine wind and wave loads are summarized below.

- Wind load

  From the spectra of wind turbulence represented in Figure 2.3, the frequency of the wind turbulence peak is much lower than the typical natural frequency of an offshore wind turbine, which is approximately equal to $0.2\ Hz$ (as seen in Chapter 1). Hence, the wind loading is considered as a quasi-static loading, composed of a mean wind speed and a turbulent component, and applied at the level of the rotor center. The corresponding formulation of the thrust force on a wind turbine has the following form:

$$F_{wind} = \frac{1}{2}\rho_a A_R C_T (U_R + u)^2 \tag{2.9}$$

Where A_R is the swept area of the rotor, C_T is the thrust coefficient, and ρ_a is the density of air. U_R is the rated wind speed, the higher band of the wind speed range within which the turbines operate normally and beyond which the pitch control alleviates the loading, and u is the turbulence component. In this range, C_T is assumed as follows (with U_R in *m/s*):

$$C_T = \frac{3.5(2U_R + 3.5)}{U_R^2} \tag{2.10}$$

The turbulent component of the wind speed depends on the considered load scenario. Arany et al., 2017 presents the methodology of its estimation following IEC-61400-1, 2005.

- Wave load

The spectra of waves represented in Figure 2.4a show that the peak frequency of waves is close to the typical offshore wind turbine natural frequency. Hence, the wave loading is considered as a dynamic loading. The determination of wave loading starts by assuming that the wave-particle motion follows the linear (Airy) wave theory. The equation of surface elevation is:

$$\eta = \frac{H}{2}\cos\left(\frac{2\pi t}{T} - kx\right) \tag{2.11}$$

where H is the wave height, T is the wave period, k is the wave number related to the wave length through $2\pi/L$, t is time in seconds, and x is the horizontal distance from the pile.

Similarly, the velocity w and the acceleration $\dot{w}$ at time t and at distance x from the origin (the monopile) are given by the following equations:

$$w = \frac{\pi H \cosh\left(k(S+z)\right)}{T\sinh(kS)}\cos\left(\frac{2\pi t}{T} - kx\right) \tag{2.12}$$

$$\dot{w} = \frac{-2\pi^2 H \cosh\left(k(S+z)\right)}{T^2\sinh(kS)}\sin\left(\frac{2\pi t}{T} - kx\right) \tag{2.13}$$

where z is the water level above the mudline, S is the mean water depth and k, defined above, can be obtained depending on wave period from the following dispersion relation:

$$w^2 = gk\tanh(kS) \quad \text{with} \quad w = \frac{2\pi}{T} \tag{2.14}$$

Where g is the gravity acceleration. Then, Morison's equatio (Morison et al., 1950) computes the drag force F_D and the inertia force F_I on a unit length strip of the submerged pile dl:

$$dF_{wave} = dF_D + dF_I = \left(\frac{1}{2}\rho_w D_P C_D w|w| + \frac{1}{4}\pi\rho_w D_P^2 C_m \dot{w}\right) dl \tag{2.15}$$

where D_P is the diameter of the pile and ρ_w is the density of water. C_D and C_m are respectively the drag and inertia coefficients depending on the pile diameter, pile material, and wave height. Calculation methods for these coefficients are shown in DNV GL, 2014.

The maximum inertia force occurs at $t = 0$ and $\eta = 0$ whilst the maximum drag force occurs at $\eta = H/2$ and $t = T/4$. For conservative reason, the maximum components are added directly. After performing the integration along the submerged pile, the final formulations of force and moment induced by the waves become:

$$F_{wave} = F_{D,max} + F_{I,max} \tag{2.16}$$

$$F_{D,max} = \left(\frac{1}{2}\rho_w D_P C_D \frac{\pi^2 H^2}{T^2 \sinh^2(kS)}\right)\left(\frac{e^{2k(S+\eta)} - e^{-2k(S+\eta)}}{8k} + \frac{S+\eta}{2}\right)$$

$$F_{I,max} = \left(\frac{1}{2}\rho_w D_P^2 C_m \frac{\pi^3 H}{T^2 \sinh^2(kS)}\right)\left(\frac{\sinh(k(S+\eta))}{k}\right)$$

$$M_{wave} = M_{D,max} + M_{I,max} \tag{2.17}$$

$$M_{D,max} = \left(\frac{1}{2}\rho_w D_P C_D \frac{\pi^2 H^2}{T^2 \sinh^2(kS)}\right)\left(\left(\frac{S+\eta}{8k} - \frac{1}{16k^2}\right)e^{2k(S+\eta)} - \left(\frac{S+\eta}{8k} - \frac{1}{16k^2}\right)e^{-2k(S+\eta)} + \left(\frac{S+\eta}{2}\right)^2 + \frac{1}{8k^2}\right)$$

$$M_{I,max} = \left(\frac{1}{2}\rho_w D_P^2 C_m \frac{\pi^3 H}{T^2 \sinh^2(kS)}\right)\left(\left(\frac{S+\eta}{2k} - \frac{1}{2k^2}\right)e^{k(S+\eta)} - \left(\frac{S+\eta}{2k} - \frac{1}{2k^2}\right)e^{-k(S+\eta)} + \left(\frac{1}{k}^2\right)\right)$$

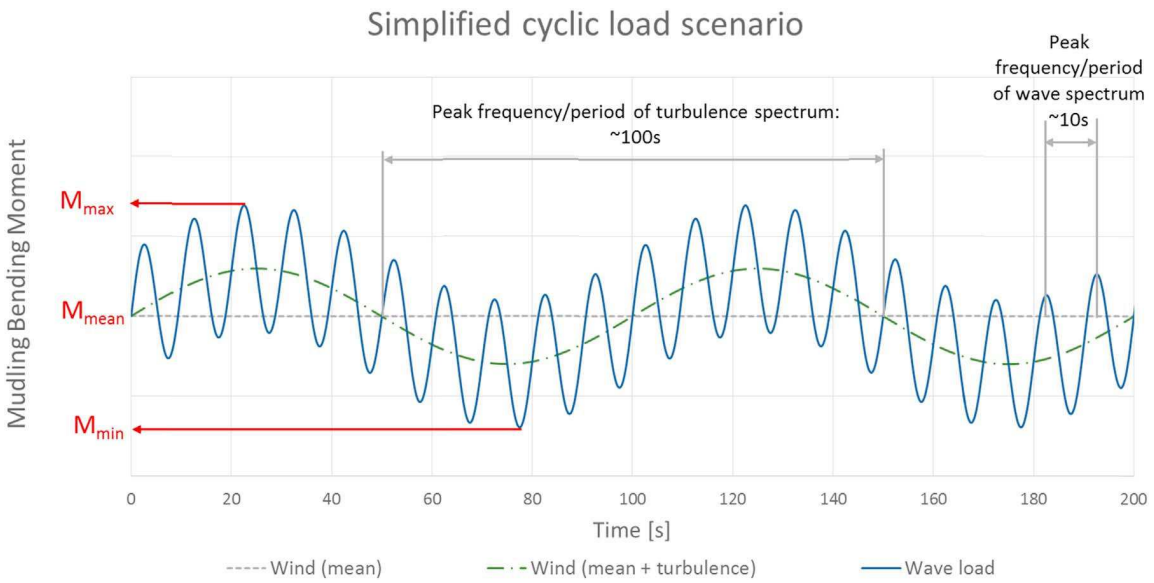

Fig. 2.5.: Schematic of global simplified loading following Arany et al., 2017

Finally, the global loading acting on an offshore wind turbine is assumed to be an addition of quasi-static wind loading and dynamic wave loading (Figure 2.5). The equivalent eccentricity of resulting force can be determined based on the forces matrix (for more details, refer to kerner, 2017).

Relevant research efforts

Generally, the environmental cyclic loading takes a sinusoidal form. The characteristics of this loading depend on the wind turbine dimensions, environmental conditions on the site location, and studied load case. The cyclic loading can be a one- or two-way loading. To characterize the cyclic loading, LeBlanc et al., 2010 defines the two following parameters:

- Parameter ζ_b (cyclic magnitude ratio; Truong et al., 2018) normalizing the loading amplitude by dividing the maximum moment by the static moment capacity of the foundation (M_{ult}).

$$\zeta_b = \frac{M_{max}}{M_{ult}} \tag{2.18}$$

- Parameter ζ_c (cyclic load ratio; Truong et al., 2018) quantifying the characteristics of the cyclic loading. It is defined as the ratio of minimum and maximum moment. It gives 1 for static loading, 0 for one-way loading, and -1 for two-way loading.

$$\zeta_c = \frac{M_{min}}{M_{max}} \tag{2.19}$$

Basing on the environmental data of 12 wind farms, Jalbi et al., 2019 estimates the loading characteristics of 15 offshore wind turbines. They adopted the methodology presented in Section 2.1.1 and determined the loading characteristics of three extreme load cases shown in Table 2.1 ($E-1$, $E-2$, and $E-3$). The obtained results for 3.0 *MW* and 3.6 *MW* wind turbines are shown in the Figure 2.6.

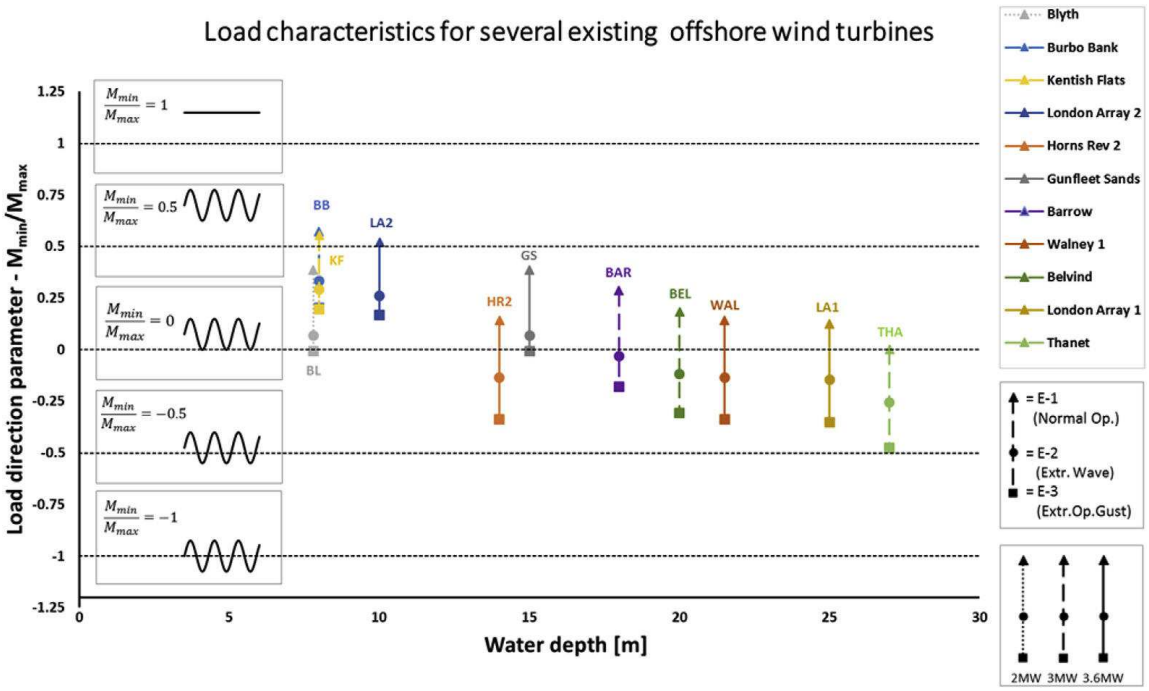

Fig. 2.6.: M_{min}/M_{max} for different load cases for 3.0 MW and 3.6 MW wind turbines from Jalbi et al., 2019

Furthermore, Jalbi et al., 2019 determines the load characteristics of large wind turbines (Vestas V164 8.0 *MW* and the DTU reference 10 *MW* wind turbines) in the same site conditions. Then, the same methodology is applied, and similar results are obtained.

The number of studied cases and the variability of water depth covered by Jalbi et al., 2019 conduct to some significant insights in the prediction of loading characteristics:

- ζ_b varies between 5% and 20% for normal operational conditions.

- In general, especially in normal operational conditions and shallow water, wind loading dominates, leading to one-way loading in most cases.

- The deep water level of the site and the extreme environmental conditions promote the effect of wave loading. Hence, ζ_c tends to decrease, leading to a two-way loading in some cases.

- The study extended to large wind turbines shows almost similar findings in terms of ζ_c. However, this kind of wind turbines should be installed on deeper water and then the wave loading effect would become more dominant.

2.1.2 Monopile foundation and design considerations

Monopile foundation

Due to economic and practical reasons, monopile foundations are commonly used in the wind energy domain. In Europe, monopile foundations represent 81.2% of wind turbine foundations installed in 2020 (Wind Europe, 2020). Initially, the monopile foundations are adopted in shallow and intermediate water while alternative solutions, e.g. jacket/tripod, floating spar, etc. are adopted in relatively deep water. After decades of experience and proven performance, monopiles have become an attractive option for larger turbines and deeper water.

Offshore wind turbine monopile foundation is characterized by a large diameter and small length to diameter ratio (L/D). Nowadays, monopiles have diameters up to 8 m, length to diameter ratio ranging between 3 and 6, and thickness of about 100 mm (Sorenson et al., 2017, Schroeder et al., 2015). The Figure 2.7 shows the dimensions of these monopiles. The diameter of the next generation of offshore wind turbines is expected to exceed 10 m.

Fig. 2.7.: Fabricated monopile for Veja Mate offshore wind farm Windindustrie in Deutschland, 2016

Consequently, these specific forms and dimensions govern the monopile response under lateral loading: short or rigid piles tend to rotate while long or flexible piles tend to bend. Poulos and Hull, 1989 proposed criteria to classify the pile rigidity:

$$\frac{E_s L^4}{E_p I_p} \begin{cases} < 4.8 & \text{Rigid pile behavior} \\ > 388.6 & \text{Flexible pile behavior} \end{cases}$$

where $E_p I_p$ is the pile bending stiffness, E_s is the soil Young's modulus, and L is the embedded length of the monopile. It can be suggested that a perfectly rigid pile response mainly depends on the length to diameter ratio (L/D) while a perfectly flexible pile response depends more on the bending stiffness $E_p I_p$ (Peralta and Achmus, 2010, Dietrich, 1982). Figure 2.8 shows a schematic of different types of pile response.

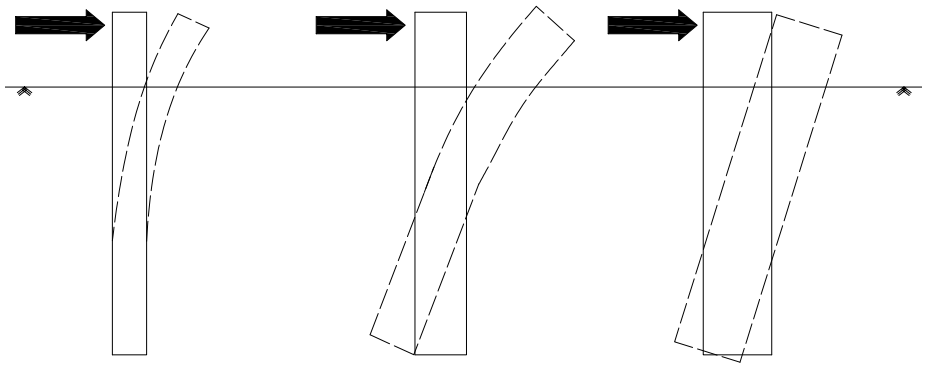

Fig. 2.8.: Schematic of different pile behaviors: flexible (left), semi-rigid (middle), and perfectly-rigid (right)

Most current wind turbines' monopiles have flexible to semi-rigid behaviors, while the trend is moving to smaller length to diameter ratios and thus to more rigid behavior in the future.

Design limit states

The foundation design aims to ensure stability and serviceability. Therefore, some limitations are defined, which lead to the required performance of the overall structure. In the case of offshore wind turbine monopile foundation, these limitations are the following:

- Ultimate limit state (ULS): the maximum loads acting on the monopile foundation must not exceed its ultimate capacity. The DNV-OS-J101, 2014 and the IEC-61400-1, 2005 provide numerous load cases to estimate the maximum loads and recommend applying a safety factor of 1.35 to environmental loads. The criterion to define the

ultimate lateral capacity of rigid monopiles is still ambiguous: $2°$ of pile rotation or $0.1D$ of displacement at the mudline are commonly used (refer to Chapter 7).

- Service limit state (SLS): the repeated cyclic loading could induce excessive deformations and then affect the serviceability of the structure. The guides (e.g. DNV-OS-J101, 2014) define some limitations in terms of deflection and rotation. Initial rotation and permanent accumulated rotation should be within an allowable limit, which is currently equal to $0.25°$ (initial + accumulated $< 0.5°$). Besides, initial deflection and permanent accumulated deflection at mudline level should be within an allowable limit which is currently equal to 0.1 *m* (initial + accumulated < 0.2 *m*). The corresponding number of cycles differs according to considered load scenarios and their occurrence during the design lifetime.

- Fatigue limit state (FLS): the effect of repeated loads of small amplitude along the design lifetime could lead to failure. Over the lifetime of an offshore wind turbine, the number of environmental loads cycles can exceed 10^8 cycles.

On another side, due to the dynamic sensitivity of offshore wind turbines, the system's natural frequency (foundation and structure) should be within an allowed range (as seen in Chapter 1). Over the structure lifetime, the system's natural frequency should maintain a margin of at least 10% with the excitation frequencies.

Relevant load scenarios

The design starts by defining the critical load cases of offshore wind turbine foundations. The long-term behavior of the monopile foundation should be regarded as one of the principal objectives of this thesis. A load case recommended by DNV-OS-J101, 2014 for the fatigue limit state (FLS) is characterized by environmental parameters generated from normal sea state and normal turbulence models at 10-min mean wind speed. It is specified by a relatively small load, considered acting along the lifetime of the structure ($F-1$; Table 2.1). For more severe load scenarios, Jalbi et al., 2019 focus on the prediction of cyclic loading characteristics and regard three extreme load cases considering them the most relevant to foundation design($E-1$,$E-2$, and $E-3$; Table 2.1).

It should be noted that wind and wave loads are considered unidirectional in the framework of this thesis.

According to DNV-OS-J101, 2014, the most severe wind and wave scenarios have a negligible chance to occur at the same time. Therefore, extreme wave load scenario $(E-2)$ and extreme wind load scenario $(E-3)$ are considered the most critical load cases to verify the ultimate limit state (ULS).

Tab. 2.1.: Relevant load scenarios to the design of an offshore wind turbine from DNV-OS-J101, 2014; Jalbi et al., 2019

Load scenario	Wind model	Wave model
Fatigue load scenario $F-1$	Normal turbulence model (NTM) at U_{10}	Normal sea state NSS (H_S)
Normal operational conditions $E-1$	Normal turbulence model (NTM) at U_R	1-Year extreme sea state ESS ($H_{S,1}$)
Extreme wave load scenario $E-2$	Extreme turbulence model (ETM) at U_R	50-Year extreme wave height EWH ($H_{m,50}$)
Extreme wind load scenario $E-3$	Extreme operating gust (EOG) at U_R	1-Year extreme wave height EWH ($H_{m,1}$)

Analysis of monopile foundation

The design of a wind turbine monopile foundation implies to check the defined design limits. In this context, theoretical and numerical methods are developed to analyze the response of monopile foundations:

- The first method is based on the soil resistance to the movement of the rigid monopile. Based on the theoretical pressure distribution along the embedded depth of the monopile proposed by Parsad and Chari, 1970, and the front earth pressure and the side shear around the monopile proposed by Smith, 1987. An equilibrium equation is determined, which can be solved to estimate the ultimate capacity of the monopile. This method serves to verify the ultimate limit state only. For more detail, refer to Section 7.1.2.

- The second method, called "macro-element model", represents the foundation by springs at the soil surface (Figure 2.9a; Nova and Montrasio, 1991). This method is simple and computationally fast, but it is considered the least accurate. As a type of foundations, numerous macro-element models are proposed for monopiles, some of them being developed to capture the cyclic behavior: Correia et al., 2012, Li et al., 2016, Carstensen et al., 2018, Page et al., 2018... These models are generally validated against a 3D Finite Element model and have proven good performance. Besides, aiming to evaluate the dynamic stiffness of monopiles foundation, formulas depending on monopile and soil properties are defined. A literature review of these formulas is presented by Arany et al., 2017.

- The third method, called "Winkler model", represents the monopile as a beam and the soil-pile interaction response as independent lateral springs (Figure 2.9b, Winkler, 1867). It is computationally fast and considered a practical method, compromising between

time and accuracy. A nonlinear p-y curve governs the response of each uncoupled spring. The p-y curves depend on the soil profile and pile geometry. This method was originally validated against large-scale field tests on long flexible piles (Cox et al., 1974; Reese, 1974). Then, this method was recommended by the API and DNV design guidelines for the design of wind farm's monopiles in cohesionless soil (DNV-OS-J101, 2014, API (American Petroleum Institute), 2010). A degradation coefficient is recommended to be applied to the proposed p-y curves considering the cyclic effect. In the last years, "SOLCYP" joint industry project focused on flexible piles and proposed an approach to degrade the p-y curves with empirical expressions depending on cycle number and cyclic amplitude (Puech and Garnier, 2017). The efficiency of this method on short rigid piles was reviewed, especially in the case of relatively small length to diameter ratios (Alderlieste et al., 2011, Doherty and Gavin, 2012, Byrne et al., 2017, Igoe et al., 2018). Recently, substantial efforts are devoted to propose new p-y curves, including additional components of the soil reaction, whose omission is at the basis of the deficiency of conventional p-y method (Byrne et al., 2020a). Due to the reasonable computation time, a similar 1D hyperplastic model is developed to simulate the cyclic behavior of the monopile foundations. This model is based on multi-surface kinematic plasticity and ratcheting element, and informed by experimental findings from physical modeling (Houlsby et al., 2017). Besides, a new 1D hypoplastic spring element is proposed and validated against 3D FE-modeling of a limited number of cycles (Carstensen et al., 2018).

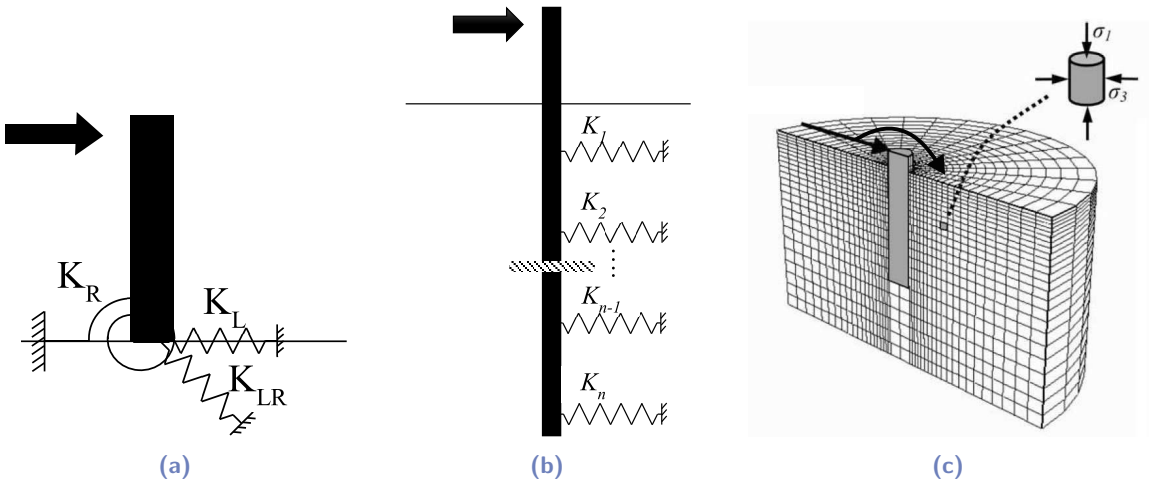

Fig. 2.9.: Schematic representation of different numerical methods to simulate monopile response:(a) "macro-element model"; (b) "Winkler model" from kerner, 2017; (c) "FEM model" from Achmus et al., 2009

- The last method is the Finite Element analysis of the pile surrounded by the soil mass (Figure 2.9c). The performance of this method depends on the appropriateness of the constitutive model and input soil parameters. After providing these conditions, it is considered the most accurate numerical modeling method. However, the long computation time is still a serious drawback of this method. Numerous constitutive models are capable of simulating the monotonic response. However, additional research efforts

are still required to simulate the complex cyclic behavior of cohesionless soil. Achmus et al., 2009 proposed the idea of a degradation stiffness model where the degradation of the secant stiffness of the soil induces an accumulation of displacements. The rate of degradation is calibrated depending on soil profile, pile geometry, and loading characteristics. This model provides reasonable results without simulating the realistic behavior. Besides, "Hardening soil model with small-strain stiffness" and "Hypoplastic model with intergranular strain concept" show a good performance comparing over a limited number of cycles (Sheil and McCabe, 2017). Recently, a critical state-bounding surface model "SANISAND04" shows a reliable simulation of sand behavior under high number of cycles (Liu et al., 2019a). Due to the expensive computation time, applying these models in the wind turbine domain is unrealistic using the actual available techniques. Explicit modeling seems to be a reasonable solution, for exampleNiemunis et al., 2005 proposed the high cycle accumulation model. It consists of an implicit model to simulate the first cycle and an empirical model to capture the ratcheting response. This model is also implemented in 1D models and applied to monopile foundations Wichtmann et al., 2017. Besides, aiming to overcome the computational time challenge, Abadie et al., 2020 presented a numerical method for modeling the cyclic response of monopiles until large cycle numbers, by combining the *PISA* design model for monotonic response (Byrne et al., 2019) and the HARM framework (*0D* macro-element model for cyclic loading; Abadie et al., 2017, Houlsby et al., 2017). On another side, sustained efforts are conducted to reach advanced geotechnical modeling to consider the monopile response subjected to irregular cyclic loading (Pisanò, 2019).

As seen before, serious difficulties hinder the development of a numerical model capable of simulating efficiently the cyclic response of a rigid monopile foundation subjected to lateral loading. Widely adopted methods are the empirical relationships for ratcheting and evolution of cyclic stiffness as the function of the cycles number and the system conditions (e.g. loading characteristics, soil profile). These relationships are presented by LeBlanc et al., 2010 and Klinkvort and Hededal, 2013 basing on smale-scale models. Recently, several scale models are developed to verify the validity of these relationships and extending them to larger variety of testing conditions (Arshad and O'Kelly, 2016, Albiker et al., 2017, Abadie et al., 2019, Frick and Achmus, 2020...). In addition, cyclic contour diagram is generated by Bayton et al., 2018 to predict the cyclic response of the monopile model in dry sand. This diagram permits to estimate the accumulative rotation depending on the loading characteristics (ζ_b and ζ_c) and number of cycles (Figure 2.10).

These empirical methods seem to be relevant in verifying the design serviceability. However, a definitive design method still requires some additional efforts:

- Calibration method against pile geometry and soil profile.
- Consideration of the complexity of loading and the dynamic aspect.

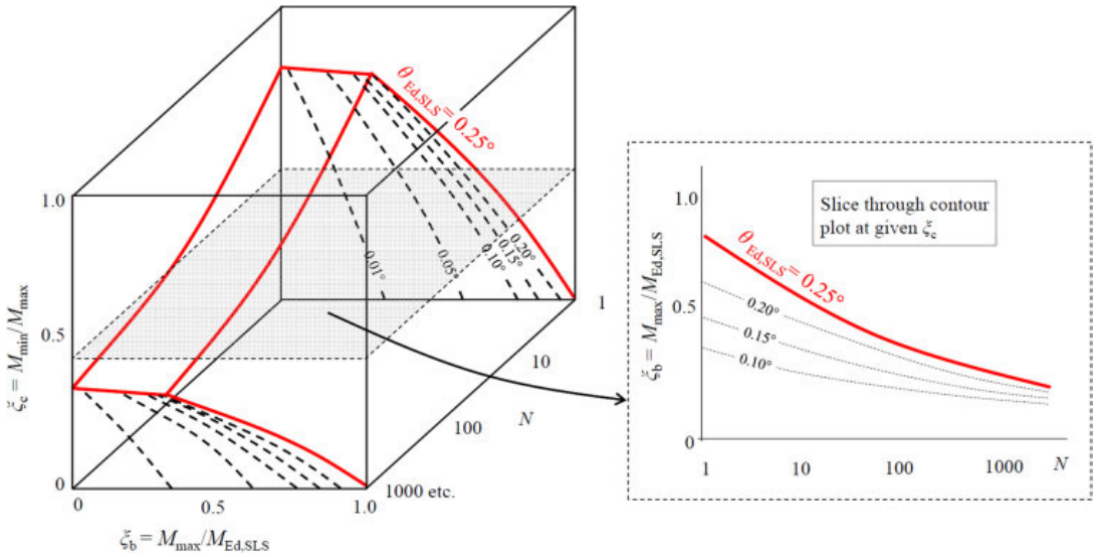

Fig. 2.10.: Illustrative cyclic accumulation contour plot from Bayton et al., 2018

2.1.3 Physical modeling

Generalities on physical modeling

Full-scale modeling can be considered a particular case of physical modeling, able to simply simulate the realistic parameters underlying the behavior of the prototype. It is the most accurate way to determine the key mechanisms of any geotechnical problem, and validate numerical or theoretical models. However, several experiments are required to calibrate a theoretical model. Furthermore, to ensure the reliability of any representative model, the repeatability of experiments should be verified. Physical modeling is thus associated to enormous cost and time needed to perform numerous models, which constitutes a hindrance to its adoption.

Due to the limitations of full-scale modeling, physical modeling in the geotechnical domain has been oriented toward small-scale laboratory models. Two main techniques are adopted to perform experiments: unit gravity (1-g) and geotechnical centrifuge (n-g).

The centrifuge technique involves performing the test in a specific container, rotating around a vertical axis. This rotation induces artificial gravity depending on the rotational velocity. The main idea is to produce similar stresses between the prototype and the scale model and then obtain similar soil behavior. This idea solves a principal challenge in geotechnical modeling and permits enhancing the reliability of obtained results. Reversely, centrifuge modeling includes some limitations, where the limited size of the container imposes difficulties on the loading and monitoring systems.

The second technique is the unit gravity laboratory modeling, which means conducting tests at normal gravity in the laboratory. This technique is commonly used in the geotechnical field. It allows the realization of larger models, more complex loading and monitoring systems, and a higher number of tests. However, the low level of stresses encountered imposes practical difficulties. First, this difference in stress levels should be compensated by appropriate scaling laws, to obtain significant results. Second, experimental variability (system mounting, vibrations, ...) becomes more influential and affects repeatability.

State of art: Relevant research efforts

Every phenomenon involves a set of variables, which should be consciously regarded to obtain a representative scale model. The methodology adopted to scale the prototype is defined as "Scaling laws". As the centrifuge modeling is able to conserve the realistic stress level, and then the soil behavior, it is characterized by relatively light scaling laws. In addition to the dimensions, these laws consider other parameters depending on the tackled problem (time, fluid viscosity, permeability,...). Centrifuge scaling laws are discussed in some relevant works (Corté, 1989, Wood, 2006, Garnier et al., 2007, McNamara and Klinkvort, 2018,...). In the framework of this study, the 1g scaling is adopted. This method includes additional laws, aiming to compensate for the variation of the stress level between the prototype and the scale model. Numerous 1g scale models have been developed to study the behavior of relatively rigid monopiles subjected to cyclic loading, and different scaling laws have been proposed. Most of these works ignore the dynamic aspect of the OWT foundation, considering the problem as a quasi-static loading of a rigid monopile without modeling the OWT structure. According to scaling methodology, these scale models can be divided into two main categories:

- Scaling based on dimensionless groups:

  The simplest way to obtain a representative scale model is to apply scale factors to all governing variables, which is practically impossible. Hence, the Buckingham π theorem is applied in this domain. "Buckingham π theorem" (Buckingham, 1914) constitutes the base of dimensional analysis: *if a problem involves m physical variables, including l independent quantities, $m - l$ dimensionless parameters governing this problem can be deducted*. Therefore, two models having different scales but similar dimensionless parameters behave identically. In parallel, a method called the "Buckingham π method" is commonly used to determine the dimensionless group. The first step is to list all the variables of this problem (m variables). Then, select "repeating" or "governing" variables (l variables), which are used to nondimensionalizing the remaining variables ($m - l$ variables). The application of this method presents some difficulties: the selection of "repeating variables" and the adoption of the optimal functional form of the dimensional group from $m - l$ possible forms. Peralta and Achmus, 2010 used this method and

determined a set of dimensionless parameters , which are adopted later on by several works: Albiker et al., 2017, Frick and Achmus, 2020, ...

Based on Kelly et al., 2006, LeBlanc et al., 2010 started from a fundamental equation of laterally loaded monopile response and reforms it to obtain a normalized equation, leading to deduct a set of dimensionless parameters. This work is considered the base of several other works: Roesen et al., 2013, Abadie et al., 2019, Richards, 2019, ...

The details of these dimensionless groups are presented in Table 2.2.

Tab. 2.2.: Literature review of relevant dimensionless groups

Dimensionless parameters	Peralta and Achmus, 2010	LeBlanc et al., 2010
Moment	-	$\frac{M}{L^3 D\gamma'}$
Axial load	-	$\frac{V}{L^2 D\gamma'}$
Lateral load	$\frac{H}{L^3\gamma'}$	$\frac{H}{L^2 D\gamma'}$
Rotation	-	$\theta\sqrt{\frac{p_a}{L\gamma'}}$
Eccentricity	$\frac{e}{L}$	$\frac{M}{HL}$
Pile rigidity	$\frac{EI}{L^5\gamma'}$	-
Length to diameter ratio	$\frac{L}{D}$	$\frac{L}{D}$
Soil similarity	n	ϕ'_p

H: lateral load, V: vertical load, M: moment, L: embedded length, D: monopile diameter, e: loading eccentricity, EI: bending stiffness, θ: rotation, p_a: atmospheric pressure, γ': effective unit weight, n: sand porosity, ϕ'_p: peak friction angle

The common points of the two groups are pile length to diameter ratio and loading eccentricity. The dynamic aspect of an OWT structure was disregarded in the two approaches by adopting a low loading frequency, which corresponds to the frequency of wind and waves. LeBlanc et al., 2010 has changed the density index of soil used in the laboratory model to maintain the same sand behavior as the prototype soil (Bolton, 1986), whereas Peralta and Achmus, 2010 has conserved the same density index (or porosity n). Besides, Peralta and Achmus, 2010 conserved the same pile rigidity in terms of rigidity factor (Poulos and Hull, 1989), whereas LeBlanc et al., 2010 passed to perfectly rigid case.

- Scaling based on scale factors:

Another methodology is adopted to generate scaling laws. It consists of defining the fundamental scale factors, identifying the parameters governing the main physical phenomena

affecting the behavior, and then linking these parameters to the fundamental scale factors. A scale model is considered representative of the prototype when all governing laws of similitude (Scaling laws) are satisfied. Based on this methodology, Wood, 2006 has carried out a rigorous revision of the scaling laws of physical geotechnical modeling.

In the domain of offshore wind turbines, Cuéllar, 2011 has adopted this methodology to define a set of scaling laws. The aim was to design a 1g scale model capable of simulating the qualitative behavior of a laterally loaded pile in saturated sand. Cuéllar, 2011 started by defining two fundamental scale factors:

- Scale factor for length: $\lambda_L = \frac{L_{model}}{L_{prototype}} = \frac{L_m}{L_p}$

- Scale factor for acceleration relative to 1g modeling : $\lambda_g = \frac{g_m}{g_p} = 1$

Then the scale factors corresponding to governing parameters are determined in function of the defined scale factors. Cuéllar, 2011 has used a soil identical to the prototype, so that the scale factor for density defined by Wood, 2006 was ignored. Table 2.3 summarizes the scaling laws obtained for relevant physical quantities.

The scaling laws adopted by Cuéllar, 2011 satisfy the similarity of pile length to diameter ratio, loading eccentricity, pile rigidity, and loading level. Contrary to all previous works, this set of scaling laws regards the loading frequency. However, Cuéllar, 2011 has used the same prototype soil, ignoring the effect of the low-stress level on soil behavior. Also the system natural frequency was disregarded, which affects the simulation of its dynamic response.

Despite the dynamic sensitivity of an offshore wind turbine, rare works include the dynamic aspect while studying the behavior of the system's foundation. One of these works is the specific group of similitude relationships proposed by Bhattacharya et al., 2011. A dimensional analysis starts with the identification of main physical mechanisms to develop a set of dimensionless groups. Bhattacharya et al., 2011 has worked with saturated kaolin clay as soil mass. In order to simulate the system dynamics, Bhattacharya et al., 2011 conserved the ratio between the loading frequency and the system natural frequency. Table 2.4 presents the considered main physical mechanisms and the corresponding dimensionless groups. This set of dimensionless groups are adopted later in some works: Yu et al., 2015, Liang et al., 2020...

Tab. 2.3.: Scaling laws adopted by Cuéllar, 2011

Physical quantity	Scaling Law
Length (L)	$\frac{1}{\lambda_L}$
Force (F)	$\frac{1}{\lambda_L^3}$
Distributed line load (q)	$\frac{1}{\lambda_L^2}$
Stress (σ)	$\frac{1}{\lambda_L}$
Unit weight (γ)	1
Moment (M)	$\frac{1}{\lambda_L^4}$
Bending stiffness (EI)	$\frac{1}{\lambda_L^5}$
Time (T)	$\frac{1}{\lambda_L^{0.5}}$
Frequency (f)	$\lambda_L^{0.5}$

Tab. 2.4.: Dimensionless groups proposed by Bhattacharya et al., 2011

Physical mechanism	Dimensionless group
Strain field in the soil and cyclic stress ratio (CSR)	$\frac{P}{GD^2}$
Rate of loading	$\frac{k_h}{f_f D}$
System dynamics	$\frac{f_f}{f_n}$
Bending strain in the monopile	$\frac{Py}{ED^2t_w}$
Fatigue in the monopile	$\frac{Py}{\sigma_y D^2 t_w}$

P: lateral load, y: loading eccentricity, D: monopile diameter, G: soil shear modulus, k_h: horizontal coefficient of soil permeability, f_f: loading frequency, f_n: natural frequency, t_w: monopile wall thickness, E: monopile Young's modulus, σ_y: monopile yield stress

Based on the same methodology, kerner, 2017 adopted a set of dimensionless groups to simulate the static and dynamic behavior of the system's foundation. kerner, 2017 performed two scale models at two different scales, aiming to deduct results at prototype scale. Table 2.5 presents the main physical phenomena and the corresponding dimensionless groups.

The presented works constitute an overview of the most relevant research efforts in this field. As shown, the scaling laws adopted to develop 1g scale models vary widely. Their adoption depends on the principal physical phenomena identified and the aim of the scale

model. Most of the works attempts to obtain a satisfying reproduction of pile response. The ways to achieve this goal differ, the varying physical quantities being:

- Pile length to diameter ratio (L/D)
- Pile rigidity $(E_s L^4/E_p I_p)$
- Effect of stress level on soil behavior

Tab. 2.5.: Dimensionless groups adopted by kerner, 2017

Physical mechanism	Dimensionless group
Pile rigidity	$\frac{E_s L^4}{E_p I_p}$
Lateral load	$\frac{H}{\gamma L^3}$
Ratio of pile diameter and soil grains diameter	$\frac{D_p}{D_{sand}}$
Static soil-structure interaction	$\frac{G L^4}{E_p I_p}$
Dynamic soil-structure interaction	$\frac{\rho_p A_p}{\rho_s L^2}$

H: lateral load, L: monopile embedded length, D_p: monopile diameter, $E_p I_p$: monopile bending stiffness, ρ_p: monopile density, A_p: monopile section, E_s: soil Young's modulus, G: soil shear modulus, D_{sand}: grain diameter, γ: unit weight, ρ_s: sand density

On another side, works that regarded the dynamic aspect are satisfied by the conservation of ratio between the excitation frequency and the system natural frequency, while they ignored the structure scaling, which affects the induced inertia force due to the dynamic sensitivity. Each considered phenomenon in physical modeling imposes some restrictions in dimensions, materials, or other model characteristics. Due to the numerous parameters governing the behavior of offshore wind turbines' foundations, the proposition of an adequate set of scaling laws still forms a serious challenge. Hence, the need for a more rigorous revision appears, especially for the dynamic aspect.

2.2 An overview of DTU 10 MW reference wind turbine

As seen in Chapter 1, the field of offshore wind turbines is growing exponentially. This growth appears clearly in the increase of the dimensions and capacities of these structures. In the framework of this thesis, scale models should be developed from realistic offshore wind turbines (prototype). Since research should be aimed at the future, the "DTU 10 MW reference wind turbine" is considered as the prototype in the current work. The North Sea or the North Atlantic Ocean (coastal zone of France) with a water depth of 35

m (relatively deep water) are chosen as site locations to install these wind turbines. It is supposed that the soil profile consists in a dense sand layer. The adopted foundation for this structure is a monopile foundation, which is generally considered for shallow and intermediate water depths. It is predicted to be characterized by a large diameter ($D \sim 7$ to 10 m) and small length to diameter ratio ($L/D \sim 2$ to 6). This section starts by displaying the standard dimensions of the "DTU 10 MW RWT" and the estimation of loads acting on this structure, and ends by proposing two monopile foundations. These two monopile foundations have respective diameters of 7.5 and 10 m. The capacity of smaller diameter monopile is compensated by increasing its length-to-diameter ratio. The aim is to investigate the feasibility of monopile foundations in deeper waters and to understand the behavior of the two foundations subjected to cyclic/dynamic loading.

2.2.1 Key parameters of DTU 10 MW reference wind turbine

Danish Energy Agency has founded the Light Rotor project to keep pace with the development of offshore wind turbines. The cooperation with Denmark Technical University (DTU) and Vestas Wind Systems led to establish the "DTU 10 MW Reference Wind Turbine", or in short *"DTU 10 MW RWT"*. It constitutes a design benchmark for future large offshore wind turbines. Based on Velarde, 2016 following a DTU wind energy report (Bak et al., 2013), Table 2.6 summarizes the key parameters of this reference wind turbine.

Tab. 2.6.: Key parameters of the DTU 10 MW reference wind turbine

Key parameters	Unit	Value
Wind regime	-	IEC Class 1A
Cut in wind speed	*m/s*	4
Cut out wind speed	*m/s*	25
Rated wind speed	*m/s*	11.4
Rated power	*MW*	10
Number of blades	-	3
Rotor diameter	*m*	178.3
Hub height	*m*	119
Rotor speed range	*rpm*	6 - 9.6
Rotor mass	*kg*	227,962
Nacelle mass	*kg*	446,036
Tower top diameter, thickness	*m*; *mm*	5.5; 20
Tower bottom diameter, thickness	*m*; *mm*	8.3; 38

The tower material is $S355$ steel, whose density is increased by 8%. The material properties are defined in Table 2.7.

The tower should be installed above the water level. It is connected to the monopile foundation via a transition piece. The platform height from mudline to the top of the transition piece is determined following DNV-OS-J101, 2014, as follows:

$$L_S = S + H_{m,50} + 0.2H_{S,50} \tag{2.20}$$

Where L_S is the length of the structure, S is the mean water depth, $H_{m,50}$ is the 50-year extreme wave height, and $H_{S,50}$ is the 50-year significant wave height.

Tab. 2.7.: Properties of tower material

Tower material property	Unit	Value
Density ρ	kg/m^2	8500
Yield strength σ_y	*MPa*	355
Young's modulus E	*GPa*	210
Poisson's ratio ν	-	0.3

2.2.2 Determination of wind and wave parameters

As seen before, the North Sea and the North Atlantic Ocean at water depths of 35 m (relatively deep water) are chosen as possible site locations to install these wind turbines. The first step is to determine wind and wave parameters representing the environmental conditions. Then, these parameters are the basis of the estimation of the environmental loading.

The DNV GL AS, 2016 recommends considering both wind sea and swell. Hence, the wind and wave data are regarded independently basing on realistic measurements. Guide recommendations and statistical methods are adopted to deduce representative short- and long-term wind and wave parameters for the site location.

Referring to Table 2.1, the wind speed adopted in the three load cases is the rated wind speed, which is equal to 11.4 *m/s* for *"DTU 10 MW RWT"*. This value is compared to actual average wind speeds at the site locations. The mean height of the rotor is about 135 *m* (see Section 2.2.1), the hub height is about 119 *m* without considering the additional height of the transition piece installed between the foundation and the structure. Following Coelingh

et al., 1996 and after analysis of wind speed observations over the North Sea, the mean wind speeds and statistical parameters over the period $1985 - 1992$ at three stations are shown in Table 2.8, together with the corresponding wind speeds at 135 m deduced basing on logarithmic and power laws seen in Section 2.1.1. The obtained wind speed ranges between 10 and 11 m/s. Besides, following Van der Tempel, 2006, Figure 2.11 shows the average annual wind speed for the North Sea and the North Atlantic Ocean. At these locations, the yearly average wind speed ranges between 8.5 and 10 m/s. The wind speeds deduced from the two methods and shown in Table 2.8 are in good agreement with the value of rated wind speed considered in the load cases (11.4 m/s).

Tab. 2.8.: Wind parameters based on observations over the North Sea following Coelingh et al., 1996

Station	Measuring height (m)	Mean wind speed (m/s)	Weibull parameters		Mean wind speed at 135 m (m/s)	
			Shape-	Scale-	Logarithmic	Power
$K13$	74.8	9.8	2.1	11.1	10.6	10.5
EPF	29.1	8.9	2.1	9.8	11.0	10.7
MPN	27.6	8.5	2.1	9.3	10.6	10.3

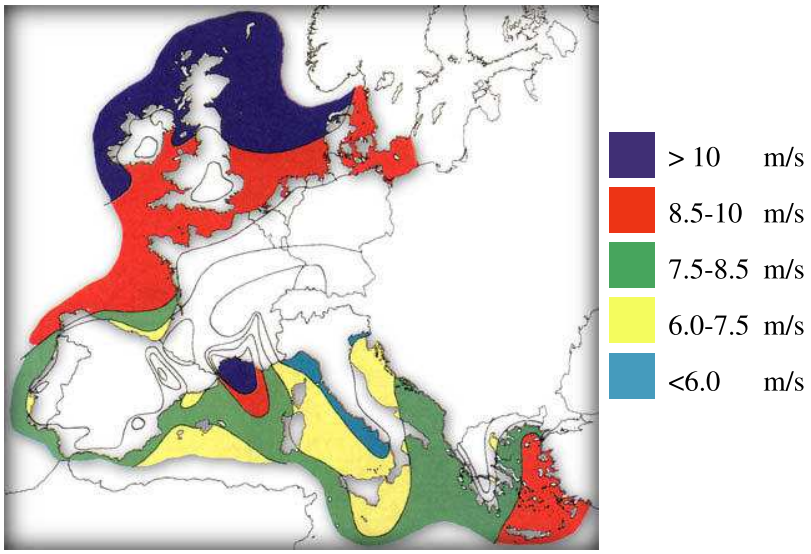

Fig. 2.11.: Yearly average wind speed at 100 m height for the European Seas following Van der Tempel, 2006

Similarly, wave parameters are deduced according to relevant statistical data and available maps. Firstly, Weibull parameters of significant wave heights for both locations are proposed by Shariff and Hadi Hafezi, 2012 and Galanis et al., 2012. These studies are based on surveying methods and satellite records. The essential wave parameters are deducted and

shown in Table 2.9. The obtained parameters are compared to a contour map of 100-significant wave height. This map is provided by the UK Department of Energy in terms of $H_{S,50}$ basing on NEXTRA model hindcast, and updated later in terms of $H_{S,100}$ by Health and Safety Executive (Williams, 2008). The deduced parameters are in good agreement with the contour values of the map displayed in Figure 2.12. Finally, moderate values are proposed and adopted to determine the corresponding environmental loads. These values are also reported in Table 2.9.

Tab. 2.9.: Wave parameters for North Sea (Shariff and Hadi Hafezi, 2012) and North Atlantic Ocean (Galanis et al., 2012)

Site	Mean H_S	Weibull parameters		$H_{S,50}$	$H_{S,1}$	$H_{S,100}$	$H_{m,50}$	$H_{m,1}$
	(m)	Shape-	Scale-	(m)	(m)	(m)	(m)	(m)
North Sea	1.34	1.434	1.478	8.30	6.64	8.72	15.49	12.49
North Atlantic Ocean	2.46	3.35	3.40	7.12	5.70	7.48	13.36	10.77
Proposed values	2.00			7.50	6.00	7.88	14.04	11.33

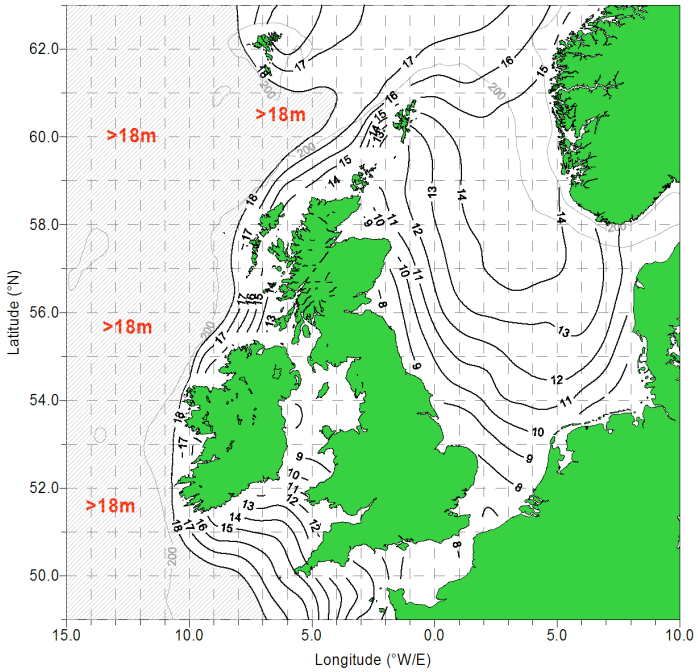

Fig. 2.12.: $H_{S,100}$ contour map of the North Sea

2.2.3 Estimation of loading characteristics

The methodology proposed to calculate environmental loads should be applied on *"DTU 10 MW RWT"*. The load cases of this study are shown in the Table 2.1.

The wave load acts on the transition piece; whose diameter is equal to the sum of pile diameter, two wall thicknesses of the transition piece, and two grout thicknesses. Following Arany et al., 2017, the total width of the grout and the transition piece is taken as $0.15\ m$. The drag and inertia coefficients are taken equal to 0.7 and 2, respectively, as conservative values in the framework of this thesis. The methodology presented in Section 2.1.1 is applied to determine the environmental loads acting on the "DTU 10 MW RWT" supported by monopiles of 7.5 and $10\ m$ in diameter. The adopted metocean data for the site locations are displayed in Table 2.10 and the characteristics of the loads obtained are presented in Table 2.11.

Tab. 2.10.: Metocean data

Parameter	Symbol	Unit	Value
Wind speed Weibull distribution scale parameter	A	m/s	11.1
Wind speed Weibull distribution shape parameter	k	-	2.1
Reference turbulence intensity	I	%	18
Turbulence integral length scale	L_k	m	18
Density of air	ρ_a	kg/m^3	1.225
Significant wave height	H_S	m	2.0
Peak wave period (Figure 2.4b)	T_P	s	7.0
Significant wave height with 50-year return period	$H_{S,50}$	m	7.5
Peak wave period with 50-year return period	$T_{S,50}$	s	9.7
Maximum mean water depth (during 50-year)	S	m	35
Density of water	ρ_w	kg/m^3	1030

According to the loading characteristics obtained (Table 2.11), the *"DTU 10 MW RWT"* installed at a water depth of $35\ m$ is subjected to different types of loading: one- and two-way loading. The type of loading depends on the load case and the monopile diameter. In this case, the global loading can be considered a one-way loading for fatigue load scenario and normal operational loading ($F-1$ and $E-1$) and two-ways loading for extreme wind and wave scenarios ($E-2$ and $E-3$). It should be noted that the adopted load cases provide representative loads, which serve as a basis for a conceptual design of a monopile foundation. A final design requires a detailed study, including several additional load cases (refer to DNV-OS-J101, 2014). Figure 2.13 shows the effect of water depth on loading characteristic for different types of offshore wind turbines basing on realistic data (Jalbi et al., 2019). This figure also shows that the current findings are in good agreement with the general trend found by Jalbi et al., 2019. The small divergence in the case of monopile

of 7.5 in diameter is due to the relatively smaller diameter proposed to obtain a semi-rigid behavior, as an aim of this study.

Tab. 2.11.: Environmental loads acting on the "DTU 10 MW RWT" supported by monopiles of 7.5 and 10 m in diameter

Loading	Unit	Monopile of 7.5 m				Monopile of 10 m			
		$F-1$	$E-1$	$E-2$	$E-3$	$F-1$	$E-1$	$E-2$	$E-3$
Mean wind load	*MN.m*	174.9	206.1	206.1	206.1	174.9	206.1	206.1	206.1
Max wind load	*MN.m*	209.9	246.0	309.7	646.0	209.9	246.0	309.7	646.0
Min wind load	*MN.m*	143.1	169.8	123.6	123.6	143.1	169.8	123.6	123.6
Max wave load	*MN.m*	30.6	99.4	246.6	187.3	51.5	165.4	410.4	312.3
Min wave load	*MN.m*	−30.6	−99.4	−246.6	−187.3	−51.5	−165.4	−410.4	−312.3
Max global load	*MN.m*	240.5	345.4	556.3	833.3	261.4	411.4	720.1	958.3
Min global load	*MN.m*	112.4	70.4	−123.0	−63.8	91.5	4.4	−286.8	−188.8
ζ_c	-	0.47	0.2	−0.22	−0.08	0.35	0.01	−0.40	−0.20
Eccentricity	*m*	104.5	69.7	55.2	80.2	84.9	55.1	46.2	64.3

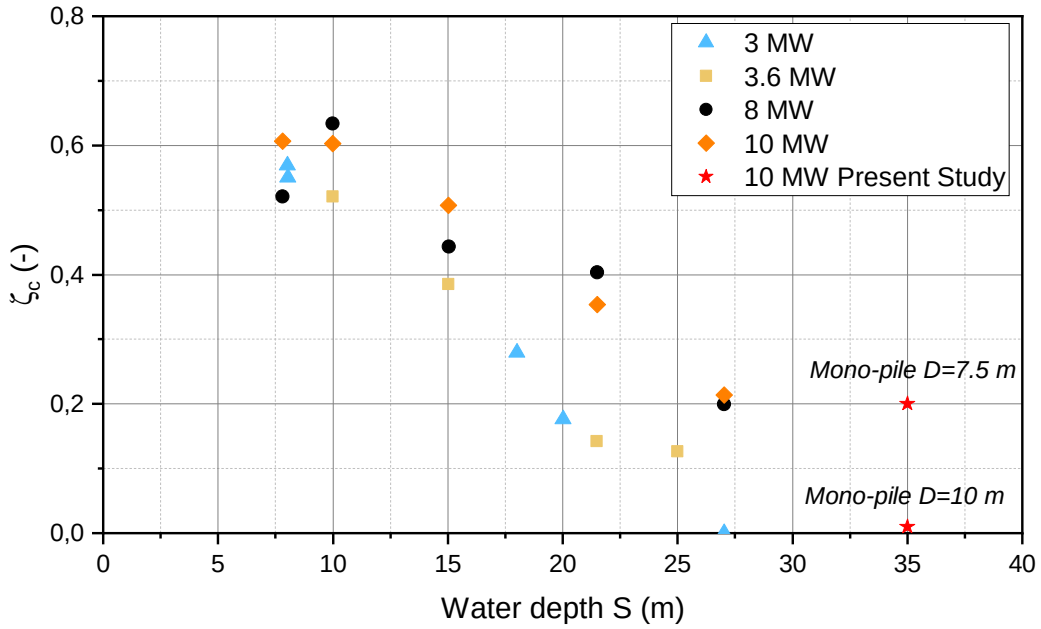

Fig. 2.13.: Cyclic load characteristic ζ_c as a function of water depth for normal operational conditions

2.2.4 Proposition of two types of foundations

Two reasonable sets of monopile dimensions are proposed in a way to obtain different factors of rigidity (Section 2.1.2). The aim is to examine the cyclic behavior of each monopile foundation and then evaluate their performance as a foundation for *"DTU 10 MW RWT"* in relatively deep waters. The soil profile consists in a dense sand layer (Fontainebleau Sand NE34). The corresponding soil parameters are determined according to Chapter 3.

The current proposal aims to obtain monopile dimensions representative of this kind of offshore wind turbine. So, the verification of the satisfaction of the design limits was not regarded strictly. The proposed dimensions were inspired from similar available data (Velarde and Bachynski, 2017, Comité Francais de Mecanique des soils et de Géotechnique, 2020...), validation of monopile ultimate capacity basing on simplified theoretical methods (refer to Section 7.1.2), and numerical simulations basing on Finite Element analysis with Cesar-LCPC 3D (refer to Section 7.8). The properties of two monopile foundations are displayed in Table 2.12. The determination of these properties respects the following criteria:

- The monopiles are formed of steel materials. In the framework of this thesis, the properties of monopile steel are considered identical to tower steel.

- The thickness of monopile is chosen according to API (American Petroleum Institute), 2010, $t_p \geq 6.35 + D_p/100$ (monopile diameter and wall thickness in mm), and respecting the average diameter to thickness ratio, which is assumed to be of about 80 (OE5665, 2015).

- The relative density index of the sand layer is considered to be equal to 0.80, as dense sand.

- The soil parameters are adopted according to the findings of Chapter 3, Young's modulus used in the calculation of rigidity factor is the secant modulus corresponding to the half-failure of soil, E_{50}. However, the relevant value of Young's modulus which should be used depends on the strain level (Section 3.1) and thus depends on the loading amplitude. It should be noted that the behavior of monopile foundation tends to be more rigid with increasing loading amplitude due to soil modulus degradation. Using E_{50} as Young's modulus, the rigidity factor obtained can be considered as an upper bound of rigidity reached during the service life of the monopile.

- The representative soil effective stress along the monopile foundation is assumed corresponding to $0.7L$ beneath the mudline (Abadie, 2015).

Tab. 2.12.: Properties of the two monopile foundations

Monopile foundation	Diameter (m)	L/D ratio	Thickness (mm)	Rigidity Factor	Classification
Foundation 1	7.5	4	100	~ 33.3	Semi rigid behavior
Foundation 2	10	2.5	125	~ 4.5	Perfectly rigid behavior

Abadie et al., 2019 has presented the dimensionless pile flexibility factor (the inverse of rigidity factor defined in section 2.1.2) plotted against L/D ratio for three datasets, which are: (i) current wind farms monopiles in sand and clay, (ii) expected futuristic wind farm monopiles in sand and clay, and (iii) piles that were used in the $1960s$ and $1970s$ for the development of the p-y method. Abadie et al., 2019 proposed a different methodology to define the Young's modulus of soil (initial Young's modulus at monopile tip); however the adopted values seem to be reasonable for the current methodology: 50 *MPa* for dense sand, 300 *MPa* for hard clay,.... The dimensionless pile flexibility factor of the two proposed foundations is estimated and presented beside the previous three sets in Figure 2.14. The monopiles of futuristic wind farms tend to have a more rigid behavior. The two proposed foundations $F1$ and $F2$ respectively are at the lower and upper bounds of expected monopiles rigidity.

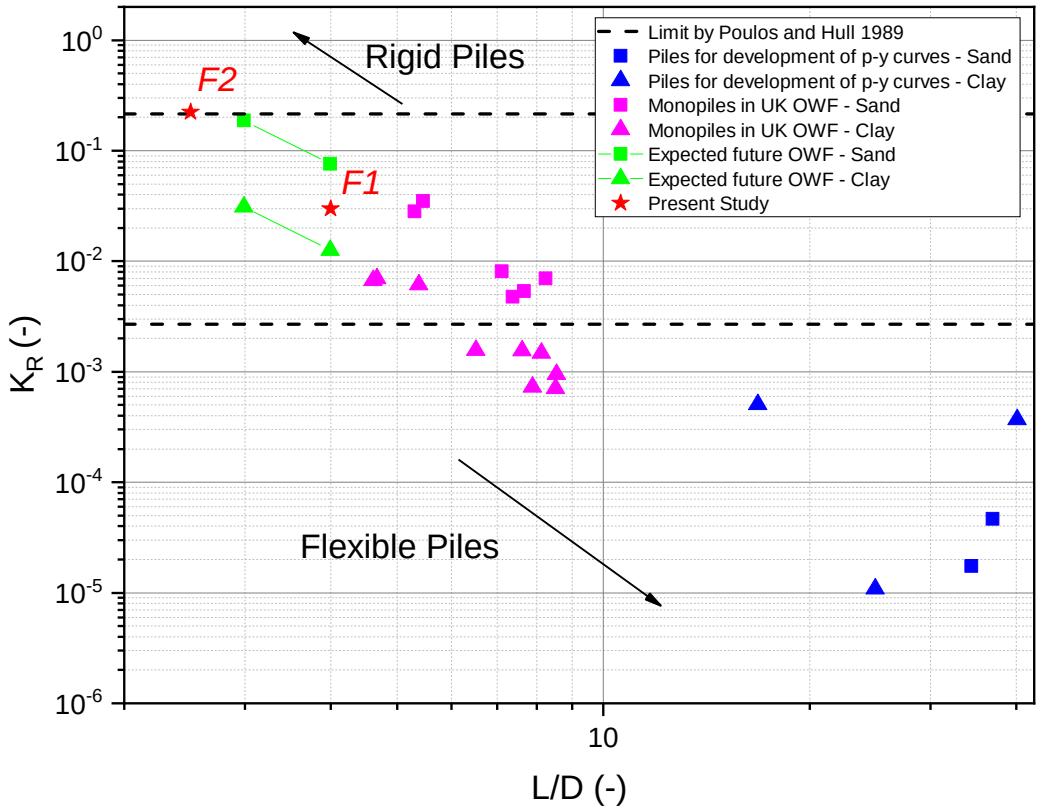

Fig. 2.14.: Dimensionless pile flexibility factor against L/D ratio for different sets of monopiles (adapted from Abadie et al., 2019)

2.3 Development of scale models

2.3.1 Scaling laws

Despite the dynamic sensitivity of offshore wind turbines, most of the proposed scaling laws do not carefully regard the reproduction of dynamic aspects (Section 2.1.3). The soil-structure interaction at the foundation level and the dynamic response at the structure level are the main aspects underlying the behavior of an offshore wind turbine. Based on similar research efforts and after a careful analysis of governing physical phenomena, a new set of scaling laws is extracted and applied to develop two scale models. Adequate adherence to governing parameters allows the passage of results from the model scale to the prototype scale or, at least, provides a quantitative idea about the behavior.

The adopted methodology starts by proposing some fundamental scaling factors and then links the governing parameters to these scaling factors. The scaling of some parameters can encounter some practical difficulties (e.g. materials rigidity, thicknesses), which can be compensated by conscious passage to global dimensionless groups or/and varying the used materials.

As the basic idea of small scale physical modeling, the scale factor responsible for dimensions reduction is considered as the main scale factor:

$$\lambda_L = \frac{L_{model}}{L_{prototype}} = \frac{L_m}{L_p}$$

Besides, some hypotheses form the basis of the scaling laws adopted in the current work, and permit to generate fundamental scale factors:

- The physical modeling is conducted at normal laboratory gravity. Thus, the scale factor for acceleration relative to 1g modeling is equal to one:

$$\lambda_g = \frac{g_m}{g_p} = 1$$

- In the geotechnical problems, the effective unit weight of soil materials, which is the product of submerged density and gravitational acceleration, often controls the response. The soil material at the prototype scale is saturated dense sand. Due to the relatively low loading frequency of wind and waves and the relatively high permeability of sand, the accumulation of pore pressure is neglected, and fully drained conditions are assumed (Table 2.13). Hence, dry sand can be used in the scale model, imposing a scale factor for density:

$$\lambda_\rho = \frac{\gamma'_m}{\gamma'_p} = \frac{(\gamma_d)_m}{(\gamma_d)_p + (n-1)\gamma_w}$$

where γ_d and γ' respectively are the dry and the submerged unit weight, γ_w is the water unit weight, and n is the soil porosity.

This hypothesis regarding drainage conditions should be reviewed in some extreme climate conditions (gusts and hurricanes), which can induce an accumulation of pore pressure (leading to liquefaction) due to the variation of loading frequencies (Cuéllar, 2011). In this context, Li et al., 2019 shows that the soil close to large diameter monopiles behaves as partially drained. In the framework of this thesis, fully drained conditions are assumed, focusing on targeted aspects. However, it would be interesting to extend research efforts considering the effect of partially drained conditions and pore pressure accumulation. On another side, it should be well distinguished between the dynamic aspect of the structure considered on this study and the assumed quasi-static response of the sand around the monopile.

Tab. 2.13.: Approximate soil behavior classification under repeated loading (Peralta, 2010 following Gotschol, 2002)

Repeated loading of soil	Cyclic	Cyclic/Dynamic	Dynamic
Frequency	0 to 1 *Hz*	1 to 10 *Hz*	> 10 *Hz*
Inertia	Negligible	Relevant	Relevant

The scaling laws are divided into two categories: (i) Static scaling laws considering the physical phenomena which underlie the monopile behavior under lateral loading, and (ii) Dynamic scaling laws focusing on the physical quantities which govern the dynamic response of the structure. The adequate scaling of these two aspects provides representative scale models of offshore wind turbines.

Static scaling laws

In this part, the governing parameters which affect the monopile behavior under lateral loading are interpreted against the scale change. Then, corresponding scale factors are derived based on fundamental scale factors defined previously. The adopted methodology to extract an adequate set of scaling laws is now presented:

- Monopile geometry:
  For sake of simplicity, similar monopile shafts are chosen for the full scale and the scale model. This conservation of the shape permits an easier understanding of the soil-structure interaction simulation. Therefore, the length scale factor λ_L is directly applied to monopile diameter and embedded length. This idea ensures the conservation

of a similar length-to-diameter ratio, which is considered as a key mechanism of rigid monopile behavior (LeBlanc et al., 2010).

$$\frac{D_m}{D_p} = \lambda_L \qquad \frac{L_m}{L_p} = \lambda_L$$

- Soil stress along monopile foundation:
  The vertical stress level in a location of the soil mass depends on the depth and the unit weight of the soil. The horizontal stress level depends on the vertical stress level and the coefficient of lateral earth pressure. Then, for similar soils, the global stress field can be related to the unit weight γ and the depth z:

$$\sigma \propto \gamma z$$

  The length scale factor is applied to monopile length, and the density scale factor is the ratio between scale model and full-scale soil mass density. The scale factor for soil stress distribution along the monopile thus reads:

$$\frac{\sigma_m}{\sigma_p} = \lambda_L \lambda_\rho$$

- Soil scaling:
  Since the ratio of foundation diameter to grain size (D/d_{50}) is greater than 30 to 60, a real size sand can be used in the scale model (Cuéllar, 2011 following Ovesen, 1980, Remaud, 1999, Sedran et al., 2001 and Verdure et al., 2003).
  Besides, the full-scale model and the scale model are conducted at different stress levels. Due to non-linear phenomena, it is not simple to establish a relationship between the soil behaviors in the two cases. Such difficulties can be remarked with the conflicting hypotheses adopted by similar works. Indeed, while Peralta and Achmus, 2010 and Cuéllar, 2011 use identical sand (same density index), LeBlanc et al., 2010 recommend the conservation of friction angle by using looser sand (Bolton, 1986). Altaee and Fellenius, 1994 studied the physical modeling in sand materials and compared the behavior of the two following cases: (i) sands with same density index at laboratory and full-scale stress levels, and (ii) sands with the same distance to the steady-state line at laboratory and full-scale stress levels (Figure 2.15a). After the normalization of soil responses to initial mean stress, Altaee and Fellenius, 1994 shows that the sand at full-scale stress level behaves similarly to sand characterized by the same distance to the steady-state line at laboratory stress level (Figure 2.15b). The similarity was also proven in terms of volumetric strain.

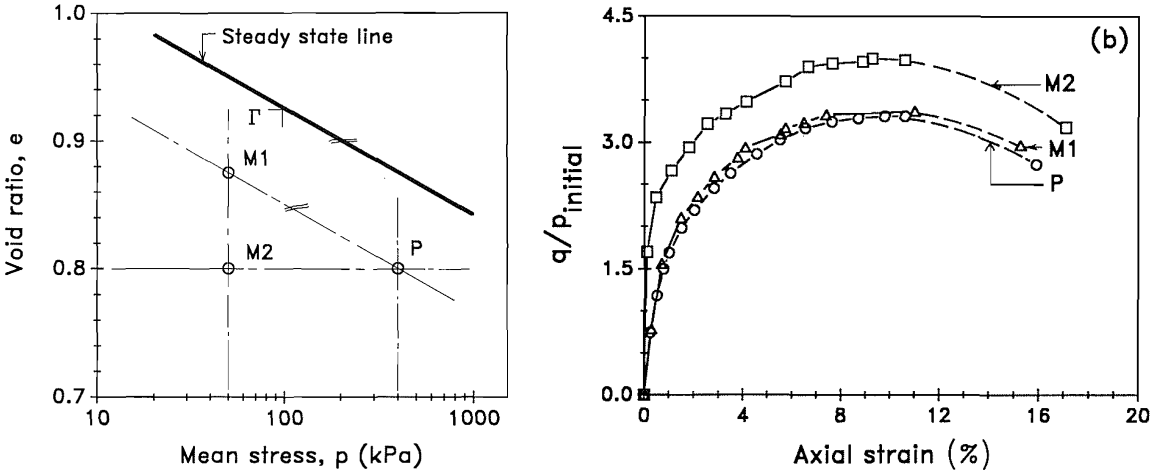

Fig. 2.15.: (a) Initial void ratio and mean stress of samples P, M1, and M2 with respect of the steady state line of the crushed quartz 430/0 sand. (b) Triaxial drained response of samples P, M1, and M2: normalized deviatoric stress vs axial strain (from Altaee and Fellenius, 1994).

- Soil stiffness:
  According to Jardine et al., 1986 and Mair, 1992, the typical shear strain around piles ranges between 0.01 and 0.1%, which corresponds to small to medium strain level. As shown in the previous paragraph, once the distance to the steady-state line (State parameter) is conserved, a unified sand response is obtained after normalization to the stress level. Then, the secant soil modulus at different strain levels can be related to the stress level. Therefore, the scale factor for soil stiffness becomes:

$$\frac{E_m}{E_p} \propto \frac{\sigma_m}{\sigma_p} = \lambda_L \lambda_\rho$$

- Monopile bending stiffness:
  The pile rigidity factor is an important parameter governing the monopile behavior under lateral loading. As seen in Section 2.1.2, the pile rigidity factor depends on the ratio between the monopile bending stiffness ($E_p I_p$) and the soil rigidity ($E_s L^4$). The scaling laws already regarded impose the soil modulus, the monopile length, and the monopile diameter. Still, the thickness and the material modulus of the monopile can be controlled to conserve similar pile rigidity.
  For perfectly rigid monopiles, the bending stiffness becomes without effect due to the perfect rotational response. So, it is recommended to use the prototype material, which ensures similar friction conditions with the soil.
  In case of semi-rigid and flexible monopiles, the scale factor for monopile bending stiffness becomes:

$$\frac{(E_p I_p)_m}{(E_p I_p)_p} \propto \frac{(E_s L^4)_m}{(E_s L^4)_p} = \lambda_L^5 \lambda_\rho$$

Practically, it is impossible to use the same material while reducing the monopile thickness, even though it seems to be the best way to conserve the soil-pile friction conditions. The solution is to adopt softer materials, like Polyvinyl Chloride (PVC) or High-Density Polyethylene (HDPE), which have adequate elastic modulus and reasonable ductility.

- Force and moment:
  The external forces acting on the monopile foundation should be scaled in the same way as internal forces. The force is the integration of stress over a defined surface. Then, the force scale factor can be defined as:

$$\frac{F_m}{F_p} = \lambda_L^3 \lambda_\rho$$

  Similarly, the moment is the product of force and distance. As the length factor is applied to the eccentricity of force acting on the monopile, the moment scale factor can be defined as:

$$\frac{M_m}{M_p} = \lambda_L^4 \lambda_\rho$$

- Strain:
  Strain results from the variation of stresses and material stiffness. The strain scale factor corresponds to the ratio between those for stress and stiffness. As seen before, the stiffness of scaled soil is normalized according to the stress level. Then, the strain scale factor is equal to the unit:

$$\varepsilon_i \propto \frac{\sigma_i}{E_i} \qquad \text{with} \quad i : p, n \qquad \frac{\varepsilon_m}{\varepsilon_p} = 1$$

- Displacement and rotation:
  The displacement is the strain integration over the length. Then the displacement scale factor is the product of strain and length scale factors, which corresponds to the length scale factor. The rotation is the derivation of displacement along the monopile length, then the scale factor for the rotation is equal to the unit:

$$\frac{u_m}{u_p} = \lambda_L \qquad \frac{\theta_m}{\theta_p} = 1$$

Applying this set of scaling laws leads to representative 1g laboratory scale models of all types of monopiles under static/quasi-static loading. Theoretically, the obtained results can be transmitted to scale 1 (e.g. displacements, rotations, and stresses). This transmission is validated by the investigation of sand behavior at different stress levels (Chapter 3). Due to the low stress level at the laboratory scale, the experimental procedure should be applied in a delicate mode to ensure results reliability.
The dynamic sensitivity of offshore wind turbines imposes additional parameters, which

govern the dynamic response. Therefore, the set of scaling laws is extended in the next section to ensure the dynamic similarity of the first mode of vibration.

Dynamic scaling laws

Firstly, the dynamic phenomena at full scale should be presented as an introduction for its simulation on the scale model. The convergence between the excitation frequencies and the natural frequency of an offshore wind turbine induces a dynamic load, which depends on the tower mass and the acceleration of the created movement, following Newton's second law:

$$F \propto ma$$

where F is the induced force, M is the mass under motion and a is the motion acceleration. The induced dynamic force is highly dependent on the ratio of the loading frequency to the natural frequency of the system, which in turn depends on the mass, geometry, and rigidity of the system (the tower is the dominant part). Generally, damping is a primary parameter of the dynamic response affecting the percentage of dynamic load contribution. Figure 2.16 clarifies this phenomenon.

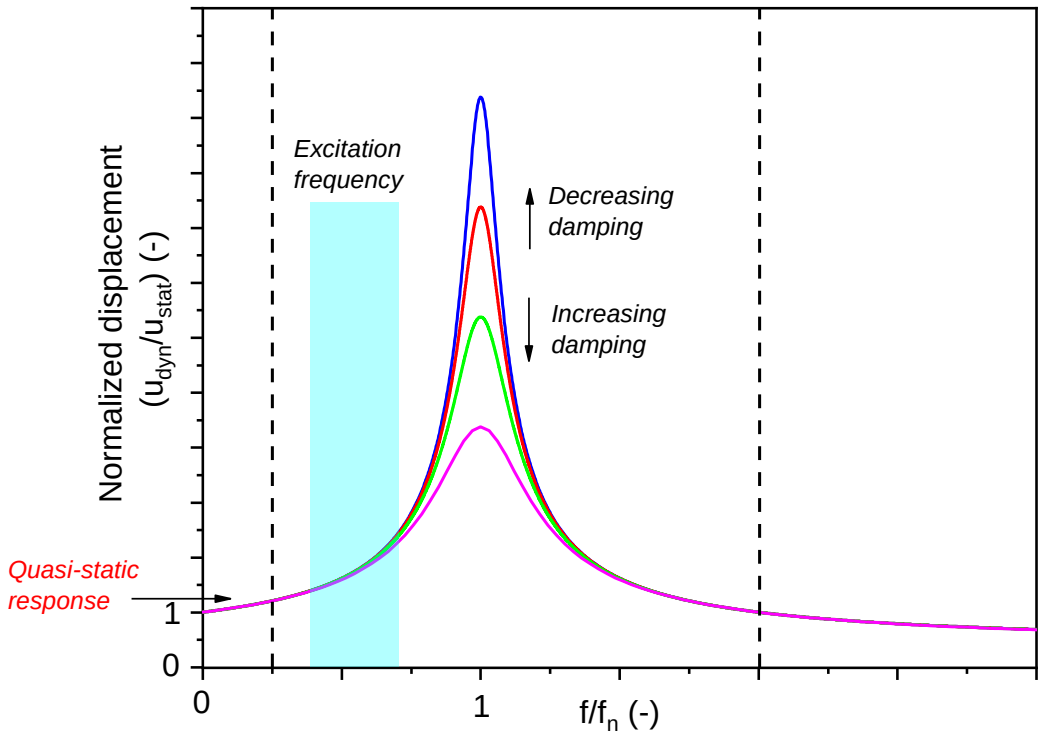

Fig. 2.16.: Normalized dynamic response in function of frequencies ratio and system damping

Similar to static behavior, a set of scaling laws, able to simulate the appropriate dynamic response of the system, has been extracted. The offshore wind turbine consists of two

principal parts: (i) the structure formed by the transition piece, the tower and the turbine system, and (ii) the foundation formed by the monopile foundation embedded in the soil mass. The sensitive part which governs the dynamic response is the structure. According to Table 2.13, the soil behaves statically under relatively low frequencies (about 0.1 *Hz*). It is assumed that the foundation is not dynamically sensitive due to the difference between its natural frequency (exceeding 2 *Hz*; estimated numerically) and excitation frequencies. For simplicity, the transition piece and the tower are considered as equivalent Euler-Bernoulli beams, and the turbine system is idealized as a top mass. The following points present the scaling methodology of the governing parameters:

- Mass:
  As the source of dynamic force, the scaling of mass respect the scale factors defined previously to scale the static forces. The mass scale factor is the product of the density scale factor and the volume scale factor (λ_L^3):

  $$\frac{Mass_m}{Mass_p} = \lambda_L^3 \lambda_\rho$$

  For Euler-Bernoulli beam, the linear mass should be considered. The length scale factor is applied to define the length of the beam. Then, the mass scale factor per unit length is defined as:

  $$\frac{m_m}{m_p} = \lambda_L^2 \lambda_\rho$$

- Time and loading frequency:
  Governing the induced dynamic force, the horizontal acceleration should respect the scale factor defined for accelerations. Besides, Pöschel et al., 2001 proposed that all accelerations (not only the gravity) should be unaffected when 1g physical modeling is considered. This can be expressed as follows:

  $$a_p = \frac{d^2 x_p}{{dt_p}^2} = \frac{d^2 (x_m/\lambda_L)}{{dt_p}^2} = \frac{d^2 x_m}{{dt_m}^2} = a_m$$

  From where, the scale factor for time can be extracted as:

  $$\frac{t_m}{t_p} = \sqrt{\lambda_L}$$

  The loading frequency can be deduced as the inverse of the cycle period (time).

- Natural frequency:
  As mentioned before and referring to Figure 2.16, the ratio of excitation frequency and natural frequency is a significant parameter affecting the contribution of dynamic force to

the global response of the system. The natural frequency of an Euler-Bernoulli beam is expressed as:

$$f_{n,i} \propto \frac{1}{L_i^2}\sqrt{\frac{(EI)_i}{m_i}} \quad \text{with} \quad i : p, n$$

Where L is the length of the beam, EI is the bending stiffness, and m is the linear mass. Similar to length and mass scaling, applying the static scale factor for bending stiffness leads to the following equation:

$$\frac{(f_n)_m}{(f_n)_p} = \frac{L_p^2}{L_m^2}\sqrt{\frac{(EI)_m}{(EI)_p}\frac{m_p}{m_m}} = \frac{1}{\lambda_L^2}\sqrt{\frac{\lambda_L^5\lambda_\rho}{\lambda_L^2\lambda_\rho}} = 1/\sqrt{\lambda_L}$$

The adoption of the bending stiffness scaling factor leads to the same scaling factor for natural frequency as loading frequency, which conserves the same ratio between them. The respect of scale factors defined for linear mass and bending stiffness simultaneously is not a trivial work. The use of prototype materials involves practical difficulties. It is recommended to change the beam section and the material to obtain adequate quantities.

- Damping:
  Different sources constitute the global damping in the prototype (e.g. seawater, wind, soil,...), while it is impossible to reproduce all of them in the scale model. An equivalent damping can be created using eddy currents by hooking a magnet to the top mass and approaching a copper plate with controlling the distance between them. For more detail, refer to Section 4.3.2.

The proposed methodology of scaling ensures the conservation of relevant dimensionless groups adopted by similar works (Section 2.1.3). Besides, the consideration of the dynamic aspect constitutes an original contribution of the present work. After an appropriate testing procedure, theoretically, qualitative and quantitative evaluations of the offshore wind turbine foundation can be carried out. The two sets of scaling laws are applied to scale the *"DTU 10 MW RWT"* installed on two types of monopiles foundations. The development of scale models is presented in the next section. The validation of the dynamic similarity is checked experimentally and numerically as part of the present work. For more details, refer to Chapter 4.

2.3.2 1g-scale models

This section presents the development of two $1/100$ scale models of the "DTU 10 MW RWT" installed on two different monopile foundations: semi-rigid and perfectly rigid monopiles. The foundation details are displayed in Table 2.12, and the structure parameters are detailed in Section 2.2.1.

The length scale factor is equal to $1/100$ as the models scale factor. The soil density scale factor is equal to 1.5 since dry sand is used in the scale model.

Development of monopile foundation

In the scaling of monopile foundation, two cases are distinguished:

- Semi-rigid foundation $F1$:
  The length scale factor is applied to the embedded length and the diameter to obtain a similar monopile shaft. Two factors can be controlled, thickness and material modulus, to conserve the same rigidity factor. HDPE 100 material is adopted, characterized by an adequate Young's modulus ranging between 0.9 and 1.5 *GPa*. Finally, a HDPE tube of 75 *mm* diameter, 2.3 *mm* thickness, and 300 *mm* length is used to simulate the foundation $F1$.

- Perfectly rigid foundation $F2$:
  The length scale factor is applied to the embedded length and the diameter to obtain a similar monopile shaft. Due to its perfectly rotational motion, the monopile bending stiffness does not affect the lateral behavior. Steel material is used to conserve the friction conditions with soil. Finally, a $S275$ steel tube of 100 *mm* diameter, 2 *mm* thickness, and 250 *mm* length is used to simulate the foundation $F2$.

The main idea of monopile scaling is to conserve similar pile shafts and rigidity. The rigidity of ten scaled monopiles on sand material are evaluated and compared to the corresponding length to diameter ratio. The evaluation of the rigidity is based on the following criteria:

- The monopiles dimensions and properties are extracted from the published works. In the case of the monopile Young's modulus is not available, a reasonable value is attributed.

- Based on the sand properties, monopile length, and drainage condition (dry or saturated sand), reasonable ranges of the soil Young's modulus are attributed for each case following the methodology presented in Section 2.2.4. It should be mentioned that these values are relatively small due to the corresponding low-stress levels, characterizing the 1g scale models (similar ranges taken by Albiker et al., 2017).

Figure 2.17 show that the usage of metal tubes (usually steel, aluminum, copper, ...) at the laboratory stress level and conservation of the pile geometry leads to perfectly rigid bodies, which can not simulate the prototype rigidity. Besides, it shows the necessity to use HDPE or PVC to develop representative models of semi-rigid monopiles.

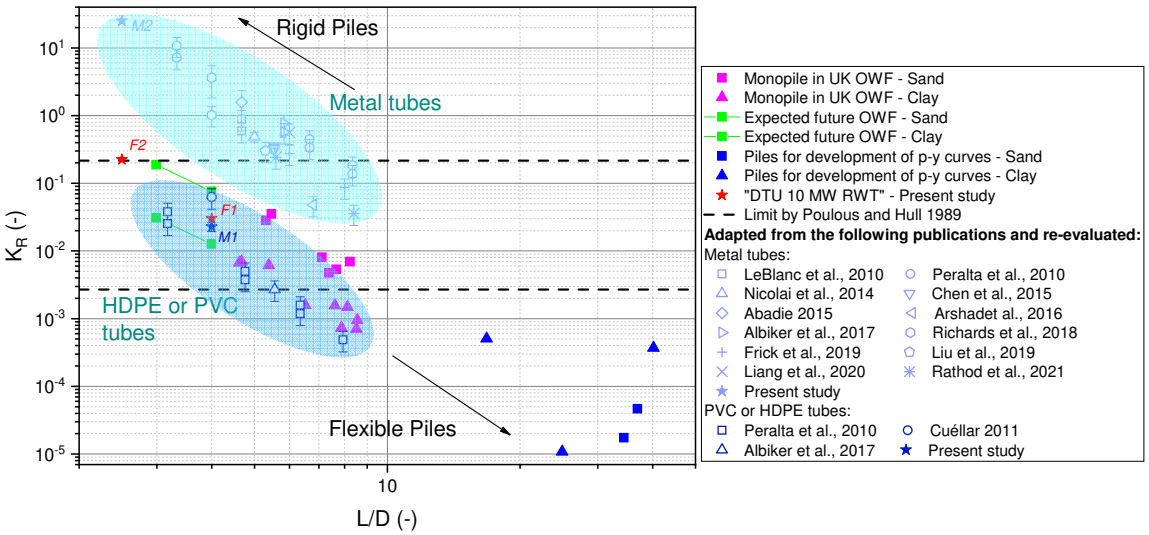

Fig. 2.17.: Dimensionless pile flexibility factor against L/D ratio for different sets of monopiles and scale models (adapted from Abadie et al., 2019)

As seen before, the sand behavior depends on density index and stress level. The state of the sand should be at the same distance to the steady-state line in the scale model and at full scale. Referring to Chapter 3, the suitable density index is determined to obtain similar behavior of sand.

Development of offshore wind turbine's structure

The offshore wind turbine structure consists of three principal parts: the substructure, the tower, and the turbine system. The scaling methodology of the different parts is now presented:

- The substructure:
  The substructure consists of the monopile free length and the transition piece (Figure 2.18). The substructure properties, including the transition piece, are assumed to be identical to the monopile properties. The length scale factor is applied to determine the height of the scaled substructure. Brass rods of 18 and 24 *mm* provide similar linear mass and bending stiffness for $F1$ and $F2$, respectively.

- The tower:
  The diameter and thickness vary along the tower length. Equivalent diameter and thickness were determined conserving similar dynamic properties. The length scale factor is applied to determine the height of the scaled substructure. Brass tube of 13 *mm* diameter and 3 *mm* thickness provides the conservation of linear mass and bending stiffness simultaneously.

- The turbine system:
  The mass of the turbine system is a factor affecting the dynamic response. It was replaced by an idealized mass respecting the corresponding scale factor. The scaled mass is about $1.01\ kg$.

Loading system

The environmental loads applied to an offshore wind turbine are estimated and idealized as a sinusoidal form in Section 2.2.3. The force scale factor is applied to determine the equivalent load on the scale models. A linear actuator is used to generate a force-controlled motion acting on the scale models to simulate the equivalent loading (Section 4.4.3; Chapter 4). The scaled loading frequency is equal to $1\ Hz$ leading to maintain the validity of the quasi-static sand behavior (Section 2.13).

The properties of all used materials are displayed in Table 2.14.

Tab. 2.14.: Properties of materials used for the design of the scale models

Material property	Unit	Steel $S275$	HDPE	Brass
Density ρ	kg/m^3	7650	960	8490
Yield strength σ_y	*MPa*	275	$[23; 29.5]$	$[338; 469]$
Young's modulus E	*GPa*	210	$[0.9; 1.5]$	97
Poisson's ratio ν	-	0.3	0.46	0.31

Figure 2.18 presents a schematic to clarify the similarity between the present scale models and the prototype.

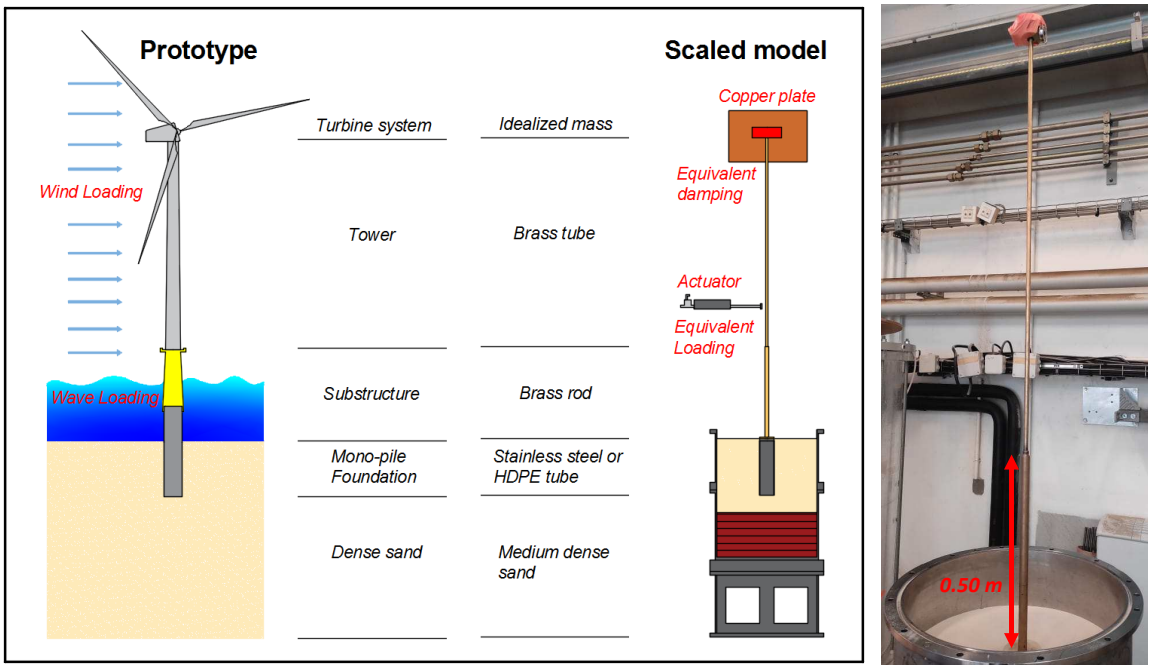

(a) (b)

Fig. 2.18.: (a) Schematic of similarity between the designed scale models and the prototype; (b) photo of scale model *M2*

Dimensions, details, and scale factors satisfaction are presented in Table 2.15. The scale models were manufactured by a specialized company to ensure good workability. The pieces ensuring the connection between structure parts and between the structure and the foundation have taken particular attention to avoid vibration issues after a high number of cycles.

Tab. 2.15.: Evaluation of scale factors satisfaction on proposed scale models

Prototype Part	scale model part	Parameter	Unit	Prototype	scale model	Ideal scale factor	Actual scale factor
Foudation $F1$	HDPE tube	length	*m*	30	0.3	0.01	0.01
		Diameter	*m*	7.5	0.075	0.01	0.01
		Effective stress	*kPa*	160	2.5	0.015	0.015
		Sand I_d	–	0.80	0.52	Chapter 3	
		Rigidity factor	–	33.5	$[38.1; 51.8]$	1	$[1.14; 1.54]$
Foundation $F2$	Steel tube	length	*m*	25	0.25	0.01	0.01
		Diameter	*m*	10	0.1	0.01	0.01
		Effective stress	*kPa*	140	2.1	0.015	0.015
		Sand I_d	–	0.80	0.52	Chapter 3	
		Rigidity factor	–	4.5	0.04	Perfectly rigid	
Substructure 1	Brass rod $\phi 18$	length	*m*	50	0.5	0.01	0.01
		Linear mass	*kg/m*	$1.98 * 10^4$	2.16	$1.5 * 10^{-4}$	$1.10 * 10^{-4}$
		Bending stiffness	$N.m^2$	$3.34 * 10^{12}$	499.6	$1.50 * 10^{-10}$	$1.50 * 10^{-10}$
Substructure 2	Brass rod $\phi 24$	length	*m*	50	0.5	0.01	0.01
		Linear mass	*kg/m*	$3.29 * 10^4$	3.84	$1.5 * 10^{-4}$	$1.16 * 10^{-4}$
		Bending stiffness	$N.m^2$	$9.92 * 10^{12}$	1578.9	$1.50 * 10^{-10}$	$1.59 * 10^{-10}$
Tower	Brass tube $\phi 13 - t3$	length	*m*	115	1.15	0.01	0.01
		Linear mass	*kg/m*	$5.4 * 10^3$	0.81	$1.50 * 10^{-4}$	$1.50 * 10^{-4}$
		Bending stiffness	$N.m^2$	$8.28 * 10^{11}$	124.2	$1.50 * 10^{-10}$	$1.50 * 10^{-10}$
Turbine system	Idealized mass	Mass	*kg*	$6.74 * 10^5$	1.01	$1.50 * 10^{-6}$	$1.50 * 10^{-6}$
External loads	Actuator load	Amplitude	*N*	Table 2.11	Controlled	$1.50 * 10^{-6}$	$1.50 * 10^{-6}$
		Eccentricity	*m*	62	0.62	0.01	0.01
		Frequency	*Hz*	0.1	1	10	10
		f/f_n	-	0.52	0.52	1	1

2.4 Conclusion of the chapter

This chapter constitutes a background of many aspects of the current study: (i) recent method to estimate and idealize the environmental loads acting on an offshore wind turbine; (ii) different methods adopted to design monopile foundation subjected to cyclic loading; and (iii) different methodologies and corresponding scaling laws proposed to develop 1g scale models.

This chapter presents a reference offshore wind turbine (*DTU 10MW RWT*), the estimation of corresponding environmental loads, and the proposition of two reasonable monopile foundations.

This chapter ends with the proposition of a new set of scaling laws considering different geotechnical aspects of the problem and the development of two representative scale models.

3 Sand behavior at different stress levels

Several geotechnical problems require the understanding of the soil behavior at low-stress levels like the design of physical models, shallow foundations, soil stability, and soil liquefaction.

In the framework of this thesis, the 1g modeling is characterized by relatively low-stress levels, constituting a challenge of this type of physical modeling. The difference in stress level between the prototype and the scale model affects the soil behavior. Then, significant results on 1-g scale model are conditioned by a deep comprehension of the soil behavior at the two stress levels. In this thesis, sand materials are considered using a reference sand, which is the *Fontainebleau* sand *NE34*. This sand is commonly used for research purposes. However, data at low stresses are scarce. Numerous tests are conducted, and some available data are treated to characterize the *NE34* sand at different stress levels. The obtained data is analyzed to ensure and validate the similarity of soil behavior between the scale model and the prototype.

3.1 Literature review

3.1.1 Generalities on the mechanical behavior of soils

Numerous tests are conducted to determine the global behavior of soil materials. As soils exhibit a non-linear stress-strain behavior, the identification of required tests depends on the geotechnical problem considered and its strain level (Figure 3.1).

Very-small strain levels are generally encountered in seismic or dynamic problems. The behavior is considered quasi-elastic in this range of deformation, defining the initial modulus of the soil. This modulus is a significant parameter in the dynamic behavior of soils or the soil-structure systems. Tests based on wave propagation (e.g. in-situ geophysical tests, bender element tests) are applied to determine the parameters affecting the dynamic behavior of soils (e.g. initial modulus, damping).

A common test adopted to determine the soil behavior at larger strain levels is the triaxial

test, which is used for the serviceability and the ultimate limit state analysis of geotechnical problems. The triaxial test provides a satisfactory simulation of the in-situ stress conditions and then a reliable evaluation of the soil strength and its volumetric (dilatation/contraction) behaviour. In addition, the principal parameters governing these physical phenomena can be quantified using this test, and numerical models can be calibrated.

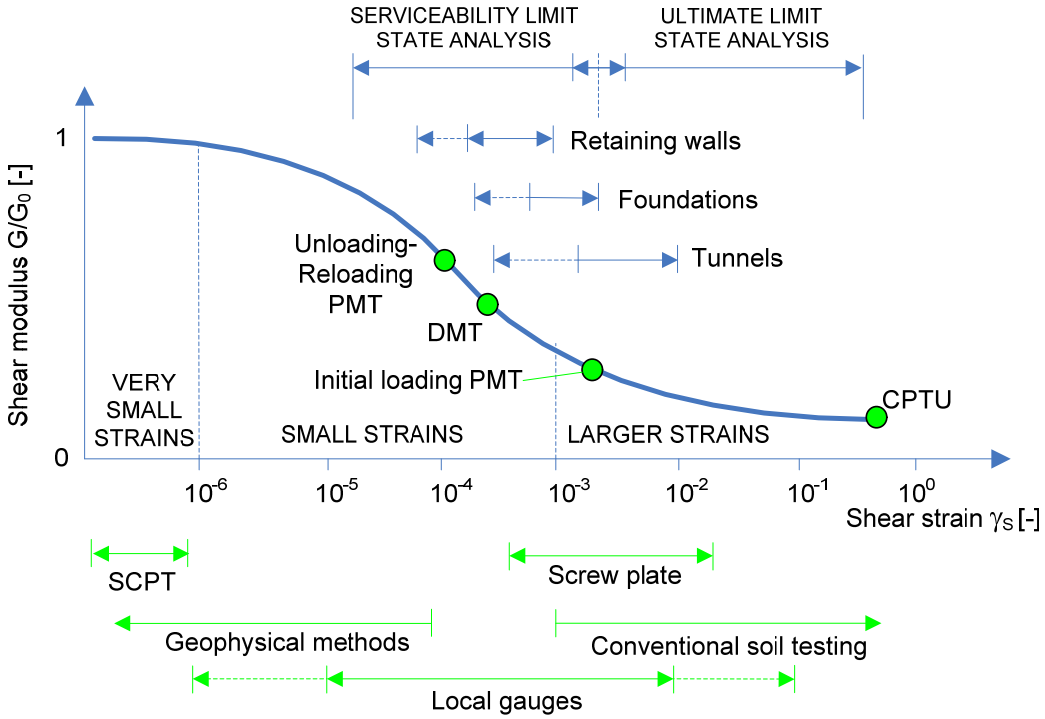

Fig. 3.1.: Typical representation of shear stiffness variation (so called "degradation") as a function of the shear strain levels; comparison with the ranges for typical geotechnical problems and different tests (from Obrzud, 2010)

The stability of offshore wind turbines includes two aspects: (i) dynamic sensitivity, affected by the initial soil modulus and the soil damping, and (ii) serviceability and ultimate limit state analysis, affected by the conventional parameters deducted from soil tests at relatively larger soil strains. Therefore, the present study aims to characterize the *NE34* sand behavior at different stress and strain levels.

3.1.2 Dynamic soil properties

Initial shear modulus profile

The initial shear modulus G_0 is defined as the modulus governing the soil behavior at very-small strain level. Numerous studies have been conducted to identify the factors affecting G_0 profile of fine grained sand materials: Hardin and Richart, 1963, Hardin and Drnevich, 1972b, Iwasaki et al., 1978, Seed et al., 1986, Sibuya et al., 1992, Zdravkovic et al., 2020, ... Therefore, the classical expression adopted to estimate G_0 profile is:

$$G_0 = Af(e)\left(\frac{p'}{p'_{ref}}\right)^n \tag{3.1}$$

where $f(e)$ is the function introducing the effect of the void ratio, p' is the mean effective stress, p'_{ref} is a reference pressure assumed equal to the atmospheric pressure (101.3 *kPa*), and A and n are constant parameters depending on the studied sand.

Based on Hardin and Richart, 1963 and validated later by numerous studies (Iwasaki et al., 1978, Hameury, 1995, Delfosse-Ribay et al., 2004, ...), the commonly adopted form for $f(e)$ is:

$$f(e) = \frac{(b-e)^2}{1+e} \tag{3.2}$$

where b is a constant depending on the studied sand and generally takes a value of 2.17 for round grains and 2.97 for angular grains.

An alternative form is proposed by Hardin, 1978, showing equally good fits to the experimental findings (Zdravkovic et al., 2020):

$$f(e) = \frac{1}{a+be^2} \tag{3.3}$$

where a and b are constants depending on the studied sand.

Regarding the *NE34* sand, Delfosse-Ribay et al., 2004 determined the corresponding G_0 profile using resonant column tests. Besides, Irina AndriaNtoanina, 2011 conducted a set of bender element tests and determined G_0 by varying the void ratio and the confining stress. The obtained results constitute a database, used in the current study to propose new G_0 profiles for *NE34* sand. Table 3.1 presents the different proposed forms of G_0 profiles. Figure 3.2 shows the good agreement between the profile proposed by Delfosse-Ribay et al., 2004 and the profile $P1$ proposed in this study based on Irina AndriaNtoanina, 2011 results.

Tab. 3.1.: Proposed forms of G_0 profile for *NE34* sand

G_0 profile	A	$f(e)$	n	r^2
Delfosse-Ribay et al., 2004	68.2	$(2.17-e)^2/(1+e)$	0.47	–
Present Study $P1$	63.7	$(2.17-e)^2/(1+e)$	0.43	0.979
Present Study $P2$	20.1	$1/(0.019+0.50e^2)$	0.43	0.995

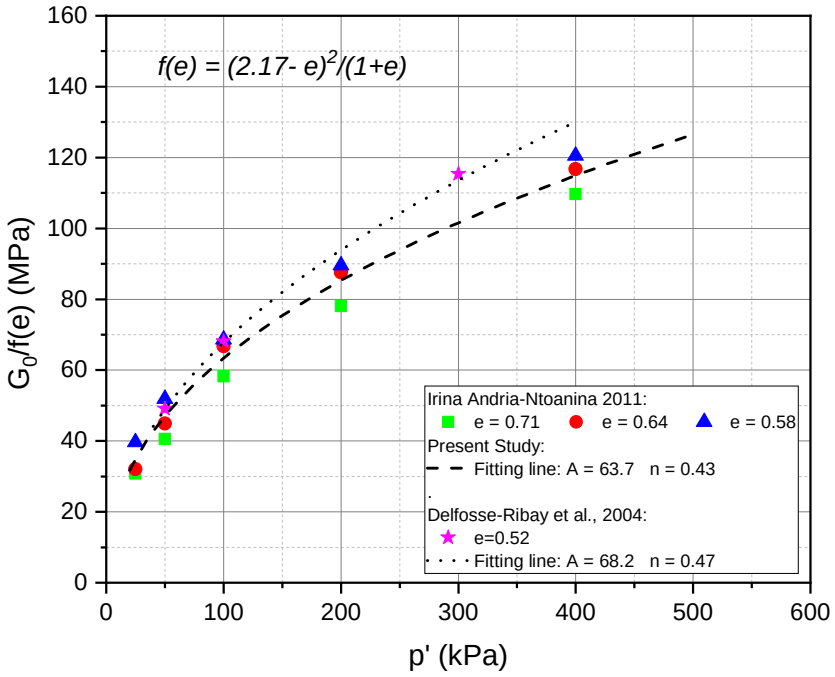

Fig. 3.2.: Comparison between proposed forms of G_0 profile for *NE34* sand

Shear modulus and soil damping evolution

As seen in the previous section, the principal parameters affecting the initial modulus of sands are the confining stress level and the void ratio. As a key feature governing the non-linear behavior of sands, the effect of these two parameters on shear modulus degradation is regarded by numerous studies:

- Iwasaki et al., 1978, Kokusho, 1980, Seed et al., 1986, and many others found that the increase of confining stress decelerates the shear modulus degradation with strain level (Figure 3.3a).

- Kokusho, 1980, Wichtmann and Triantafyllidis, 2004, and others found that the variation of the sand void ratio did not affect the rate of shear modulus degradation with strain level (Figure 3.3b).

Similarly, the evolution of soil damping has been investigated and the following conclusions were drawn:

- Hardin and Drnevich, 1972b, Iwasaki et al., 1978, Kokusho, 1980, Vucetic et al., 1998, and others found that the soil damping decreases with an increase in the confining stress. Besides, an increase in the confining stress decelerates the rise in soil damping with strain level.

- Hardin and Drnevich, 1972b, Iwasaki et al., 1978, Kokusho, 1980, Wichtmann and Triantafyllidis, 2004, and others found that the soil damping seems to be independent of the sand void ratio, while Seed et al., 1986 found that an increase in the void ratio decelerates the increase of soil damping with strain level.

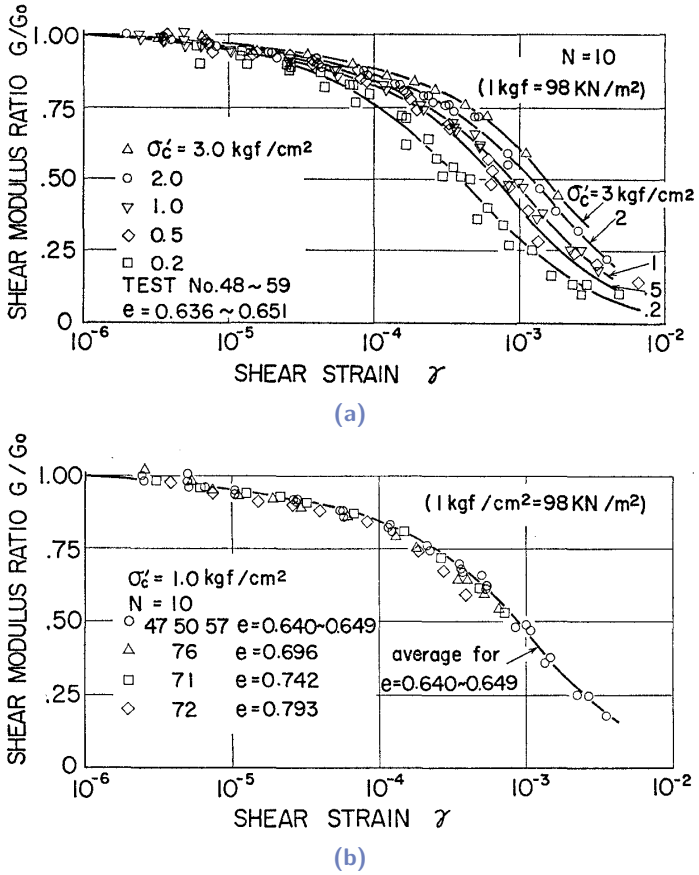

Fig. 3.3.: G/G_0 *vs* $\log(\gamma)$ relationships for dense sand with different (a) confining stresses and (b) void ratios (from Kokusho, 1980)

The shear modulus degradation is generally represented by a hyperbolic function of shear strains. Numerous forms are available in the literature, starting with the relation proposed by Hardin and Drnevich, 1972a, which is modified later by Fahey and Carter, 1993 and Darendeli, 2001. Based on a large database constructed from 454 tests from the literature, OZTOPRAK and BOLTON, 2013 proposed the following best-fit curve:

$$\frac{G}{G_0} = \frac{1}{\left[1 + \left(\frac{\gamma - \gamma_e}{\gamma_r}\right)^a\right]} \tag{3.4}$$

It is worth noting that γ_e is a threshold below which the shear modulus remains unchanged, i.e. for $\gamma < \gamma_e$, $G/G_0 = 1$, γ_r is the characteristic reference shear strain at which $G/G_0 = 0.5$, and a is the curvature parameter. Empirical relationships were also proposed to determine γ_e, γ_r, and a depending on effective mean stress (p'), relative density index I_d (and void ratio e), and the granular soil uniformity U_c. They read as follows:

$$\gamma_r(\%) = 0.01 U_c^{-0.3} \left(\frac{p'}{p_a}\right) + 0.08 e I_d \tag{3.5}$$

$$\gamma_e(\%) = 0.0002 + 0.012 \gamma_r(\%) \tag{3.6}$$

$$a = U_c^{-0.075} \tag{3.7}$$

where p_a is the atmospheric pressure. Typical values of these fitting parameters and obtained general form of the shear modulus degradation curve are presented in Figure 3.4.

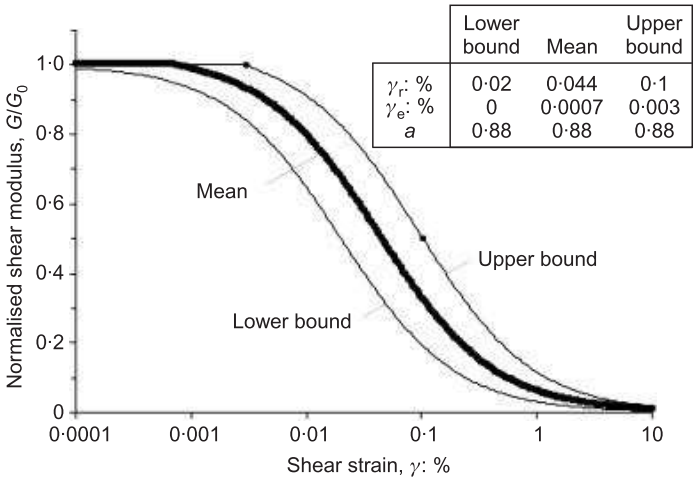

Fig. 3.4.: Shear modulus degradation curve proposed by OZTOPRAK and BOLTON, 2013

Regarding *NE34* sand, Li et al., 2013 identified the evolution of the shear modulus and the damping ratio with the shear strain using the experimental findings of a dynamic centrifuge program. Li et al., 2013 studied the effect of the confining stress on the shear modulus and the damping ratio evolution of *NE34* sand at a void ratio equal to 0.52 (figure 3.5). Further, Li et al., 2013 determined specific parameters for the empirical equation proposed by Ishibashi and Zhang, 1993. The empirical equation and the obtained parameters are (with γ in *m/m* and p' in *kPa*):

$$\frac{G}{G_0} = K(\gamma)(p')^{m(\gamma)-m_0} \tag{3.8}$$

$$K(\gamma) = 0.5\left[1+\tanh\left\{\ln\left(\frac{0.000102}{\gamma}\right)^{0.613}\right\}\right] \tag{3.9}$$

$$m(\gamma)-m_0 = 0.34\left[1-\tanh\left\{\ln\left(\frac{0.000556}{\gamma}\right)^{0.4}\right\}\right] \tag{3.10}$$

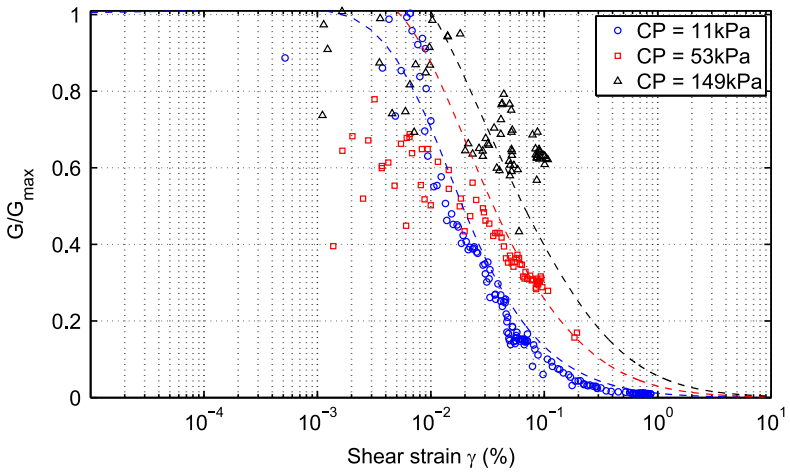

(a)

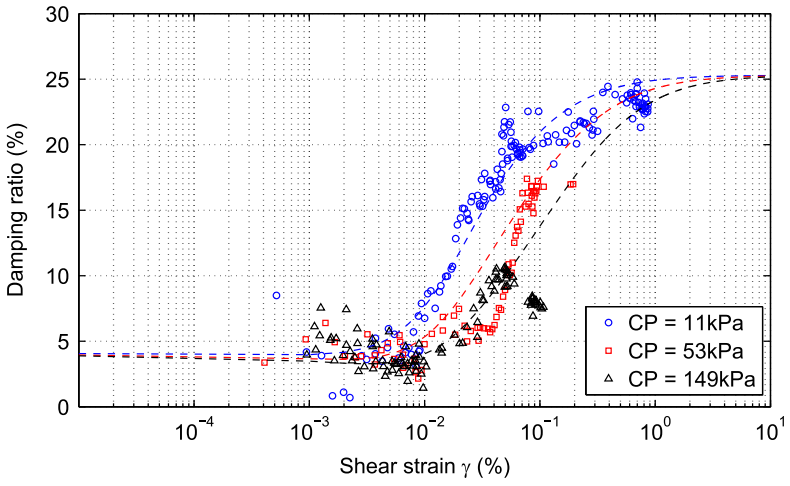

(b)

Fig. 3.5.: Influence of the confining pressure on the evolution of (a) shear modulus and (b) damping ratio of *NE34* sand; experimental data and fitted empirical equations (following Li et al., 2013)

Hardin et al., 1994 and Iwasaki et al., 1978 proposed that the damping ratio can be expressed as a function of G/G_0. The proposal of Ishibashi and Zhang, 1993 is extended to obtain the following expression of the damping ratio (note that damping ratio is a percentage):

$$D = f\left(\frac{G}{G_0}\right) = 25.3\left\{0.513\left(\frac{G}{G_0}\right)^2 - 1.351\left(\frac{G}{G_0}\right) + 1\right\} \tag{3.11}$$

3.1.3 Monotonic sand behavior at different stress levels

Strength and dilatancy of sand at different stress levels

The sand under shearing contracts or dilates depending on the relative density index and the effective confining stress. Changes in dilatancy rate have been well established: it increases with increasing relative density index and decreasing effective confining stress. This increase in dilatancy rate is accompanied by an increase in the peak friction angle (Cornforth, 1964, Lee and Seed, 1967, Bishop, 1971, Kolymbas and Wu, 1990, ...). Figure 3.6 illustrates the effect of effective confining stress on the strength and the dilation of sand. Many researchers have studied the sand response achieving low stress levels (< 50 *kPa*): Ponce and Bell, 1971, Tatsuoka, 1984, Lancelot, Laurent Shahrour and Mahmoud, 1996, Hsu and Liao, 1998, HOR, 2012, Huang et al., 2015, ... It was found that even loose sands can exhibit dilatancy at very low effective confining stresses.

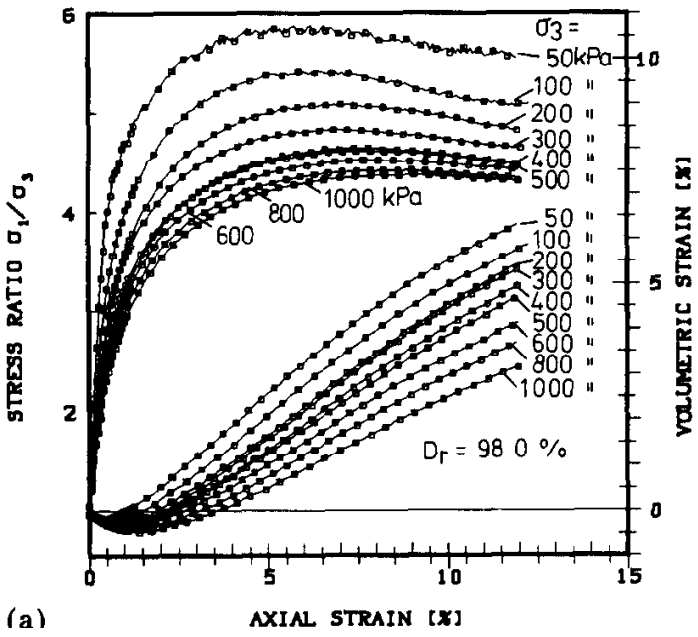

Fig. 3.6.: Behaviour of Karlsruhe sand at different stress levels following Kolymbas and Wu, 1990

The stress-dilatancy theory has been developed by Rowe, 1962, who have shown that the dilatancy could be expressed as a function of the stress ratio and the friction angle. The theory has then been enhanced and consolidated by De Josselin De Jong, 1976. The relationship between dilatancy and soil state has been the subject of several works: Wroth and Bassett, 1965, Sladen et al., 1985, Been and Jefferies, 1985, Sladen and Oswell, 1989,

Li and Dafalias, 2000, ...

Moreover, it was found that at the ultimate state of shear failure for either loose or dense sands, the soil continues to deform at constant stress and constant void ratio. This ultimate state, widely known as the critical state (Roscoe et al., 1958; Schofeld and Wroth, 1968), is unique for each sand, which means it is independent of the initial void ratio, initial stress conditions, and the followed stress path. Besides, Poulos, 1981 defines "the state in which the mass is continuously deforming at constant volume, constant normal effective stress, constant shear stress, and constant velocity" as the steady state. Been et al., 1991 examined the difference between the critical and the steady state and concluded that, for practical purposes, equivalence could be assumed. Therefore, it is justifiable to use a single term, the critical state, for both the critical and the steady state of sands. According to Schofeld and Wroth, 1968, the critical state is located in the $e - p'$ plane according to the following equation:

$$e = \Gamma + \lambda \ln \left(\frac{p'}{p'_{ref}}\right) \tag{3.12}$$

where Γ is the void ratio at the reference mean stress ($p'_{ref} = 101.3\ kPa$) and λ is the slope of the critical state line in the $e - \ln(p')$ plane.

Li and Wang, 1998 proposed the following expression for the critical state line to improve the fitting with experimental data for sands:

$$e = e_{0,ref} - \lambda \left(\frac{p'}{p'_{ref}}\right)^{\xi} \tag{3.13}$$

where $e_{0,ref}$ is the critical state void ratio under zero effective stress and it is assumed to be similar to e_{max} (Riemer et al., 1990). λ and ξ are fitting parameters depending on the studied soil.

It was clearly shown that the relative density index is not sufficient to describe the state of sand and then predict its behavior. Research efforts have focused on the proposition of a global parameter considering the sand density and the effective confining stress. Been and Jefferies, 1985 defined the "state parameter" as the difference between the current void ratio and the critical void ratio corresponding to the current mean effective stress (Figure 3.7). This parameter governs the sand behavior: if the distance is negative, the sand is considered in a dense state and exhibits dilation, and reversely, if it is positive, the sand is in a loose state and exhibits contraction. Referring to Section 2.3.1, the work of Altaee and Fellenius, 1994 is based on the "state parameter" proposition and compares the sand

behavior in the following cases: (i) sands with the same void ratio at two different effective confining stresses, and (ii) sands with the same distance to the steady-state line at two different effective confining stresses. Altaee and Fellenius, 1994 shows that the sands which behave similarly are those characterized by the same distance to the steady-state line. The similarity of the behavior includes the shear strength, represented by the deviatoric stress normalized to the mean stress, and the sand dilatancy, represented by the volumetric strain as a function of axial strain.

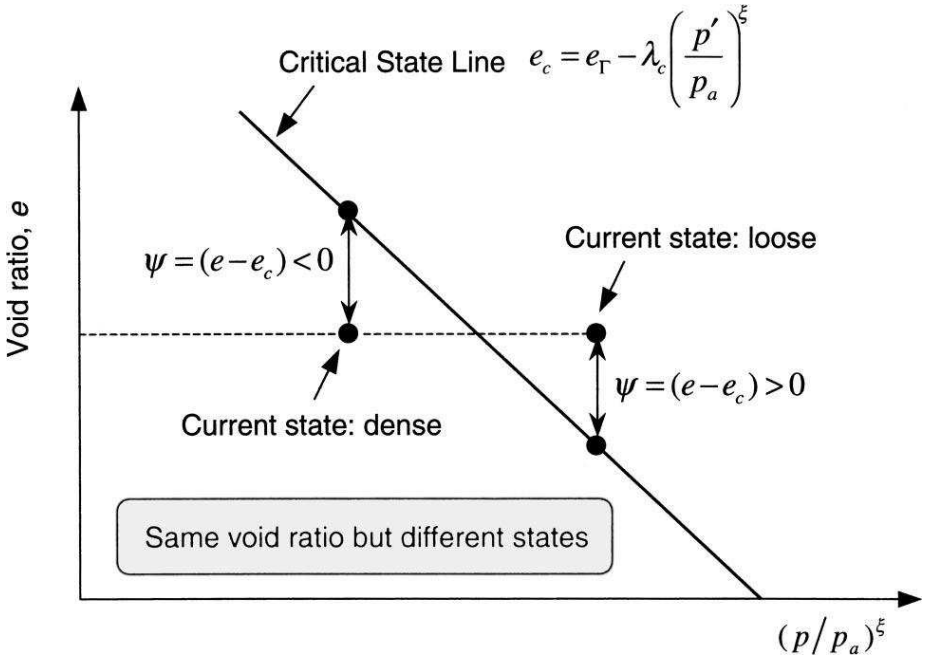

Fig. 3.7.: State parameter and critical state line after Yang and Li, 2004

Empirical relations to estimate the mechanical parameters

Based on the acquired knowledge about sand behavior, attempts to propose empirical relationships to predict the strength and the dilatancy parameters of sand, depending on its state, started with Vesic and Clough, 1968 and Billam, 1972. A seminal work is due to Bolton, 1986, after the examination of large quantities of data for various sands. Bolton, 1986 defined a relative dilatancy index having the following form:

$$I_R = I_D(Q - \ln p'_f) - R \qquad \text{with} \qquad \left(-\frac{d\epsilon_v}{d\epsilon_1}\right) = 0.3 I_R \tag{3.14}$$

where the dilatancy of sand represented by I_R depends on the sand state which is a combination of the relative density index ($I_D = (e_{max} - e_0)/(e_{max} - e_{min})$) and the mean effective stress at failure p'_f. Q and R are fitting parameters that depend on the intrinsic sand characteristics. It was found that values $Q = 10$ and $R = 1$ can be assumed for all the sands studied by Bolton, 1986.

Furthermore, Bolton, 1986 shows that a linear function relates the difference between friction angles at the peak shear strength (ϕ'_p) and the critical state (ϕ'_{cr}) with the peak dilatancy (ψ_p or I_R). Proposed correlations take the following forms:

$$\phi'_p - \phi'_{cr} = \beta\psi_p \tag{3.15}$$

$$\phi'_p - \phi'_{cr} = A_f I_R \tag{3.16}$$

where β and A_f are fitting parameters that depend on the intrinsic sand characteristics. Bolton, 1986 also found that the following values are useful for the studied sands and that I_R ranges between 0 and 4:

- $\beta = 0.5$ and $A_f = 3$ for triaxial conditions
- $\beta = 0.8$ and $A_f = 5$ for plane strain conditions

Finally, an empirical relation capable to predict the peak friction angle of sand from the sand state can be deducted, as shown below:

$$\phi'_p - \phi'_{cr} = A_f(I_D(Q - \ln p'_f) - R) \tag{3.17}$$

Since the database used by Bolton, 1986 did not contain tests at very low effective confining stresses, the extrapolation of the obtained relationships to this particular range of stresses should be validated. Chakraborty and Salgado, 2010 analyzed triaxial and plane strain tests on $Toyoura$ sand at confining stresses down to 4 *kPa* performed by Tatsuoka, 1984, Tatsuoka et al., 1986, Tatsuoka, 1987. Chakraborty and Salgado, 2010 found that Q, defined as a constant by Bolton, 1986, increases with the confining stress level. Moreover, a logarithmic relationship has been established between Q and the confining stress; it has the following form (in triaxial conditions):

$$Q = A + B\ln(p'_0) \tag{3.18}$$

where A and B are constants depending on the studied soil.

Besides, Giampa and Bradshaw, 2018 proposed a simple method to estimate the peak friction angle at extremely-low stress levels (refer to Section 3.1.3). Moreover, Giampa and Bradshaw, 2018 showed that the relations proposed by Bolton, 1986 overestimate the sand strength and dilatancy at low confining stresses. A modified stress-dilatancy relation based on Bolton's relation has been proposed and validated. This relation includes an additional

parameter ΔQ enhancing the fitting to the experimental findings. This relation has the following form:

$$\phi'_p - \phi'_{cr} = A_f(I_D(Q + \Delta Q \ln p'_f - \ln p'_f) - R) \tag{3.19}$$

Challenges to triaxial testing at low stress levels

As seen before, numerous studies considered triaxial tests at very low confining stresses, dropping below $10\,kPa$ (Ponce and Bell, 1971, Tatsuoka, 1984, Huang et al., 2015). However, the reliability of obtained results is affected by several factors, which are normally neglected at relatively higher confining stresses:

- An additional rigidity is imposed by the rubber membrane. This rigidity depends on the rubber elasticity, the membrane thickness, and the strain level. Some methods are published to estimate and then correct the effect of the membrane (e.g. Tatsuoka, 1984, ASTM, 1996).

- The sample and upper base weights affect the initial stress conditions applied to the specimen. The induced error can be approximated based on the mass of the base and the volume of the specimen.

- Generally, the triaxial cell should be filled with water to control the confining stress. The water level difference along the specimen induces a variation in the confining stress applied to the specimen. However, this variation is compensated in the saturated case by the water used to saturate the specimen (For more detail, refer to Mahmoud, 1997).

- Incertitude due to sensors precision: triaxial device includes some sensors to measure the variation of the stresses and the strains. These sensors involve incertitude ranges depending on their measurement ranges and performance, which leads to an increase in the percentage of errors at low-stress levels. The calibration of these sensors permits to limit and evaluate this incertitude.

- Incertitude due to the specimen preparation and demoulding. It is impossible to quantify the error induced, but repeatability tests can validate the reliability of tests including this incertitude.

Alternative methods to estimate the peak friction angle at extremely low stress levels

Due to the difficulties encountered during triaxial testing at very low-stress levels, some researchers proposed alternative methods capable of covering some knowledge gaps. Com-

forth, 1973, Santamarina and Cho, 2001, and Sadrekarimi and Olson, 2011 have proposed simple methods based on the measurement of the angle of repose to assess the critical friction angle of sand. Besides, Huang et al., 2015 developed a triaxial testing system specific for low confining stresses and a model test for slope failure flow under micro-gravity to validate its findings. Recently, Giampa and Bradshaw, 2018 presented a simple method to estimate the peak friction angle at extremely low-stress levels. The proposed method is based on the theory of infinite slopes, which determines the conditions leading to the soil slip along a plane parallel to the ground surface. Based on an infinite slope analysis of dry cohesionless soil, the slope angle at impending failure is considered equal to the peak friction angle representing the soil strength (Duncan and Wright, 2005). The method starts by forming a sand mass with a controlled relative density index. Then, the mold containing the mass is slowly tilted till the occurrence of slope failure, at which point the tilt angle is recorded. Figure 3.8 illustrates the test performed and gives a curve representing obtained results of the peak friction angle variation with the relative density index at extremely low stress.

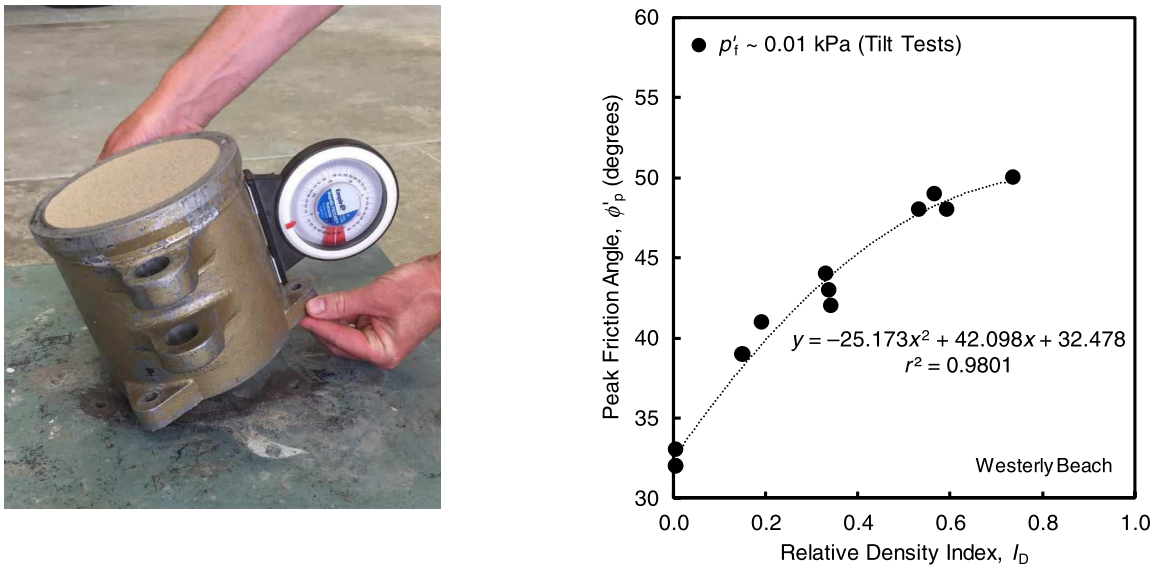

Fig. 3.8.: (a) Photograph and (b) typical results of the simple method proposed by Giampa and Bradshaw, 2018 to estimate peak friction angle at extremely low stress levels.

Sand similarity at different stress levels

As the sand behavior is controlled by the state parameter depending on relative density index and confining stress, Altaee and Fellenius, 1994 studied the possibility to utilize this feature in 1g-physical modeling. Then, Altaee and Fellenius, 1994 successfully validated the similarity of two sands characterized by the same state parameter at different stress levels under monotonic shearing. This idea was adopted by LeBlanc et al., 2010 to perform

a 1g-scale model of offshore wind turbine monopile subjected to cyclic loading.

Huang et al., 2015 conducted undrained strain-controlled cyclic triaxial tests and proved the similarity between loose sand at low confining stress and medium-dense sand at relatively higher confining stress. Due to the limited number of performed tests, the limited range of varied relative density index and confining stress, and the limited number of cycles, Huang et al., 2015 findings do not fill this knowledge gap.

3.2 Sand behavior under monotonic shearing at different stress levels

Fontainebleau *NE34* sand is a reference sand, commonly used in academia. As this sand is used in a 1g physical model, conserving the parameters underlying the stress-dilatancy dependence is essential. However, the available data at very low confining stresses are scarce. Therefore, in this part, drained monotonic triaxial tests are conducted at different sand states (relative density index and confining stress) to determine the shearing parameters. Based on this experimental work, empirical relations will be deduced, permitting the estimation of these parameters depending on the sand state. The aim is to propose reliable tools to ensure the similarity of the two sand states with different stress levels.

3.2.1 Characterization of the studied material

Fontainebleau *NE34* sand was used for the tests conducted in the framework of this thesis. This reference sand is commonly used in laboratory tests. Fontainebleau *NE34* sand mainly consists of silica grains (99%) and has sub-rounded grains as seen in the scanning electron microscope image in Figure 3.9.

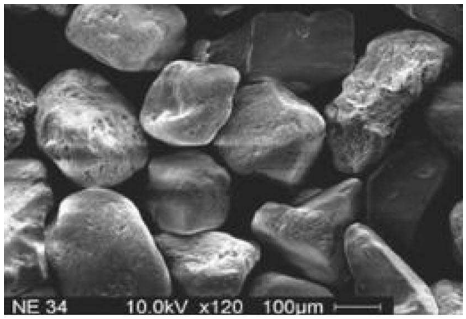

Fig. 3.9.: Scanning electron microscope image of *NE34* sand (from Benahmed, 2001

Tab. 3.2.: Adopted properties for *NE34* sand

Property	Unit	Description	Value
G_s	–	Specific gravity	2.65
e_{max}	–	Maximum void ratio	0.88
e_{min}	–	Minimum void ratio	0.56
D_{50}	*mm*	Mean grain size	0.21
C_u	–	Uniformity coefficient	1.52

The grading curves, provided by the supplier (SIFRACO company) and performed by Alvarado, 2000 at Navier laboratory, are presented in Figure 3.10. Therefore, *NE34* sand is classified as fine, uniformly graded silica sand. Relevant parameters are presented in Table 3.2, where some parameters are taken from Feia et al., 2016.

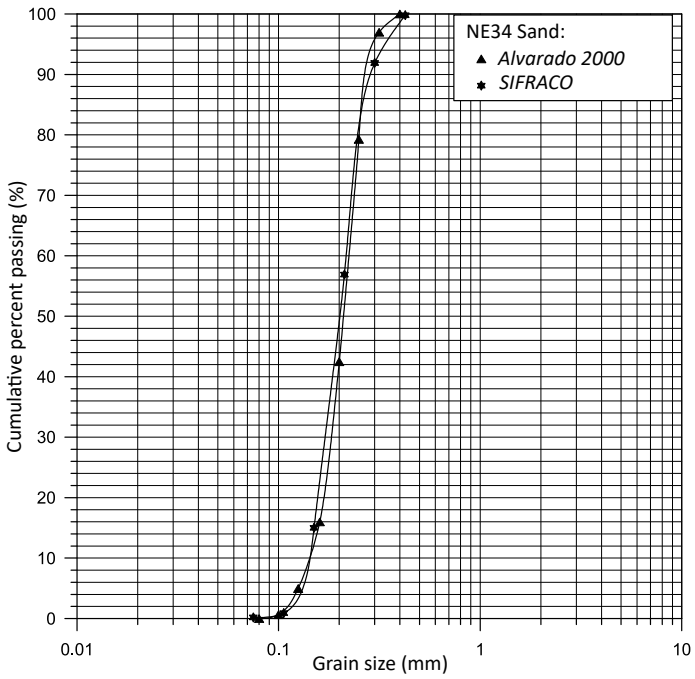

Fig. 3.10.: Grading curve of *NE34* sand

3.2.2 Monotonic triaxial device and testing procedure

The tests are conducted using a classical triaxial device developed at Navier laboratory. This device is adopted to a specimen diameter of $\Phi 100$ *mm* and height of 200 *mm*. The device is composed of the following elements:

- Triaxial cell placed on a *TRI-SCAN50* mechanical press with a capacity of 50 *kN*. The plate of the press is controllable in displacement and used to conduct the strain-controlled triaxial tests.

- Air/water cells serving to apply the confining and the back pressure to the specimen.

- Two force sensors (internal and external) are used to measure the axial force applied to the specimen. The outputs of the internal force sensor are adopted in the results treatment (no cell friction). The sensor has a capacity of 50 *kN* and shows good performance and precision (refer to Appendix A.1).

- Three pressure sensors to measure: the confining pressure in the triaxial cell and the pore pressure at the lower and upper bases of the specimen.

- Flowmeter system connected to the specimen serves to measure the volume variation (contraction/dilation).

- Displacement *LVDT* sensor used to measure the axial displacement with a measuring range of 40 *mm*.

- CO_2 gas system and water deaeration device used to saturate the specimen.

- Data acquisition system developed under LabVIEW program.

Figure 3.11 presents a view of the triaxial device.

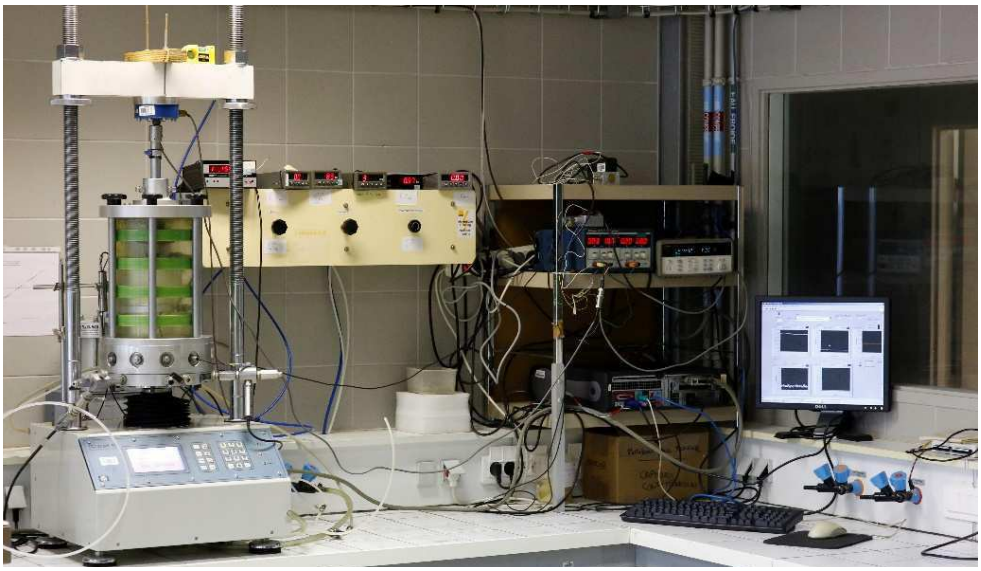

Fig. 3.11.: Photo of the strain-controlled triaxial device used in this study

The test procedure largely conforms to NF P94-074, 1994 with a difference in the specimen preparation. The main steps of testing are presented:

- Specimen preparation: The method adopted is the "dry compaction method". The specimen is divided into 10 layers, where the mass of each layer is determined depending on the targeted density. An adapted mold is placed on the lower base, connected with the vacuum pressure, to well-reshape the rubber membrane. The sand layers were formed progressively using a tamper to obtain the targeted density (Figures 3.12a and 3.12b). Then, the vacuum pressure (which should not exceed the confining pressure of the test) is applied to maintain the specimen after the demoulding and during the assembly of the triaxial cell to apply a confining pressure (Figure 3.12c).

- Saturation: A flow is CO_2 gas is imposed through the specimen during 10 to 15 *min* at a pressure of 10 *kPa*. Then, a flow of deaerated water is imposed for a minimum duration of 25 *min*. The Skempton coefficient is determined, before and after the consolidation, to verify the specimen saturation. A minimum value of 98 % after the consolidation should be obtained.

- Consolidation: The confining and back pressures are increased progressively to obtain the targeted confining stress at the specimen. A back pressure of 100 *kPa* is used to enhance the specimen saturation.

- Shearing: The displacement of the mechanical press plate induces an axial force to the specimen, leading to the shearing failure at a relative strain level (Figure 3.12d). The press is controled with a constant displacement velocity of 1 *mm/min*, which is equivalent to 0.5 %/*min* in terms of strain velocity.

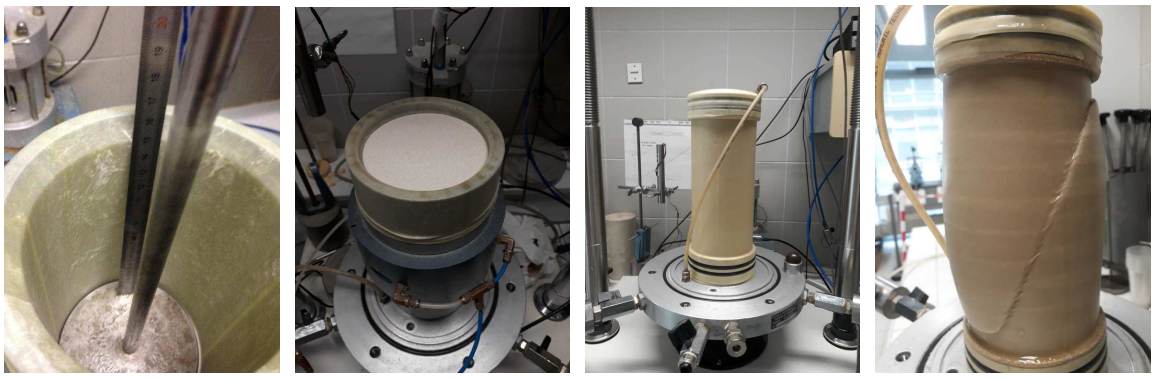

(a) (b) (c) (d)

Fig. 3.12.: Sand specimen at different steps of monotonic triaxial testing procedure

3.2.3 Tests program

As mentioned before, the experimental program is defined to highlight the effect of the confining stress and the relative density index at different stress levels. Therefore, drained monotonic triaxial compression tests are performed to determine the strength and the dilatancy parameters. 3 testing sets of different relative density indices ($I_d = 0.50$; 0.70; and 0.90) are conducted at confining stresses varying from 15 *kPa* to 400 *kPa*. Some tests of low and high confining stress levels are repeated to validate the reliability of the obtained results. Besides, the identification of the critical state line *CSL* is important and helps in fulfilling the purpose of this study. Thus, some additional tests on specimens at very loose state are conducted. Table 3.3 presents the characteristics of performed tests.

Tab. 3.3.: Tests program on the monotonic triaxial device

Test set	Initial relative density index $I_{d,0}$ ($I_{d,c}$)	Test identifier	Confining stress p'_0 (kPa)
Set 1	0.50 (~ 0.50)	TX-1-1	15
		TX-1-2	25
		TX-1-3	50
		TX-1-4	99
		TX-1-5	199
		TX-1-6	400
Set 2	0.70 (~ 0.70)	TX-2-1	15
		TX-2-2	25
		TX-2-3	50
		TX-2-4	99
		TX-2-5	199
		TX-2-6	400
Set 3	0.90 (~ 0.90)	TX-3-1	15
		TX-3-2	26
		TX-3-3	50
		TX-3-4	101
		TX-3-5	198
		TX-3-6	398
Set 4	0.70 (~ 0.70)	TX-2-1-R	15
	0.70 (~ 0.70)	TX-2-5-R	200
Set 5	-0.05 (0.06)	TX-5-1	200
	-0.05 (0.08)	TX-5-2	400
	-0.05 (0.09)	TX-5-3	500

$I_{d,c}$ is the relative density index after the consolidation. The contraction due to the consolidation is neglected in medium-dense to dense sand cases, while it cannot be neglected in very loose and loose sand cases. The values obtained for set 5 are according to the calibration performed by Benahmed, 2001 for *NE34* sand. The very loose specimens are formed by a method called "wet compaction". This method is similar to the "dry compaction" while 5% of water was added to the sand materials. For more details, refer to Benahmed, 2001.

3.2.4 Results and discussions

Results smoothing and repeatability

The triaxial device used in the present study is not developed for tests with low confining stress levels. The error margin of the confining and the back-pressure applied to the specimen becomes relatively important in this range of stresses. The observed drops of the deviatoric stress mainly occurred at the maximal resistance of the sand (failure state). These drops can be attributed to the occurrence of shearing strain localization due to low confining stress levels. The obtained curves are smoothed using the feature *adjacent-averaging* available on the *OriginPro* program (Figure 3.13). A global margin error of this operation is evaluated and considered during the results analysis.

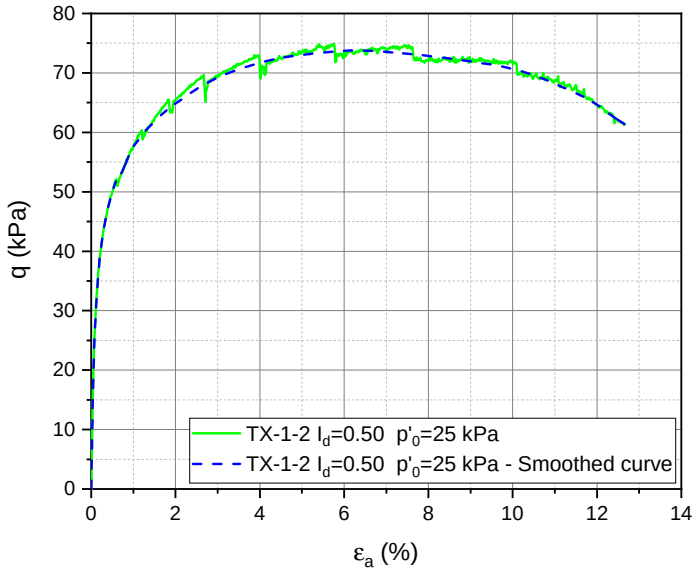

Fig. 3.13.: Smoothing of stress-strain curves ($q - \epsilon_a$) at low confining stress level

The set 3 of tests program consists of the repetition of two tests at different stress levels to validate the repeatability of the testing procedure and, then, the obtained results. This set shows good repeatability at a low confining stress level (Figure 3.14) and perfect repeatability at a relatively high confining stress level (Figure 3.15).

Estimation of the uncertainties

As seen in Section 3.1.3, the investigation of sand behavior at low stress levels involves some difficulties. In this part, an estimation of the uncertainties are carried out:

- The estimation of the rubber membrane effect is according to ASTM, 1996:

$$\Delta q = (4E_m t_m \epsilon_a)/D_c = 0.168\epsilon_a \tag{3.20}$$

where E_m is the Young's modulus of rubber membrane, t_m is the membrane thickness, ϵ_a is the axial strain, and D_c is the specimen diameter after the consolidation. At 5% of axial strain, which is a mean value corresponding to the peak of soil response, the effect of the rubber membrane is estimated to be 0.8 *kPa*. The obtained results are corrected according to Equation 3.20, while the realistic effect of membrane can be smaller or higher. A margin error of ± 0.4 *kPa* is taken as uncertainty.

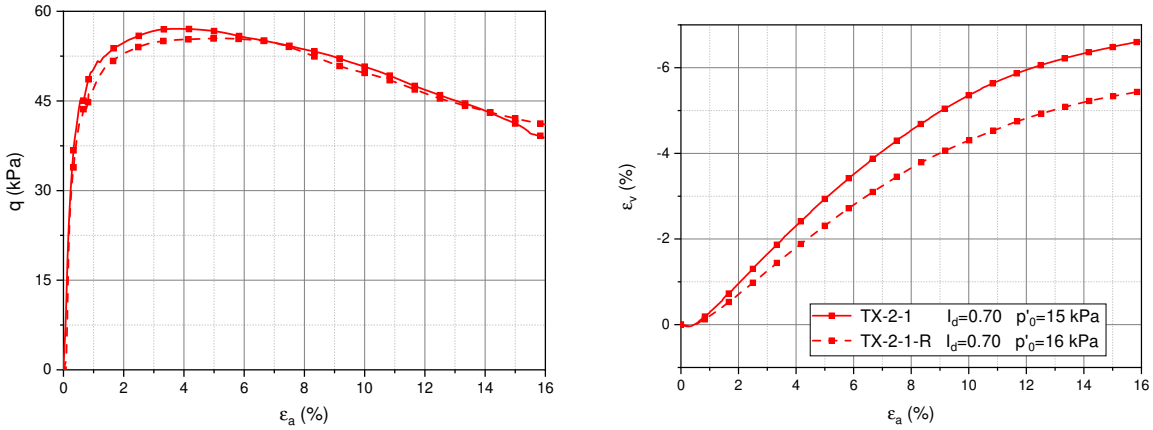

Fig. 3.14.: Tests repeatability at low confining stress level: (a) $q - \epsilon_a$ (b) $\epsilon_v - \epsilon_a$

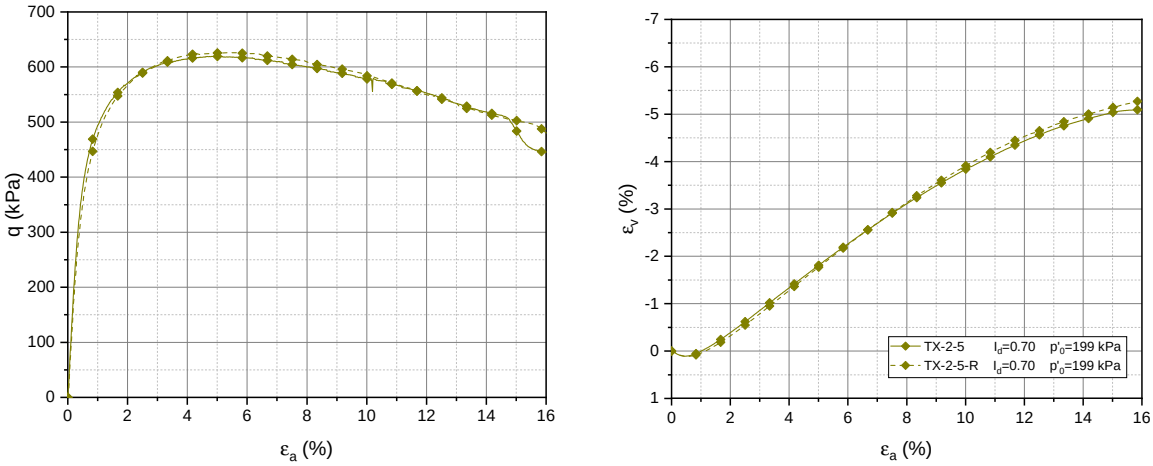

Fig. 3.15.: Tests repeatability at high confining stress level: (a) $q - \epsilon_a$ (b) $\epsilon_v - \epsilon_a$

- The uncertainties due to the pressure sensors measurement are taken as ± 0.7 *kPa* according to the sensors precision.

- The upper base weight of 8.75 *N* applies an axial stress of about 1.1 *kPa* to the sand specimen. Besides, the upper half of the specimen also applies an axial stress of about 1.5 *kPa*. The induced axial stress is considered as an uncertainty affecting the sand response.

- The smoothing of curves at low-stress levels (15 and 25 *kPa*) can affect the obtained results. The impact of this operation is evaluated in each test and then considered for the analysis of the results. This impact varies between 1 and 4 *kPa* depending on the confining stress level and the relative density index.

Typical triaxial results

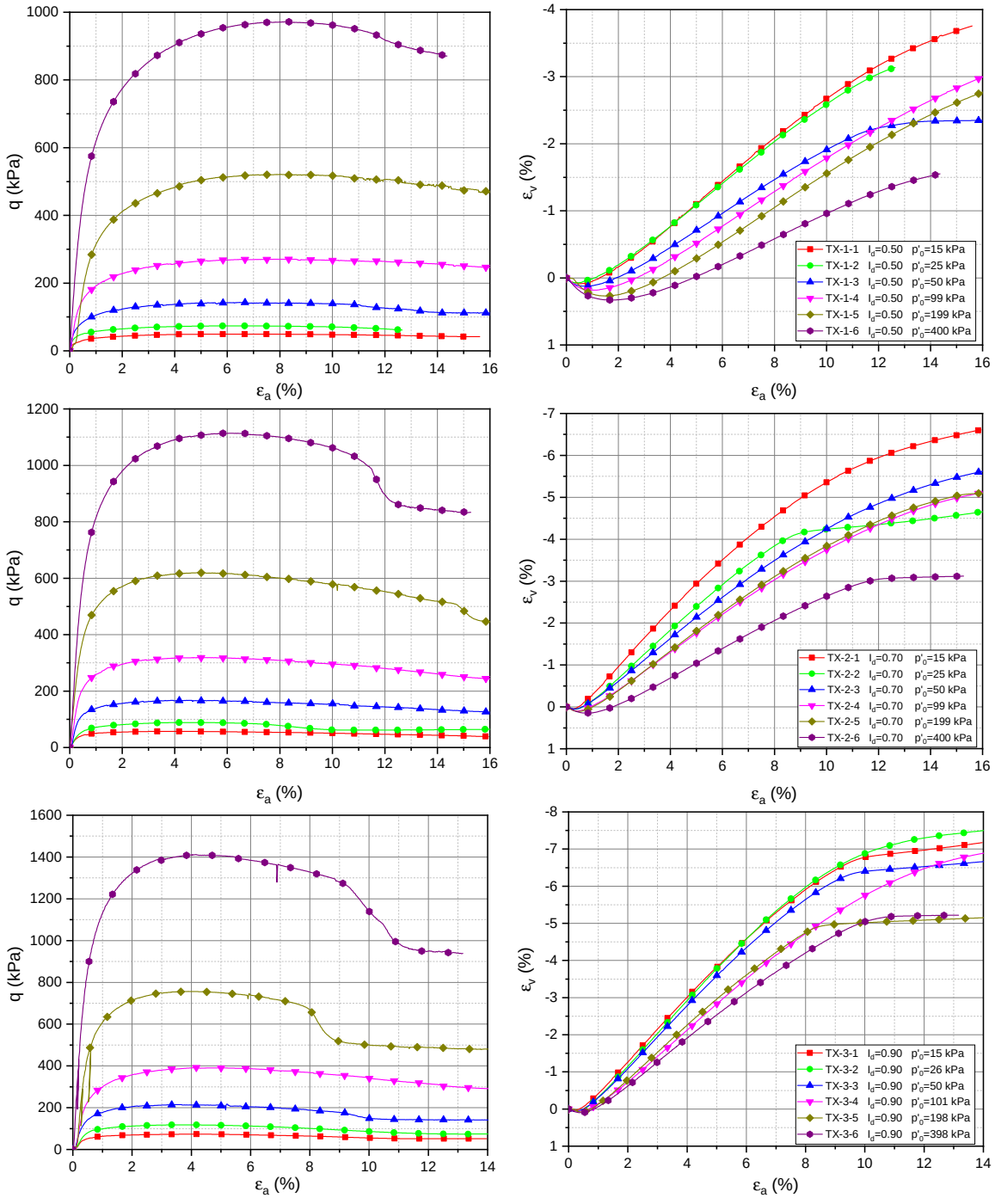

Fig. 3.16.: Typical monotonic triaxial results: (a) $q - \epsilon_a$ (b) $\epsilon_v - \epsilon_a$

The results obtained for sets 1, 2, and 3 are presented in Figure 3.16: (a) the deviatoric stress as a function of the axial strain, and (b) the volumetric strain as a function of the axial strain.

Effect of the relative density index I_d

The figure 3.17 presents the sand response for 3 tests at different relative density indices but at the same confining stress level. The relative density index varies from medium dense sand ($I_d = 0.50$) to dense sand ($I_d = 0.90$). The 3 tests show the same general behavior in terms of strength and dilatancy responses: (i) the deviatoric stress increases with the axial strain up to a peak, followed by strength softening until the critical state is reached, (ii) the sand exhibits contraction in a short phase, followed by a phase of dilatancy stabilizing at the critical state. The strain level corresponding to this phase change is called the characteristic state. The influence of an increase in the relative density index lies in the following points:

- An increase in the global stiffness and strength of the sand response, shown at small strain level as an increase of the initial rigidity and at the failure state as an increase in the peak of the normalized deviatoric stress (q/p'_0) which means an increase of the peak friction angle.
- A shift of the strength peak position towards smaller axial strain level.
- A decrease of the contraction rate and an increase of the dilation rate.
- A shift of the characteristic state position towards smaller axial strain level.

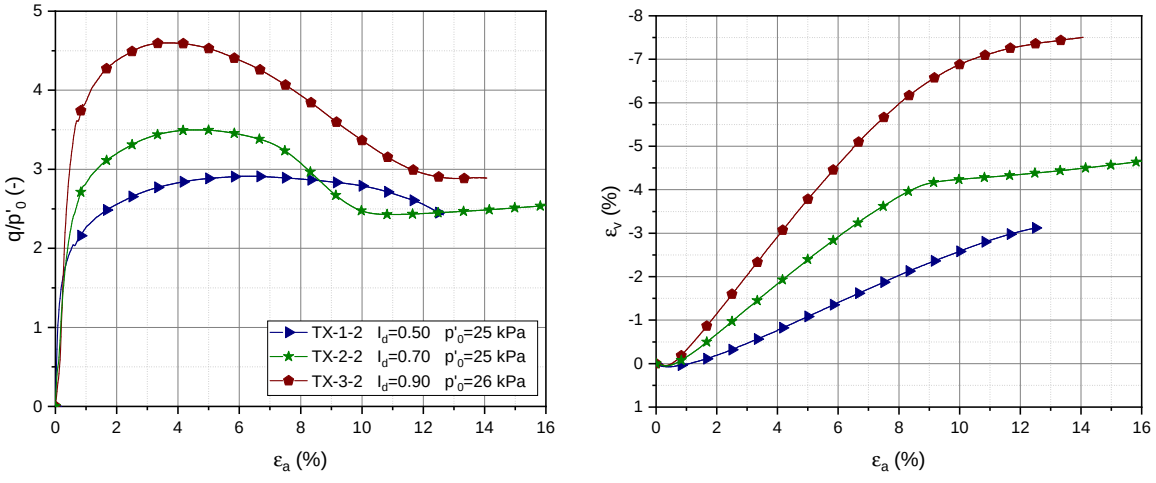

Fig. 3.17.: Influence of relative density index on sand behavior at low confining stress level ($p'_0 = 25$ *kPa*): (a) $q - \epsilon_a$ (b) $\epsilon_v - \epsilon_a$

These findings are similarly observed at relatively higher confining stress level (Figure 3.18), while the rates of the post-peak softening and dilatancy are affected. The obtained rates are attributed to the coupling of the relative density index and the confining stress effects on the sand behavior. The next section shows the confining stress effect by comparing tests with the same relative density index at different stress levels.

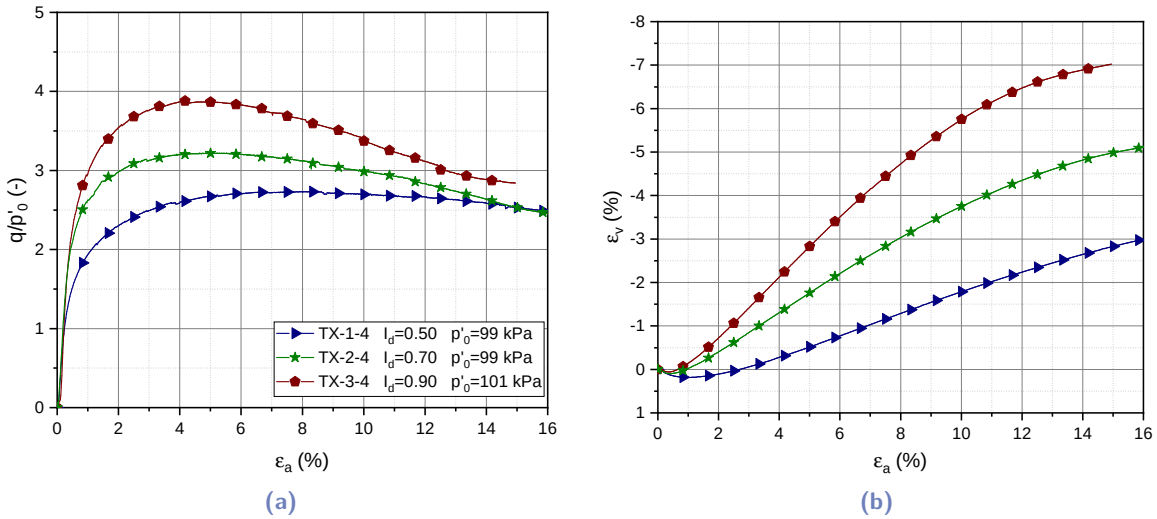

(a) (b)

Fig. 3.18.: Influence of relative density index on sand behavior at relatively high confining stress level ($p'_0 = 100$ *kPa*): (a) $q - \epsilon_a$ (b) $\epsilon_v - \epsilon_a$

Effect of confining stress level

Figure 3.19 presents the sand response for 6 tests (set 1), with the same relative density index ($I_d = 0.50$), at different confining stresses varying from low confining stress ($p'_0 = 15$ *kPa*) to relatively high confining stress ($p'_0 = 400$ *kPa*). The influence of an increase of the confining stress lies in the following points:

- A decrease in the global stiffness and strength of the sand response, shown at small strain level as a decrease of the initial rigidity and at the failure state as a decrease in the peak of the normalized deviatoric stress (q/p'_0) which means a decrease of the peak friction angle.

- A shift of the strenght peak towards higher axial strain level.

- An increase of the contraction rate and a decrease of the dilation rate.

- A shift of the characteristic state position towards higher axial strain level.

The effect of confining stress is established at 3 different relative density indices ($I_d = 0.50$; 0.70; 0.90), and similar findings are obtained.

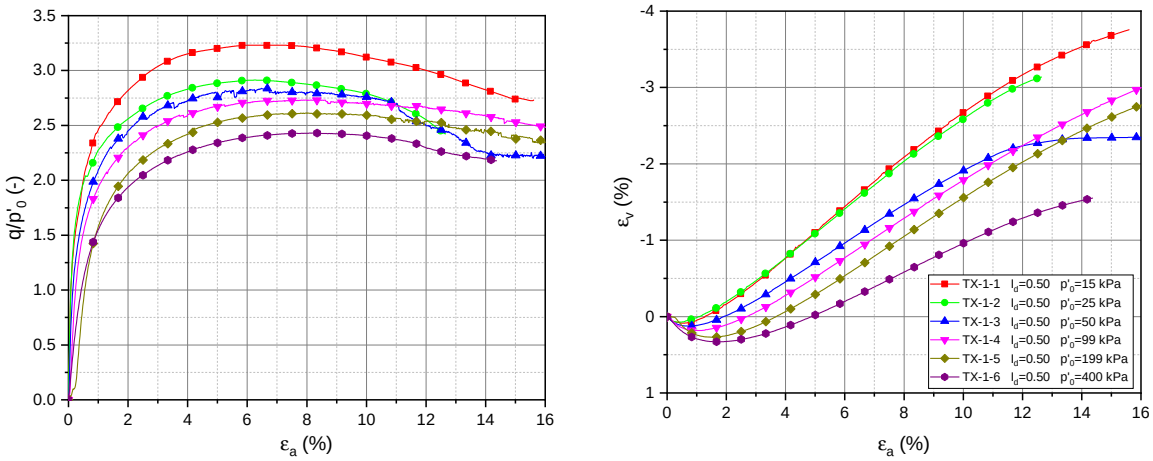

(a) (b)

Fig. 3.19.: Influence of confining stress level on sand behavior $I_d = 0.50$: (a) $q - \epsilon_a$ (b) $\epsilon_v - \epsilon_a$

Identification of critical state line

Section 3.1.3 shows that the "state parameter" governs the monotonic sand behavior. Therefore, the void ratio path is presented in $e - p'$ space (Figure 3.20), aiming to assess the position of the critical state line (*CSL*). It is clearly shown that tests with different conditions did not converge to a unified line. This issue can be justified by some information about the determination of critical state line:

- According to Klotz and Coop, 2002, one of the principal challenges in the identification of the *CSL* in granular materials is the occurrence of premature strain localization due to shearing samples at low-stress levels. Thus, it is recommended to conduct the tests at relatively high confining stress levels.

- According to Zdravkovic et al., 2020 following Jefferies and Been, 2006, very loose samples, consolidated to reasonably high confining stress levels, should be used to identify the location of the *CSL*. Indeed, under such conditions, the initial state is above the *CSL* in $e - p'$ space and the sample contracts to reach the *CSL*. The test interpretation becomes simpler due to the absence of shear banding and strain localization.

  Other researchers have generally relied on drained strain rate controlled tests on dilatant samples to determine the critical state (Jefferies and Been, 2006).

Therefore, a set of very loose samples ($I_d = -0.05$) and medium-dense samples ($I_d = 0.50$) at relatively high confining stress levels ($p'_0 > 200$ *kPa*) are used in the identification of *CSL*. Some points, theoretically belonging to the *CSL*, are fitted to identify a new equation with a margin of uncertainty for *NE34* sand. The power expression, proposed by Li and Wang, 1998, is adopted and the following expression is obtained:

$$e = 0.88 - 0.0717\left(\frac{p'}{101.3}\right)^{0.236} \qquad \text{with} \qquad p' \quad \text{in} \quad kPa \tag{3.21}$$

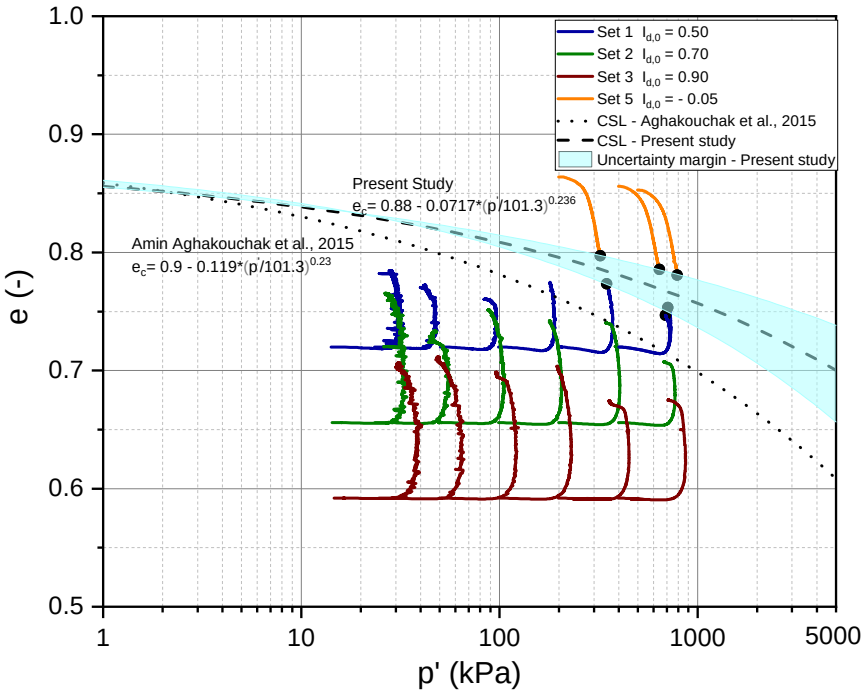

Fig. 3.20.: Identification of the critical state line for *NE34* sand

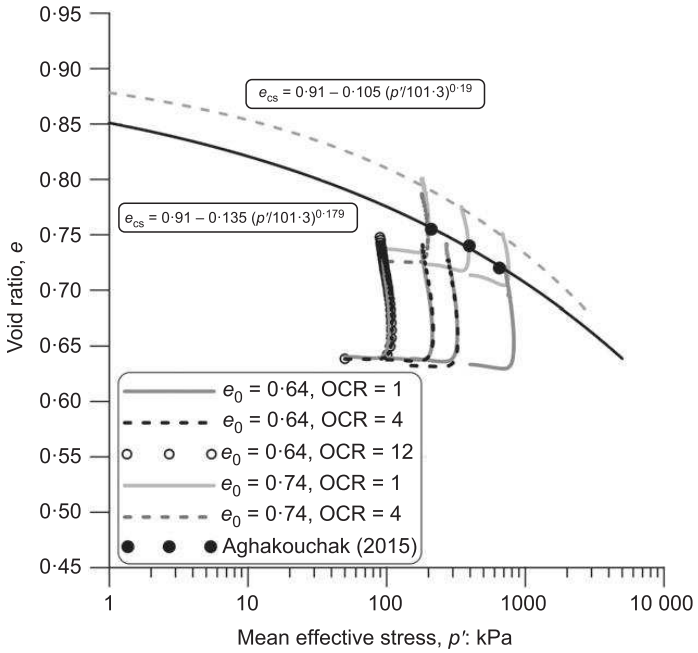

Fig. 3.21.: Critical state lines for *Dunkirk* sand (Zdravkovic et al., 2020)

The comparison of the proposed *CSL* with that proposed by Aghakouchak et al., 2015 shows a large contrast, since the actual equation translates the *CSL* position by Δe of about $+0.05$

in the studied range of mean stresses. Similar findings are presented by Zdravkovic et al., 2020, where a similar translation Δe of about $+0.04$ was encountered with the *CSL* position identified by Aghakouchak et al., 2015 for *Dunkirk* sand (Figure 3.21).

3.2.5 Empirical relations to estimate mechanical parameters

Determination of the mechanical parameters

The mechanical parameter representing the shear strength of sand is the peak friction angle. This parameter is determined for each conducted triaxial test using the following equation:

$$\phi'_p = \arcsin\left(\frac{3M}{6+M}\right) \qquad \text{with} \qquad M = \frac{q_f}{p'_f} \tag{3.22}$$

Figure 3.22 presents the obtained friction angles for all the tests as a function of confining stress level (initial effective mean stress), with the margin of uncertainties shown in Section 3.2.4. It is clearly shown that the increase of confining stress level causes a decrease in shear strength at different relative density indices.

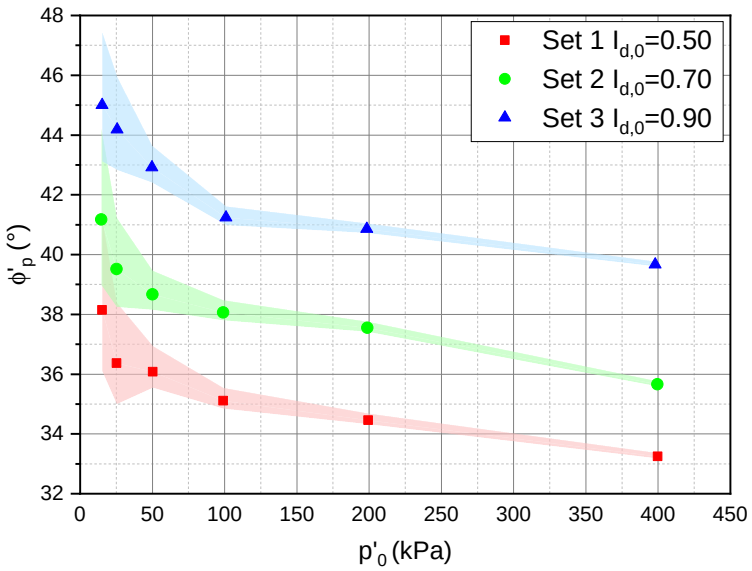

Fig. 3.22.: Peak fiction angle for different relative density indices as a function of the initial mean effective stress

The mechanical parameter representing the sand dilatancy at failure is the peak dilation angle. This parameter is determined for each conducted triaxial test using the following equation:

$$\psi_p = -\frac{\delta\epsilon_v/\delta\epsilon_a}{2-\delta\epsilon_v/\delta\epsilon_a} \qquad \text{with} \qquad \delta\epsilon_a > 0 \quad \text{and} \quad \delta\epsilon_v < 0 \tag{3.23}$$

Figure 3.23 presents the obtained dilation angles for all the tests as a function of confining stress level. This measurement is sensitive to the test conditions and can be influenced by numerous issues. Thus, the estimation of uncertainties is difficult task. It is clearly shown that the increase of confining stress level causes a decrease in the sand dilatancy at different relative density indices.

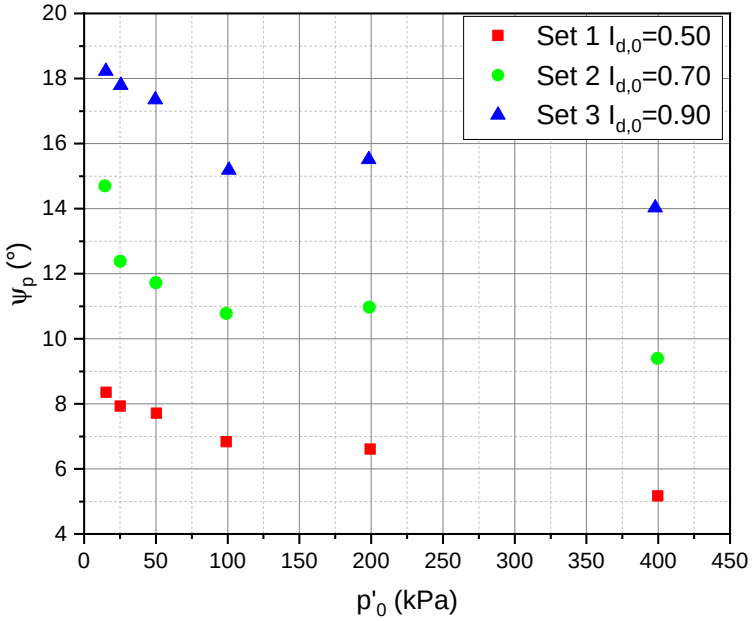

Fig. 3.23.: Peak dilation angle for different relative density indices as a function of initial mean effective stress

Deduction of the empirical relations

As seen in Section 3.1.3, Bolton, 1986 shows that a linear function relates the difference between the friction angles at the peak shear strength (ϕ'_p) and the critical state (ϕ'_{cr}) with the peak sand dilatancy (ψ_p or I_R). Figure 3.24 shows the application of the proposed relations to experimental results on *NE34* sand, leading to the following equations:

$$\phi'_p = \phi'_{cr} + \beta\psi_p \qquad \text{with} \qquad \phi'_{cr} = 29.6 \quad \text{and} \quad \beta = 0.78 \tag{3.24}$$

$$\phi'_p - \phi'_{cr} = A_f I_R \qquad \text{with} \qquad A_f = 5.08 \tag{3.25}$$

The obtained value of ϕ'_{cr} is verified by the analysis of very loose specimens results (Set 5 of the test program). Figure 3.25 presents the variation of the deviatoric to the mean stress ratio as a function of axial strain. As the loose specimens converge to the critical state, it is clear that the stress ratio will not exceed the value of 1.2, which is equivalent to ϕ'_{cr} equal to $30°$.

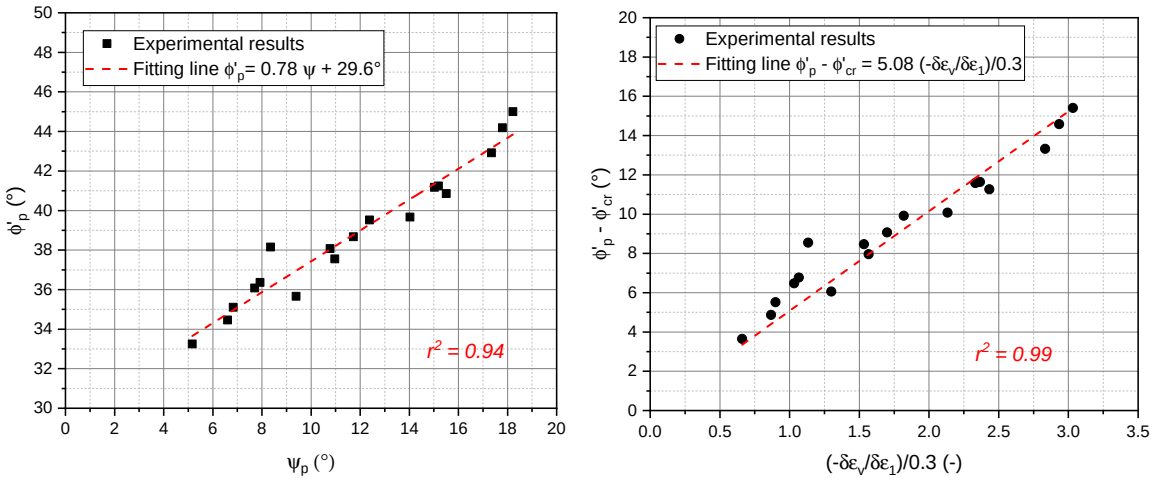

Fig. 3.24.: Linear relations between strength and dilatancy of sand at failure

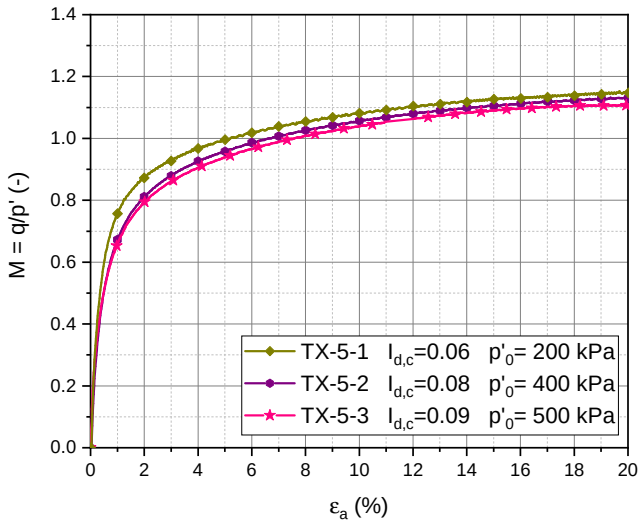

Fig. 3.25.: Monotonic triaxial response of very loose *NE34* sand: $q/p' - \epsilon_a$

The dilatancy-stress relation proposed by Bolton, 1986 ends by the proposition of an empirical relation between the relative dilatancy index I_R and the sand state conditions (relative density index I_d and mean effective stress p'_f), leading to equation 3.17. Figure 3.26 shows the application of this relation to *NE34* sand. Poor regression ($r^2 = 0.48$) is obtained between the following fitted relation and the experimental results:

$$\phi'_p = 29.6 + 5.08(I_d(8.75 - \ln p'_f) - 0.77) \tag{3.26}$$

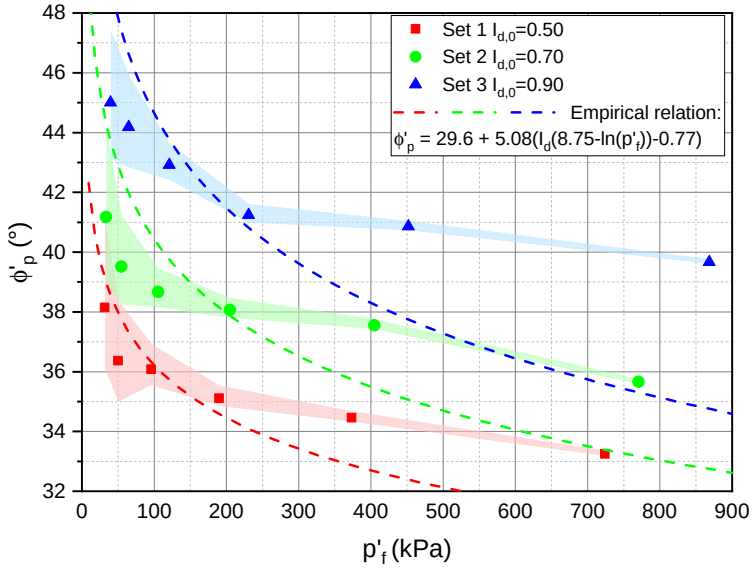

Fig. 3.26.: Application of Bolton, 1986 stress-dilatancy relationship for *NE34* sand

As seen in Section 3.1.3, Chakraborty and Salgado, 2010 and Giampa and Bradshaw, 2018 introduce a modification to the relation, by varying Q as a function of the mean stress level. Figure 3.26 shows the application of the modified relation to *NE34* sand. Very good regression ($r^2 = 0.98$, Figure 3.27) is obtained between the following fitted relation and the experimental results:

$$\phi'_p = 29.6 + 5.08(I_d(5.60 + 0.58 \ln p'_f - \ln p'_f) - 0.62) \tag{3.27}$$

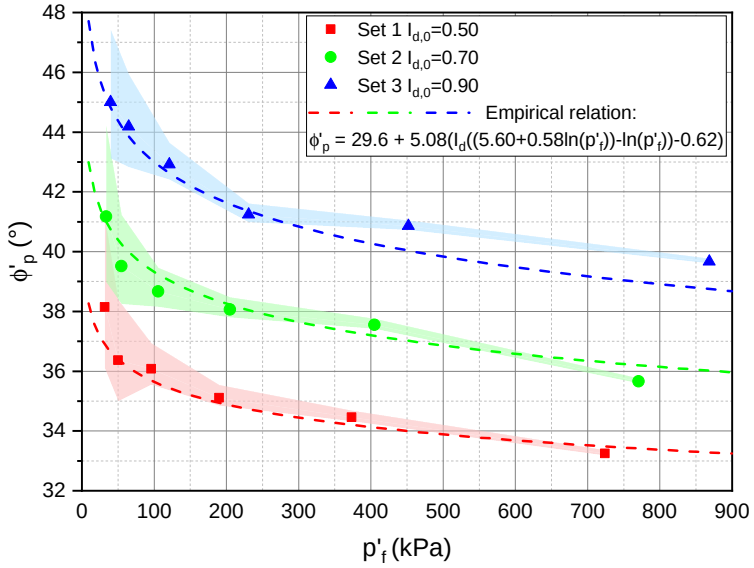

Fig. 3.27.: Application of modified Bolton, 1986 stress-dilatancy relationship for *NE34* sand

Table 3.4 presents the properties of each sand, the tests conditions, and corresponding stress-dilatancy parameters. The obtained parameters will be interpreted according to the sand properties, trying to show the agreement between them.

Tab. 3.4.: Literature review of stress-dilatancy relations and comparison with present study findings

Parameter (Unit)	Sand type (Reference)			
	Westerly Beach (Giampa and Bradshaw, 2018)	Golden Flint (Giampa and Bradshaw, 2018)	Toyoura (Chakraborty and Salgado, 2010)	Fontainebleau (Present study)
Morphology	–	Angular	Angular	Sub-rounded
I_d	$[0.13; 0.53]$	$[0.0; 0.65]^*$	$[0.2; 0.8]$	$[0.5; 0.9]$
p'_0 *(kPa)*	$[8; 100]^{**}$	$[10; 150]^{**}$	$[4; 197.2]$	$[15; 400]$
G_s	2.65	2.68	2.64	2.65
e_{max}	0.844	0.847	0.940	0.88
e_{min}	0.436	0.487	0.616	0.56
D_{50} *(mm)*	0.30	0.25	0.22	0.21
C_u	1.63	1.61	1.37	1.52
ϕ'_{cr} (°)	32.3	33.9	32.8	29.6
β	0.69	0.64	0.62	0.78
A_f	4.8	3.6	3.8	5.08
Q^{***}_{Bolton}	7.03	9.61	–	8.75
R^{***}_{Bolton}	-0.12	-0.69	–	0.77
Q	3.89	5.51	6.60	5.60
ΔQ	0.66	0.85	0.58	0.58
R	-0.28	-0.69	1	0.62

* $25/28$ specimens are at loose to medium dense state $[0.0; 0.65]$ while $3/28$ specimens are at dense state ($I_d = 0.81$). Besides, it is not clear if the dense specimens are used in this part of the study.
** This range corresponds to triaxial tests used in the study. A simple method is presented where the corresponding stress is estimated to 0.01 *kPa*.
*** In addition to the present work, some works determined the Q and R parameters proposed by Bolton, 1986, which found useful values of $Q = 10$ and $R = 1$ based on a large set of quartz sand experimental results.

A value of $29.6°$ is obtained for the critical friction angle of *NE34* sand. This value seems to be smaller than typical values obtained in the literature. However, it was validated by performing additional tests on specimens at very loose state and sheared to exceed 20% of axial strain (Figure 3.25). Furthermore, Hamidi et al., 2012 and Mostefa Kara et al., 2013 show that the decrease of the grains diameter (D_{50}) decreases the critical friction angle of granular materials. Xiao et al., 2019 conducts a series of drained triaxial compression tests on sands mixed with angular and sub-rounded glass beads at different proportions and showed that the critical friction angle decreases with particle regularity. This finding supports the observations by Yang and Luo, 2018, who proposed a linear relationship between the critical friction angle and defined coefficient representing the overall regularity of particles. These findings justify the critical friction angle value obtained for *NE34* sand, characterized by relatively small grain diameter and sub-rounded morphology.

The coefficient β (or similarly A_f, equations 3.15 and 3.16) obtained for *NE34* sand is found slightly higher than those obtained for other sands by similar works. Harehdasht et al., 2019 found that the increase of the grains diameter (D_{50}) and the grain regularity lead to a decrease in this coefficient. In contrast, Xiao et al., 2019 found that particle regularity does not affect this coefficient, proposing a value of 0.6 for the studied material. Therefore, the value obtained for *NE34* sand is in good agreement with the literature findings. However, the coefficient obtained for *Westerly Beach* sand is higher than those obtained for *Golden Flint* sand and *Toyoura* sand, despite the former having a larger grain diameter. This contradiction can be attributed to the undefined morphology or to the relatively limited number of tests used to determine this coefficient.

The remaining parameters, which govern the sand dilatancy as a function of the sand state (relative density index and mean effective stress at failure, equation 3.19), are Q, ΔQ, and R. The obtained values will now be discussed according to the sand properties. The effect of the particles shape on the sand dilatancy was investigated by Xiao et al., 2019 and Arda and Cinicioglu, 2021. The two works found that the increase in the overall regularity at a given confining stress leads to an increase in the dilation rate at the strength peak. Besides, Arda and Cinicioglu, 2021 showed a slight influence of the sand gradation on the dilation rate, which seems to be independent of the grain size. These findings are generated based on sand and glass beads mixtures and by relatively limited recent studies, which could affect the reliability of the results.

It should be noted that Q and ΔQ values presented in Table 3.4 for *Toyoura* sand are redetermined as a function of the mean effective stress at failure (p'_f) since the original data are given as a function of the initial mean effective stress (p'_0). This modification aims to ensure a fair comparison between different cases. Figure 3.28 shows the relationship between the excess friction angle ($\phi'_p - \phi'_{cr}$), the mean effective stress at failure (p'_f) and the relative density index (I_d). A good agreement was found between the present study and Chakraborty and Salgado, 2010 findings, while a relative divergence was remarked with the

findings of Giampa and Bradshaw, 2018 (especially in case of *Westerly Beach* sand).

Empirical relations obtained by Giampa and Bradshaw, 2018 (Figure 3.28a involve some conflicts: (i) parameter R took negative values in the two studied materials, which leads to an excess in friction angle and to a dilation behavior in very loose states at relatively high confining stress. This conflict is also shown in the experimental results (triaxial) adopted in the study. (ii) The relationship simulating *Westerly Beach* sand behavior diverges widely from all the other cases. The excess friction angle is strongly dependent on the relative density index, while it has a relatively weaker dependence on the stress conditions. This finding can be attributed to the limited number of tests, measuring sand dilatancy (saturated case), and the results of the simple tilt method used in the study. This method will be reviewed in section 3.3.

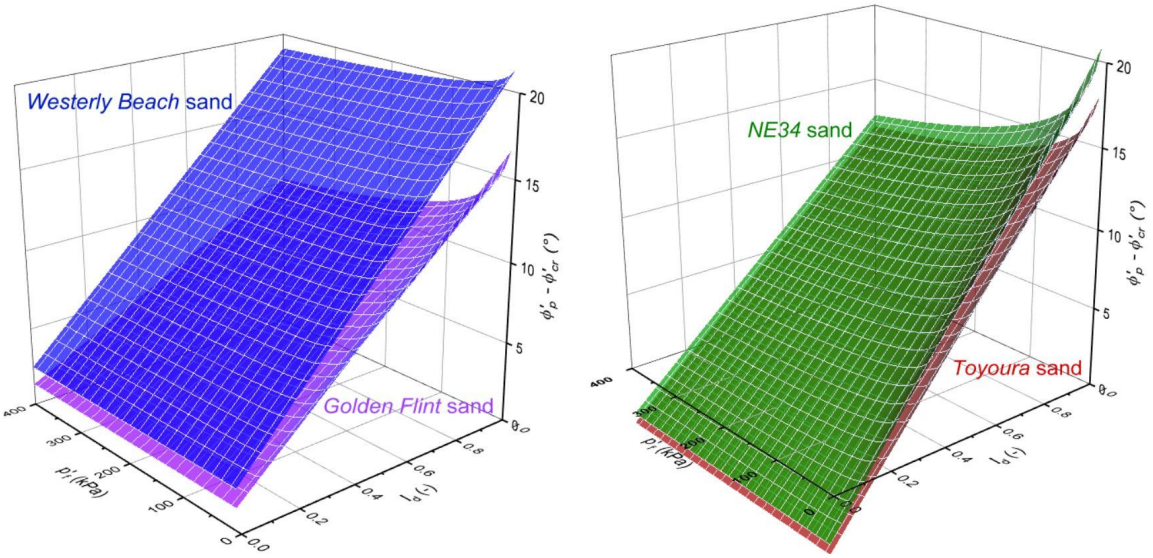

Fig. 3.28.: Excess friction angles ($\phi'_p - \phi'_{cr}$) as a function of the mean effective stress at failure (p'_f) and relative density index (I_d) for different cases: (a) *Westerly Beach* and *Golden Flint* sands (Giampa and Bradshaw, 2018); (b) *Toyoura* and *NE34* sands (Chakraborty and Salgado, 2010 and present study)

Toyoura and *NE34* sands share similar grain diameters and gradation uniformity features, while they differ in the morphology: *Toyoura* sand is characterized by angular shape, and *NE34* sand is characterized by sub-rounded shape. This can justify the relative similarity of the behaviors obtained with a slight higher excess friction angle for the *NE34* sand (Figure 3.28b). The positive values of the R parameter induce negative values of the dilation and excess friction angle at very loose states, which should be adjusted to 0 corresponding to a contractive behavior.

Further research efforts (e.g. large parametric study) are required to reveal the relationship between the stress-dilatancy parameters and the sand properties. However, the

presented interpretation validates the reliability of values obtained for *NE34* sand. Besides, this study ensures useful values of the stress-dilatancy parameters, which can be adopted for granular materials having similar or close properties.

3.2.6 Similarity of the monotonic behavior at different stress levels

The main aim of this study is to ensure similarity between the prototype sand and the sand used for the physical modeling at a relatively low confining stress. Two methods are adopted and their application to *NE34* sand are now presented:

- Modified stress-dilatancy relationship:
  This relationship estimates the sand dilatancy (similarly excess friction angle) depending on the sand relative density index and the stress level. As the relative density index of the prototype sand and the stress level of the prototype and the scale model are available, the relative density index of the scale model sand can be estimated to obtain similar dilatancy and peak friction angle. The challenge is that the modified stress-dilatancy relationship adopted in the literature is a function of the mean effective stress at failure, which cannot be easily determined. Therefore, as part of the present study, an alternative form of modified stress-dilatancy relationship is deducted, depending on the relative density index and the initial mean effective stress. Very good regression ($r^2 = 0.98$, Figure 3.29) is obtained between the following fitted relation and the experimental results:

$$\phi'_p = 29.6 + 5.08\left(I_d(5.04 + 0.60 \ln p'_0 - \ln p'_0) - 0.52\right) \tag{3.28}$$

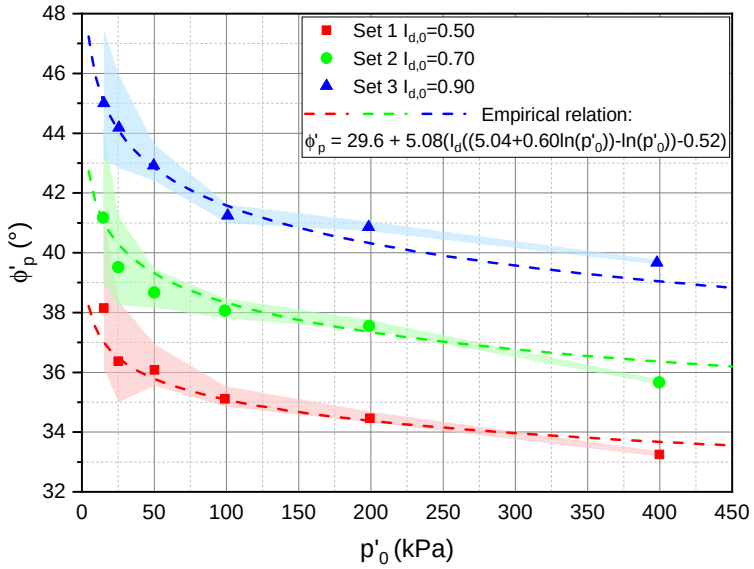

Fig. 3.29.: Application of modified Bolton, 1986 stress-dilatancy relationship for *NE34* sand as a function of the initial effective mean stress

- State parameter approach:
  As seen in Section 3.1.3, the state parameter, defined as the distance between the sand state and the critical state line in $e - \ln p'$ space, governs the monotonic sand behavior. The critical state line of *NE34* sand is identified as a part of this study (Equation 3.13) and used to determine the state parameter corresponding to the prototype sand. Knowing the initial mean effective stress of the scale model case, the relative density index of sand can be estimated to ensure the behavior similarity between the two cases.

These two methods will be applied to scale the two foundations proposed to support the "DTU 10 MW reference wind turbine" (Section 2.2.4). The relative density index of the sand layer is considered to be equal to 0.80, corresponding to a dense sand. The mean effective stress is calculated using the following equation:

$$p' = \frac{\sigma_1 + 2\sigma_3}{3} = \frac{(1 + 2K_0)\gamma z}{3} \qquad \text{with} \qquad K_0 = \frac{\nu}{1 - \nu} \tag{3.29}$$

where K_0 expresses the coefficient of lateral sand pressure at rest, γ is the unit weight, z is the depth (equal to 70% of pile embedded length; Abadie, 2015), and ν is the Poisson ratio of the sand taken equal to 0.3 (Section 6.2.3).

Tables 3.5 and 3.6 present the application of the two sand scaling methods to determine the relative density indices of sand to be used in the scale models, ensuring the similarity with the prototype dense sand of the foundations $F1$ and $F2$ respectively.

Both methods show the similarity between the dense sand at the prototype stress level and the medium-dense sand at the scale model stress level. However, the relative density indices obtained by the state parameter approach, conserving the same distance with the critical state line, are slightly higher than those obtained by the modified stress-dilatancy relation, especially using the *CSL* proposed in the present study. This issue can be related to the important uncertainties involved in the identification of the *CSL* (Section 3.2.4), which is clearly shown by the divergence between the *CSL* proposed by Aghakouchak et al., 2015 and the one from the present study. Besides, the values identified as the maximum void ratio for *NE34* sand varies widely between different studies: 0.87 adopted by Irina AndriaNtoanina, 2011; 0.88 adopted by Feia et al., 2016, kerner, 2017, and present study; 0.90 adopted by Aghakouchak et al., 2015; 0.94 adopted by Alvarado, 2000 and Benahmed, 2001. This uncertainty considerably affects the state parameter of sand at relatively low mean effective stress levels. In this study, the method adopted is the modified stress-dilatancy relation, and the dense sand of the prototype ($I_d = 0.80$) should be represented by a sand with a relative density index equal to 0.52.

Tab. 3.5.: Calculation of sand relative density index I_d to be considered in scale model - Case of Foundation $F1$

Scaling method	Prototype			Scale model		
	p'_0 (*kPa*)	$e_c - e$ (−)	I_d (−)	p'_0 (*kPa*)	$e_c - e$ (−)	I_d (−)
Modified stress-dilatancy relation (Equation 3.28)	134	–	0.80	2.0	–	0.52
State parameter (*CSL* of present study, Equation 3.21)	134	0.18	0.80	2.0	0.18	0.66
State parameter (*CSL* proposed by Aghakouchak et al., 2015)	134	0.15	0.80	2.0	0.15	0.56

Tab. 3.6.: Calculation of sand relative density index I_d to be considered in scale model - Case of Foundation $F2$

Scaling method	Prototype			Scale model		
	p'_0 (*kPa*)	$e_c - e$ (−)	I_d (−)	p'_0 (*kPa*)	$e_c - e$ (−)	I_d (−)
Modified stress-dilatancy relation (Equation 3.28)	112	–	0.80	1.7	–	0.52
State parameter (*CSL* of present study, Equation 3.21)	112	0.18	0.80	1.7	0.18	0.66
state parameter (*CSL* proposed by Aghakouchak et al., 2015)	112	0.16	0.80	1.7	0.16	0.56

3.3 Tilt method to estimate the friction angle at extremely low stress level

To tackle the difficulties underlying the performance of triaxial tests at relatively low-stress levels, Giampa and Bradshaw, 2018 proposed a tilt test to measure the peak friction angle of sands at extremely low-stress level, estimated at 0.01 *kPa*. As Section 3.2 studied the sand behavior at different stress levels, the described method permits extending this study to extremely low stress values. The method of specimen tilting, which was manually performed by Giampa and Bradshaw, 2018, was automatized to enhance the reliability of the obtained results. Specimens with different relative density indices were tested, and the agreement with triaxial findings was evaluated.

3.3.1 Tilting device and testing procedure

Figure 3.30 presents the developed tilting device used in this part of the study. The sand specimen was formed on a horizontal plate, able to rotate around a pin joint. The plate is connected to a rotational actuator by a wire and two pulleys, inducing a vertical motion at the plate extremity. The velocity of this actuator depends on the controlled voltage of the power supply. An inclinometer is hooked to the plate to measure the slope angle of the specimen. A camera was used to film the test and accurately determine values of the failure angle.

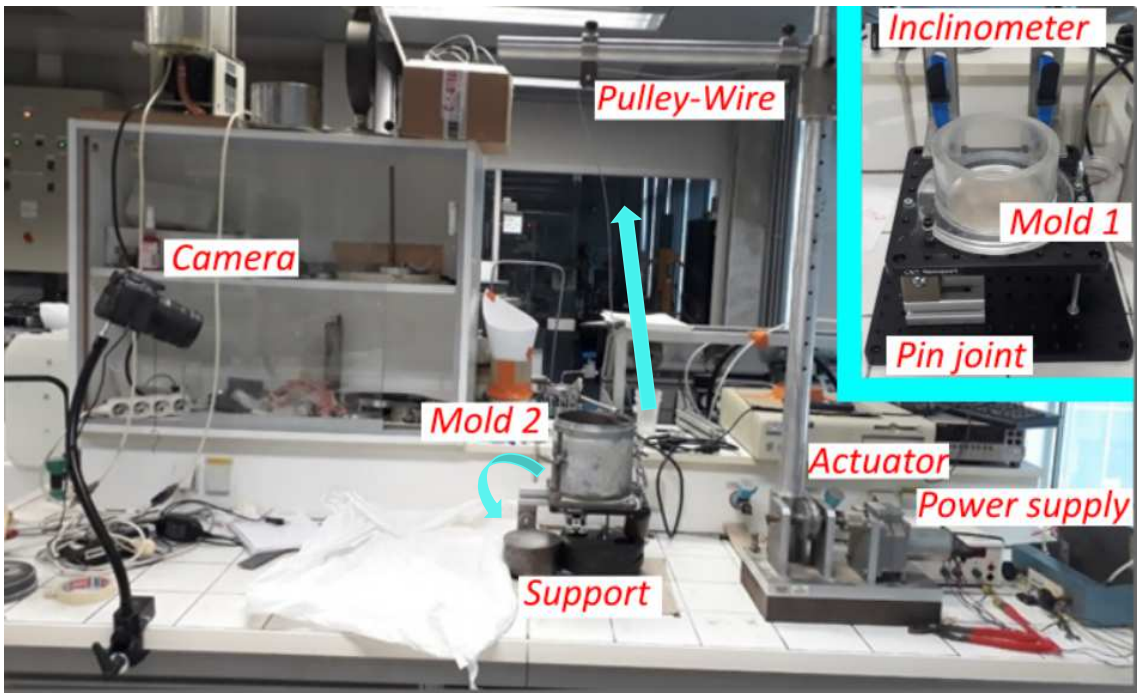

Fig. 3.30.: Tilting device used to estimate the peak friction angle at extremely low stress level

Three categories of specimens can be distinguished depending on the mold dimensions and the method of formation:

- Case 1: A plexiglas cylindrical mold with a diameter of 100 *mm* and height of 67 *mm* is filled by the pluviation method. The relative density index is controlled depending on the diameter and the number of sieve holes and the pluviation height. The calibration of the pluviator is carried out by Irina AndriaNtoanina, 2011 and verified before starting the current study. Once the mold was filled, excess sand was struck with a straight flat bar to make the specimen level with the top of the mold.

- Case 2: The previous mold is used, but the specimen is formed using the dry compaction method (used in section 3.2.2).

- Case 3: The same mold used by Giampa and Bradshaw, 2018, with diameter and height of 152.4 *mm* (Proctor mold) is considered. The specimen is formed by the dry compaction method.

3.3.2 Testing program

Similar to the testing program on monotonic triaxial shearing, the tests are mostly performed on medium dense to dense specimens. Table 3.7 presents the characteristics and details of the current testing program.

Tab. 3.7.: Testing program on tilting device

Test set	Mold	Specimen formation mold	Test identifier	Relative density index I_d
Set 1	Mold 1 (Plexiglas $\phi 100$)	Dry compaction	T-1	0.5
			T-2	0.7
			T-3	0.9
Set 2	Mold 1 (Plexiglas $\phi 100$)	Pluviation	T-4	0.72
			T-5	0.73
			T-6	0.80
			T-7	0.85
			T-8	0.91
Set 3	Mold 2 (Proctor)	Dry compaction	T-9	0.3
			T-10	0.5
			T-11	0.5
			T-12	0.7
			T-13	0.7
			T-14	0.9
			T-15	0.9

3.3.3 Results and discussions

The current testing program has been proposed as an extension of the monotonic triaxial testing program to investigate the sand behavior at extremely low-stress level. An automatic tilting device is developed using a Plexiglas $\phi 100$ *mm* mold. Firstly, the dry compaction

method is adopted to form the sand specimens (Set 1). The obtained results, as the peak friction angles of sand, seem to be independent of the relative density index (Figure 3.31). The pluviation method is then adopted using the same mold to verify the reliability of the specimen formation method (Set 2). The obtained results are in good agreement in terms of both values and trends (Figure 3.31), highlighting the same issue. The analysis of the recorded videos shows that the slope failure starts at the specimen borders (Figure 3.32), leading to question the effect of the specimen diameter and the mold material. Therefore, a third set of tests is conducted with the same mold used by Giampa and Bradshaw, 2018, ensuring a fair comparison. Due to the absence of a pluviator adapted for this diameter, and as the different specimen formation methods are in good agreement, the specimens were formed by the dry compaction method. It was shown that the increase of the diameter has no effect of the obtained results. Figure 3.31 shows the global results, assuming the peak friction angle of the loosest case is equivalent to the critical friction angle (Giampa and Bradshaw, 2018). Similar to the findings of Giampa and Bradshaw, 2018, it is concluded that the peak friction angle increases with the relative density index following a quadratic equation stabilizing at medium dense to dense sand cases ($I_d > 0.5 \sim 0.6$).

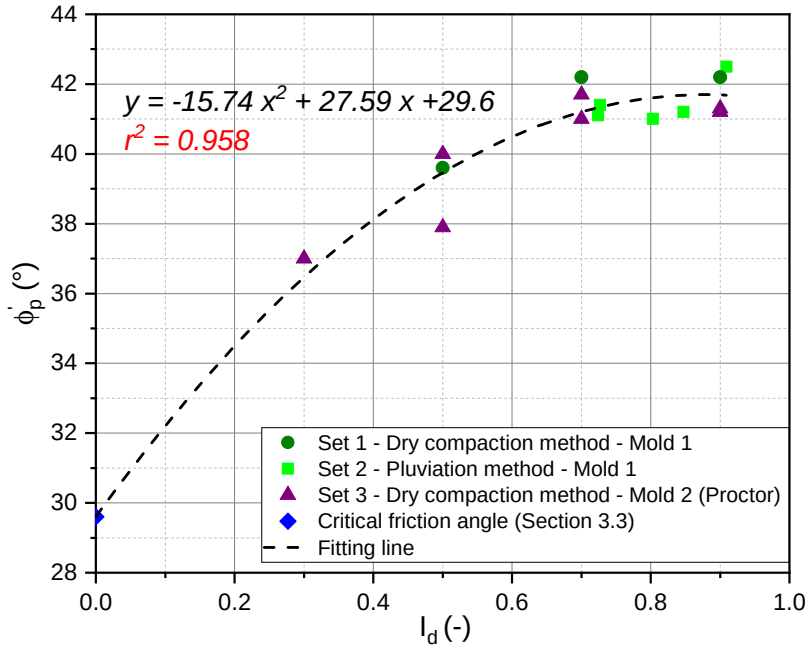

Fig. 3.31.: Peak friction angle versus relative density index, obtained by the tilt method for *NE34* sand.

The obtained curve plateau can be related to the failure localization at the borders of the specimens, as remarked by the video analysis. The active part of the tested specimen is a thin layer at the sand surface, and the failure can occur at any weak location of this layer before spreading out. The precise control of the relative density index at the whole specimen surface, especially at the borders, seems to be impossible. This hypothesis can justify the stabilization of the peak friction angles obtained in relatively dense cases, where it is impossible to ensure the required relative density index along the sand surface. The

validation of this proposal requires additional studies. A proposed methodology is to freeze the specimens by special solutions and use imaging techniques to study the homogeneity of the specimens formed by different methods.

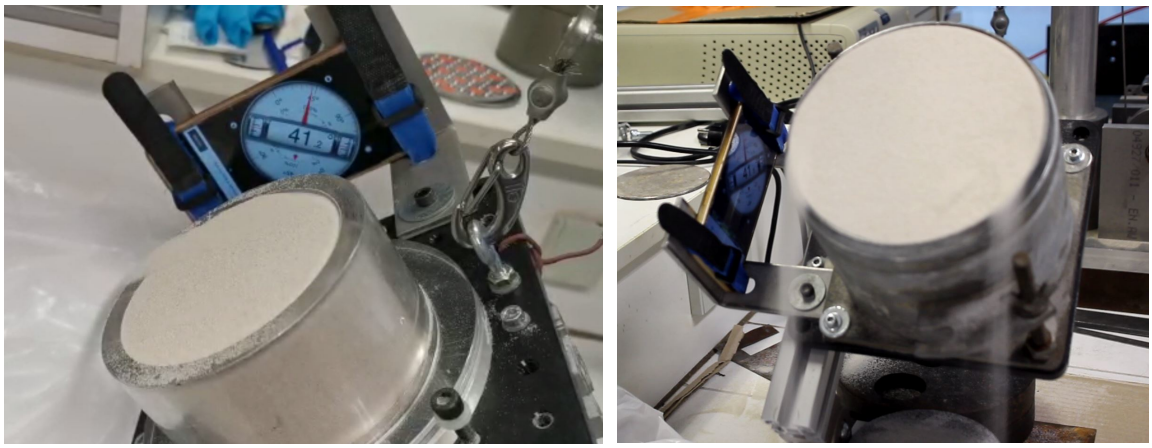

(a) (b)

Fig. 3.32.: Failure mode obtained by the tilt method: (a) Mold 1; (b) Mold 2

Giampa and Bradshaw, 2018 determined the modified stress-dilatancy relation based on the results obtained by the tilt method and the triaxial tests. Figure 3.33a shows a convergence between the two methods in cases of loose to medium dense sand while a divergence is observed in denser cases. It can be concluded that the use of tilt method results induces a decrease in the rate of peak friction angle increase at low-stress levels, leading to the agreement between the two methods in the range of the relative density index of the study. In the current study, the tilt method and the stress-dilatancy relation are studied independently. The increase rate of the peak friction angle at low-stress levels is more important than that obtained by Giampa and Bradshaw, 2018, leading to a global divergence of the two methods (Figure 3.33b). However, a similar trend of tilt method findings is found.

Due to serious difficulties underlying the validation of the tilt method and the unclear understanding of its findings, it is not reliable to extract quantitative contributions. However, it can be shown that the application of stress-dilatancy relation, extracted from the triaxial results only, at extremely low stresses seems to over-estimate the associated peak angle friction of sand. This remark is in agreement with the findings presented in Section 3.2.6, where the "state parameter" methodology leads to higher relative density indexes. A hypothesis to justify this divergence is that the stress-dilatancy relation over-estimates the peak friction angle at low-stress levels.

Nevertheless, the stress-dilatancy relation (triaxial results) is adopted in the current study due to the relatively significant doubts underlying the tilting device findings and the limited available tests used to determine the critical state line. However, the possibility of an over-estimation in some cases will be considered in the analysis of the results. Finally,

additional research efforts are required to reveal and understand the parameters governing the sand behavior at extremely low-stress levels.

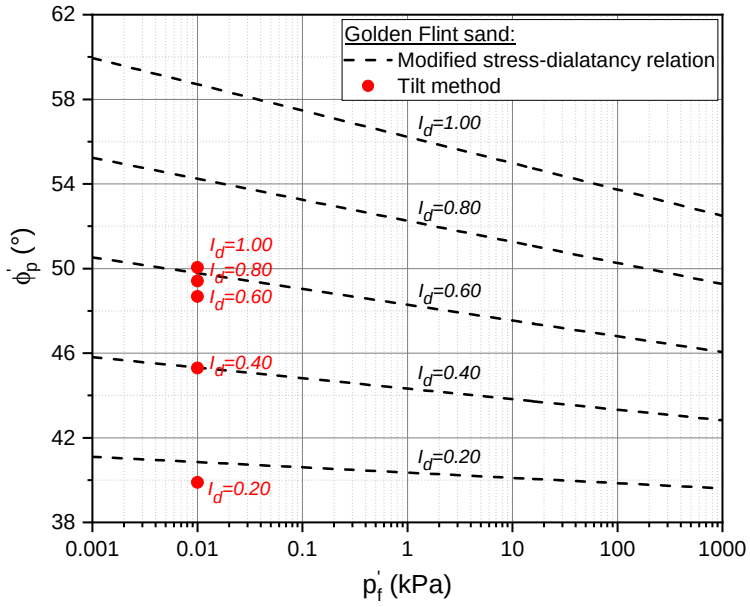

(a)

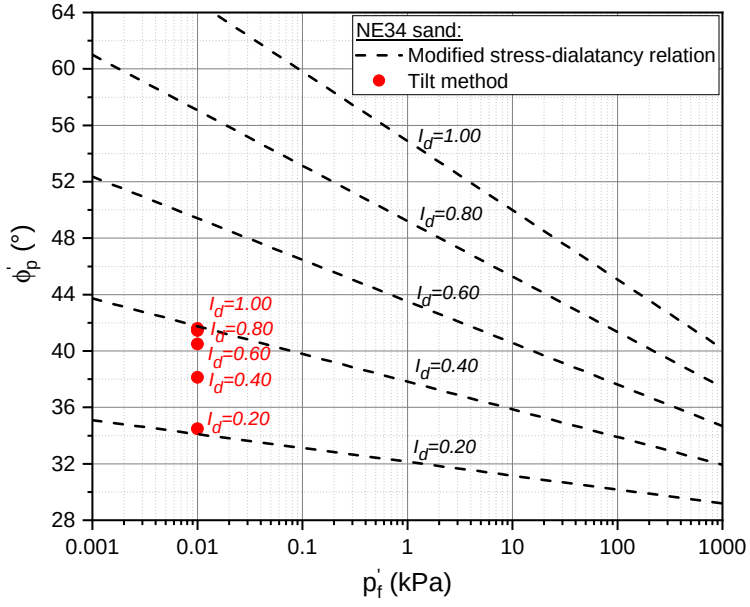

(b)

Fig. 3.33.: Agreement evaluation between the modified stress-dilatancy relationship and the tilt method: (a) *Golden Flint* sand following Giampa and Bradshaw, 2018; (b) *NE34* sand - Present study

3.4 Conclusion of the chapter

This chapter illustrates the findings of an experimental campaign conducted to determine the parameters governing the *NE34* sand parameters at different stress levels. The obtained parameters are discussed according to similar findings available in the literature, showing a good agreement.

These parameters are required as part of the 1g scaling methodology presented in Chapter 2, which aims to identify the sand state ensuring the similarity of soil behavior between the scale model and the prototype. As general conclusion, the dense sand at the prototype scale should be simulated by a medium dense sand at the 1g model scale.

4 Capability and validity of proposed models

Recently, several physical models have been developed to understand the cyclic response of offshore wind turbine monopile, aiming to propose a conservative design method. Due to the problem complexity (soil-structure interaction, dynamic aspect, soil liquefaction, scouring...) and despite the progress achieved in this field, conflicting findings are still encountered, and many knowledge gaps still require answers. In the framework of this thesis, two 1g scale models are developed based on a new set of scaling laws, ensuring an accurate similarity of governing physical quantities with the prototype (Chapters 2 and 3). The developed models are mainly characterized by the consideration of dynamic similarity of the first mode of vibration. The aim is to obtain representative scale models, leading to significant results able to resolve the conflicting points and fulfill the knowledge gaps.

This chapter starts with a literature review of similar physical models and their findings. The conflicting points and the knowledge gaps are deducted, and the capability of the developed models is discussed. As the developed scale models are conducted at 1g gravity, the low-stress level constitute a serious challenge for results reliability. Cautious testing procedures are presented and the reliability of obtained results is validated. Then, available analytical methods and developed numerical model (*3D FEM Cesar-LCPC* model) estimating the system natural frequency are evaluated by comparing with experimental findings. This numerical model is used to verify the dynamic similarity between the current scale models and the prototype.

4.1 Literature review: physical models simulating offshore wind turbine foundation behavior

Numerous 1g and centrifuge scale models are developed to study the cyclic response of offshore wind turbine monopile. The proposed models and test conditions varied depending on adopted scaling laws, problem approach, and aims of the study. A synthesis of recent similar works is carried out, presenting scale models and tests conditions, and the corresponding findings. Summaries of similar 1g scale models and centrifuge scale models are presented in Tables 4.1 and 4.2 respectively.

Tab. 4.1.: Summary of similar 1g scale models simulating OWT foundation behavior

Work	Pile properties					Sand properties					Loading characteristics				Findings
	Material	D	t	L	L/D	Sand	State	I_d	D_{50}	e	Type	f_{exc}	N	FC	
	–	*mm*	*mm*	*mm*	–	–	–	–	*mm*	*mm*	–	*Hz*	*cycles*	–	
Peralta and Achmus,2010 Hanover University Germany	HDPE Steel	63 60	1.8 3	200 300 400 500	3.3 5 6.6 8.3	Quartz	Dry	0.40 0.60	0.21	240	1-way	0.14	10^4	$0.1L$	Exponential law to predict the permanent displacement for rigid monopiles; Logarithmic law to predict the permanent displacement for flexible piles; Accumulation rate is independent of loading amplitude; Pile-soil system does not strictly follow Miner's rule; Sand density index affects strain accumulation.
LeBlanc et al., 2010 Oxford University UK	Copper	80	2	360	4.5	YLB	Dry	0.04 0.38	0.8	430	1-way 2-ways	0.1	65370	4°	Exponential law to predict the displacement accumulation; Proposed law depends on cyclic loading type, loading amplitude, and density index; Logarithmic law to predict the increase of pile-soil system rigidity; The increase of system rigidity is independent of loading characteristics and initial density index.
Peng et al., 2011 Newcastle University UK	Steel	44.5	2.15	400	9	–	Dry	0.72	–	30	1-way 2-ways	0.94 0.65 0.94	10^4	$0.1D$	Lateral displacement increases with loading frequency increase; Accumulated lateral displacement increases with loading amplitude increase; Unbalanced loading is more detrimental than balanced loading.
Cuéllar, 2011 Berlin University Germany	PVC	75	5	300	4	Berliner	Dry	0.89	0.21	115	1-way 2-ways	1	$5 * 10^4$	$0.1D$	Investigation of densification-dominated phase followed by convection-dominated phase occurring around the pile; Proposition of empirical relations to predict the permanent displacement: logarithmic law, linear law then power-law, depending on cycles number; Bending moment decreases during cyclic loading, showing an increase of the system rigidity.

D: Pile diameter t: Pile thickness L: Pile embedded length I_d: Relative density index D_{50}: Mean grain size e: Loading eccentricity f_{exc}: Loading frequency
N: Number of cycles FC: Failure criteria

Continue on next page

Tab. 4.1.: Summary of similar 1g scale models simulating OWT foundation behavior (cont.)

Work	Pile properties					Sand properties					Loading characteristics				Findings
	Material	D	t	L	L/D	Sand	State	I_d	D_{50}	e	Type	f_{exc}	N	FC	
	–	*mm*	*mm*	*mm*	–	–	–	–	*mm*	*mm*	–	*Hz*	*cycles*	–	
Yu et al., 2015 Zhejiang University China	Steel	43	2	450	10.5	RH 110	Dry	0.63	0.144	1000	1-way 2-ways	$f_{exc}/f_n = 1.30\ 0.85$	196515	–	System natural frequency increases till reaching a specific number of cycles before decreasing; Higher loading amplitude leads to a higher increase in the system's natural frequency; Two-directional loading accelerates the reaching of the system's natural frequency peak.
Chen et al., 2015 Zhejiang University China	Steel	165	3	915	5.5	Qiantang river Silt	Sat	0.70 0.88	0.0328	990	1-way	0.067	10015	$0.1D$	Logarithmic law to predict displacement accumulation and unloading stiffness evolution; Loading amplitude affects the displacement accumulation; Density index affects the evolution of unloading stiffness; Slight degradation of the soil pressure during first 10 cycles before stabilization; Great influence of the first 10 cycles on cyclic response.
Abadie, 2015 Oxford University UK	Copper	77	2	360	4.5	YLB	Dry	0.02	0.8	430	1-way	0.1	10^5	$0.1D$	Adopts the empirical relation form proposed by LeBlanc et al., 2010 to predict the displacement accumulation with cycles number; Starting by high amplitude loading reduces the strain induced by smaller loading (Multi-amplitude); The variation of hysteresis loop shape and secant stiffness dominates in the first 50 cycles.
Arshad and O'kelly, 2016 Trenty College Dublin Ireland	Brass	53	0.8	360	6.8	–	Dry	[0.70; 0.74]	0.27	90	1-way 2-ways	0.25	6000	1.5°	Logarithmic law captures the rotation accumulation more precisely than power law; Rotation accumulation depends on the type of cyclic loading and loading amplitude; Secant stiffness increases with cycles number.

D: Pile diameter t: Pile thickness L: Pile embedded length I_d: Relative density index D_{50}: Mean grain size e: Loading eccentricity f_{exc}: Loading frequency
N: Number of cycles FC: Failure criteria

Continue on next page

Tab. 4.1.: Summary of similar 1g scale models simulating OWT foundation behavior (cont.)

Work	Pile properties					Sand properties					Loading characteristics				Findings
	Material	D	t	L	L/D	Sand	State	I_d	D_{50}	e	Type	f_{exc}	N	FC	
	–	*mm*	*mm*	*mm*	–	–	–	–	*mm*	*mm*	–	*Hz*	*cycles*	–	
Nicolai et al., 2017 Aalborg University Denmark	Aluminum	100	5	500	5	Aalborg	Dry	0.81 0.90	0.14	600	1-way 2-ways	0.1	50810	4° or curve plateau	Adopts the empirical relation form proposed by LeBlanc et al., 2010 to predict the displacement accumulation with cycles number; Empirical relation to estimate the increase in the post cyclic ultimate moment; The post cyclic ultimate moment depends on cyclic loading type, loading amplitude, and cycles number.
Albiker et al., 2017 Hanover University Germany	HDPE Steel	63 60	1.8 3	350	5.83	Quartz	Dry	0.44 0.64	0.18	240	1-way 2-ways	0.14	2500	20 *mm* $\sim 3°$	Adopts the empirical relation form proposed by LeBlanc et al., 2010 to predict the displacement accumulation with cycles number; Investigation of eccentricity effect on displacement accumulation; Maximal accumulation rate occurred under asymmetric lateral loading for rigid monopiles, under 1-way loading for flexible monopiles.
Liu et al., 2019a Qingdao University China	Aluminum	140	10	740	5.3	–	Dry	–	~ 0.7	240	1-way 2-ways	4	1000	$0.1D$	Accumulation of displacement and decrease of lateral secant stiffness occur mainly on the first 100 cycles; Decrease in the post-cyclic pile-soil system capacity.

D: Pile diameter t: Pile thickness L: Pile embedded length I_d: Relative density index D_{50}: Mean grain size e: Loading eccentricity f_{exc}: Loading frequency
N: Number of cycles FC: Failure criteria

Continue on next page

Tab. 4.1.: Summary of similar 1g scale models simulating OWT foundation behavior (cont.)

Work	Pile properties					Sand properties					Loading characteristics				Findings
	Material	D	t	L	L/D	Sand	State	I_d	D_{50}	e	Type	f_{exc}	N	FC	
	–	*mm*	*mm*	*mm*	–	–	–	–	*mm*	*mm*	–	*Hz*	*cycles*	–	
Richards, 2019 Oxford University UK	Aluminum	80	5	320	4	YLB	Dry	0.01 0.60	0.81	800	1-way 2-ways	0.1	10^4	2°	Qualitatively similar responses are shown at different density indices; Multi-directional loading: the ratcheting occurs in the direction of loading bias and is largely unaffected by loading direction; Multi-directional loading increases displacement accumulation; Increase in the post-cyclic capacity of the pile-soil system; Realistic multi-amplitude multi-directional loading is consistent with observations from constant amplitude tests; Maximum rotation during a short storm in dry sand can be estimated by the monotonic response.
Liang et al., 2020 Tianjin University China	Stainless Steel	50	2	300	6	Fujian	Sat	0.76	0.17	200 900	1-way 2-ways	Speed of excitation 2 *mm/s*	56831	2°	Proposition of power law to predict the displacement accumulation, depending on cyclic loading type, loading amplitude, and cycles number; Previous small-amplitude loading history accelerates the process of stiffness degradation under a large amplitude loading; Most of the tilt, nearly 90%, was observed within few cycles; Increase in the system's natural frequency depending on loading amplitude; Peak followed by a decrease in the system's natural frequency occurred on 2-way high-amplitude loading; Slight increase in post-cyclic capacity of the pile-soil system.

D: Pile diameter t: Pile thickness L: Pile embedded length I_d: Relative density index D_{50}: Mean grain size e: Loading eccentricity f_{exc}: Loading frequency
N: Number of cycles FC: Failure criteria

Continue on next page

Tab. 4.1.: Summary of similar 1g scale models simulating OWT foundation behavior (cont.)

Work	Pile properties					Sand properties					Loading characteristics				Findings
	Material	D	t	L	L/D	Sand	State	I_d	D_{50}	e	Type	f_{exc}	N	FC	
	–	*mm*	*mm*	*mm*	–	–	–	–	*mm*	*mm*	–	*Hz*	*cycles*	–	
Frick and Achmus,2020 Hanover University Germany	Aluminum	50	3.2	300 400	6 8	F34 Silica	Dry	0.40	0.18	240 320 400 300 360	1-way 2-ways	0.1	10^4	Manoliu criteria Sec.7.1	Adopts the empirical relation form proposed by LeBlanc et al., 2010 to predict the displacement accumulation; Displacement accumulation is independent of loading amplitude and eccentricity; The coefficient α (Sect. 4.2) seems to be affected by both pile slenderness L/D and sand density index; PIV observations of strain patterns indicate that reason for higher accumulation rates under asymmetric two-way loading is that minimum soil compaction occurs.
Zhang et al., 2020 Chang'an University China	Aluminum	30	2.5	300	10	Shanghai	Dry	0.28 0.60 0.85	0.37	100	1-way 2-ways	0.1	10^4	Solcyp criteria	Proposition of two explicit models to predict the displacement accumulation and the unloading stiffness evolution, depending on cyclic loading type, loading amplitude, and cycles number; Accumulation and evolution rates increase rapidly in the former cycles and gradually stabilize in the subsequent cycles; Asymmetric two-way cyclic loading causes a peak of the accumulated residual displacement.
Rathod et al., 2021 National Institute of Technology India	Aluminum	63.5	2.5	355 533	5.6 8.4	River	Dry	0.55	–	381	2-ways	0.25	1000	1.5°	Proposition of two logarithmic laws to predict the displacement accumulation and the cyclic secant stiffness evolution, depending on cyclic loading type, loading amplitude, monopile rigidity factor, and cycles number; In contrast with all previous works, negative accumulation was encountered, favored by low loading amplitude, relatively flexible behavior, and more symmetrical loading; Evolution rate of cyclic secant stiffness depends only on the monopile rigidity factor.

D: Pile diameter t: Pile thickness L: Pile embedded length I_d: Relative density index D_{50}: Mean grain size e: Loading eccentricity f_{exc}: Loading frequency
N: Number of cycles FC: Failure criteria

Tab. 4.2.: Summary of centrifuge scale models simulating OWT foundation behavior

Work	Pile properties						Sand properties					Loading characteristics					Findings
	Material	D	t	L	L/D	Inst	Sand	State	I_d	D_{50}	n-g	e	Type	f_{exc}	N	FC	
	–	*mm*	*mm*	*mm*	–	–	–	–	–	*mm*	–	*mm*	–	*Hz*	*cycles*	–	
Li et al., 2010 Cambridge University UK	Stainless Steel	50	4	250	5	Jacked at 1g	Wunder	Sat	0.97	0.52	100	~ 700	1-way	0.02 0.7	1000	–	No evident pile head settlement occurred; Proposition of logarithmic law to predict the permanent and maximum lateral displacement, depending on loading amplitude; Secant cyclic stiffness increases, especially during the first cycles.
Klinkvort and Hededal, 2013 Technical University of Denmark	Steel	28* (2) 40* (2)	–	168 240	6	Jacked at 1g	NE34	Dry	0.79 0.96	0.18	71.4 46.6	420 600	1-way 2-ways	0.1	10^4	4°	Displacement accumulation and secant stiffness increase depend on loading amplitude, cyclic loading type, and cycles number; Power law to predict the displacement accumulation and logarithmic law to predict the secant stiffness increase.
Kirkwood and Haigh, 2013, 2014 Cambridge University UK	Aluminum	45	1.5	200	4.4	Driven at 1g	Hostun	Dry	0.62	0.48	100	300	1-way 2-ways	–	3000	–	Two-way asymmetrical loading is the most detrimental case; Secant stiffness evolution is related to the blocked moment in the soil surrounding the pile.
Nicolai et al., 2017 Aalborg University Denmark	Aluminum	25	3	125	5	Jacked at 1g	Silica	Dry	0.826	0.19	100	150	1-way 2-ways	0.5	1000	4°	Empirical relation to predict the increase in post cycling ultimate moment; The post cyclic ultimate moment depends on cyclic loading type, loading amplitude, and cycles number.

D: Pile diameter t: Pile thickness L: Pile embedded length Inst: Pile installation method I_d: Relative density index D_{50}: Mean grain size n-g: Gravity acceleration e: Loading eccentricity f_{exc}: Loading frequency N: Number of cycles FC: Failure criteria *: Total pile diameter; (): Thickness of epoxy coating

Continue on next page

Tab. 4.2.: Summary of centrifuge scale models simulating OWT foundation behavior (cont.)

Work	Pile properties						Sand properties					Loading characteristics					Findings
	Material	D	t	L	L/D	Inst	Sand	State	I_d	D_{50}	n-g	e	Type	f_{exc}	N	FC	
	–	*mm*	*mm*	*mm*	–	–	–	–	–	*mm*	–	*mm*	–	*Hz*	*cycles*	–	
Truong et al., 2018 Western University Australia Technical University of Denmark	Alumi-num	11* (0.5)	1	125	11.4	Jacked at 1g	UAW Silica	Sat	0.68	0.18	250	22	1-way	0.015 *mm/s*	50	4°	Proposition of power law to predict the displacement accumulation, depending on cyclic loading type, density index, and cycles number; Residual moment is developed, reaching 50% of peak moment. It is prominent at lower density indices, one-way loading, and higher loading amplitude; Post-cyclic capacity is considered unaffected within the serviceability limit (0.5° of permanent rotation).
	Steel	40* (1)	1.5	240	6		NE34	Dry	[0.50; 0.99]		60	120	1-way 2-ways	0.1	1500		
Bayton et al., 2018 Sheffield University UK	Alumi-num	50	2.8	250	5	Placed before pluvia-tion	HST95	Dry	∼ 0.8	0.20	100	250	1-way	–	145550	–	Displacement accumulation and increase in secant stiffness; SLS is not reached by loading amplitude smaller than 40% of failure capacity; Contour lines plotted to predict rotation accumulation, depending on cyclic loading type, loading amplitude, and cycles number; Model extended and applied for a load ramp test (with good performance).
Li et al., 2020 Delf University of Technology Netherlands	Alumi-num	18	1	90	5	Jacked at 1g	Geba	Dry	0.50 0.80	0.11	100	144	1-way 2-ways	–	153	0.075 D	Reformulation of power laws proposed by Klinkvort and Hededal, 2013 to predict the displacement accumulation and the increase in initial and secant stiffnesses; Displacement accumulation is independent of loading amplitude, whereas the increase in stiffness is independent of density index; Proposed model is compared to field measurement and shows a very good agreement.

D: Pile diameter t: Pile thickness L: Pile embedded length Inst: Pile installation method I_d: Relative density index D_{50}: Mean grain size n-g: Gravity acceleration e: Loading eccentricity f_{exc}: Loading frequency N: Number of cycles FC: Failure criteria *: Total pile diameter; (): Thickness of epoxy coating

4.2 Knowledge gaps and present model capability

The literature review presented in the previous section shows that the different physical models concur in some points, constituting the top-lines of the cyclic response of offshore wind turbine monopile. These points can be briefly presented as follows:

- Lateral displacement accumulation depends on loading characteristics and sand relative density index.
- Asymmetric two-way loading is found to be the most detrimental case in terms of displacement accumulation.
- Increase in the foundation-soil rigidity, due to the densification of the soil mass around the monopile, is observed.
- The majority of works show an increase in the post-cyclic ultimate capacity of the monopile.
- Variation of the system natural frequency related to the granular micro-mechanisms within the soil mass around the monopile: an increase of the natural frequency due to the densification-dominated phase followed by a decrease due to the convection-dominated phase.

After revealing the key-mechanisms governing the cyclic response of rigid monopile, numerous works attempt to propose empirical relations to predict the displacement accumulation and the system rigidity evolution with cycles number. These relations are proposed as reasonable and simple design procedure due to the difficulties underlying the conventional design methodologies (Finite element simulations, "p-y" models,...). Relevant relations are proposed by LeBlanc et al., 2010 and Klinkvort and Hededal, 2013, focusing on the effect of loading characteristics (ζ_b and ζ_c; Section 2.1.1). The two proposed empirical relations are presented below:

- LeBlanc et al., 2010 relation based on 1g model:

$$\frac{\Delta\theta(N)}{\theta(s)} = T_b(\zeta_b, I_d)T_c(\zeta_c)N^{\alpha} \qquad \text{with} \qquad \alpha = 0.31 \tag{4.1}$$

  where $\Delta\theta(N)$ is the difference between pile rotation at the first cycle and at the cycle number N, $\theta(s)$ is the static pile rotation, T_b and T_c are functions introducing the effect of the loading characteristics and the relative density index.

$$\tilde{k}_N = \tilde{k}_0 + A_k \ln(N) \qquad \text{with} \qquad A_k = 8.02 \qquad \text{and} \qquad \tilde{k}_0 = K_b(\zeta_b)K_c(\zeta_c) \tag{4.2}$$

where $\tilde{k}_0$ is the pile stiffness at the first cycle, $\tilde{k}_N$ is the pile stiffness at the cycle number N, K_b and K_c are functions introducing the effect of the loading characteristics.

- Klinkvort and Hededal, 2013 relation based on centrifuge model:

$$\tilde{Y}_{max,N} = \tilde{Y}_{max,1} N^{\alpha} \qquad \text{with} \qquad \alpha = T_c(\zeta_c)T_b(\zeta_b) \tag{4.3}$$

where $\tilde{Y}_{max,1}$ is the maximum displacement for the first cycle, $\tilde{Y}_{max,N}$ is the maximum displacement for cycle number N.

$$\tilde{K}_N = \tilde{K}_1[1 + \kappa \ln(N)] \qquad \text{with} \qquad \kappa(\zeta_c, \zeta_b) = \kappa_c(\zeta_c)\kappa_b(\zeta_b) \tag{4.4}$$

where $\tilde{K}_1$ is the cyclic secant stiffness at the first cycle, $\tilde{K}_N$ is the cyclic secant stiffness at the cycle number N.

The relations proposed to predict the stiffness evolution are in contrast: LeBlanc et al., 2010 found that the evolution of stiffness is independent of loading characteristics and initial relative density index (A_k defined as a constant) while Klinkvort and Hededal, 2013 found that the rate of stiffness evolution depends on loading characteristics (effect of relative density index was not studied). Later, this methodology was widely adopted, and numerous empirical relations were generated based on those relations. Due to the problem complexity, variation in adopted scaling laws, and the high number of parameters affecting the cyclic response, the obtained empirical relations diverged, and conflicting findings are found:

- In contrast with LeBlanc et al., 2010, Chen et al., 2015 show the effect of sand relative density index on the constant governing the rate of the foundation stiffness evolution.

- Albiker et al., 2017 investigate the effect of loading eccentricity on the rate of displacement accumulation without achieving a clear conclusion.

- In contrast with several works (LeBlanc et al., 2010;Klinkvort and Hededal, 2013;Liang et al., 2020), Truong et al., 2018, based on a large set of centrifuge tests, show that the displacement accumulation rate is independent of loading amplitude (ζ_b) and depends mainly on cyclic loading type (ζ_c) and sand relative density index. Similarly, Zhang et al., 2020, based on a 1g scale model, found that the loading amplitude (ζ_b) did not affect the displacement accumulation rate.

- Frick and Achmus, 2020 and Rathod et al., 2021 show the effect of pile rigidity factor on the rate of displacement accumulation, and Rathod et al., 2021 show its effect on the foundation stiffness evolution.

In addition, the variation of system natural frequency was rarely investigated despite its consideration as principal design criterion. The valid judgment of all these points required a large parametric study on a high-confidence scale model, allowing the variation of studied parameters and the monitoring of results necessary for the analysis.

On another side, the extracted empirical relations should be used to predict the displacement accumulation and foundation stiffness evolution after a defined number of cycles, as design methodology of the prototype. Therefore, since these relations provide quantitative inspirations, the corresponding scale models should be cautiously developed to provide representative results of the principal physical quantities governing the behavior.

The scale models developed in this study are characterized by the following points: (i) two monopiles with different rigidity behavior (perfectly rigid and semi-rigid behavior), (ii) accurate simulation of the dynamic aspect in addition to all physical quantities governing the global behavior, (iii) the ability to vary the sand relative density index and loading characteristics, and (iv) various and high-accuracy monitoring system (presented in Section 4.4.3). Therefore, the current scale models are capable of contributing to fulfill the knowledge gaps in this domain.

4.3 Experimental challenges and adopted solutions

After defining the scaling laws and applying them to obtain representative scale models, the tubes and rods used to represent the wind offshore structure and foundation are manufactured by a specialized company to ensure good workability. However, the testing procedure involved some serious challenges. Particular efforts are dedicated to finding appropriate solutions to conserve the reliability of targeted results. This section presents the different challenges encountered and the corresponding solutions adopted.

4.3.1 Guidance and driving system

As the current physical model is tested under normal gravity, the soil mass is characterized by relatively low-stress levels. The sand behavior at this level of stress is carefully considered, as seen in Chapters 2 and 3. However, the impact of the variability of testing preparation and monopile installation can affect the reliability of obtained results. The solution adopted is the development of a guidance and driving system, ensuring the repeatability of installation and the verticality of the installed model. This system permits the installation of the totality of

the scale model, where the monopile, structure, and mass are assembled before installation. The aim is to minimize the impact of testing preparation, leading to enhance the testing repeatability.

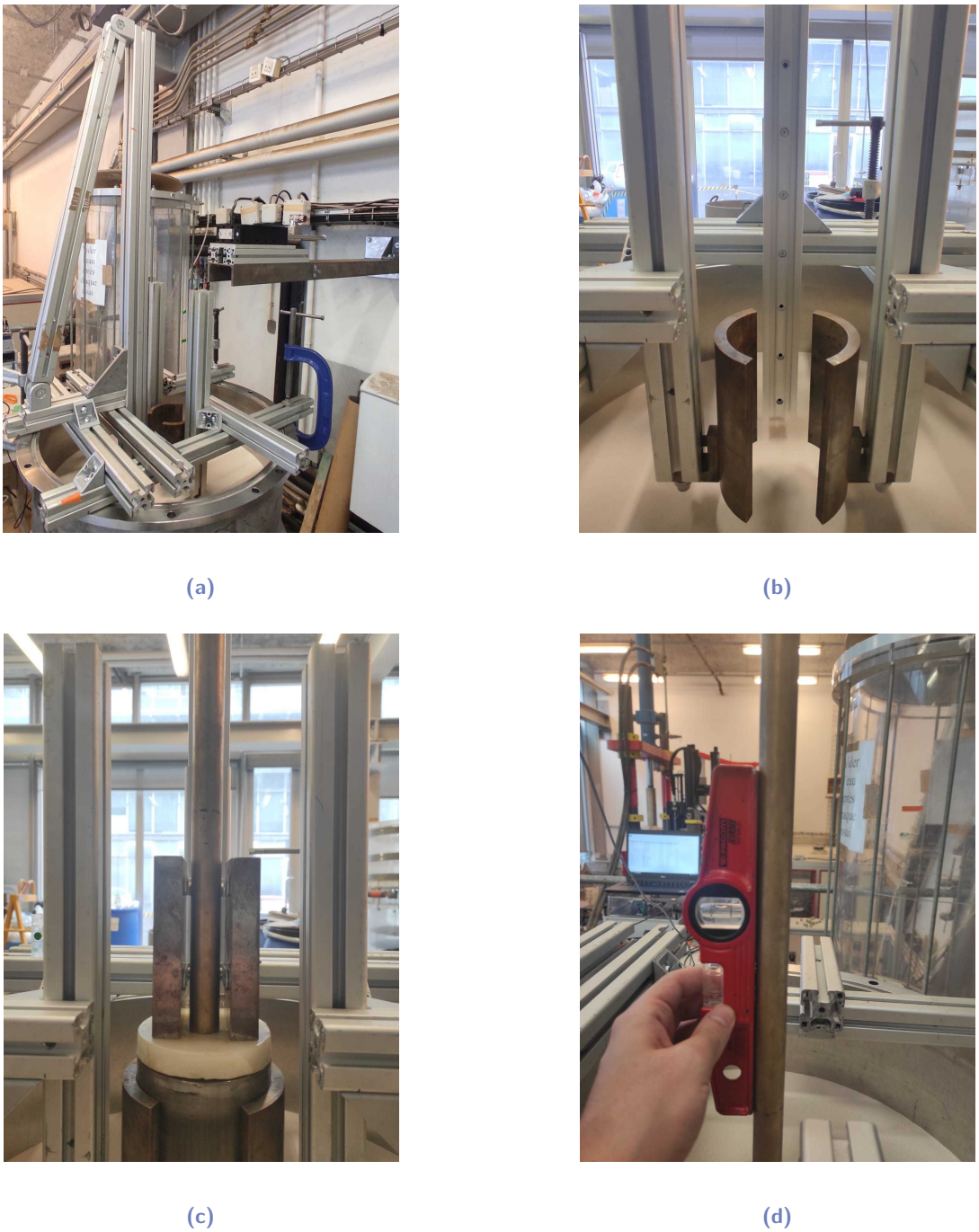

(a) (b)

(c) (d)

Fig. 4.1.: Guidance and driving system used to install the scaled monopile: (a) system frame (b) rail for the mass guidance and mold for the monopile guidance (c) placement of the driving mass and the scale model (d) check of the verticality after the installation

Figure 4.1 presents some pictures of the guidance and driving system. The system is constituted of the following parts:

- Two sets of divided steel cylinders with an inner diameter of 75 and 100 *mm*, equal to the outer diameter of scale models monopiles, that can be substituted depending on the installed model (figure 4.1b). These pieces are fixed vertically to ensure the vertical guidance of the monopile during installation in the soil mass.

- A mass of 2.7 *kg* sliding on a vertical rail and centered around the brass rod (Figure 4.1c). The mass is dropped from a constant height of 50 *cm* from the monopile head, pushing it into the soil.

The divided cylinders and the mass are designed to be easily removed after the installation, while the frame will be adapted to perform another task during testing. For the same relative density index of the sand ($I_d = 0.53$) and the same scale model *M2*, three tests have been performed, and 26 *blows* were required for each installation, showing excellent repeatability and performance of the current system.

4.3.2 Damping device

The main sources constituting the damping of the first bending mode of the offshore wind turbines are reviewed by Arany et al., 2016, based on the available data and studies. The damping ratio contributions are the following:

- Structural damping between 0.15 and 1.5%. This value depends on the material damping and the connections in the structure.

- Soil damping between 0.44 and 1%. This value depends on the type of the soil and the strain level.

- Hydrodynamic damping between 0.07 and 0.23%, resulting from wave radiation damping.

- Aerodynamic damping between 1 and 6% in the fore–aft direction for an operational turbine. For a parking turbine or in the crosswind direction, the value ranges between 0.06 and 0.23%.

Therefore, the damping ratio of the first mode of vibration ranges typically between 1.6 and 8% for an operational wind turbine in the fore–aft direction.

The aerodynamic damping has a dominant contribution to the total damping, while its

reproducing in the laboratory is an difficult task. The solution proposed is to use eddy currents to create an equivalent modal damping ratio by hooking a magnet to the top mass and approaching a copper plate with a controlled distance between them, using a micrometer screw. Figure 4.2 shows the application of this idea on the scale model. The frame used in the monopile installation is re-adapted to fix the copper plate. The distance between the plate and the magnet ensures the control of the system damping.

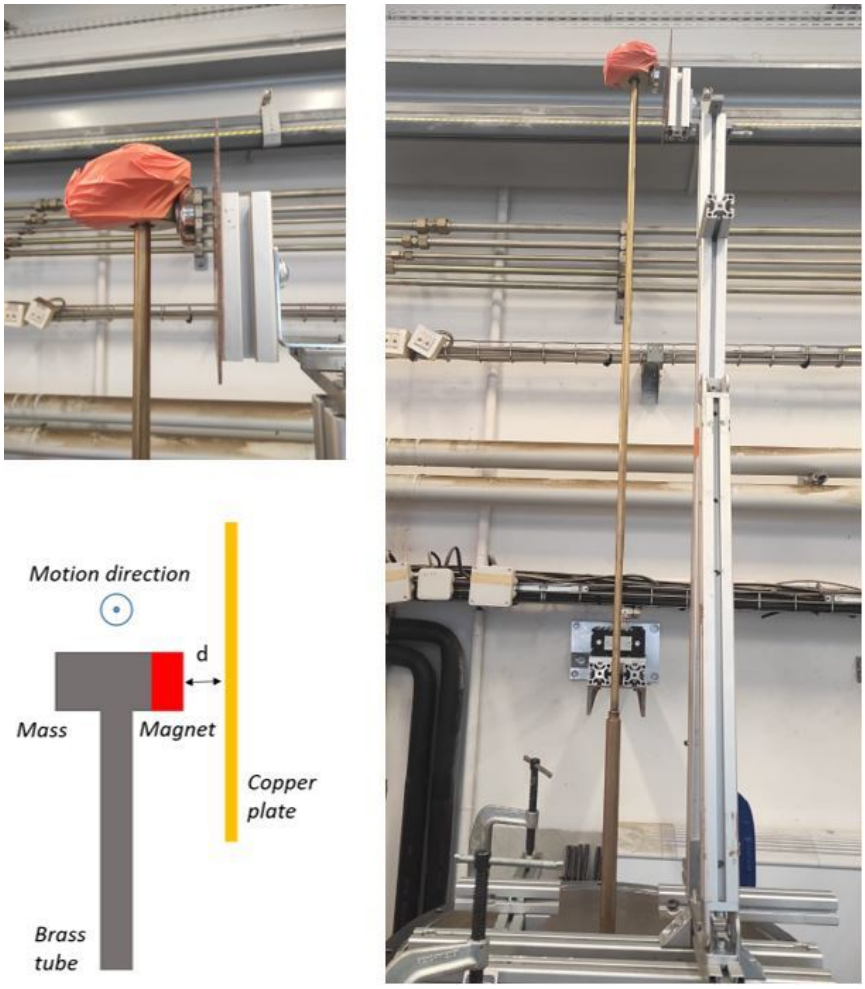

Fig. 4.2.: Additional device to control the damping of the scale model.

The system damping is calibrated in relation to the distance d between the magnet and the copper plate. The distance d is varied from 3 to 20 *mm*, and the corresponding modal damping ratio of the system is determined by analyzing the free vibration response of the system excited by a punctual shock. The experimental procedure is presented in Section 4.4.2. Figure 4.3 shows the typical accelerometer response placed at ~ 30 *cm* below the mass, and the corresponding Fourier transform for $d = 15$ *mm*. A cubic spline interpolation is performed to enhance the resolution of the Fourier transform. Some tests are repeated twice to validate the results reliability.

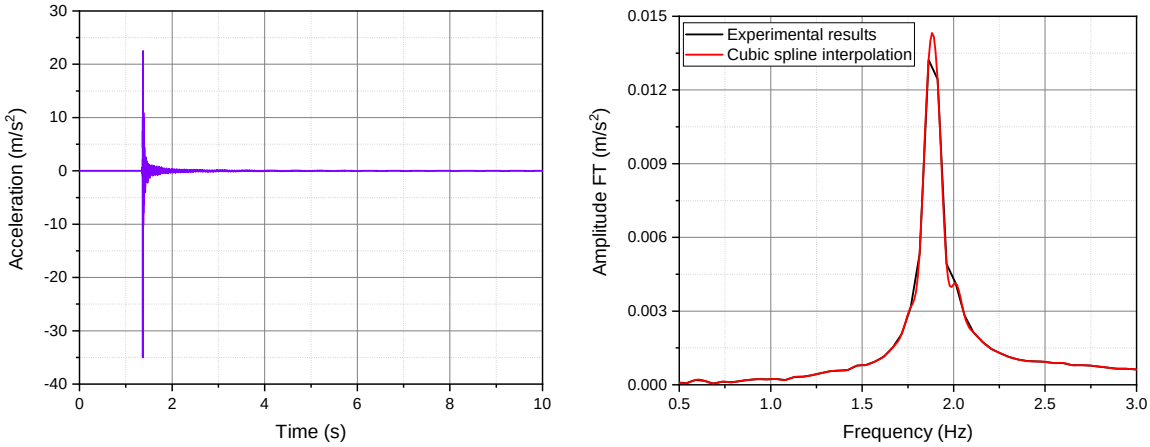

Fig. 4.3.: (a) Typical accelerometer response after a shock test and (b) corresponding Fourier transform for $d = 15$ *mm*

The Fourier transform (Figure 4.3b) of the accelerometer signal permits to identify the natural frequency of the system (f_n) as the frequency corresponding to the maximum amplitude of the peak. The system damping ratio can be estimated by the application of the half-power bandwidth method:

$$\xi(\%) = \frac{|B - A|}{2f_n} * 100 \tag{4.5}$$

where A and B are the frequencies corresponding to the amplitudes equal to $1/\sqrt{2}$ of the maximum amplitude at the peak. The obtained values are presented in Figure 4.4.

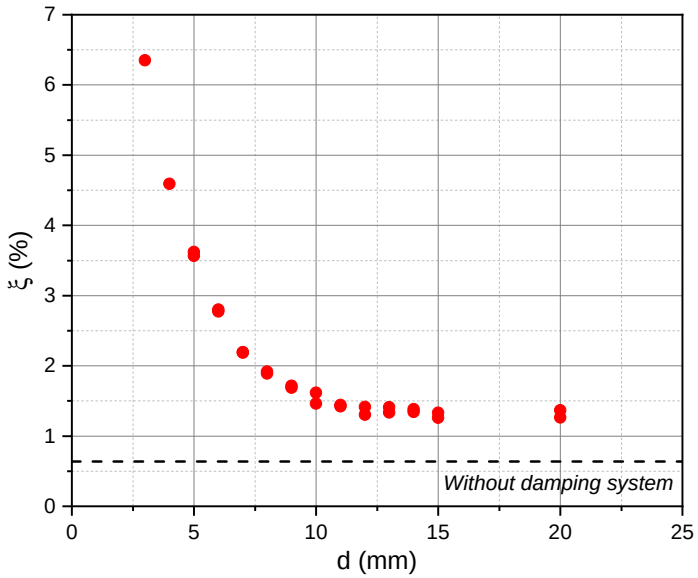

Fig. 4.4.: Calibration of the system damping as a function of the distance between the magnet and the copper plate.

The system damping without using the additional device is approximately 0.6%. The additional device can effectively enhance the system damping, exceeding 6% at a distance of 3 *mm*. It can be noted that a quite constant damping of 1.4% is obtained for a distance ranging between 10 and 20 *mm*, while it increases exponentially below 10 *mm*. Due to practical reasons and to avoid the variation of system damping ratio during loading, a distance of 15 *mm* is adopted for the current scale models.

4.3.3 Ball joint

As the loading is applied at an eccentricity of 0.62 *m*, the lateral displacement at this position is relatively high. This lateral displacement causes differential height levels, inducing a significant moment due to the actuator rigidity. The solution adopted is the insertion of a ball joint between the actuator and the brass tube to cancel the induced moment, as seen in Figure 4.5.

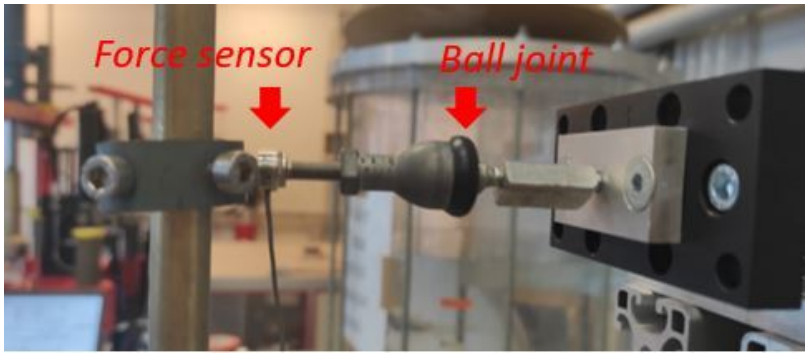

Fig. 4.5.: Ball joint used to avoid additional moment

Based on experimental observations, it is recommended to adopt a double universal joint due to the vertical displacement that occurred during cyclic loading.

4.4 Validity of experimental testing procedures

As seen in Section 4.3.1, specific procedures are followed to ensure tests repeatability at laboratory stress levels. This section presents the experimental procedures followed during different types of tests performed and the typical results obtained. The different types of tests are repeated to verify the results' repeatability and the reliability of testing procedures.

4.4.1 Evaluation of monopile ultimate capacity

A monotonic test procedure was adopted to evaluate the ultimate capacity of the scale models of the monopile foundations. This evaluation of ultimate capacity leads to significant findings: (i) evaluation of the reasonableness of the ultimate load capacity obtained after the transition to the prototype scale, which shows the performance of the scaling laws proposed; (ii) verification of the satisfaction of the ultimate limit state by the proposed foundations; and (iii) normalization of the loading amplitude applied for the cyclic loading (determination of ζ_b).

Set-up and test procedure

The testing set-up and the adopted procedure for monotonic tests are presented in Figure 4.6, and are defined as follows:

- Soil mass preparation: The soil mass was formed in a container (*Chamber* K_0 used by kerner, 2017) with a diameter of 550 *mm*. In the framework of this thesis, the Fontainebleau sand *NE34* was used as soil material. The dry compaction method was adopted: successive layers of 50 *mm* height were formed by adding a mass of sand determined depending on the targeted density. The depth of the sand mass varied in each test to ensure a distance greater than the monopile diameter between the monopile tip and the base, aiming to neglect the boundary conditions effect.

- monopile installation: The guidance and driving system presented in Section 4.3.1 was used to install the monopile. In this test, a steel tube with the same properties as the scale model of the monopile was used to avoid any damage on the developed scale model. Therefore, manual driving is performed because the rail and the mass are adapted for the complete scale model.

- Loading system: At the eccentricity position, the monopile was connected by a wire to a rotational actuator with a maximum capacity of 500 *N*. The velocity of the actuator is constant and slow, permitting an accurate monitoring of the force and displacement evolution.

- Monitoring system: *Schlumberger U7000* force sensor is inserted within the wire connection between the actuator and the monopile. This force sensor has a maximum capacity of 1000 *N*. The displacement of the monopile was measured by two laser sensors (*Keyence IL-030*), having a measurement range exceeding 250 *mm* with a precision of micrometer order. Besides, the rotation of the monopile was measured by an inclinometer (*Sensel Measurement SM-NA10*), having a measurement range of $\pm 10°$, and a precision of $0.002°$. The sensors were placed in a way to ensure the determination of displacement and

rotation at the sand surface. The outputs of sensors were connected to a *NI CompactDAQ (cDAQ-9234)*, and the values were input to an acquisition program developed under *LabVIEW* software.

The calibrations of some sensors are available in Appendix A.1.

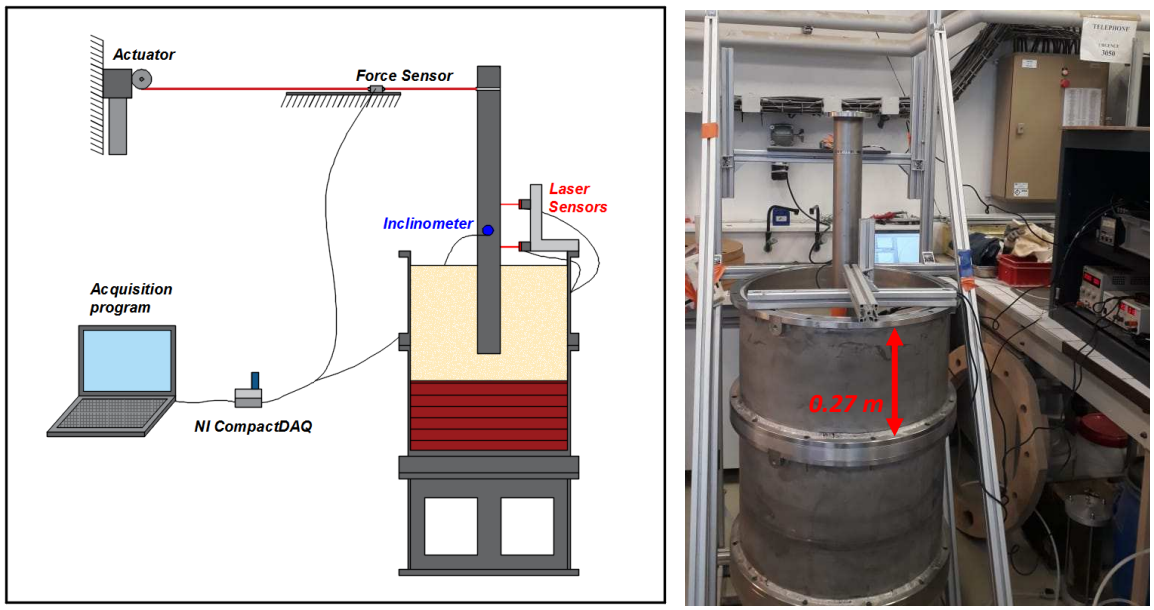

(a) (b)

Fig. 4.6.: (a) Schematic and (b) photo of the monotonic test set-up

Typical results and repeatability

The ultimate capacity is determined for the monopile of the scale model *M2*. Two tests (called M-R-1 and M-R-2) were performed with the same conditions to verify the repeatability of the results. Lateral loading was applied at an eccentricity of 620 *mm*, and the sand had a relative density index of 0.53. Figure 4.7 presents the full monotonic response and shows rigorous results with very good repeatability. The monotonic responses are presented in moment-rotation space since monopile design criteria are typically defined in terms of foundation rotation (DNVGL-ST-0126, 2016).

Generally, small deformation levels are relevant for cyclic loading. Therefore, the experimental challenge is to obtain good repeatability at these levels of deformation, corresponding to the typical amplitudes of cyclic loading. Figure 4.8 presents the repeatability at medium and small deformation levels, also showing good repeatability. The satisfactory repeatability obtained at different levels of deformation highlights the excellent performance of the followed test procedure.

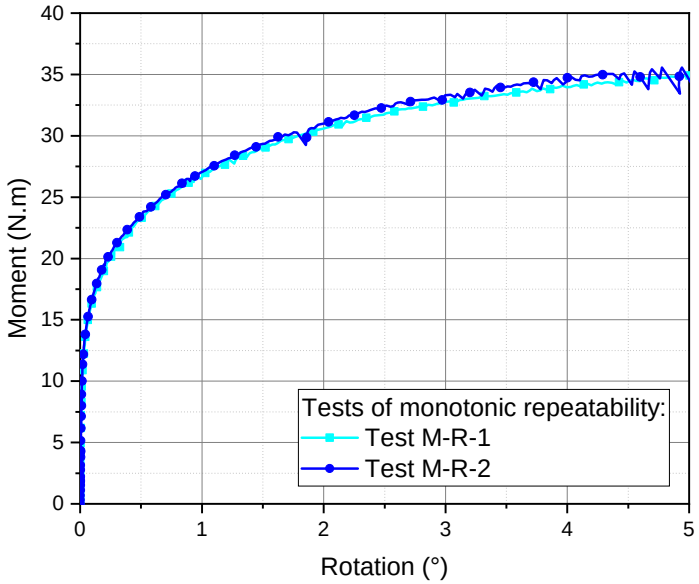

Fig. 4.7.: Ultimate response repeatability of the foundation of the scale model *M2*

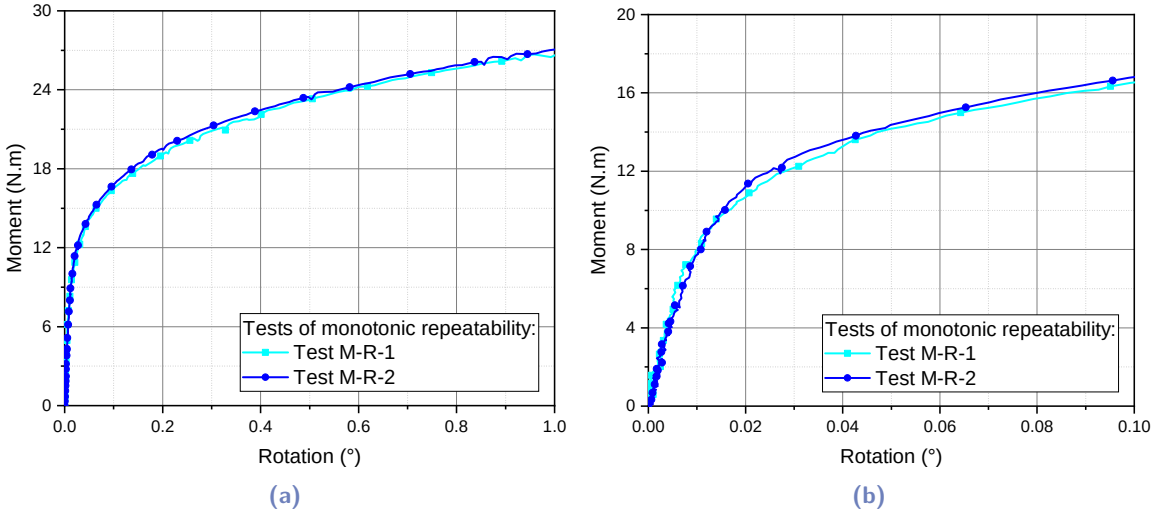

Fig. 4.8.: Monotonic response repeatability of the foundation of the scale model *M2* at (a) medium and (b) small deformation levels

It should be noted that the tested tube has a thickness of $3\ mm$, while the thickness of the tube designed to represent the prototype foundation and then used in the cyclic scale model *M2* has a thickness of $2\ mm$. This difference has two reflections in the monotonic response: (i) a large increase in the mass of the tube and (ii) a variation of the stress field induced around the monopile after the installation. These two points can induce a considerable effect on the monopile ultimate capacity. Fan, 2020 showed a more significant effect of pile installation on the monopile response in case of smaller diameter-to-thickness ratio. The validation of the test procedure is still valid, while it is recommended to repeat the tests using a tube with the same thickness in case of the adoption of the results to normalize the cyclic loading (determination of ζ_b)

4.4.2 Experimental evaluation of the system natural frequency

As part of this study, the natural frequency of the scale model should be identified to verify the respect of scaling laws, and to investigate its variation due to cyclic loading. A simple experimental method is adopted by kerner, 2017, and has shown good performance. This method is also adopted in the framework of this thesis. This section presents the testing and analysis procedure, typical results obtained, and the corresponding repeatability.

Set-up and test procedure

The test consists of a free vibration test, and the analysis of the obtained signal:

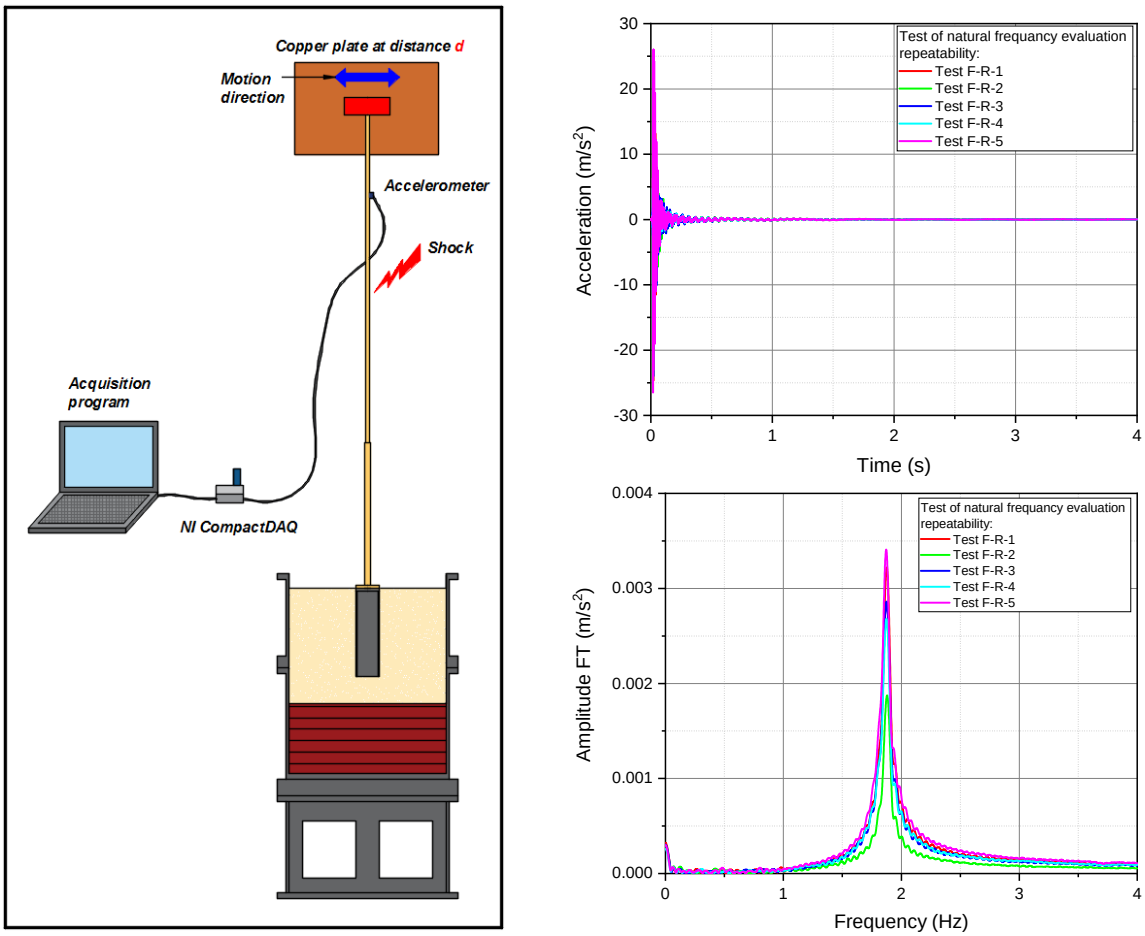

Fig. 4.9.: (a) Schematic of the test procedure adopted to evaluate the first natural frequency of the system (b) Typical accelerometer signals and corresponding Fourier transforms

An impact is applied to the brass tube using an impact hammer (*Brüel & Kjær type 8206*) and the induced motion is measured by an accelerometer (*Brüel & Kjær type 4507 B004*) also fixed on the brass tube. It should be noted that kerner, 2017 has shown the possibility to place the accelerometer at different heights along the scale model. Figure 4.9a shows the testing set-up. The output of the accelerometer is connected to a *NI CompactDAQ (cDAQ-9234)*, and the values are input to an acquisition program developed under *LabVIEW* software, with a sampling frequency of $\sim 1650\ Hz$. Fast Fourier transform of the obtained signal is performed, and the first natural frequency of the system is the frequency corresponding to the maximum amplitude of the resonance peak. Figure 4.9b shows the acceleration signals and the corresponding Fourier transforms of some measurements performed. A cubic spline interpolation is applied to Fourier transforms to enhance the resolution of the obtained curves. Five measurements were generally performed, and the average is considered as the natural frequency of the scale model.

Typical results and repeatability

The test procedure presented in the previous section is applied to the scale model *M2*. Five signals obtained and the corresponding Fourier transforms are presented in Figure 4.9b, showing a very good agreement between the different measurements. The natural frequency and the modal damping ratio extracted from the five signals analysis are presented in Table 4.3.

Tab. 4.3.: Repeatability of natural frequency evaluation

Test identifier	Natural frequency f_n (*Hz*)	Modal damping ratio ξ (%)
F-R-1	1.876	1.46
F-R-2	1.879	1.41
F-R-3	1.874	1.52
F-R-4	1.874	1.47
F-R-5	1.871	1.44
Average	1.875	1.46
Relative standard deviation (%)	0.2	4.1

Table 4.3 clearly shows the validity of the test procedure adopted to evaluate experimentally the natural frequency of the scale model.

4.4.3 Cyclic/dynamic response of offshore wind turbine scale model

As the main purpose of the current study, a test procedure is adopted to understand the cyclic/dynamic response of the scale model after a high number of loading cycles. This test procedure should ensure the identification and the quantification of principal phenomena underlying the cyclic/dynamic response: (i) lateral displacement accumulation, (ii) foundation stiffness evolution, and (iii) variation of the system natural frequency.

Set-up and test procedure

The testing set-up and the adopted procedure for cyclic/dynamic tests are presented in Figure 4.10, and listed hereafter:

- Soil mass preparation: The soil mass is formed in the same way as for the monotonic testing.
- Monopile installation: The guidance and driving system presented in Section 4.3.1 is used to install the scale model.
- The guidance and driving system was re-adapted to fix the copper plate at a distance d of the magnet attached to the top mass.
- The natural frequency of the system is evaluated before the cyclic loading, using the method presented in Section 4.4.2.
- Loading system: *PS01-37x120F-HP-C LinMot* motor is used to apply the cyclic loading, with specification summarized in Table 4.4. *LinMot* motors have electromagnetic direct drives in tubular form. The motor is fixed on a rigid support at the defined eccentricity, piloted by a control box using a specific program (*LinMotTalk*), based on the defined loading characteristics.
- Monitoring system: *Futek LCM100 25lb* force sensor is installed between the *linMot* motor and the brass tube. This force sensor has a maximum capacity of 111 *N*. A ball joint is inserted between the force sensor and the motor to cancel all additional moments, as seen in Section 4.3.3. The displacement of the monopile is measured by three laser sensors (*(Keyence IL-030*). Besides, the rotation of the monopile is measured by an inclinometer (*Sensel Measurement SM-NA10*). The sensors are placed in a way to ensure the determination of displacement and rotation at the sand surface. The outputs of the sensors are connected to two *NI CompactDAQ (cDAQ-9234)*, and the values are input to an acquisition program developed under *LabVIEW* software.

Tab. 4.4.: *LinMot* motor specification summary

Specification	Value	Unit
Travel	180	*mm*
Position resolution	0.005	*mm*
Maximum velocity	3800	*mm/s*
Maximum force	255	*N*
Maximum continuous force	48	*N*
Force constant	17	*N/A*

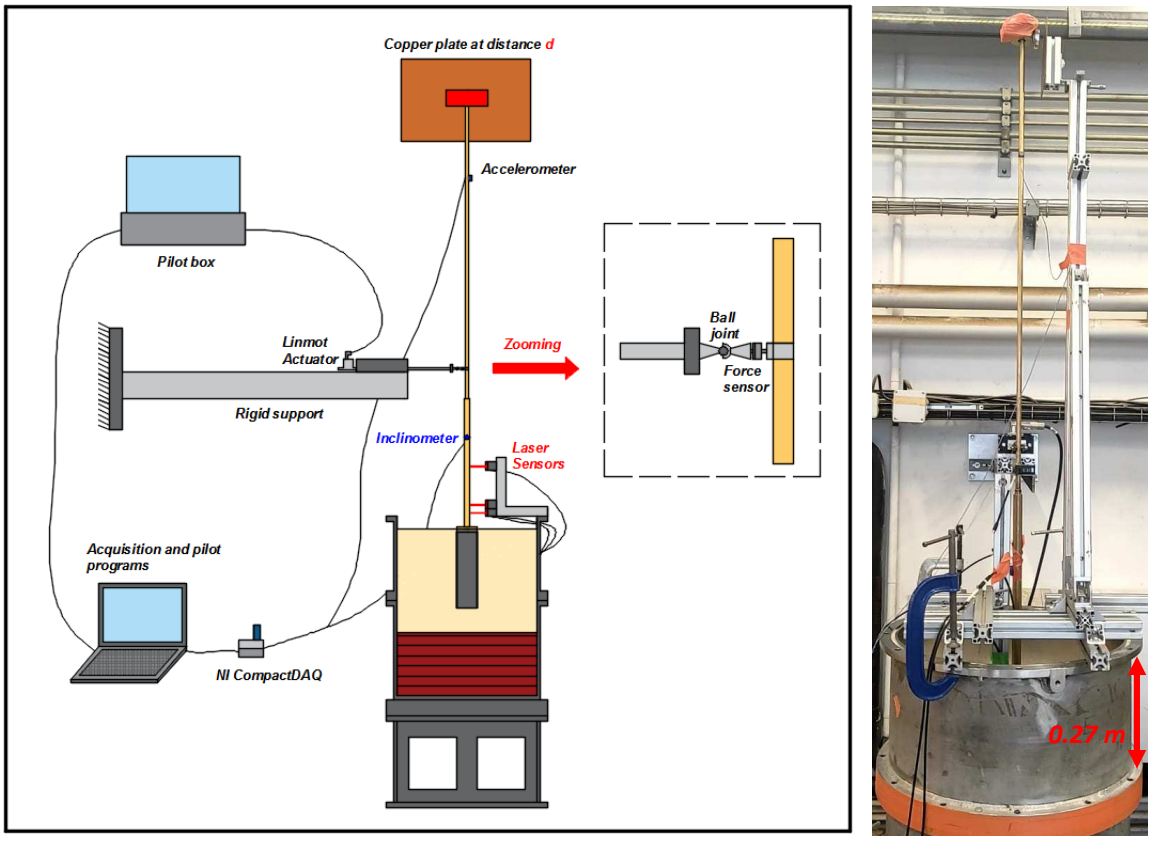

(a) (b)

Fig. 4.10.: (a) Schematic and (b) photo of the cyclic test set-up

- The natural frequency of the system is evaluated after the cyclic loading.
- The subsidence cone around the monopile is investigated: radius, depth, ... Besides, the vertical displacement of the scale model is determined at the end of the test.

The calibrations of some sensors are available in Appendix A.1.

Similar to the monotonic test procedure, two tests (called C-R-1 and C-R-2; Section 5.1.2) with the same conditions are repeated to check the repeatability of the results and the validity of the current procedure. The tests were performed on the scale model *M2*, with a density index of the sand mass equal to 0.53, and the cyclic loading is applied at an eccentricity of 620 *mm*. Due to some difficulties with the motor control program, generating force-controlled motions is not possible actually. Therefore, a sinusoidal displacement controlled motion, alternating between $+4$ and -2 *mm*, was applied to the system with a frequency of 1 *Hz* up to 2000 *cycles*.

The cyclic response is presented in the moment-rotation space, as shown in Figure 4.11a. The evolution of the secant stiffness of the foundation with cycles number is determined and presented in Figure 4.11b. The obtained curves show satisfying repeatability, especially in the case of stiffness evolution, which is rarely similarly achieved in the literature. Therefore, the cyclic test procedure is validated, highlighting the effect of guidance and driving system.

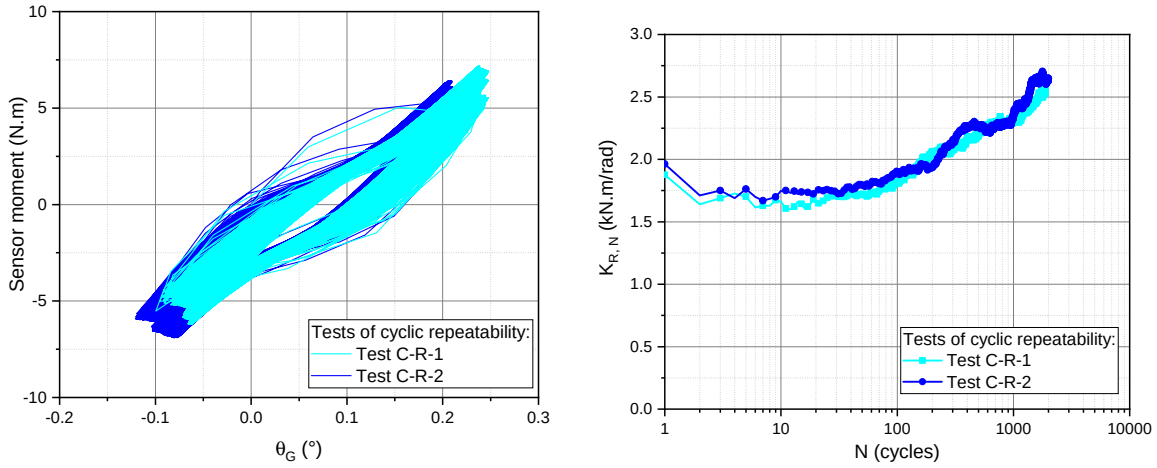

Fig. 4.11.: Cyclic response repeatability of the foundation of the scale model *M2* within 2000 cycles: (a) Moment-rotation at sand surface and (b) evolution of the secant stiffness with the cycles number

4.5 Alternative methods to estimate the first system natural frequency

As offshore wind turbines are dynamically sensitive structures, the estimation of the first natural frequency is an important design criterion. This section will present and evaluate available numerical methods adopted to predict the system's natural frequency and the dynamic response of the first vibration mode. The aim is to assess the tools required to verify

the dynamic similarity between the proposed scale models and corresponding prototypes.

Three methods are considered to estimate the system's natural frequency:

- Method 1: Dynamic *3D FEM Cesar-LCPC* model simulating the foundation-structure system.

- Method 2: Combination of (i) calculation method proposed by Arany et al., 2016 based on *Euler-Bernoulli* and *Timoshenko* beam theories, where the foundation is idealized by three coupled springs (lateral, rocking, and cross-coupling), and (ii) static *3D FEM Cesar-LCPC* model used to determine the stiffness of the springs.

- Method 3: Combination of (i) calculation method proposed by Bouzid et al., 2018 based on *Euler-Bernoulli* and *Timoshenko* beam theories, where the foundation is idealized by three coupled springs (lateral, rocking, and cross-coupling), and (ii) static *3D FEM Cesar-LCPC* model used to determine the stiffness of the springs.

The three methods will be evaluated against experimental results and then used to determine the first natural frequency of the prototypes and the scale models.

4.5.1 Experimental database: kerner, 2017

As part of a study conducted to evaluate the natural frequency of an offshore wind turbine, kerner, 2017 performed a test program to study the effect of vertical stress applied at the sand surface on the natural frequency of a scale model.

Figure 4.12 presents a schematic and a photo of the testing set-up and the studied scale model. The scale model consists of two stainless steel tubes connected by a fixation system. One tube represents the monopile foundation and the transition piece, having a diameter of 80 *mm* and a thickness of 2 *mm*. The other one represents the offshore wind turbine tower, having a diameter of 70 *mm* and a thickness of 2 *mm*. The monopile foundation was installed into a Fontainebleau *NE34* sand mass with a relative density index equal to 0.65. kerner, 2017 can be referred to for more details about the scale model dimensions and development. Vertical stress was applied at the sand surface by increasing the water pressure is a specific balloon placed between the sand surface and a rigid cover. The vertical stress varied between 0 and 200 *kPa*, and the natural frequency was evaluated by the experimental method presented in Section 4.4.3.

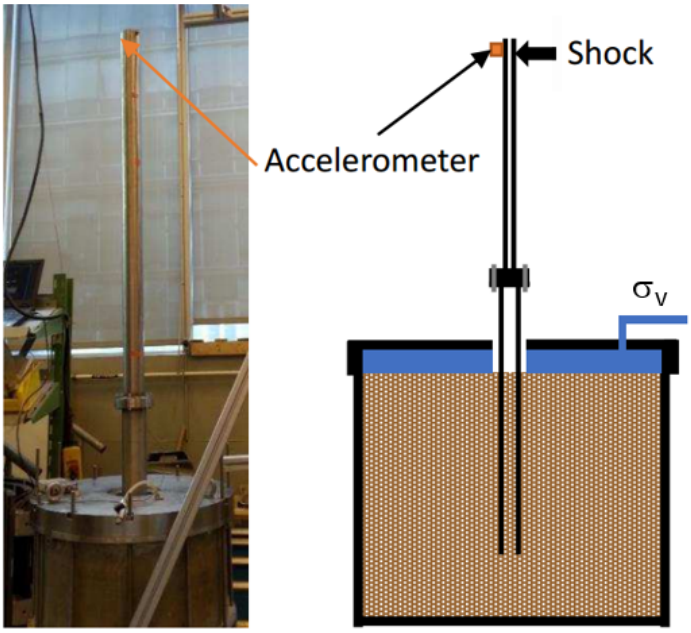

Fig. 4.12.: Schematic and photo of the scale model studied by kerner, 2017

The obtained results are presented in Table 4.5, and used to evaluate the three numerical methods proposed to estimate the system natural frequency.

Tab. 4.5.: First natural frequency of kerner, 2017 scale model as a function of vertical stress level applied on the sand mass

Vertical stress σ'_v (kPa)	0	10	50	100	200
Natural frequency f_n (Hz)	23.93	24.42	25.27	25.68	26.07

4.5.2 Dynamic *3D FEM Cesar-LCPC* model to estimate system natural frequency

The first method used to estimate the natural frequency of the scale model studied by kerner, 2017 is the use of a *3D* dynamic simulation using *Cesar 3D - LCPC* software. *MODE* solver is available in *Cesar 3D - LCPC* package, designed to determine the natural frequencies of a defined model. An accurate model is carried out, including the fixation system between the monopile and the tower. The geometry of the model is presented in Figure 4.13a.

An isotropic linear elastic behavior law is defined for all materials, including the sand. Materials properties adopted for the simulation are presented in Tables 4.6 and 4.7. The dynamic Young's modulus of the sand mass at different stress levels are determined according

to Section 3.1.2. The initial shear modulus profile is estimated as a function of the mean confining stress, taking the following form (G_0 in *MPa* and p' in *kPa*):

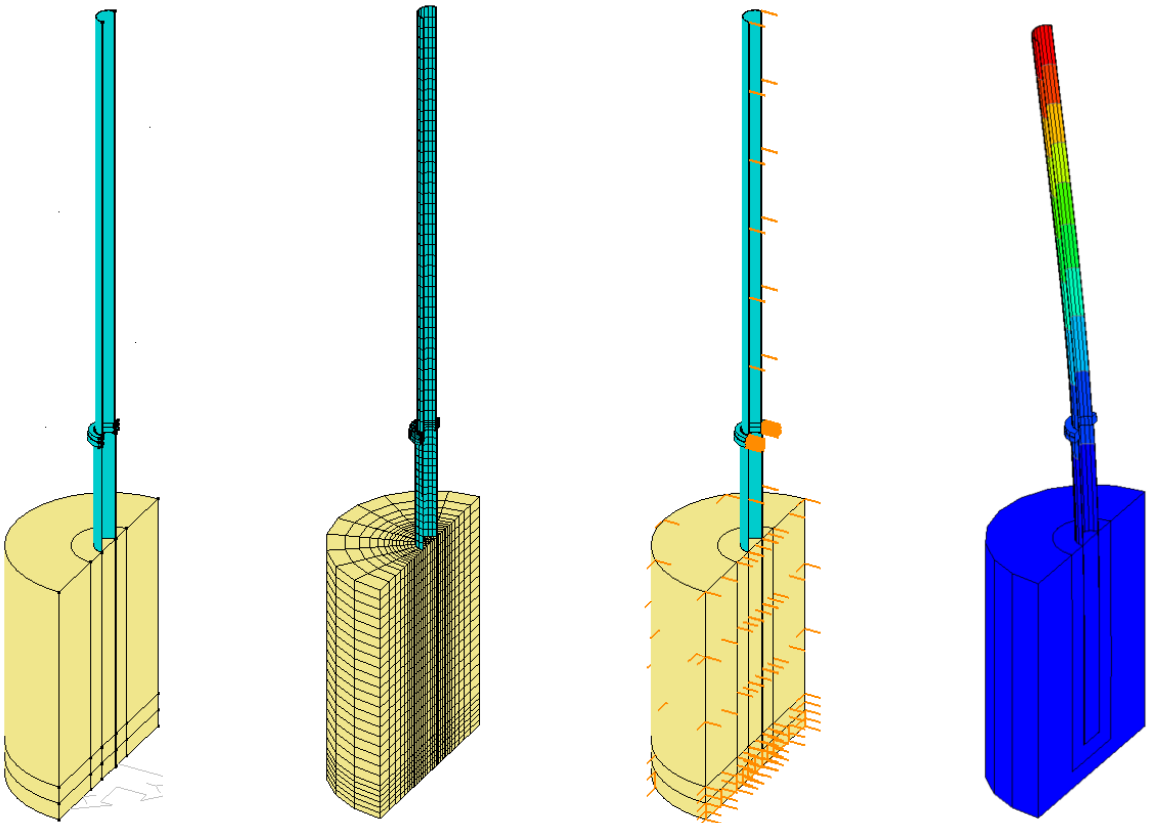

Fig. 4.13.: Presentation of the *3D* simulation carried out on *Cesar 3D - LCPC* to evaluate the natural frequency of the scale model studied by kerner, 2017: (a) Geometry (b) Mesh (c) Boundary conditions (d) Vibration mode shape at the first natural frequency

$$G_0 = 20.1 \frac{1}{0.019 + 0.50e^2} \left(\frac{p'}{101.3} \right)^{0.43} \quad ; \quad E_0 = 2(1+\nu)G_0 \tag{4.6}$$

where e is the void index equal to 0.672 in this case, ν is the Poisson's ratio taken as 0.3 (Section 6.2.3), and p' is the mean effective stress at 70% of the monopile embedded depth (Abadie, 2015), considered as the effective stress level along the monopile depth.

Tab. 4.6.: Properties of materials defined in the *MODE* solver for the analysis of the scale model studied by kerner, 2017

Material property	Unit	Stainless Steel	Sand
Density ρ	kg/m^2	1585	8010
Young's modulus E	*GPa*	203	Table 4.7
Poisson's ratio ν	-	0.3	0.3

Tab. 4.7.: Dynamic Young's modulus adopted for the *NE34* sand ($I_d = 0.65$) in the *MODE* solver for the analysis of the scale model studied by kerner, 2017

Vertical stress σ'_v (*kPa*)	0	10	50	100	200
Dynamic Young's modulus E_0 (*MPa*)	54.3	80.2	135.5	177.8	236.2

Only half of the model is simulated, considering the problem symmetry. This simulation is validated by comparing the results with those of a complete model, where an identical natural frequency is obtained for both cases. A quadratic regular mesh, refined close to the monopile, is applied to the model (Figure 4.13b). Similarly, the current mesh is validated by comparing the results with a model having homogeneous extremely-fine mesh. The relative error between the two cases is less than 0.15%. These steps are also applied in the static calculations to optimize the computation time. In the current dynamic case, these steps are validated and presented in Table 4.8.

Tab. 4.8.: Validation of mesh reduction steps applied to enhance the calculation time: Application on the scale model studied by kerner, 2017 for vertical stress equal to 50 *kPa*

Calculation case	Complete model with adapted mesh	Half model with adapted mesh	Half model with homogeneous extremely-fine mesh
Number of elements (−)	13920	6960	41977
Natural frequency f_n (*Hz*)	24.98	24.98	24.95

According to the test conditions, suitable boundary conditions are applied to the model (Figure 4.13c). *MODE* solver analysis is performed on different cases for vertical stress, and the corresponding natural frequencies and mode shapes are obtained. Figure 4.13d presents the mode shape obtained for the first natural frequency, showing a *Soft-Stiff* behavior. The findings of this method are presented and discussed in Section 4.5.4.

4.5.3 Calculation methods to estimate the fist natural frequency of the system

Several quick-hand calculation methods are proposed to serve during the design optimization stage or conceptual design stage. These methods are based on the formula of a simple

cantilever beam to estimate the first natural frequency of the structure. Then, coefficients are applied to consider the flexibility of the foundation and the substructure. Therefore, Bhattacharya and Adhikari, 2011 used two springs at the ground level (lateral and rocking springs) to represent the foundation dynamic stiffnesses; later this approach was enhanced by adding spring (cross-coupling spring; Arany et al., 2016). The proposed methods also differ in the way in which the substructure is taken into account: Arany et al., 2016 applied a coefficient depending on the water depth and the monopile stiffness, while Bouzid et al., 2018 sought the physical quantities equivalent to the substructure-tower system. The stiffnesses of the springs depend on the monopile dimensions and soil profile properties, estimated by numerous impedance functions carried out by several works. Relevant functions for flexible and rigid monopiles are summarized by Arany et al., 2017. In the case of semi-rigid monopiles, numerical tools (finite element analysis, Winkler p-y method,...) are generally performed to determine the stiffnesses of the springs. In this section, two analytical methods proposed by Arany et al., 2016 and Bouzid et al., 2018 to evaluate the natural frequency of offshore wind turbines are presented, followed by the static *3D FEM Cesar-LCPC* model performed to determine the stiffnesses of the foundation springs:

- Method 2 - Arany et al., 2016:

  The global expression of the system natural frequency is defined by:

$$f_n = C_L C_R C_S f_{FB} \tag{4.7}$$

  where C_L and C_R are the coefficients of the lateral and rotational flexibility of the foundation , C_S is the substructure flexibility coefficient, and f_{FB} is the fixed base natural frequency of the tower.

  The fixed base natural frequency of the tower is determined from the equivalent stiffness k_0 and equivalent mass m_0 of the first mode of vibration, and the corresponding equation takes the following form:

$$f_{FB} = \frac{1}{2\pi}\sqrt{\frac{k_0}{m_0}} = \frac{1}{2\pi}\sqrt{\frac{3E_T I_T}{L_T^3\left(m_{RNA} + \frac{33}{140}m_T\right)}} \tag{4.8}$$

  where E_T is the Young's modulus of the tower material, I_T is the average area moment of inertia of the tower, m_T is the mass of the tower, m_{RNA} is the mass of the rotor-nacelle assembly, and L_T is the length of the tower. The average area moment of inertia is calculated by the equation:

$$I_T = \frac{1}{128}(D_b^4 + D_t^4 - (D_b - t_T)^4 - (D_t - t_T)^4) \quad \text{with} \quad t_T = \frac{m_T}{\rho_T L_T D_T \pi}; \quad D_T = \frac{D_b + D_t}{2} \tag{4.9}$$

where D_b is the tower bottom diameter, D_t is the tower top diameter, and ρ_t is the density of the tower material (steel). A simplified form is adopted by the original method, valid in case of thickness largely smaller than the diameter of cylinders. The application of this form is limited in the case of scale models.

The non-dimensional foundation stiffnesses were determined for the calculation of foundation flexibility coefficients:

$$\eta_L = \frac{K_L L_T^3}{EI_\eta} \qquad \eta_{LR} = \frac{K_{LR} L_T^2}{EI_\eta} \qquad \eta_R = \frac{K_R L_T}{EI_\eta} \tag{4.10}$$

where K_L, K_{LR}, and K_R are stiffnesses of the spring representing the foundation, EI_η is the equivalent bending stiffness of the tower calculated by the following equation:

$$EI_\eta = E_T I_t f(q) \qquad \text{with} \qquad q = \frac{D_b}{D_t} \quad ; \quad f(q) = \frac{1}{3} \frac{2q^2(q-1)^3}{2q^2 \ln(q) - 3q^2 + 4q - 1} \tag{4.11}$$

where $E_T I_t$ is the bending stiffness at the top of the tower.

Then, the foundation flexibility coefficients are determined:

$$C_R(\eta_L, \eta_R, \eta_{LR}) = 1 - \frac{1}{1 + a\left(\eta_R - \frac{\eta_{LR}^2}{\eta_L}\right)} \quad ; \quad C_L(\eta_L, \eta_R, \eta_{LR}) = 1 - \frac{1}{1 + b\left(\eta_L - \frac{\eta_{LR}^2}{\eta_R}\right)} \tag{4.12}$$

where $a = 0.6$ and $b = 0.5$ are empirical coefficients. The use of this equation is limited to the following conditions:

$$\eta_R > 1.2\frac{\eta_{LR}^2}{\eta_L} \quad ; \quad \eta_L > 1.2\frac{\eta_{LR}^2}{\eta_R} \tag{4.13}$$

For the consideration of the substructure flexibility coefficient, it is assumed to be an extension of the monopile foundation up to the bottom of the tower. The distance between the mudline and the bottom of the tower is L_S, and $E_p I_p$ is the bending stiffness of the monopile. The foundation flexibility is calculated as a function of two dimensionless parameters, the bending stiffness ratio χ and the length ratio ψ:

$$C_S = \sqrt{\frac{1}{1+(1+\psi)^3\chi-\chi}} \qquad \text{with} \qquad \chi = \frac{E_T I_T}{E_p I_p} \quad ; \quad \psi = \frac{L_S}{L_T} \tag{4.14}$$

- Method 3 - Bouzid et al., 2018:

The global expression of the system natural frequency is defined by:

$$f_n = C_L C_R f_{FB} \tag{4.15}$$

This method is similar to the method 2 in the consideration of the foundation flexibility, while it differs in the consideration of the substructure flexibility. In this method, the natural frequency of the whole structure (substructure and tower) is determined based on the beam theories. The fixed base natural frequency expression of the whole structure becomes:

$$f_{FB} = \frac{1}{2\pi}\sqrt{\frac{3EI_{TS}}{L^3\left(m_{RNA}+\frac{33}{140}m_{TS}\right)}} \tag{4.16}$$

where EI_{TS} and m_{TS} are respectively the equivalent bending stiffness and mass of the whole structure, and L is the total length. The equivalent physical quantities are calculated by:

$$EI_{TS} = (1-\alpha)EI_S + \alpha EI_\eta \qquad \text{with} \qquad \alpha = \frac{L_T}{L} \quad ; \quad L = L_T + L_S \tag{4.17}$$

$$m_{TS} = m_T + m_S \tag{4.18}$$

It should be noted that the non-dimensional foundation stiffness should take the following form:

$$\eta_L = \frac{K_L(L_T+L_S)^3}{EI_{TS}} \quad ; \quad \eta_{LR} = \frac{K_{LR}(L_T+L_S)^2}{EI_{TS}} \quad ; \quad \eta_R = \frac{K_R(L_T+L_S)}{EI_{TS}} \tag{4.19}$$

Actually, the natural frequency determined by all these methods is the undamped frequency. To consider the damping of the system, the following expression should be considered:

$$\tilde{f}_n = f_n \sqrt{1 - \xi^2} \tag{4.20}$$

Where ξ is the system damping ratio presented in Section 4.3.2.

- Static *3D FEM Cesar-LCPC* model:

The monopile foundation of the scale model studied by kerner, 2017 has a length-to-diameter ratio equal to 7.5, which is relatively high for a rigid monopile. The monopile rigidity factors were determined at different stress levels and presented in Figure 4.14, showing semi-rigid behavior in all cases. Therefore, since the impedance functions proposed to determine the stiffnesses of the springs representing rigid and flexible monopiles are not applicable, a static finite element model is carried out using *Cesar 3D - LCPC* software.

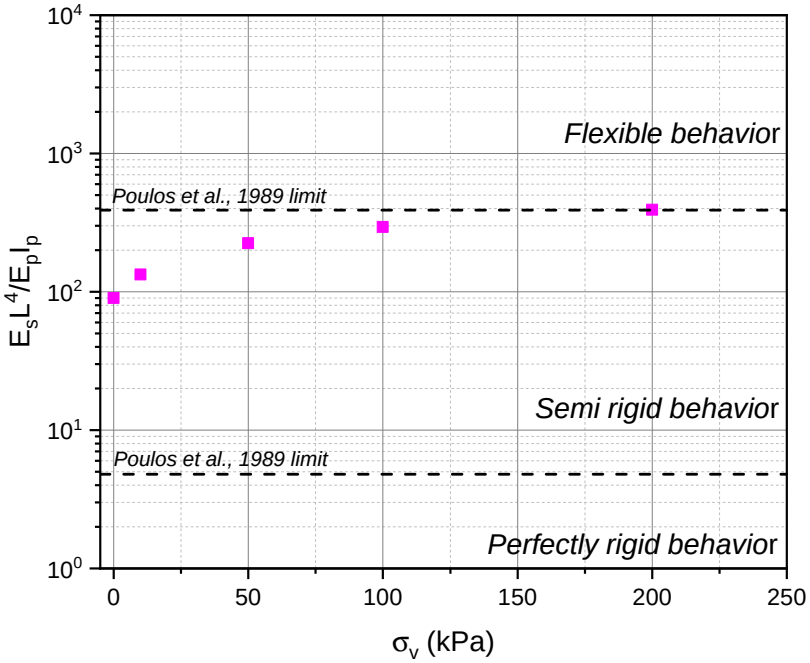

Fig. 4.14.: Monopile rigidity factors for different vertical stress levels applied at the sand surface

Geometry, mesh, boundary conditions, and materials properties are identical to the dynamic model presented in Section 4.5.2. Since the initial foundation stiffness is considered, an isotropic linear elastic behavior law is defined for all materials, including the sand. A staged calculation is applied consisting of four calculation phases:

– Initialization: Only the sand mass is activated, and the corresponding weight is applied to generate the initial stress field.

– Activation of the scale model: The geometry representing the scale model is activated, and the corresponding weight is applied as a simulation of the scale model installation.

– Application of the vertical stress: Depending on the case studied, vertical surface stress is applied at the sand surface, simulating the vertical stress applied by kerner, 2017.

– Lateral loading: Consecutively, lateral loading is applied at two different eccentricities, and the monopile displacement and rotation occurred at the sand surface are extracted. As a linear elastic behavior law is adopted for all materials, loading amplitude is disregarded. Figure 4.15a presents a schematic of the static *3D FEM Cesar-LCPC* model, showing the loading eccentricities.

This model aims to determine the stiffnesses of springs representing the monopile foundation. Therefore, the elastic stiffness matrix at the sand surface should be solved, leading to these parameters. As the monopile foundation is represented by three springs, two loadings applied to different eccentricities are required to obtain two matrices. Four equations can be extracted from these matrices, permitting the determination of the stiffnesses of the three springs. The two matrices are defined by:

$$\begin{pmatrix} F_1 \\ M_1 \end{pmatrix} = \begin{pmatrix} K_L & K_{LR} \\ K_{LR} & K_R \end{pmatrix} \begin{pmatrix} u_1 \\ \theta_1 \end{pmatrix}$$

and

$$\begin{pmatrix} F_2 \\ M_2 \end{pmatrix} = \begin{pmatrix} K_L & K_{LR} \\ K_{LR} & K_R \end{pmatrix} \begin{pmatrix} u_2 \\ \theta_2 \end{pmatrix}$$

where F_i is the loading amplitude, M_i is the moment amplitude, and u_i and θ_i are respectively the monopile displacement and rotation at the sand surface.

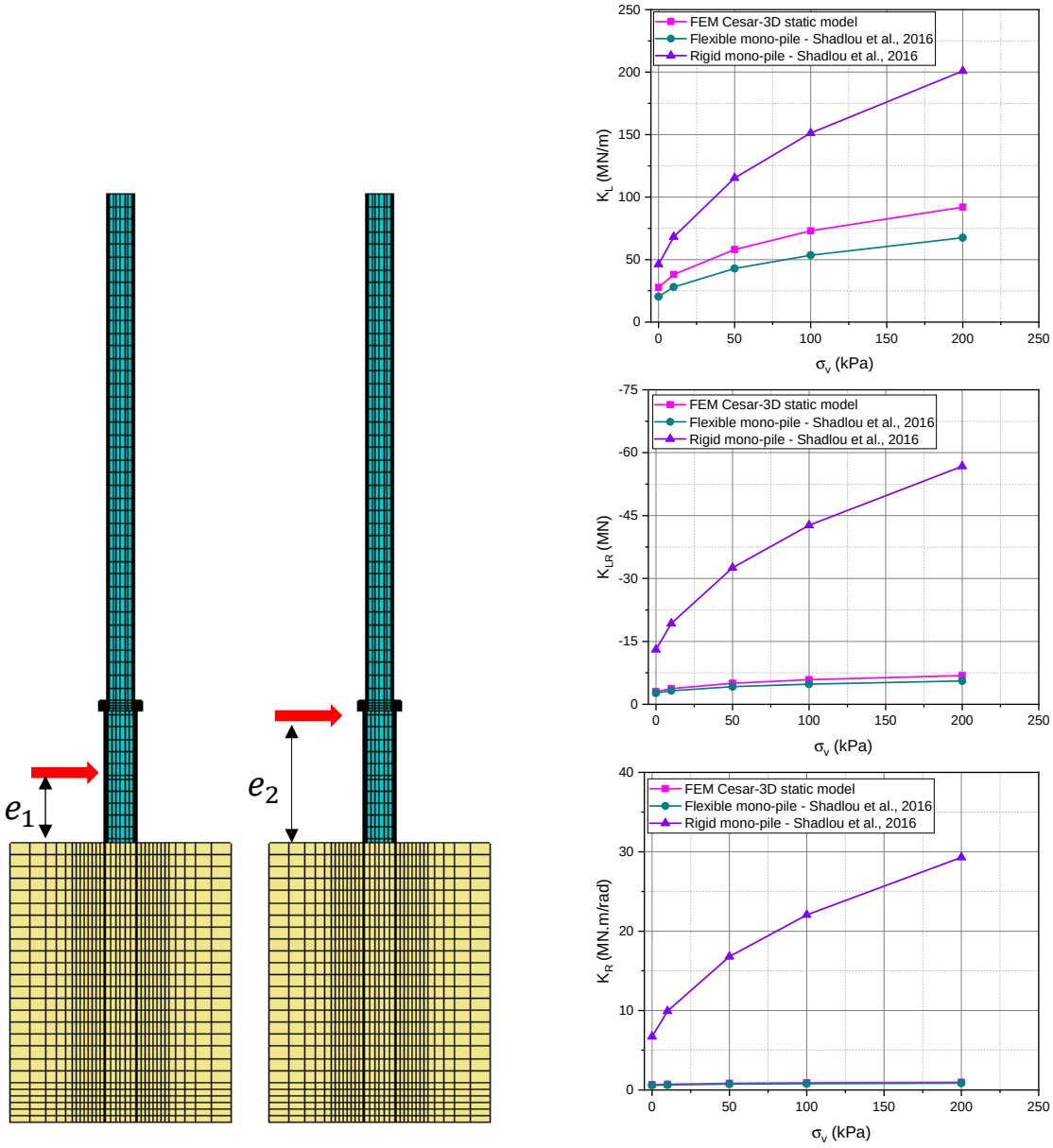

Fig. 4.15.: Determination of stiffnesses of the mono-pile foundation for different vertical stress levels applied at the sand surface: (a) Schematic of the static *3D FEM Cesar-LCPC* model (b) Obtained foundation stiffnesses

This methodology is applied for different vertical stress levels and the corresponding stiffnesses of the springs are determined. Figure 4.15b shows the variation of the stiffnesses of the springs stiffness as a function of the vertical stress applied. The obtained stiffnesses are compared to those obtained by the impedance functions proposed by Shadlou and Bhattacharya, 2016. Semi-rigid to flexible behavior is shown, in accordance with the rigidity factors predicted and presented in Figure 4.14. The parameters obtained are combined with analytical methods 2 and 3 to estimate the natural frequency of the

scale model for different cases. The results obtained by these methods are presented and discussed in the next section.

4.5.4 Evaluation of the analytical and numerical methods

The first natural frequency of the scale model studied by kerner, 2017 for different vertical stress levels is determined by three different methods. The findings of these methods are presented in Figure 4.16a, in comparison with the experimental results. The errors according to experimental results are evaluated and presented in Figure 4.16b.

The best performance is obtained by the dynamic *3D FEM Cesar-LCPC* model with an error which does not exceed $\sim 2\%$. A good performance is also achieved by the analytical methods, with an error ranging between 10 and 15% for the method 2 and between 4 and 10% for the method 3. This deviation can be attributed to the inability of these methods to consider the connection between the two parts of the scale model. It should be noted that the estimated errors for the two methods follow the same tendency, which decreases with the stress level. Thus, this tendency should be related to the capability of the foundation flexibility coefficients to represent the soil-structure interaction. On another side, Futai et al., 2018, based on a parametric study on 1g and centrifuge scale models, found serious limitations of the theoretical methods predicting the system natural frequency in the case of 1g modeling. It would be interesting to evaluate the relative performance of the theoretical methods on the current scale models, after the careful consideration of the dynamic similarity.

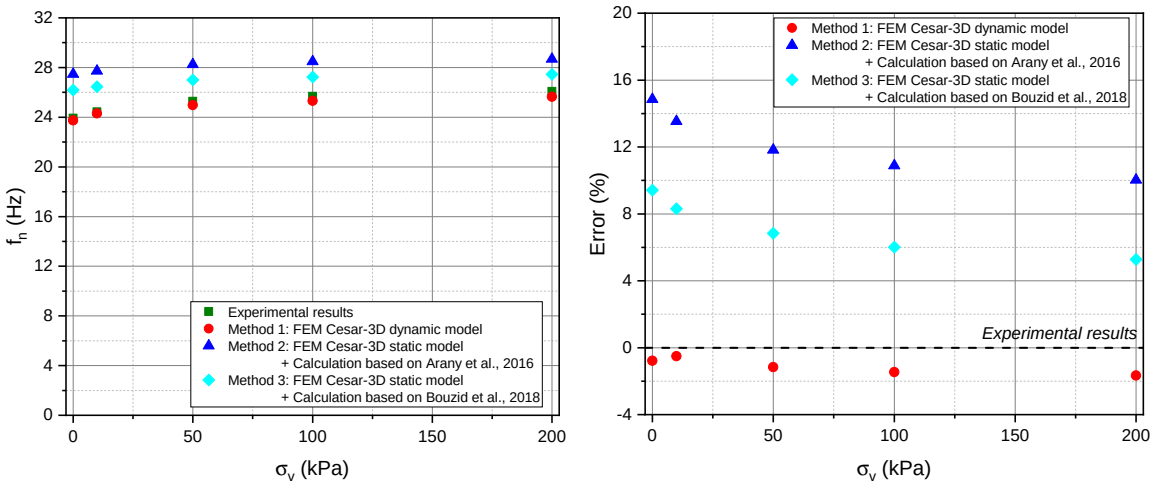

Fig. 4.16.: (a) First natural frequency of the scale model for different stress levels evaluated experimentally and by three alternative methods with (b) corresponding errors according to experimental results

This part of the study aims to certify the tools required for the prediction of the first natural frequencies of the scale models and the prototype, and the verification of the dynamic

similarity between them. This aim is satisfied by the validation of the performance of the dynamic *3D FEM Cesar-LCPC* model.

4.5.5 Application to the present study: "DTU 10 MW RWT" and scale models

After validation of the dynamic *3D FEM Cesar-LCPC* simulation in the previous section, similar models are carried out for the "DTU 10 MW RWT" supported by the two proposed foundations *F1* and *F2*, the scale model *M1*, and the scale model *M2*. Figure 4.17 presents the model geometry of "DTU 10 MW RWT" supported by the foundations *F2* and the corresponding scale model *M2*. Successive layers are modeled to increase the sand Young's modulus with the depth, according to Young's modulus profile defined in Equation 4.6. The void index and the density of the sand for the prototypes are respectively equal to 0.9 and $1660\ kg/m^3$, and the corresponding values for the scale models are respectively equal to 0.53 and $1550\ kg/m^3$. A Poisson's ratio equal to 0.3 is adopted for all cases. The models dimensions and the materials properties are available in Tables 2.15, 2.7, and 2.14 from Chapter 2. For all cases, *MODE* solver analysis is performed and the first natural frequency is obtained.

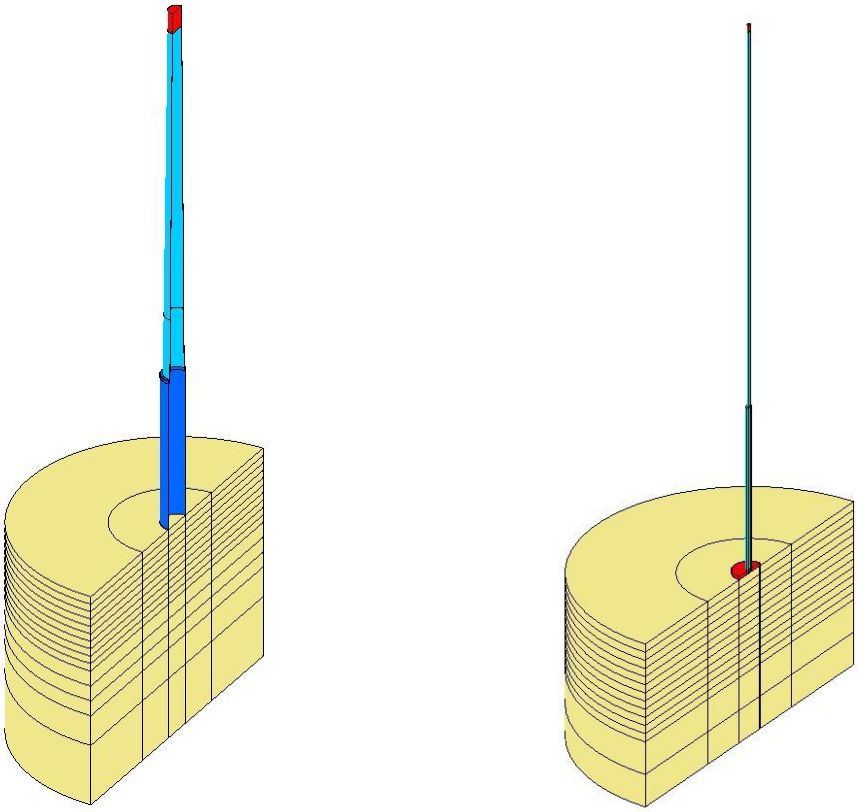

(a) (b)

Fig. 4.17.: *3D* dynamic models of (a) "DTU 10 MW RWT" supported by foundation *F2* and (b) scale model *M2*

Similarly, the first natural frequency is estimated by the methods 2 and 3, for which a static *3D FEM Cesar-LCPC* model is also performed. Besides, the natural frequency of the scale model *M2* is experimentally evaluated. All these results are presented in Figure 4.18.

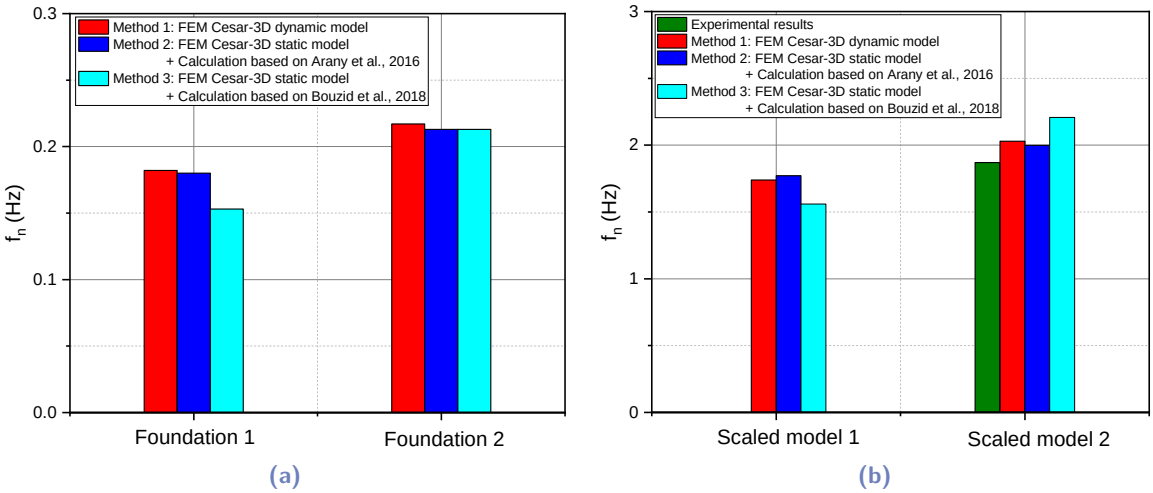

Fig. 4.18.: First natural frequencies obtained by different available methods for: (a) prototypes and (b) scale models

A good agreement is obtained between the findings of different methods, especially between the findings of the methods 1 and 2. The accordance with the experimental evaluation of the scale model *M2* verifies the validity of the dynamic *3D FEM Cesar-LCPC* model (relative error of $\sim 7.9\%$). In addition, the values obtained for the prototype are in a good agreement with the findings obtained by Alkhoury et al., 2021.

The first natural frequencies estimated for "DTU 10 MW RWT" supported by two types of foundations are depicted on a diagram containing the frequency spectrum for dynamic loads (Figure 4.19). It is shown that the two foundation-structure systems satisfy the design criterion associated with natural frequency at the installation. However, the systems are critically sensitive to any decrease in their natural frequency due to the small margin with the lower band of design limits. After the investigation of system natural frequency evolution in Chapter 5, corresponding conclusions and recommendations will be drawn and discussed.

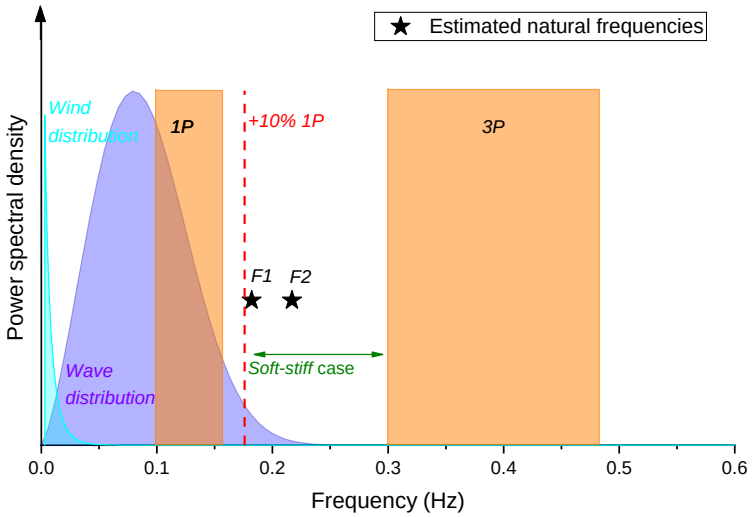

Fig. 4.19.: Frequency spectrum for dynamic loads acting on "DTU 10 MW RWT" and system natural frequencies for the two foundation cases

4.6 Dynamic similarity of the first mode of vibration

As the main purpose of this study, this section evaluates the dynamic similarity of the first mode of vibration between the "DTU 10 MW RWT" and the developed scale models. The first natural frequency estimated by the dynamic *3D FEM Cesar-LCPC* model for the two foundation cases is normalized according to the frequency scale factor and presented in Figure 4.20a. Figure 4.20b presents the relative error calculated between the full scale and the scale models, showing a satisfying similarity between them.

Furthermore, an impact response simulation is performed for the "DTU 10 MW RWT" supported by the foundation *F2* and the corresponding scale model *M2* to investigate the dynamic response similarity. The *Dyni* solver is available in *Cesar 3D* software and designed to compute the response of a system submitted to a dynamic load. It enables proceeding a step-by-step resolution of the following dynamic equilibrium equation:

$$[M]\{\ddot{X}(t)\} + [C]\{\dot{X}(t)\} + [K]\{X(t)\} = \{F(t)\} \tag{4.21}$$

where $\{X(t)\}$, $\{\dot{X}(t)\}$, and $\{\ddot{X}(t)\}$ are respectively vectors of nodal displacement, velocity, and acceleration as a function of time for a given model. $\{F(t)\}$ is the vector of imposed load as a function of time. $[M]$, $[C]$, and $[K]$ are respectively mass, damping and stiffness matrices of the model. Rayleigh-type damping matrix is defined, and takes the following form:

$$[C] = a[K] + b[M] \tag{4.22}$$

where a and b are two user-defined constants. The damping ratio of a mode of the system can be determined in function of natural frequency by the following equation:

$$\xi = \frac{a}{2w_n} + \frac{bw_n}{2} \qquad \text{with} \qquad w_n = 2\pi f_n \tag{4.23}$$

Knowing the first natural frequency of the system from the previous model, a and b are defined to obtain an equivalent modal damping ratio of 2% for the full scale and the scale model.

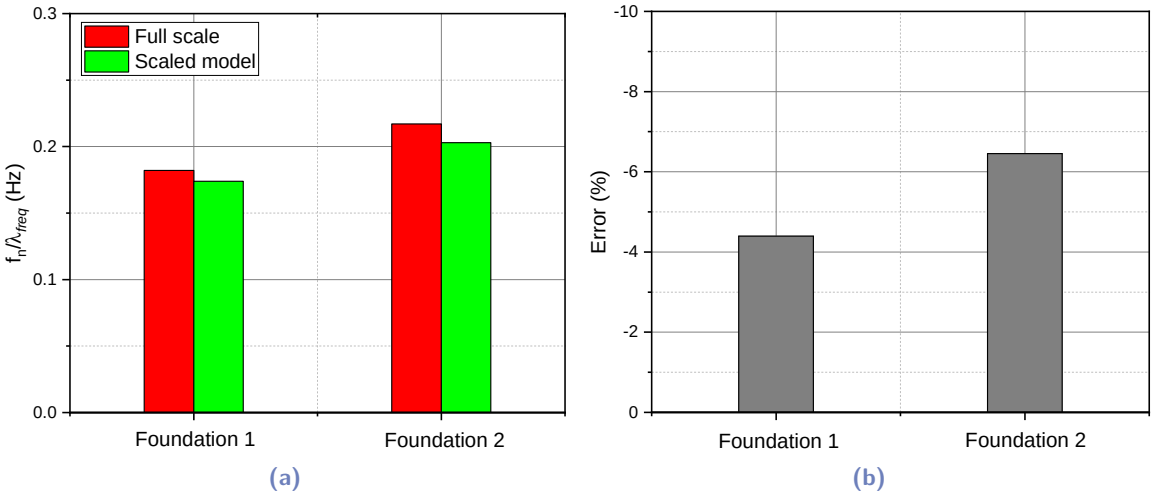

Fig. 4.20.: (a) Natural frequency similarity between "DTU 10 MW RWT" and corresponding scale models for the two foundation cases and (b) estimated error

The simulation time is equal to $250\ s$ for the full scale model and to $25\ s$ for the scale model. The obtained displacements are normalized by dividing by the maximum value and the time scale is normalized according to the corresponding scale factor ($\lambda_{time} = \sqrt{\lambda_L} = 1/10$; Section 2.3.1). Figure 4.21a presents the dynamic response at the top of the two models, showing a good similarity between them. Besides, the Fourier transforms of the dynamic responses are determined and normalized by dividing to the maximum value, and the frequency scale is normalized according to the corresponding scale factor ($\lambda_{time} = 1/\sqrt{\lambda_L} = 10$; Section 2.3.1). Figure 4.21b presents the Fourier transform, showing a good similarity between them.

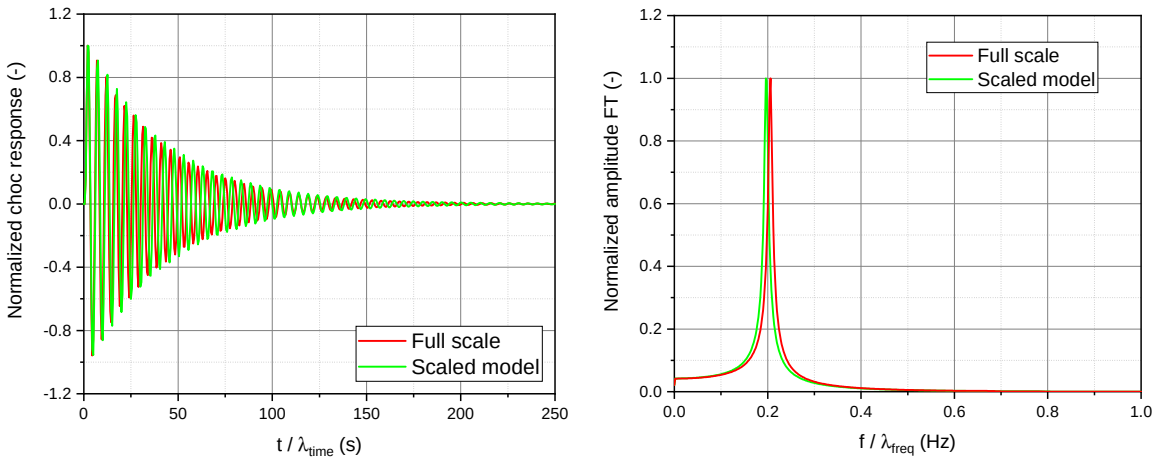

(a) (b)

Fig. 4.21.: (a) Shock response and (b) Fourier transform similarities between "DTU 10 MW RWT" supported by foundation *F2* and corresponding scale model *M2*

Finally, this section shows the validity of the proposed scale modelscale models to simulate, with high accuracy, the first vibration mode of offshore wind turbines at the laboratory scale.

4.7 Conclusion of the chapter

This chapter starts with a literature review of relevant scale models studying the cyclic response of offshore wind turbines. Then, it shows the capability and validity of the current testing setups and the corresponding procedures.

Besides, this chapter is based on numerical models to verify the dynamic similarity between the developed scale model and the prototype for the first mode of vibration.

5 On the cyclic response of offshore wind turbines

Based on the experimental and numerical tools presented and validated in Chapter 4, the cyclic response of the monopile foundation of offshore wind turbine is discussed in this chapter. Firstly, as the scale model ensures a dynamic similarity with the prototype for the first vibration mode, the inertial force is quantified at the model scale and compared to the method proposed by the design guides to consider the dynamic sensitivity. Then, the interplay between the monopile cyclic response and mechanisms occuring in the surrounding sand mass is discussed in the cases of force-controlled excitation and strain-controlled excitation. A numerical parametric study is also performed to enhance the understanding of the parameters governing the evolution of the first natural frequency of the system. Based on the results of the performed tests, the possibility of using higher frequencies during cyclic tests of the monopile is validated, which permits to reach higher numbers of cycles for a given testing time. Thus, the idea to reduce the testing time without affecting the dynamic response of the scale model is presented and verified numerically.

5.1 Performed cyclic test program

5.1.1 Strain-controlled experiments

According to the scaling laws presented in Section 2.3, cyclic force-controlled motion should be applied to the scale model at an equivalent eccentricity to simulate the environmental loads. Due to the dynamic similarity between the scale model and the prototype, the inertial force induced at the model scale will be equivalent to the inertial force induced at the prototype scale. This was the ideal loading concept envisaged in the experimental program. The *LinMot* motor which should ensure this task can be controlled in force by the intervention of an external force sensor or by the control of the supplied current.

However, due to some logistical issues and delays in the development of the motor control program, it was decided to launch some strain-controlled tests. Indeed, this is a straithforward task, since the *LinMot* motor is originally designed to produce this kind of motion. The motor is controlled by a specific program (*LinMot-Talk*), provided by the company, and has shown high performance and accuracy.

Referring to Section 4.1, relevant features of the cyclic response of offshore wind turbines are: (i) displacement accumulation, (ii) foundation stiffness and soil damping evolution, and (iii) evolution of the first natural frequency,... Controlling the strain during experiments can affect the response of the structure in an unrealistic manner. This is obviously the case regarding the displacement accumulation. Therefore, the findings will be cautiously interpreted to extract relevant conclusions.

5.1.2 Objectives and testing program

Limited by the strain-controlled motion, an adequate testing program is proposed to fulfill the following objectives:

- As seen in Section 4.1, most of the scale models adopt a loading frequency of 0.1 *Hz* to conserve the full-scale sand behavior. The conservation of this frequency limits the number of achievable cycles and thus the understanding of cyclic response in the long term.

  According to Peralta, 2010 following Gotschol, 2002, the inertial contribution (dynamic effect) in soil behavior can be neglected between 0 and 1 *Hz*, while it can be relevant between 1 and 10 *Hz* (Table 2.13). These values are approximative, and the findings available in the literature conflict with each other. The findings of numerous works based on element tests (e.g. triaxial tests) to investigate the effect of loading frequency can be found in Wichtmann, 2005, Zhu et al., 2021. Most of these works found that the effect of loading frequency becomes notable after exceeding a defined value, because of the contribution of inertial forces. However, the corresponding proposed value varies widely: 1 *Hz* proposed by Gotschol, 2002, 5 *Hz* proposed by Wichtmann, 2005, and 30 *Hz* proposed by Kempfert et al., 2000 at certain strain amplitude, while some works found a notable effect at relatively low frequencies (< 1 *Hz*; Mulilis et al., 1975). On another side, Zhu et al., 2021 shows that the inertial contribution is sensitive to test conditions (type of loading, saturation state of specimens).

  The scaling laws proposed in this study involve the adoption of a loading frequency of 1 *Hz*. This value is justified by the findings from available element tests, while it is still more reliable to investigate the loading frequency effect on the sand behavior around the monopile in realistic conditions (around laterally loaded monopile). To this aim, two tests were performed at the same conditions but varying the loading frequency: (i) 0.1 *Hz* as the full-scale case, and (ii) 1 *Hz* respecting the scaling laws proposed.

- Independent to the soil behavior, the proposed scale models simulate the dynamic response of *DTU 10 MW RWT*. The two tests proposed to investigate the effect of the loading frequency highlight the dynamic sensitivity of the structure. The inertial forces

induced can be quantified by comparing the quasi-static case ($f_{exc} = 0.1$ *Hz*) and the dynamic case ($f_{exc} = 1$ *Hz*).

- Show the repeatability of results following the proposed test procedure, as seen in Section 4.4.3.

- Verify the performance of the testing and monitoring systems under high numbers of cycles. It should be noted that the tests performed during the night allow a very high number of cycles to be reached.

- Identification of the phenomena underlying the cyclic response of the monopile foundation: sand densification and the formation of a subsidence cone around the monopile, affecting the foundation stiffness and the first natural frequency of the system.

Table 5.1 presents the characteristics of the three tests constituting the current test program.

Tab. 5.1.: Performed cyclic test program

Test Objective	Test identifier	Type of cycles (*mm*)	Frequency of excitation (*Hz*)	Number of cycles
Repeatability	C-R-1	Sinusoidal $+4/-2$	1.0	3500
Dynamic case*	C-D-1*	Sinusoidal $+4/-2$	1.0	50000
Quasi-static case	C-S-1	Sinusoidal $+4/-2$	0.1	10000

* The first 3500 *cycles* of C-R-2 are considered as a test of repeatability with C-R-1 (Section 4.4.3)

Figure 5.1 illustrates the curve of the motion applied by *LinMot* motor.

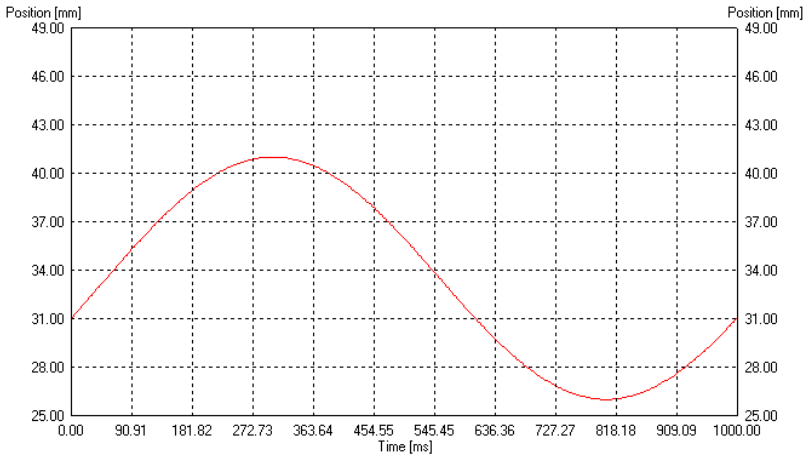

Fig. 5.1.: Imported curve to control *LinMot* motor

5.2 Presentation and interpretation of findings

5.2.1 Evaluation of dynamic contribution

As presented in Section 4.4.3, a force sensor is installed in contact with the structure to measure the force. The total force is measured by the force sensor in the quasi-static case ($f_{exc} = 0.1\ Hz$) since the motor is the unique source of the loading. However, in the dynamic case ($f_{exc} = 1.0\ Hz$), the increase of the excitation frequency induces inertial forces, which affect the amplitude of the force applied by the motor. The force to which the structure is subjected consists of two components: (i) the motor contribution and (ii) the inertial force (dynamic contribution).

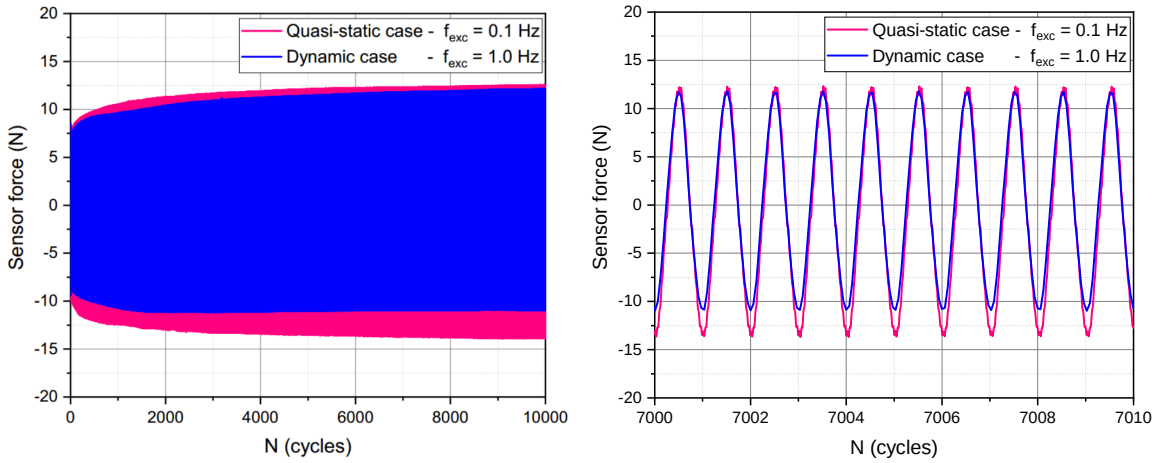

Fig. 5.2.: Output of the force sensor in quasi-static and dynamic cases: (a) $1 - 10000$ *cycles* (b) $7000 - 7010$ *cycles*

Figure 5.2 shows the force measured by the sensor in the two cases: (i) quasi-static and (ii) dynamic. As expected, the force contribution of the motor in the dynamic case is less than in the quasi-static case (it is recalled that the test is displacement-controlled). The dynamic contribution is estimated at different stages of cyclic test, showing an approximate constant percentage of 15% of the total force for these strain levels. As this percentage is determined based on two different tests and that it is relatively small, the origin of this discrepancy could also be due to the repeatability of the test. In order to remove any doubt, the dynamic contribution is validated by a new testing idea: During the same test, and after performing a high number of cycles, the force can be considered constant during a small number of cycles. 50 *cycles* are performed successively at three different excitation frequencies, which are respectively equal to 0.1 *Hz*, 0.5 *Hz*, and 1.0 *Hz*. The force measured by the sensor decreases with the increase of excitation frequency, highlighting the contribution of the inertial force (Figure 5.3). The excitation at 0.1 *Hz* is repeated to ensure the stability of total force and validate this conclusion.

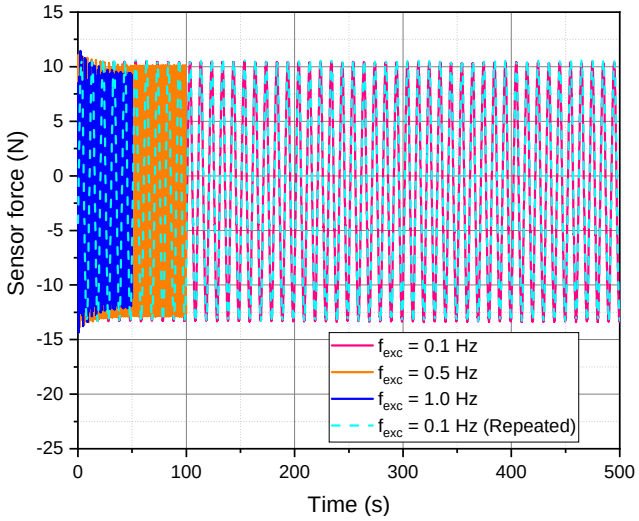

Fig. 5.3.: Variation of excitation frequency to validate the inertial force contribution

In the design methods, the dynamic contribution is considered by including a dynamic amplification factor applied to the wave loads acting on the offshore wind turbine. According to DNV-OS-J101, 2014, this factor can be calculated by the following expression:

$$DAF = \frac{1}{\sqrt{\left(1 - \left(\frac{f}{f_n}\right)^2\right)^2 + \left(2\xi\left(\frac{f}{f_n}\right)^2\right)^2}} \tag{5.1}$$

where f is the excitation frequency, f_n is the first natural frequency of the offshore wind turbine, and ξ is the modal damping ratio. The DNV-OS-J101, 2014 restricted the application of this factor to the cases where the natural period of the system is less than $2.5\ s$. Despite this condition, this method is adopted by Arany et al., 2017 for a conceptual design method of an offshore wind turbine with natural period equal to $\sim 4\ s$. In the current study, the environmental loads estimated for the case of foundation *F2* in Table 2.11 are re-calculated using the DAF methodology. A modal damping ratio of 1.5% is assumed, similar to that of the scale model, and the first natural frequency is the one estimated numerically in Chapter 4. The dynamic contribution obtained varies between 14 and 22% depending on the load scenario. These findings show a good agreement between the dynamic responses of the scale model and the prototype.

5.2.2 Soil densification and formation of subsidence cone

One of the principal phenomena observed during the lateral cyclic loading of monopile foundation is the formation of a subsidence cone around the monopile due to the sand densification. Figure 5.4 presents a photo of the subsidence cone that occurred after the test

C-S-1. In this study, a notable vertical displacement of the monopile is observed, which can be attributed to its relatively short embedded length and the mass of the structure.

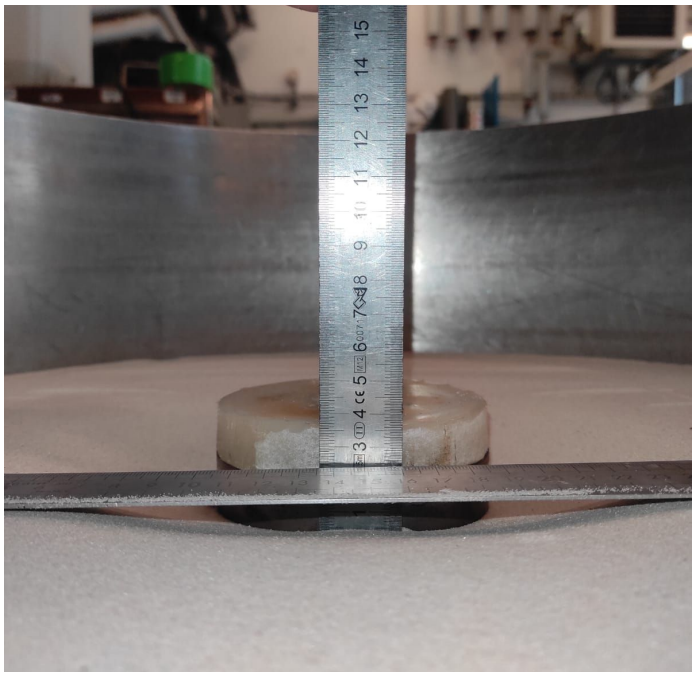

Fig. 5.4.: Photo of the subsidence cone formed around the monopile at the end of test C-S-1

The vertical displacement and the geometry of the subsidence cone formed after each test are measured and presented in Figure 5.5. The comparison of the two similar tests C-R-1 and C-D-1 shows that the densification mainly occurs within the first 10% of the cycles. This result is in agreement with the conclusion obtained by certain works highlighting the dominant effect of first few cycles in the evolution of soil stiffness (Li et al., 2010; Abadie, 2015; Zhang et al., 2020). The comparison of tests C-S-1 and C-D-1 reinforces this idea where similar subsidence cones are formed after 10000 and 50000 *cycles* respectively. Besides, Cuéllar, 2011 performed topographic measurements of the soil surface before and after cyclic loading. The measurements show that the sand densifies until a maximum density is reached, sooner or later depending on the magnitude of the loading.

This phenomenon significantly affects the first natural frequency of the system. The sand densification increases the foundation stiffness, leading to an increase in the first natural frequency. However, the formation of a subsidence cone around the monopile increases the free length of the structure and decrease the embedded length of the monopile foundation, which seems to decrease the first natural frequency. The coupling of these two phenomena depends on the foundation dimensions and properties. This issue will be the subject of the Section 5.3.

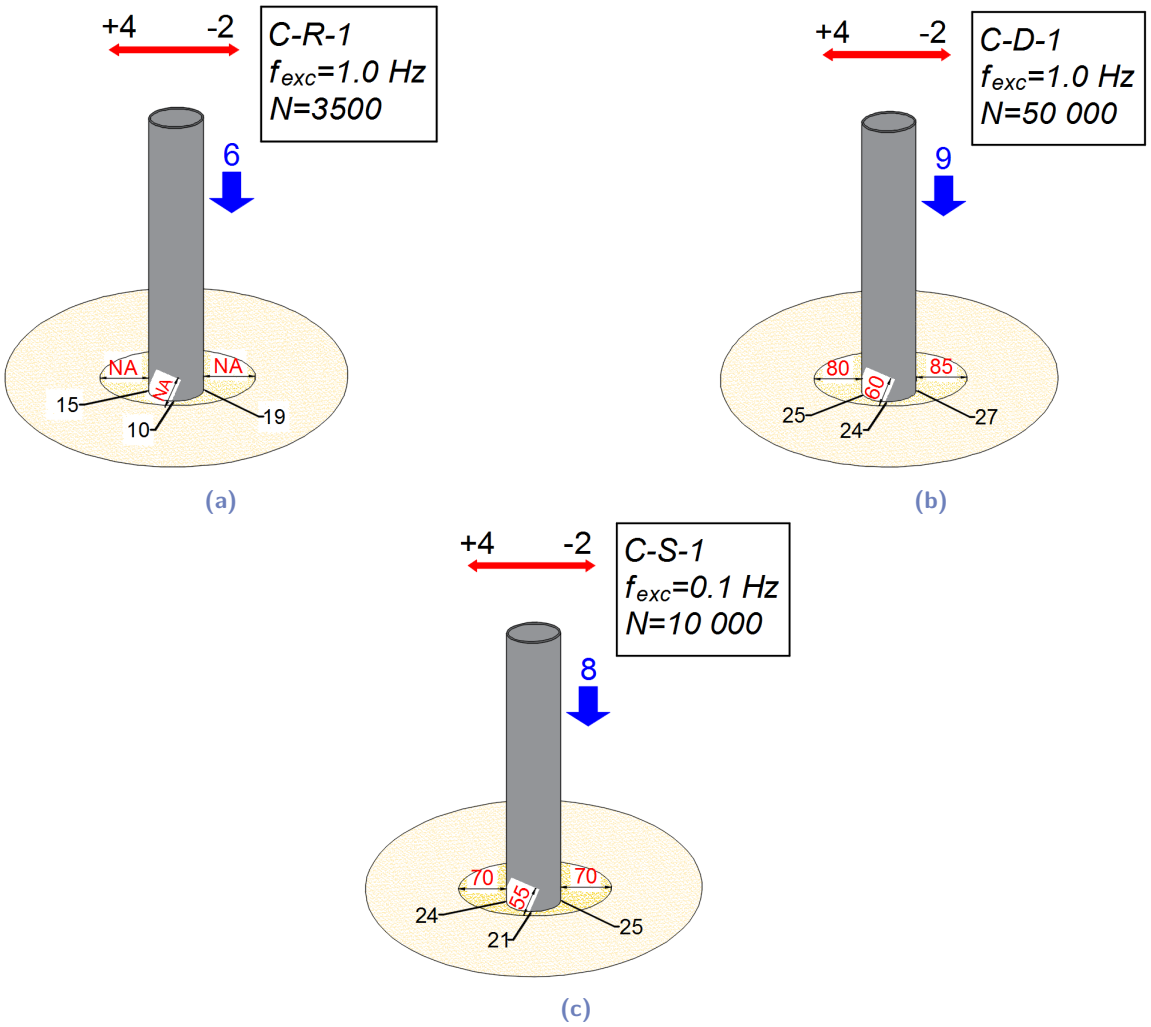

Fig. 5.5.: Vertical displacement (blue) and geometry of subsidence cone (red: horizontal spread, black: depth) around the monopile formed at the end of each test: (a) C-R-1 (b) C-D-1 (c) C-S-1 (all dimensions are in *mm*)

5.2.3 Actual strain-controlled motion

The strain-controlled motion applied to the structure is defined referring to an origin point defined before starting the test. The vertical displacement mentioned in Section 5.2.2 produces a small angle in the piece connecting the ball joint to the structure, leading to a decrease in its horizontal projection. Thus, the strain-motion applied to the structure is affected. The actual motion can be measured by an inclinometer placed at 29 *cm* above the sand surface, whose measurements are presented in Figure 5.6. It is found that the motion at this position varies from approximately $+0.3/-0.14°$ to about $+0.25/-0.19°$, corresponding to a shift of approximately $0.05°$ with respect to the initial motion. This shift does not affect the testing reliability since it occurred similarly in all performed tests, which ensures meaningful comparisons. In addition, it will not exist in the force-controlled loading tests, which is the ideal purpose of the proposed scale models.

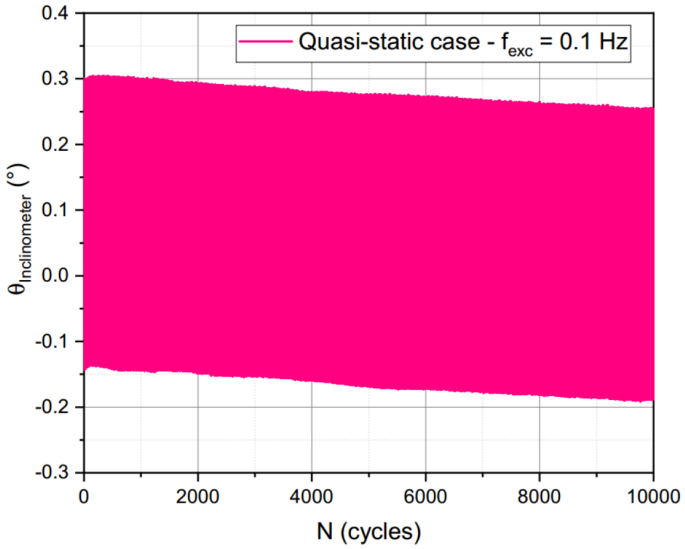

Fig. 5.6.: Actual motion imposed to the scale model *M2*

The transition piece and the tower of the scale model (brass rod and tube) bend under the effect of the applied motion, mainly in the tower part and at relatively high elevation. The strict consideration of this bending complicates the determination of the rotation and lateral displacement at the ground level. The assumption of a perfect rotation at the base of the transition piece permits the use of laser sensors to determine the monopile response at the ground level. This method leads to a relative error in the obtained results.

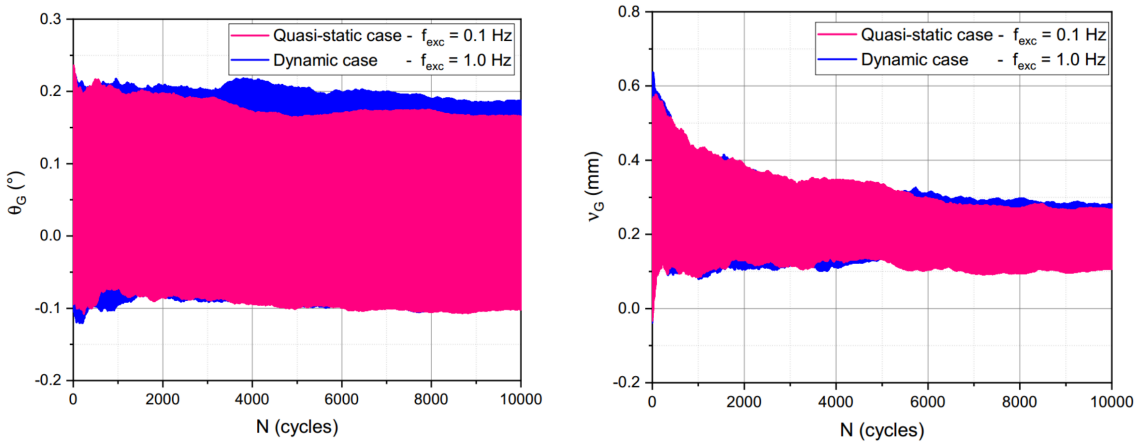

Fig. 5.7.: Evolution of (a) rotation and (b) displacement of the monopile foundation at the ground level with cycles number

A numerical model is carried out using *Cesar2D-LCPC* to evaluate this error. The following steps are applied: (i) different parts of the scale model are simulated by defining the corresponding properties; (ii) reasonable value of sand elastic modulus is adopted to simulate the sand response (Section 6.2.3); (iii) the known displacements and rotations at

different positions of the structure are imposed; (iv) lateral displacement at the ground level is obtained; (v) the obtained value is compared to that obtained by neglecting the bending at relatively low elevations, and it is found that the error did not exceed 4%. Then, the monopile lateral displacement and rotation at the ground level are determined assuming a perfect rotation at the base of the transition piece. The results are presented in Figure 5.7.

5.2.4 Monopile cyclic response

Understanding the mechanisms occurring within the sand surrounding the monopile under cyclic loading is an essential step in the investigation of the monopile cyclic response. The sand densification and the formation of a subsidence cone around the monopile are evidently considered as two principal phenomena accompanying the cyclic response. Cuéllar, 2011 studied these mechanisms using topographic measurements and colored markers, and found that the sand exhibits two main phases: a *densification-dominated phase* and a *convection-dominated phase*. Cuéllar, 2011 also considered that the opening of a small gap at the soil-pile interface is a key element in the occurrence of grain migration and the establishment of a convective cell (Figure 5.8).

Fig. 5.8.: Photo of the subsidence cone and the sand convection cell formed around the monopile after a cyclic test (from Cuéllar, 2011)

Besides, Truong et al., 2018 considered that the residual (locked-in) net lateral stresses induced by cyclic loading are a reflection of the changes in boundary conditions around the monopile (soil-pile gaps and sand densification).

In parallel, LeBlanc et al., 2010 and Arshad and O'Kelly, 2016 performed symmetrical cyclic loading ($\zeta_c = -0.98/-1$) and found rotation accumulation in the direction of the first loading. This finding highlights the primordial effect of the first cycle on the cyclic response. In the force-controlled cyclic loading, the first gaps formed behind the principal loading direction and the resulting arrangement of sand can be related to the displacement

accumulation phenomenon. This idea can be reinforced by the experimental observations showing the localization of the major subsidence cone behind the principal loading direction (Liang et al., 2020). The changes that occurred in this subsidence zone will resist the loading applied in the secondary direction, leading to favor the displacement accumulation in the principal loading direction. This idea is conceptually presented in Figure 5.9. Furthermore, this assumption is able to justify the fact that an asymmetric two-way loading is the most defavorable, being the case inducing the largest subsidence zone behind the principal loading direction.

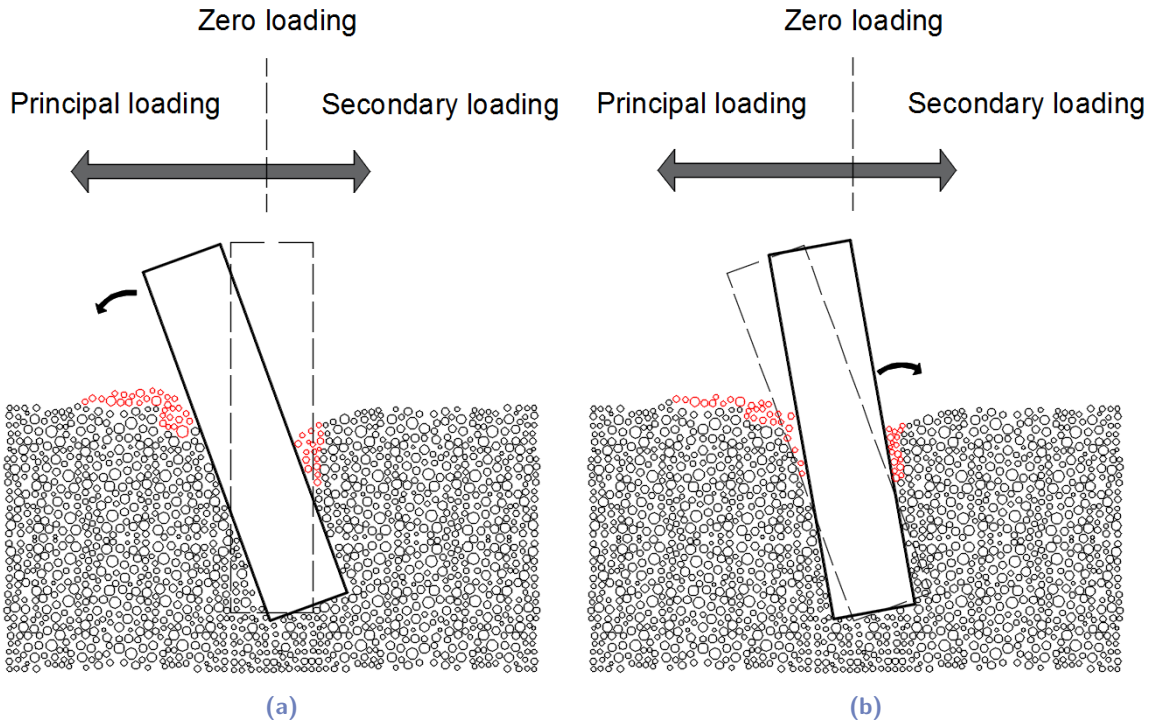

Fig. 5.9.: Conceptual idea leading to gaps formation and sand rearrangement during cycling

As mentioned before, in force-controlled cyclic loading, mechanisms occuring within the sand around the monopile are manifested in the accumulation of displacement and the increase in the soil stiffness. In strain-controlled cyclic motion, similar mechanisms are shown around the monopile: sand densification and formation of subsidence cone. However, as the motion is imposed, the phenomenon of displacement accumulation is restrained. The lateral displacement evolution at the ground level is determined in Section 5.2.3, showing a decrease with cycles number (Figure 5.7b). This decrease is a reflection of the variation in the rotation pivot of the monopile, which is determined and presented in Figure 5.10a. A schematic illustrating this phenomenon is displayed in Figure 5.10b. Figure 5.7b showed that the decrease in the ground displacement occurred firstly in the secondary motion direction, followed by the principal direction. This finding is also shown in Figure 5.10a, where the increase in the pivot level occurred mainly in the 100 first cycles for the trough motion (corresponding to a displacement of $-2\ mm$) and then occurred for the peak motion (corresponding to a displacement of $+4\ mm$). This behavior can be directly related to the

development of the subsidence zones around the monopile: (i) major subsidence zone formed behind the principal direction leading to a fast increase in the trough pivot level, and (ii) imposed motion and high number of cycles caused sand densification and formation of a relatively late subsidence cone leading to an increase in the peak pivot level.

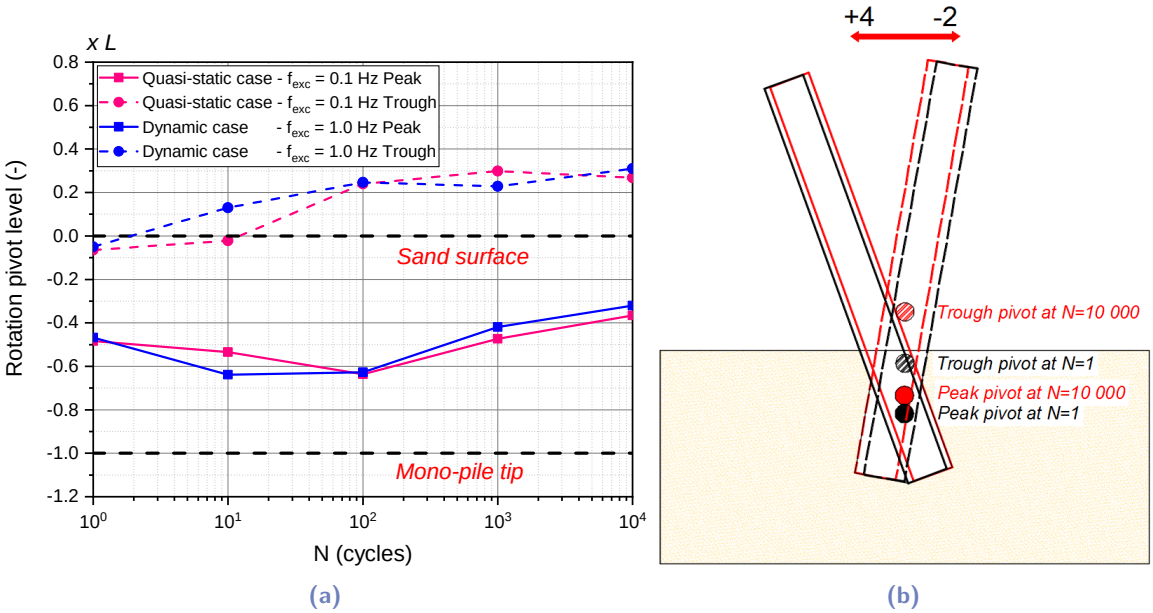

Fig. 5.10.: (a) Evolution of the position of the center of rotation of the monopile (pivot) with cycles number, (b) Representative schematic at $N = 1$ and $N = 10000$

In conclusion, the sand mechanism under strain-controlled cyclic motion is manifested by a variation in the position of the rotation pivot, leading to a decrease of the displacement at ground level due to the changes in the boundary conditions around the monopile (sand densification and subsidence zones).

5.2.5 Foundation stiffness evolution

Similar to the findings in the literature for the force-controlled loading, the sand densification around the monopile leads to an increase in the foundation stiffness in strain-controlled motion. Figures 5.11a and 5.11b present the static moment (read by the force sensor) in function of ground rotation of the monopile during some cycles, showing an increase of the secant stiffness with cycles number in the two cases: (i) quasi-static and (ii) dynamic motion. Besides, in agreement with the findings of Abadie et al., 2019, variation in the loop shape with cycles number is observed, reflecting the decrease in the soil damping. It should be noted that the vertical displacement becomes significant after a high number of cycles, which affects the resistance force measured (becomes relatively inclined and higher) and can affect the shape of the loop. This issue can be solved by replacing the ball joint with a double universal joint. The quantitative findings should be revised, while qualitatively, this issue is accepted since it is consistently occurring in the two cases.

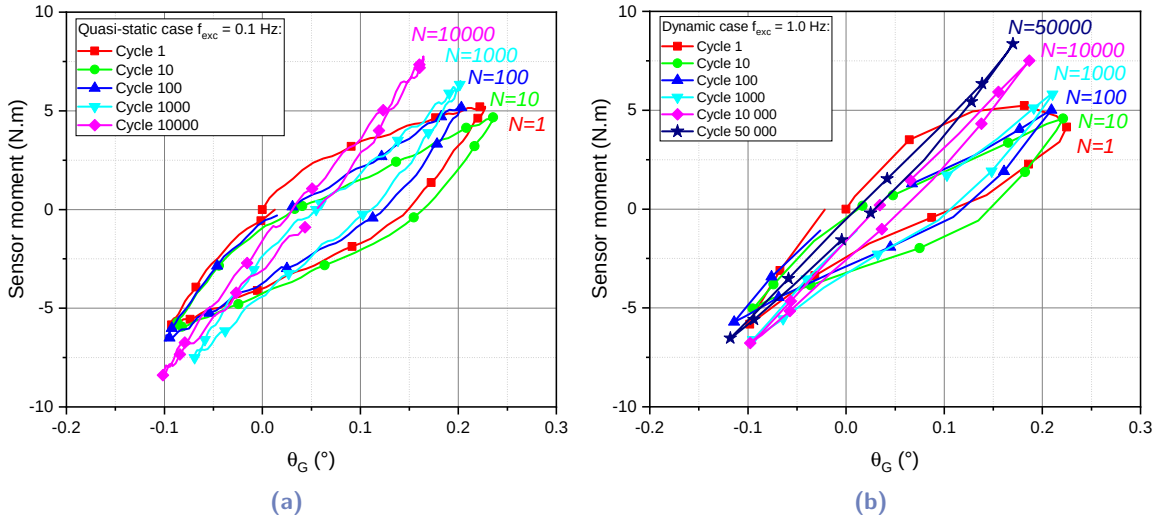

Fig. 5.11.: Static moment in function of ground rotation of the monopile during some cycles at different stages of cyclic test: (a) quasi-static case, (b) dynamic case

The evolution of the corresponding secant stiffness with cycles number is determined and presented in Figure 5.12. In the dynamic case, the secant stiffness is initially determined using the static moment before the consideration of the dynamic contribution by applying a factor corresponding to a percentage of 15%, quantified in Section 5.2.1. A good agreement is found between the global secant stiffness in quasi-static and dynamic cases, showing the similarity of the sand response. The deviation in the first cycle is attributed to the shock response of the scale model that occurred at the beginning of the test due to its dynamic sensitivity.

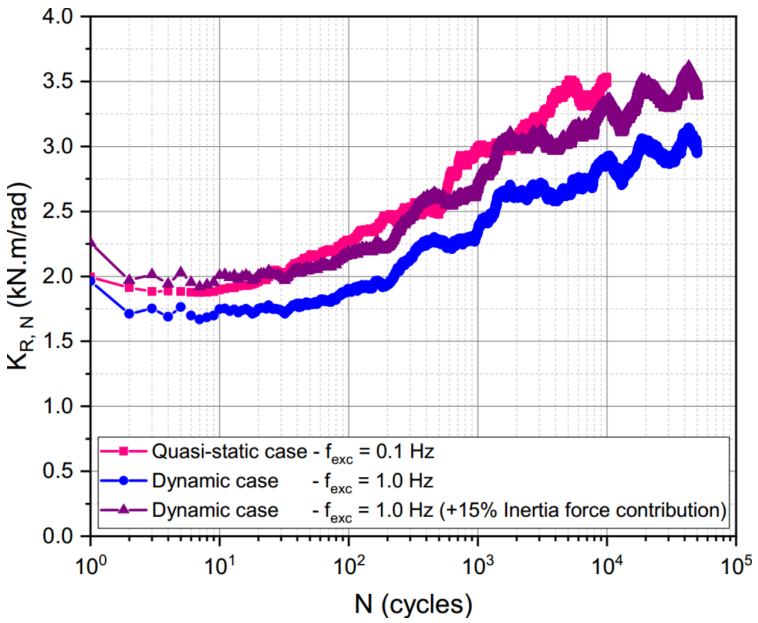

Fig. 5.12.: Evolution of monopile secant stiffness with cycles number

5.2.6 Quasi-static/dynamic responses similarity

Based on the previous sections, the similarity between the sand response in quasi-static ($f_{exc} = 0.1\ Hz$) and dynamic ($f_{exc} = 1.0\ Hz$) cases is clearly demonstrated and is manifested in different terms:

- Figures 5.7a and 5.7b show the similarity of the displacement and rotation evolution with cycles number at the ground level (Section 5.2.3).
- Figure 5.10a shows the similarity of the variation of the position of the rotation pivot with cycles number (Section 5.2.4).
- Figures 5.11 and 5.12 show the similarity of the evolution of secant stiffness and variation of loops shape with cycles number (Section 5.2.5).
- The comparison of the geometry of the subsidence cone obtained after a high number of cycles in the two cases, and based on the result of Cuéllar, 2011 stating that the development of the subsidence cone reaches a steady-state, constitutes another similarity (Figure 5.5; Section 5.2.2).

All these findings validate the use of a loading frequency of $1\ Hz$ in the scaling laws proposed in this study (Section 2.3) and justify the possibility of choosing a higher loading frequency in similar scale models to reduce the cyclic testing time or reach a higher number of cycles for a given testing time.

5.3 Natural frequency evolution

The phenomena investigated under cyclic loading have a direct effect on the evolution of the first natural frequency of the system. This evolution should be understood and evaluated to ensure the stability of the offshore wind turbine during exploitation. The two principal phenomena affecting the natural frequency are the sand densification (generally considered as an increase in the foundation stiffness) and the formation of a subsidence cone around the monopile.

According to experimental findings in this domain, Yu et al., 2015 and Liang et al., 2020 found that the natural frequency increases until reaching a peak at a certain number of cycles, followed by a decrease until the end of the test. It was also found that the number of cycles required to reach the peak depends on the loading amplitude. Yu et al., 2015 related these two phases to the behavior of the sand mass introduced by Cuéllar, 2011: the increase in the natural frequency is attributed to the *densification-dominated* mechanism,

and the followed decrease is attributed to the *convection-dominated* mechanism. Liang et al., 2020 similarly attributed the increase of the natural frequency to the *densification-dominated phase* while assuming that a slight decrease is caused by sand dilatancy and that a large drop is caused by the generation of a subsidence zone.

In the current study, the evolution of the first natural frequency will be determined and interpreted according to the phenomena underlying the cyclic response of the monopile. Inspired by the experimental findings, a numerical simulation is carried out, using the *3D FEM Cesar-LCPC* models validated in Chapter 4, to perform a parametric study assisting in the comprehension of this problem.

5.3.1 Experimental results and discussion

The first natural frequency of the scale model *M2* was experimentally evaluated before and after each cyclic test. The adopted method is presented and validated in Section 4.4.2. The obtained results are presented in Table 5.2.

Tab. 5.2.: First natural frequency of the scale model *M2* before and after cyclic tests

Test identifier	Number of cycles	Initial natural frequency (*Hz*)	Final natural frequency (*Hz*)	Natural frequency variation (%)
C-R-1	3500	1.874	1.877	$+0.16\%$
C-D-1	50000	1.875	$-^*$	$-^*$
C-S-1	10000	1.856	1.842	-0.75%

* Missed results

According to Section 5.2.6, the similarity of the three tests can be considered, which permits to identify the effect of the number of cycles on the evolution of the first natural frequency. The comparison of the initial natural frequencies obtained for the three tests shows the repeatability in the preparation of the tested scale models (standard deviation approximately equal to $\sim 1\%$). The test C-R-1 shows a slight increase of the first natural frequency after 3500 *cycles* while the test C-S-1 shows a notable decrease after 10000 *cycles*. These findings are in good agreement with those obtained by Yu et al., 2015 and Liang et al., 2020. However, in this study, the decrease in the first natural frequency is accompanied by an increase in the foundation stiffness as shown in Section 5.2.5, which contradicts the assumption of Yu et al., 2015 and Liang et al., 2020 attributing the decrease of the first natural frequency to the mechanisms occuring within the sand mass (convection-dominated phase or dilatancy). Furthermore, Section 4.1 summarizes the findings of numerous experimental works studying the evolution of the foundation stiffness without noticing any decrease after high numbers

of cycles. In addition, the attribution of the drop in the natural frequency to the generation of the subsidence zone seems to be an invalid justification, since the subsidence zone is mainly generated at the beginning of the test due to the relative loose sand state (Figure 5.5; and Cuéllar, 2011).

The effect of the combination of the two phenomena (sand densification and subsidence cone formation) seems to be the unique valid justification for the evolution of the first natural frequency.

5.3.2 Numerical parametric study

As seen before, the first natural frequency of the offshore wind turbine is affected by the coupling of several phenomena underlying the cyclic response of the monopile foundation. A parametric study has been carried out to evaluate the effect of each phenomenon taken separately and their combination. This study is based on the *3D FEM Cesar-LCPC* models, validated in Chapter 4, simulating the *DTU 10 MW RWT* supported by two types of foundation (*F1*: semi-rigid foundation; *F2*: perfectly-rigid foundation). The full-scale model is considered for two reasons: (i) the availability and relative reliability of the sand parameters at relatively high confining stresses; (ii) obtaining more significant results directly at the full-scale. The range of parameters variation adopted is based on the experimental observations and the available similar studies in the literature (e.g. Cuéllar, 2011; Arany et al., 2017...)

Soil stiffness effect

The mechanisms within the sand mass around the monopile cause a variation in the soil stiffness. This variation is simulated numerically by a variation in the soil elastic modulus. In the two cases of foundations, *MODE* analyses were applied using the dynamic *3D FEM Cesar-LCPC* model of the *DTU 10 MW RWT* to determine their first natural frequency for different soil elastic modulus. The variation of the natural frequency as a function of soil stiffness variation is determined and presented in Figure 5.13.

It is remarked that the first natural frequency of the system is more sensitive to the softening than to the hardening of the soil modulus. In parallel, the soil softening has slightly more impact in the case of the perfectly-rigid monopile, while the soil hardening has slightly more impact in the case of the semi-rigid monopile.

Based on experimental findings, sand densification is encountered, leading to an increase in the foundation stiffness, which reflects as an increase in the first natural frequency of the system.

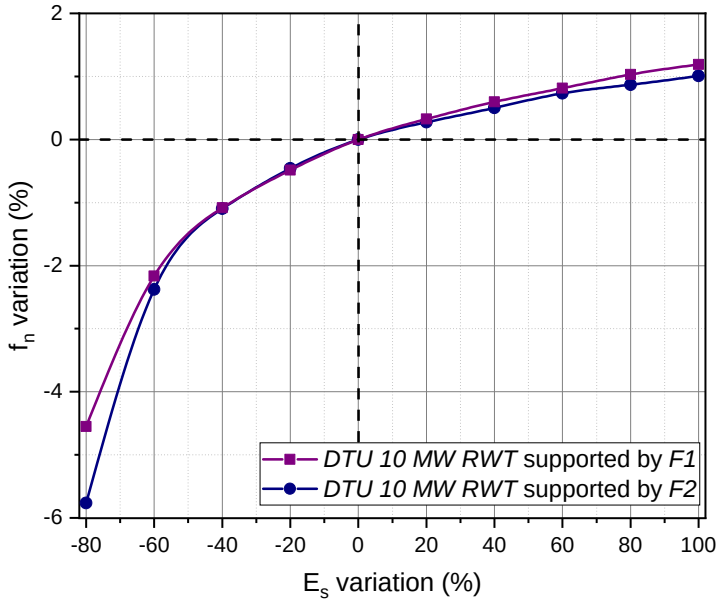

Fig. 5.13.: *DTU 10 MW RWT* natural frequency variation as a function of the soil stiffness variation

Subsidence cone formation

The mechanisms occurring within the sand mass around the monopile cause the formation of a subsidence cone, in addition to the hydrodynamic scour phenomena occurring under field conditions. The formation of this subsidence cone causes an increase in the free length of the structure, and a decrease in the embedded length of the monopile which reduces the foundation stiffness, leading to a decrease in the first natural frequency. The subsidence cone is simulated numerically by the inactivation of a soil layer at the top of the soil mass, as this study regards the natural frequency variation only (not the monopile response which can be affected by form of the scour shape; Li et al., 2020). For the two types of foundations, *MODE* analyses is applied using the dynamic *3D FEM Cesar-LCPC* model of the *DTU 10 MW RWT* to determine their first natural frequency for different subsidence cone depths. The variation of the natural frequency as a function of the subsidence cone depth is determined and presented in Figure 5.14a.

The dimensionless subsidence cone (s/D; where s is the subsidence cone depth and D is the monopile diameter) is more relevant to represent the effect of the subsidence cone formation. Therefore, the variation of the first natural frequency as a function of the dimensionless subsidence cone depth is depicted in Figure 5.14b.

It can be noted that the subsidence cone formation has more impact in the case of the semi-rigid monopile. Besides, as the range of subsidence cone depth simulated is inspired from experimental observations, its impact seems to be considerable in comparison with the effect of the soil stiffness increase.

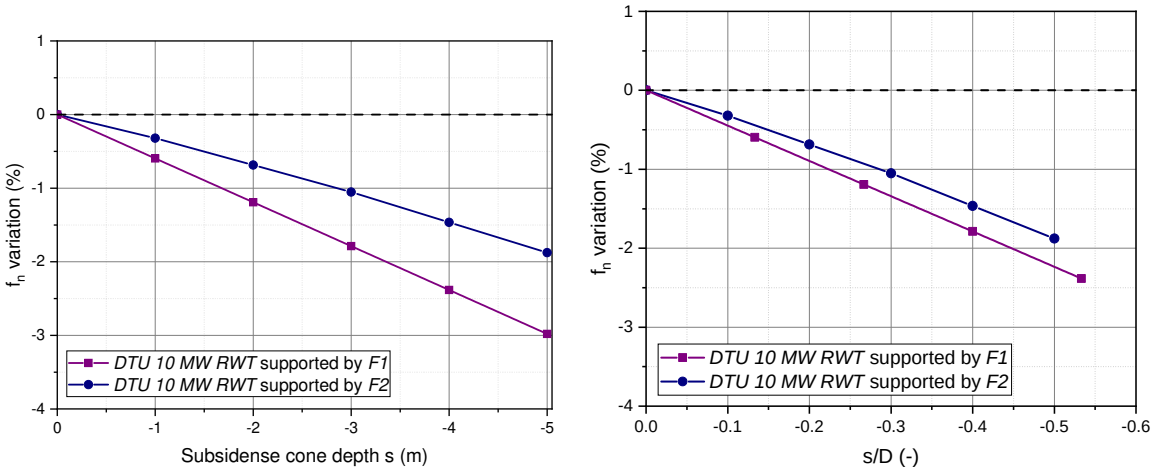

Fig. 5.14.: Variation of the first natural frequency of *DTU 10 MW RWT* as a function of (a) the subsidence cone depth, and (b) the dimensionless subsidence cone depth

5.3.3 Combination of soil stiffness change and subsidence cone formation effects

Actually, the sand densification causes the increase of the soil stiffness and the formation of the subsidence cone simultaneously, and the coupling of their effects controls the evolution of the first natural frequency of the system. A reasonable combination of the two phenomena is inspired from the experimental findings: each $1\ m$ of subsidence cone depth is combined with an increase of 20% in the soil stiffness (Section 5.2.5 shows an increase of the foundation stiffness with a factor of ~ 1.7 corresponding to a subsidence cone depth of $\sim 25\ mm$ for the scale model, equivalent to $2.5\ m$ at the full scale). This assumption aims to obtain a qualitative idea about the effect of the combination of the two phenomena. *MODE* analyses is applied using the dynamic *3D FEM Cesar-LCPC* model of the *DTU 10 MW RWT*, for the two types of foundations, to determine their first natural frequency for different combinations. The variation of the first natural frequency as a function of the corresponding combinations is determined and presented in Figure 5.15.

In the case of semi-rigid monopile, the first natural frequency directly decreases with the evolution of the assumed combination. However, in the case of perfectly-rigid monopile, a slight increase is initially obtained, followed by a decrease in the first natural frequency with the evolution of the assumed combination. This finding highlights the effect of the foundation properties in the evolution of the system first natural frequency. On another side, it seems that the numerical and experimental findings are in accordance, showing the tendency of the first natural frequency of the system to decrease according to the combination of the phenomena that occur around the monopile.

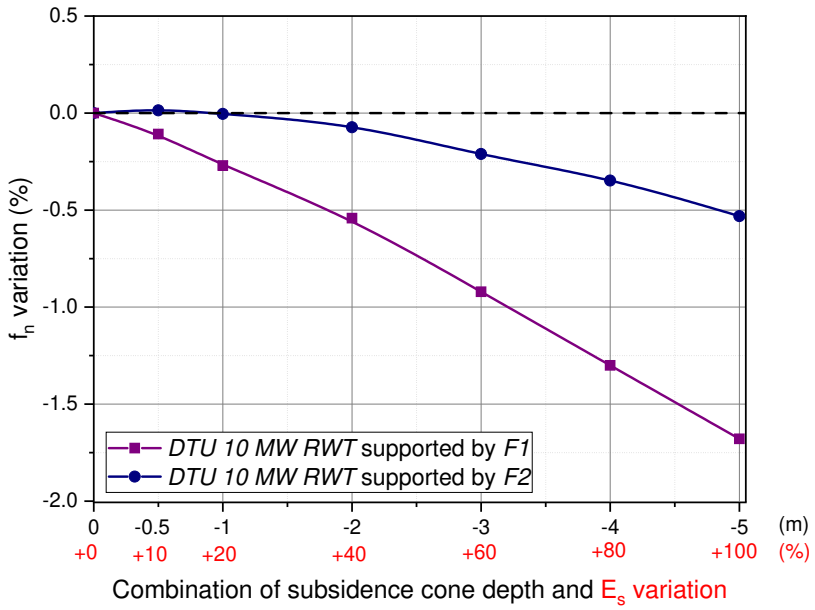

Fig. 5.15.: Variation of the first natural frequency of *DTU 10 MW RWT* as a function of the combination of soil stiffness variation and subsidence cone depth

The decrease in the first natural frequency is generally attributed to a decrease in the foundation stiffness (Yu et al., 2015, Cui and Bhattacharya, 2016, Liang et al., 2020). Aiming to disprove this proposition, the effect of the phenomena combination on the foundation stiffness is determined in the case of perfectly-rigid monopile. The method presented in Section 4.5.3 of Chapter 4 is adopted: the foundation is represented by three springs and the stiffness of these springs is determined by the application of two lateral loads at different eccentricities in a static *3D FEM Cesar-LCPC* model and by analyzing the obtained results. The variation of the foundation stiffness and the corresponding variation of the first natural frequency of the system are presented in Figure 5.16.

It is clearly seen in Figure 5.16 that the increase of the foundation stiffness can be accompanied by a stabilization or decrease in the first natural frequency of the system, which justifies the experimental observations. Besides, this finding highlights the dominance of the subsidence cone formation in the evolution of the first natural frequency of the system. Referring to the analytical methods presented in Chapter 4 to estimate the first natural frequency, the complex coupling between soil, monopile, and foundation properties to specify the first natural frequency of the system is shown.

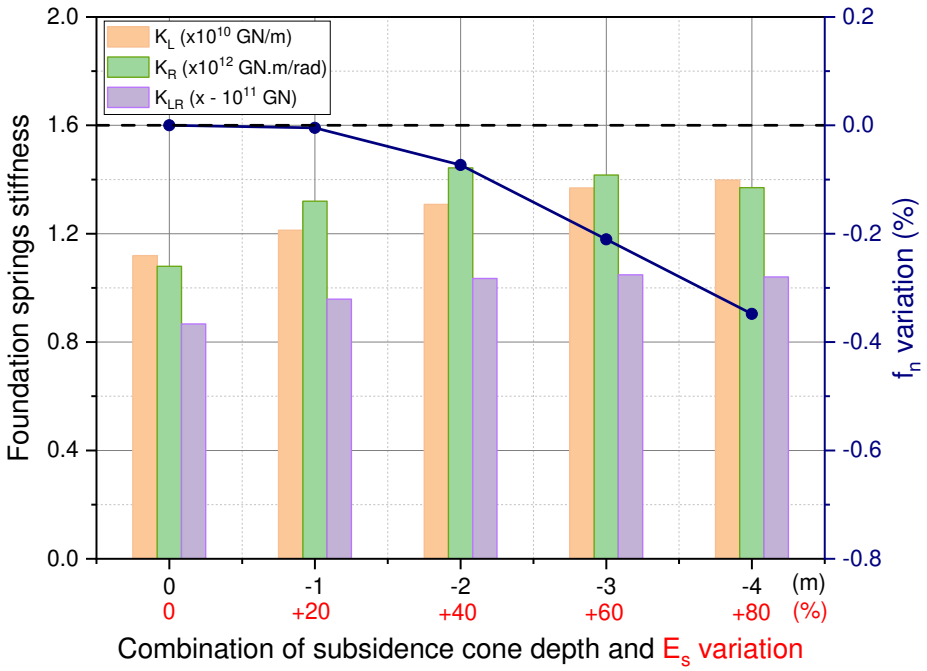

Fig. 5.16.: Variation of the foundation stiffness (*F2*) and the corresponding first natural frequency of *DTU 10 MW RWT* as a function of the combination of the soil stiffness variation and the subsidence cone depth

This finding also leads to the necessity to cautiously ensure a dynamic similarity between the prototype and the scale models regarding the evolution of the first natural frequency. The global approach to the problem is clarified in Figure 5.17 and by the following points:

- The two principal parameters affecting the first natural frequency of the system are the free length of the structure and the foundation stiffness.

- The subsidence cone formation increases the free length of the structure, imposing a reduction in the first natural frequency.

- The subsidence cone formation decreases the embedded length of the monopile foundation, which leads to a decrease in the foundation stiffness. However, this phenomenon is accompanied by an increase in the foundation stiffness (increase in soil stiffness). The coupling of these two phenomena controls the evolution of the foundation stiffness, depending on the soil and monopile properties. Based on experimental and numerical findings in this domain, the dominant phenomenon seems to be the sand densification, manifesting as an increase in the foundation stiffness with cycles number.

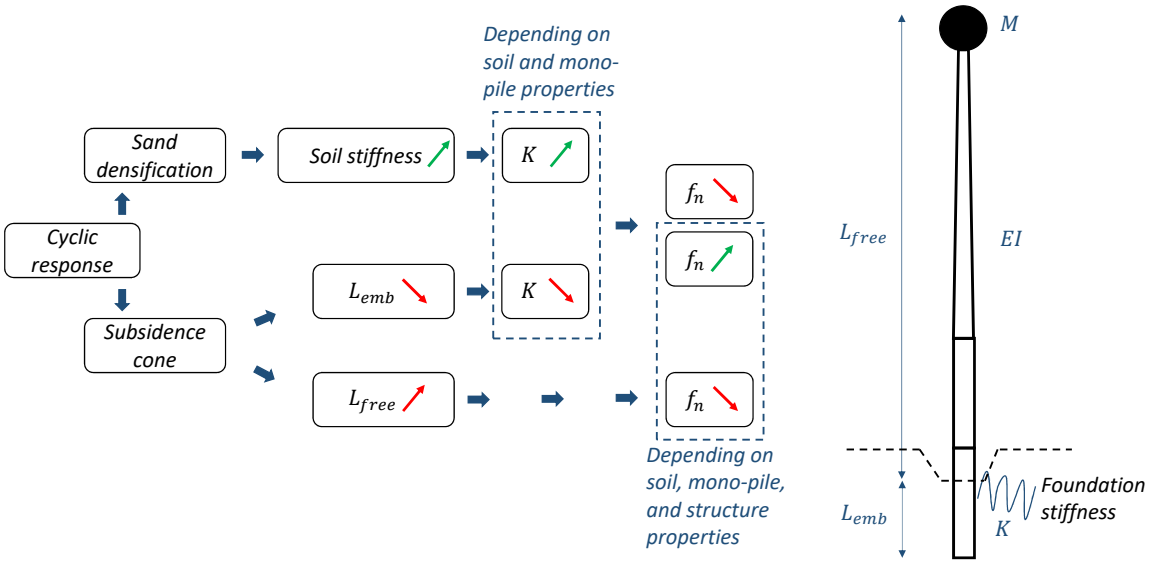

Fig. 5.17.: Effect of the phenomena underlying the cyclic response on the first natural frequency of an offshore wind turbine

- In the case of a decrease in the foundation stiffness and an increase in the structure free length, the first natural frequency will evidently decrease. However, in the case of an increase in the foundation stiffness and an increase in the structure free length, the evolution of the first natural frequency is controlled by the coupling of their impacts, depending on the soil, monopile, and structure parameters. Based on the experimental and numerical findings for rigid monopiles, the first natural frequency seems to increase for limited subsidence cone depth before decreasing for more severe subsidence cone depths despite the increase in the soil stiffness. This assumption can justify the drop in the first natural frequency at high loading amplitude remarked by Yu et al., 2015 and Liang et al., 2020.

This parametric study can be generalized to consider also the hydrodynamic scouring phenomena. This phenomena is tackled by numerous studies: Prendergast et al., 2015, Askarinejad et al., 2019, Mayall et al., 2020, Li et al., 2020. . . , showing its significant effect on the natural frequencies variation of the system.

5.4 Proposal for accelerating cyclic tests

The current study validates the use of an excitation frequency of 1 *Hz* without affecting the cyclic sand response. This finding permits to reduce the testing duration by ten, while the use of higher frequencies is still interesting to reach a higher number of cycles. As the current scale models are dynamically sensitive, the increase of the excitation frequency affects the inertial forces transferred to the monopile foundation, in addition to the possibility of

affecting the sand behavior. Aiming to outcome the challenge of the dynamic sensitivity of the scale model, an idea is presented and numerically validated in this section.

5.4.1 Concept

The contribution of the inertial forces depends on the mode shape of the structure at the excitation frequency, the amplitude of the acceleration, and the phase between the excitation and the response of the structure. The idea proposed aims to increase the excitation frequency of the cyclic tests without affecting the dynamic force contribution. It consists in exciting the scale model with higher frequencies so as to induce the same impact of the inertial forces on the monopile foundation. Figure 5.18 shows the modulus and phase of the FFT of accelerometer measurement obtained by the testing procedure adopted to evaluate the natural frequencies of the scale model *M2* (Section 4.4.2). According to the scaling laws, an excitation of 1 *Hz* represents the realistic case. Starting from this frequency, the scale model should be excited by higher frequencies and the corresponding monopile response should be evaluated. The application of this method experimentally involves many difficulties and seems to be a complex work. In a first approach, the dynamic *3D FEM Cesar-LCPC* model validated in Chapter 4 can take on this task. Once the range of the appropriate frequency is estimated numerically, this idea can be verified experimentally. In this study, since the developed system is not designed for high frequencies, this idea is only applied and validated numerically.

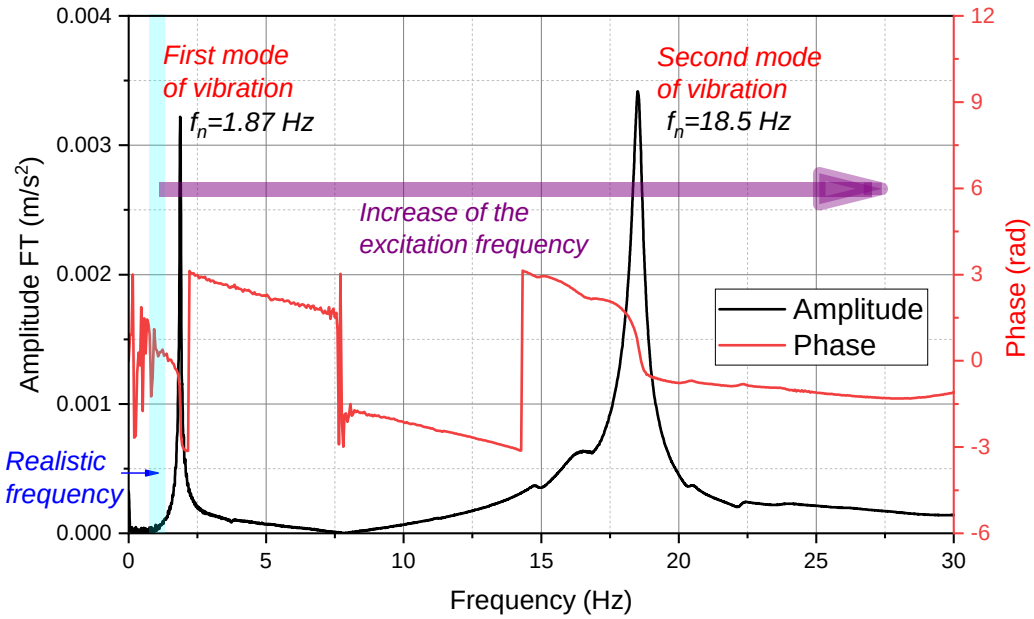

Fig. 5.18.: FFT modulus and phase of the acceleration response of the scale model *M2* and indication to increase the excitation frequency of cyclic tests

5.4.2 Numerical results

Based on the numerical model validated in Chapter 4, a symmetrical sinusoidal force of ± 4 N is applied to the scale model *M2* at an eccentricity of 620 mm. The loading frequency range is between 0.1 and 25 Hz, and the reaction of the monopile foundation is investigated. Each loading cycle is composed of 12 increments. Figure 5.19a presents the monopile profile at the peak of the tenth cycle for some frequencies. It is found that the excitation of the scale model with a frequency of 8 Hz almost leads to a similar response to that obtained with a frequency of 1 Hz. Besides, depending on the dynamic contribution, a frequency of 1.5 Hz causes higher strain, while a frequency of 5 Hz leads to lower strain. The similarity of the monopile responses obtained for excitation frequencies between 1 and 8 Hz is checked along other cycles as a function of increments (Figure 5.19b).

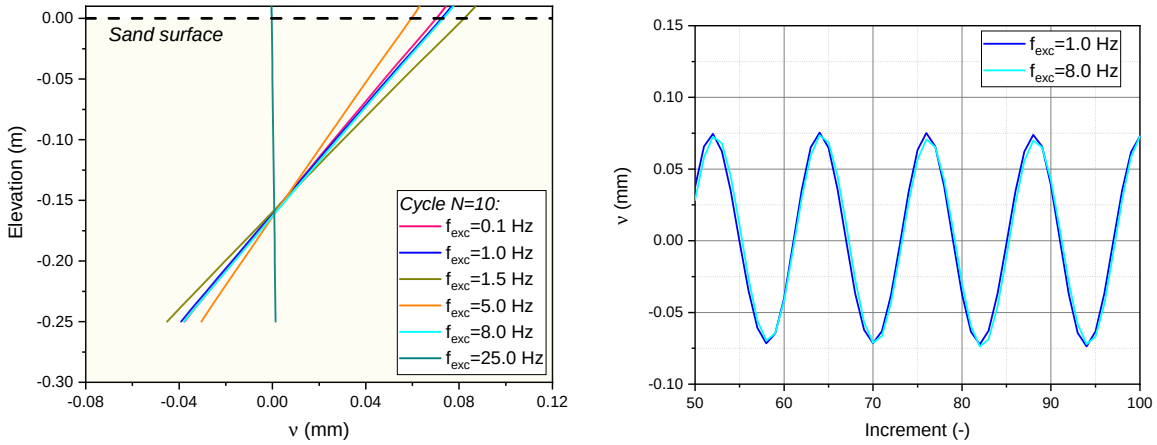

Fig. 5.19.: Monopile response at different excitation frequencies: (a) monopile profile at the peak of the tenth cycle, (b) evolution of the displacement at the ground level with cycles

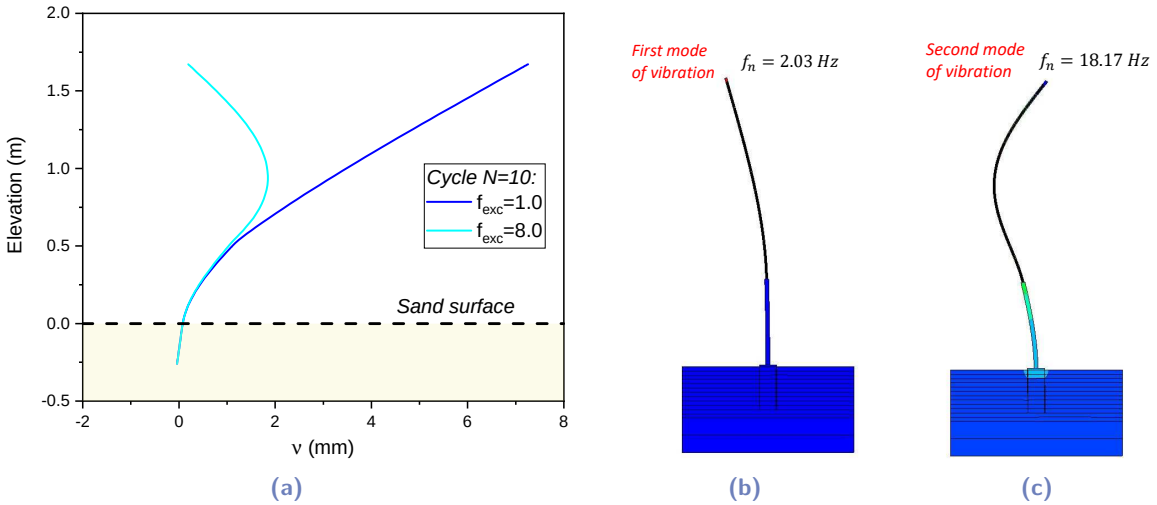

Fig. 5.20.: (a) Dynamic response of the scale model *M2* for realistic (1 Hz) and higher (8 Hz) frequencies, (b) first and (c) second mode shapes of the scale model *M2*

Then, to understand the dynamic response of the structure at the corresponding loading frequencies, the deflection of the structure at the peak of the tenth cycle is depicted in Figure 5.20a. It can be concluded that the mode shapes of the scale model for these frequencies are different, where the mode shapes are obtained using the *MODE* solver available in *Cesar-LCPC* package. For the realistic frequency of 1 *Hz*, the shape of the structure is that of the first mode, inducing an inertial force obviously transferred to the monopile foundation (Figure 5.20b), whereas for 8 *Hz* it is that of the second mode, inducing the same force transferred to the monopile (Figure 5.20c).

The reliability of this idea requires further efforts: (i) verifying the validity of this idea at a higher number of cycles, (ii) verifying accurately the similarity of the monopile response in the two cases, as the response at a frequency of 8 *Hz* seems to exhibit more bending. In parallel, the application of this idea in soil-structure interaction cases is conditioned by conserving the soil behavior at the two frequencies.

5.5 Suggested cyclic test program

Based on the findings of this study and similar works, the following recommendations are made to complete the testing program on the designed scale models:

- As the strain-controlled motion departs from the realistic cyclic response of the system (variation of rotation pivot), the force should be controlled to represent the realistic case.

- The monitoring system will be updated to ensure an accurate evaluation of the following phenomena with the cycles number: (i) lateral displacement/rotation accumulation at the ground level; (ii) evolution of the foundation stiffness; (iii) evolution of the system natural frequency; (iv) evolution of the subsidence cone formation around the monopile.

- A set of similar tests should be performed at the following frequencies: (i) 0.1 *Hz* representing the full-scale sand response; (ii) 1 *Hz* respecting the proposed scaling laws; and (iii) ~ 7 to 8 *Hz* as acceleration frequency ensuring the similar dynamic force and moment transferred to the foundation. This set of tests aims to ensure the validity of the adoption of these frequencies to accelerate the testing without affecting the realistic sand response.

- A set of tests varying the loading amplitude (ζ_b) to investigate its effect on the displacement accumulation rate.

- A set of tests will be performed at different relative density indices (I_d) to investigate its effect on the displacement accumulation rate and the evolution of the foundation stiffness.

- Performing similar tests at different loading characteristics on the two proposed foundations (semi-rigid *F1* and perfectly-rigid *F2*) to evaluate their performance as the foundation of an offshore wind turbine for different load scenarios.

- During all these tests, the subsidence cone formation and the increase in the foundation stiffness will be evaluated simultaneously, trying to establish an empirical law relating them. This law will be adopted to perform a large parametric study based on a numerical model. The aim is to understand the effect of soil, monopile, and structure properties on the evolution of the first natural frequency of the system.

- The findings of all these tests will constitute a database to adopt or propose empirical laws predicting the displacement/rotation accumulation and the foundation stiffness evolution as a function of the cycles number and the conditions of the studied case (loading characteristics, sand density index, monopile rigidity,...).

5.6 Conclusion of the chapter

This chapter illustrates the findings of a limited cyclic test program, leading to show the validity of frequency acceleration until 1 *Hz* (value respecting the frequency scaling law).

On another side, a numerical parametric study, tackling the evolution of the system first natural frequency with cycles number, shows the necessity to consider the soil, monopile, and structure properties.

This chapter ends with the proposition of a large cyclic test program capable of fulfilling some knowledge gaps in this domain.

6 Elastoplastic constitutive model for medium-dense to dense sand accounting for low stresses

Nowadays, various research efforts are dedicated to the development of simple numerical tools to predict the response of rigid monopiles subjected to lateral loading. An essential step is the ability to simulate the realistic response of the sand mass, which is affected by the variation of the stress field along the monopile and the loading level. After revealing the main features underlying the behaviour of medium-dense to dense sands in Chapter 3, this study aims to adapt a conventional elastoplastic model to simulate numerically these features. The *Hoek-Brown* failure criterion, which is generally adopted for rock materials, is used to simulate the decrease of the peak friction angle and the dilatancy of the sand with the stress level. A hardening law is proposed to consider the pre-peak hardening and the post-peak softening. The simplicity of this model will be discussed, and a calibration method will be presented. The parameters corresponding to *NE34* sand are calibrated based on the triaxial tests performed in Chapter 3. The numerical simulation of these tests, using a *Python* code, shows the good performance of the proposed model. Then, the implementation of this model in the finite element software *Cesar-LCPC* is validated.

6.1 Background

6.1.1 Sand behavior at different stress levels

Referring to Chapter 3, the principal features underlying the medium-dense to dense sand response at different stress levels are illustrated in Figure 6.1 and summarized as follows:

- The peak friction angle ($\propto q_f/p'_f$) decreases with the increase of the confining stress.
- The sand dilatancy decreases with the increase of the confining stress.
- The increase of the confining stress leads to reaching the failure and characteristic states at higher axial strain.

- In terms of stress ratio (q/p'), a pre-peak hardening is followed by a post-peak softening until a unique critical state is reached. Similarly, the dilatancy rate increases until failure is reached, and then decreases to stabilize at the critical state.

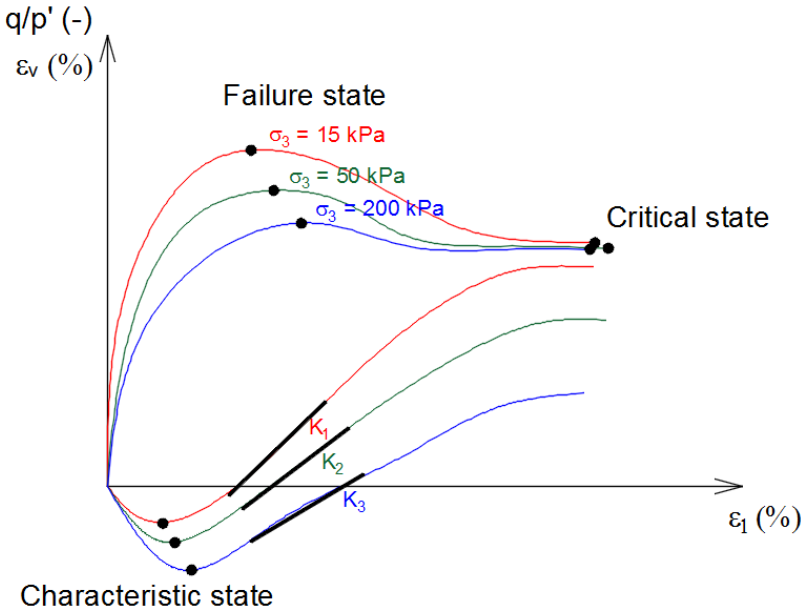

Fig. 6.1.: Typical triaxial response of medium-dense to dense sand at different stress levels

6.1.2 Finite element analysis and constitutive model

In the offshore wind turbines domain, the monopile load-carrying capacity is commonly determined by the p-y method proposed by the *API* (API (American Petroleum Institute), 2010). To consider the effect of the monopile diameter and the soil properties, modified forms and alternatives of this method are developed by several works (Wiemann et al., 2004, Kallehave et al., 2012, Kallehave et al., 2012, Thieken et al., 2015, Wang et al., 2021, ...). As seen in Section 2.1.2, the adoption of these methods for short rigid monopiles is limited due to the considerable effect of additional components of the soil reaction, such as the force and the moment at the monopile base, and the vertical shear traction at the soil-pile interface (Byrne et al., 2017). Then, Byrne et al., 2020a proposed new p-y curves informed by finite element analysis and showed a good performance against field tests, while a large set of parameters should be calibrated depending on the soil properties (16 parameters).

Despite the relatively large computation time, the finite element analysis seems to be a reasonable choice to determine the monopile response. The performance of this method is evaluated according to (i) the capability of the constitutive model to capture the main key features of the soil response and (ii) the simplicity of the model and its calibration. The conventional elastic-perfectly plastic models with a failure criterion (e.g. Mohr-coulomb *MC*) are widely adopted (M. Abdel-Rahman, 2006, Sorensen et al., 2009, Achmus et al., 2009, Kuo et al., 2011, Wolf et al., 2013,...). However, these models involve inherent limitations

when confronted to the experimentally observed sand response presented in Section 6.1.1. Therefore, Roy et al., 2016 proposed a modified form of the Mohr-Coulomb model (*MMC*) to study the lateral pipeline-soil interaction in dense sand. This model takes into account the relative density index and the confining stress effects by incorporating the stress dilatancy relation (Bolton, 1986) in the constitutive equations, and the pre-peak hardening and the post-peak softening by a mathematical function adopted to vary the friction and dilatancy angles with plastic shear strain (γ^p). This model is used by Ahmed and Hawlader, 2016 in a finite element analysis of large diameter monopile in dense sand, showing a good performance against centrifuge tests. Besides, relatively complex constitutive models are developed and adopted in similar works to simulate accurately the monopile response: (i) state parameter-based bounding surface plasticity model developed by Taborda et al., 2014 based on the model originally proposed by Manzari and Dafalias, 1997 (and adopted by Byrne et al., 2020a), (ii) two-surface-plasticity constitutive model developed by Loukidis and Salgado, 2009, and adopted in finite element analysis carried out by Qian et al., 2021.

6.1.3 Generalized Hoek-Brown failure criterion

Dedicated to the design of underground excavation in rock masses, a failure criterion is developed by Hoek and Brown, 1980. The basic equation of *Hoek-Brown* criterion writes as follows:

$$\sigma'_1 = \sigma'_3 + \sigma'_c \left(m \frac{\sigma'_3}{\sigma'_c} + s \right)^{0.5} \tag{6.1}$$

where σ'_1 and σ'_3 are respectively the major and minor principal effective stresses at the failure state, *m* and *s* are material constants, and σ'_c is the uniaxial compressive strength of the intact rock. This criterion was later updated (Hoek and Brown, 1988), and modified (Hoek et al., 1992) to obtain the current generalized form:

$$\sigma'_1 = \sigma'_3 + \sigma'_c \left(m_b \frac{\sigma'_3}{\sigma_c} + s \right)^{a} \tag{6.2}$$

where m_b depends on the type of the rock mass, and s and a are constants that depend on the characteristics of the rock mass (state and degree of fracturing). This criterion is characterized by a parabolic form, which can the basis to simulate the variation of the peak friction angle with the confining stress. Figure 6.2 shows the difference between the *Mohr-Coulomb* and the *Hoek-Brown* criteria. In laterally loaded monopile applications, the *Mohr-Coulomb* criterion defines a constant friction angle, while the realistic friction angle of the soil mass (at least for sand materials) depends on the variation of the stress field

along the monopile depth and during the loading. Therefore, the *Hoek-Brown* criterion will be adopted to constitute an elastoplastic model to simulate the realistic response of medium-dense to dense sand.

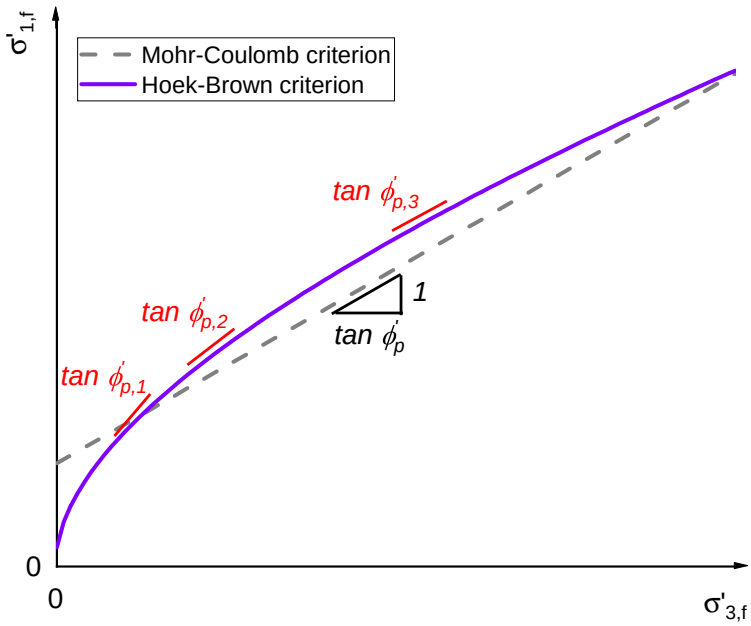

Fig. 6.2.: Schematic showing the difference between the *Mohr-Coulomb* and the *Hoek-Brown* criteria

6.2 Constitutive model

6.2.1 Failure criterion

An elastoplastic model consists of two main components: (i) the elastic regime which governs the sand behavior before reaching the yield stress (yield surface) defined by the yield criterion (corresponding to the failure criterion in case of perfect plasticity), and (ii) the plastic regime which governs the sand behavior after reaching the yield stress, where strain hardening/softening can occur. First, the conventional Mohr-Coulomb (*MC*) criterion is adopted to check its capability to describe the realistic yield limit of the stress state. This criterion can be expressed as:

$$\sigma'_1 = \frac{1+\sin\phi'_p}{1-\sin\phi'_p}\sigma'_3 + \frac{2c'\cos\phi'_p}{1-\sin\phi'_p} \tag{6.3}$$

where ϕ'_p is the effective peak friction angle (°) and c' is the effective cohesion (kPa) of the sand. This criterion is calibrated against the triaxial results obtained for *NE34* sand in Chapter 3, considering a very small cohesion $c' = 0.01$ *kPa* (reference sand with very low percentage of fine particle).

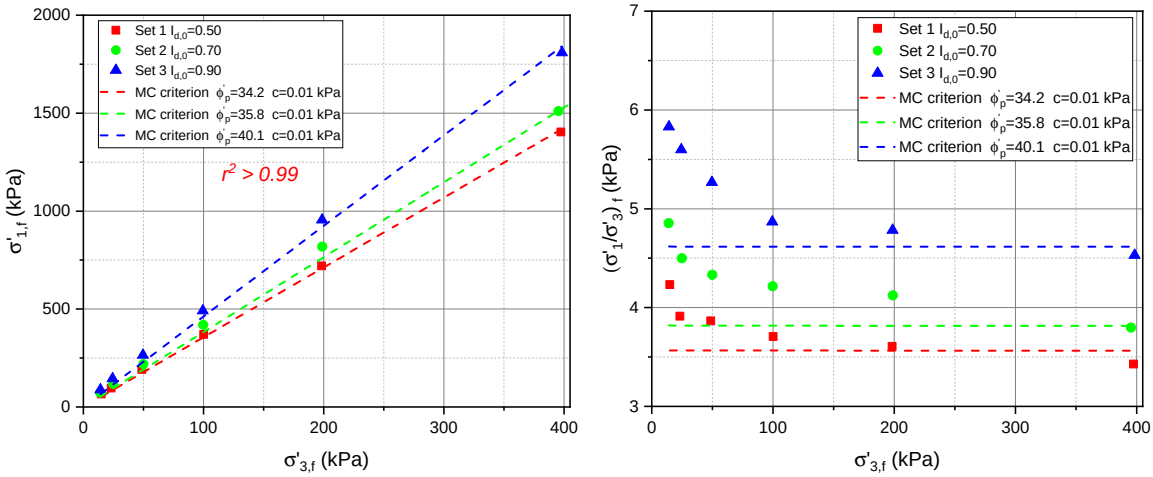

Fig. 6.3.: The calibration of *MC* criterion parameters against triaxials results

The obtained parameters show an acceptable performance at relatively high stress levels (Figure 6.3a), while the normalization of the major stress to the minor stress at failure ($(\sigma'_1/\sigma'_3)_f$) highlight the limitation of this criterion at relatively low stress levels (Figure 6.3b). As the peak friction angle ($\phi'_p \propto q_f/p'_f \propto (\sigma'_1/\sigma'_3)_f$) of the sand decreases with the increase of the confining stress (Section 6.1.1), a suitable failure criterion should be adopted to capture this behavior. The parabolic form of the *Hoek-Brown* criterion seems to be a relevant solution (Section 6.1.3). The generalized form of this criterion consists of four parameters, which can be reduced in this case: $\sigma_c = 1$ *kPa* and $s = 0.001$ are imposed to cancel their contribution. The current formulation becomes:

$$\sigma'_1 = \sigma'_3 + (m_1 \sigma'_3)^{\alpha_1} \tag{6.4}$$

where m_1 and α_1 are the two parameters governing the failure criterion. It should be noted that the s parameter can be activated to simulate the soil cohesion in specific applications. The stress state corresponding to the peak of the sand response is considered as the global failure state, which should be defined by the failure criterion. This criterion is calibrated against the triaxial results in this study (*NE34* sand), showing a good agreement with the experimental failure stress states. The fitted curves are shown in figure 6.4, and the corresponding parameters are presented in Table 6.1.

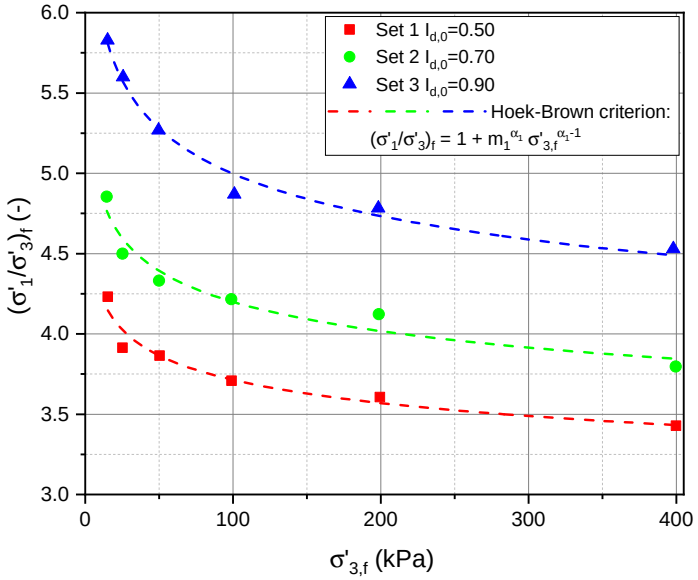

Fig. 6.4.: Experimental failure states at different stress levels and different relative density indices of *NE34* sand, and the corresponding fitted *Hoek-Brown* failure criterion

In addition, the failure criterion parameters can be directly deduced from the modified stress-dilatancy relation of the sand if it is available. In this study, this relation is determined in Section 3.2.5, having the following form:

$$\phi'_p = 29.6 + 5.08\big(I_d(5.60 + 0.58 \ln p'_f - \ln p'_f) - 0.62\big) \tag{6.5}$$

Tab. 6.1.: *Hoek-Brown* failure criterion parameters calibrated against experimental triaxial findings of *NE34* sand

Set	$I_{d,0}$	m_1	α_1	Coef. of correlation r^2
1	0.50	4.38	0.92	0.95
2	0.70	5.46	0.92	0.95
3	0.90	7.68	0.90	0.98

For each relative density index, the effective peak friction angle in the modified stress-dilatancy relation can be expressed in terms of the failure stress state, and the reformulation of the equation leads to deduce the failure criterion with the suitable parameters for the studied sand. The obtained parameters are slightly different from those obtained directly from the triaxial tests. This difference is expected as an evident reflection of the empirical relations adopted, which are already fitted in Chapter 3. The fitted curves are shown in Figure 6.5, and the corresponding parameters are presented in Table 6.2.

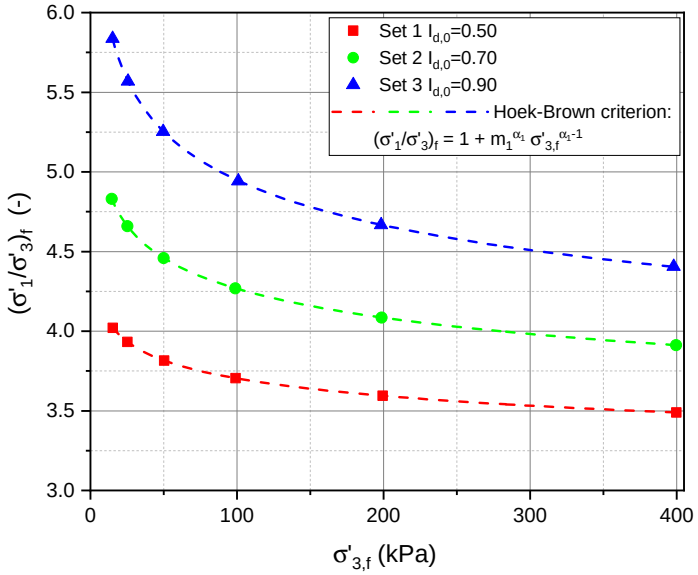

Fig. 6.5.: Failure states at different stress levels and different relative density indices of *NE34* sand and the corresponding fitted *Hoek-Brown* failure criterion obtained based on the modified stress-dilatancy relation

Tab. 6.2.: *Hoek-Brown* failure criterion parameters obtained based on modified stress-dilatancy relation of *NE34* sand

Set	$I_{d,0}$	m_1	α_1
1	0.50	3.85	0.94
2	0.70	5.51	0.92
3	0.90	8.10	0.89

6.2.2 Hardening law

After the adoption of a failure criterion considering the confining stress level, the elastoplastic model is designed to take into account the pre-peak hardening and the post-peak softening of the sand response. The concept of this model is clarified in Figure 6.6 and explained based on the triaxial response in the (p', q) space. After the determination of the global yield surface, the limit of the elastic regime should be specified, by defining an initial yield surface. In this study, the elastic limit is assumed to correspond to half of the maximum deviatoric stress in triaxial conditions. In terms of the principal stresses(σ'_1,σ'_3), the initial yield surface is expressed as:

$$f(\sigma'_1, \sigma'_3) = (\sigma'_1 - \sigma'_3)^{\frac{1}{\alpha_1}} - m_e \sigma'_3 \qquad \text{with} \qquad m_e = \frac{m_1}{2} \tag{6.6}$$

or, as a function of the mean effective and deviatoric stresses (p', q):

$$f(p',q) = q^{\frac{1}{\alpha_1}} - m_e(p' - \frac{q}{3}) \qquad \text{with} \qquad m_e = \frac{m_1}{2} \tag{6.7}$$

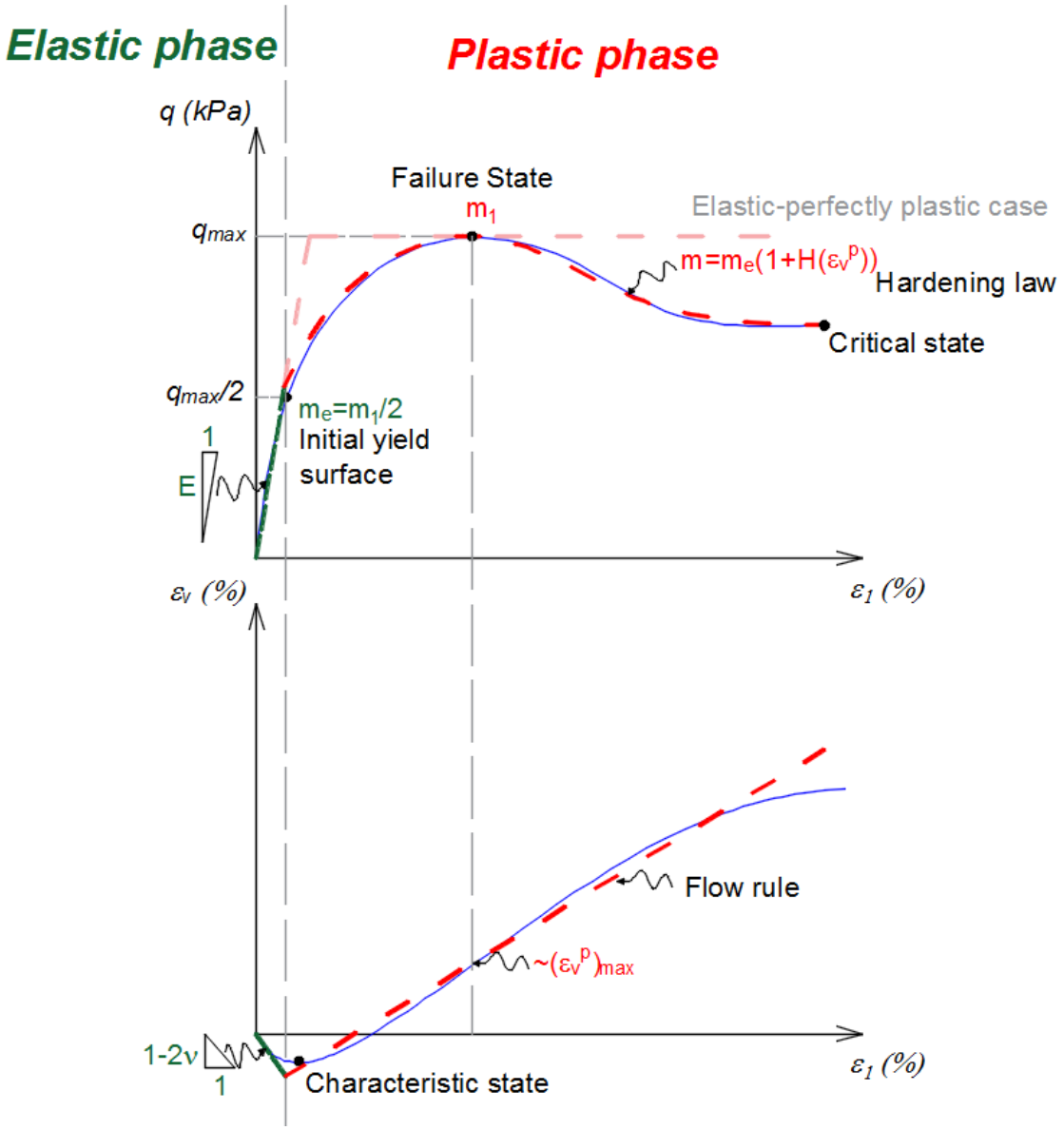

Fig. 6.6.: Concept of the proposed elastoplastic model compared with the typical triaxial response

Once the initial yield surface is reached, the plastic components of the strain will be generated by a defined flow rule ($g(p',q)$). The induced plastic deviatoric strain is considered as a hardening variable, which governs the evolution of the yield surface based on a suitable mathematical function ($H(\varepsilon_q^p)$), such that the actual yield function writes as follows:

$$f(p',q,H(\varepsilon_q^p)) = q^{\frac{1}{\alpha_1}} - m_e(1 + H(\varepsilon_q^p))(p' - \frac{q}{3}) \tag{6.8}$$

In the (p', q) space, the plastic volumetric and deviatoric strains (ε_v^p, ε_q^p) are calculated by the following equations:

$$d\varepsilon_v^p = d\lambda \frac{\partial g}{\partial p'} \qquad d\varepsilon_q^p = d\lambda \frac{\partial g}{\partial q} \tag{6.9}$$

where $d\lambda$ is the plastic multiplier, determined by the satisfaction of the consistency rule:

$$df = 0 \tag{6.10}$$

The drained triaxial response of the medium-dense to dense sand is the basis of the development of this model. The flow rule and the hardening function adopted and the calibration methods against triaxial findings will be presented in the next Sections. Then, this model will be generalized in the principal stresses space $(\sigma_1', \sigma_2', \sigma_3')$ to be implemented in a finite element software *Cesar3D-LCPC*.

6.2.3 Elasticity

In the elastic regime, the elastic stress-strain relation can be expressed as:

$$q = E\varepsilon_1 \tag{6.11}$$

where E is the Young's modulus and ε_1 is the principal axial strain. In parallel, the increase of mean effective stress (p') will induce a compressive volumetric strain (ε_v) governed by the bulk modulus (K):

$$\varepsilon_v = \frac{p'}{K} \qquad \text{with} \qquad K = \frac{E}{3(1-2\nu)} \tag{6.12}$$

where ν is the Poisson ratio. The parameters governing the elastic law can be calibrated based on the findings of triaxial tests.

The Young's modulus of the sand at different confining stresses is determined by a linear regression of the $q - \varepsilon_1$ response in the elastic range. The evolution of Young's modulus for different relative density indices are determined as a function of the initial mean effective stress (p_0'):

$$E = A \left(\frac{p_0'}{p_{ref}} \right)^B \tag{6.13}$$

where $p_{ref} = 101.3$ *kPa*, A and B are parameters depending on the studied sand. The fitted functions for different sets of relative density indices are presented in Figure 6.7 and the corresponding parameters are presented in Table 6.3.

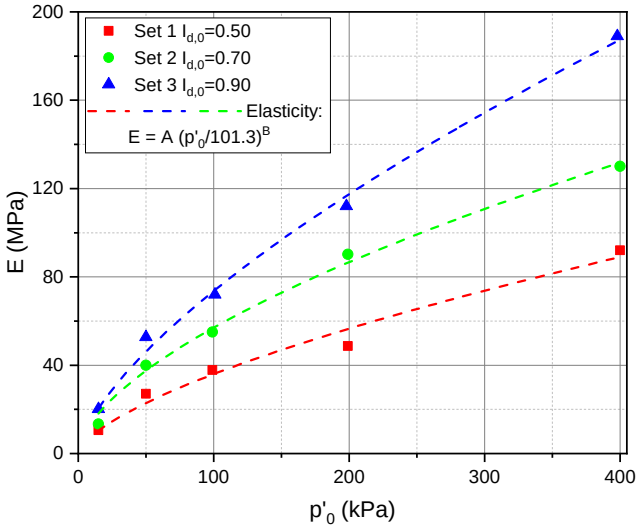

Fig. 6.7.: Young's modulus as a function of the initial mean effective stress at different relative density indices for *NE34* sand

Tab. 6.3.: Parameters of the Young's modulus function

Set	$I_{d,0}$	A (*MPa*)	B (-)	Coef. of correlation r^2
1	0.50	36.3	0.65	0.97
2	0.70	57.5	0.60	0.99
3	0.90	74.3	0.67	0.99

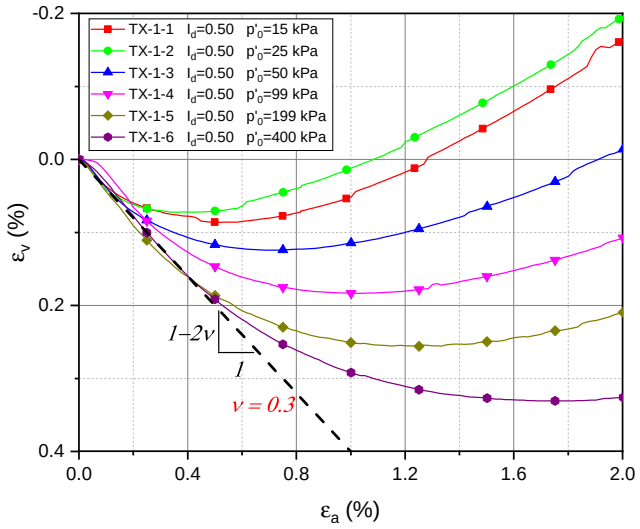

Fig. 6.8.: Determination of the Poisson ratio for *NE34* sand

Concerning the Poisson ratio of the *NE34* sand, a value of 0.3 is commonly adopted for sand materials. This value shows a good agreement with the experimental results, as shown in Figure 6.8 for a relative density index of 0.50 at different confining stresses.

6.2.4 Flow rule

Similar to the stress ratio at the failure state, the sand dilatancy decreases with the decrease of the confining stress. Besides, referring to Section 3.2.5, a linear relation between the excess friction angle ($\phi'_p - \phi'_{cr}$) and the sand dilatancy (ψ_p or I_R) was found. Thus, the simplified form *Hoek-Brown* failure criterion can be adopted to define the flow rule of the sand response. The corresponding equation in terms of the principal stresses (σ'_1, σ'_3), and the mean effective and deviatoric stresses (p', q) writes:

$$g(\sigma'_1, \sigma'_3) = (\sigma'_1 - \sigma'_3)^{\frac{1}{\alpha_2}} - m_2\sigma'_3 \tag{6.14}$$

$$g(p', q) = q^{\frac{1}{\alpha_2}} - m_2(p' - \frac{q}{3}) \tag{6.15}$$

where m_2 and α_2 are the two parameters governing the flow rule. The calibration of these parameters against the triaxial findings is based on the following equations:

$$d\varepsilon_v^p = d\lambda\frac{\partial g}{\partial p'} = -m_2 d\lambda \qquad d\varepsilon_q^p = d\lambda\frac{\partial g}{\partial q} = \left(\frac{1}{\alpha_2}q^{\frac{1}{\alpha_2}-1} + \frac{m_2}{3}\right)d\lambda \tag{6.16}$$

Then,

$$d\varepsilon_1^p = \frac{d\varepsilon_v^p}{3} + d\varepsilon_q^p = \left(\frac{1}{\alpha_2}q^{\frac{1}{\alpha_2}-1}\right)d\lambda \tag{6.17}$$

Dividing the incremental plastic volumetric strain (Equation 6.16) by the increment of the plastic axial strain (Equation 6.17) leads to the following equation:

$$\frac{d\varepsilon_v^p}{d\varepsilon_1^p} = -m_2\alpha_2 q^{1-\frac{1}{\alpha_2}} \tag{6.18}$$

which can be compared to the rate of dilation obtained experimentally from the curve $\varepsilon_v - \varepsilon_1$. This method is applied by determining the dilation rate at failure for different relative density indices of *NE34* sand and calibrating the corresponding parameters of the flow rule. The fitted curves and the parameters obtained are presented respectively in Figure 6.9 and Table 6.4.

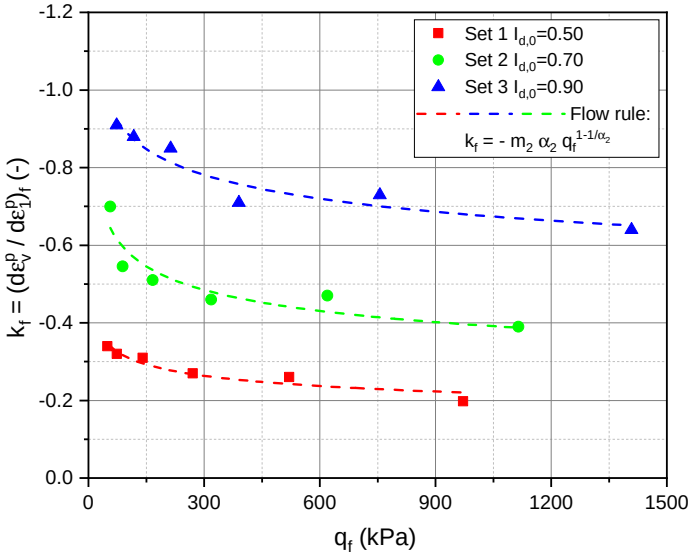

Fig. 6.9.: Experimental dilation rate at failure for different stress levels and different relative density indices of *NE34* sand, and the corresponding fitted flow rules

Tab. 6.4.: Flow rule parameters calibrated against experimental triaxial findings of *NE34* sand

Set	$I_{d,0}$	m_2	α_2	Coef. of correlation r^2
1	0.50	0.72	0.87	0.92
2	0.70	1.50	0.85	0.85
3	0.90	1.71	0.89	0.92

Similar to the failure criterion, the parameters of the flow rule can be determined by the reformulation of the modified stress-dilatancy relation. This method is also applied in this study and the corresponding fitted curves and parameters are presented respectively in Figure 6.10 and Table 6.5.

Tab. 6.5.: Flow rule parameters obtained based on modified stress-dilatancy relation of *NE34* sand

Set	$I_{d,0}$	m_2	α_2
1	0.50	1.09	0.82
2	0.70	1.92	0.83
3	0.90	3.23	0.82

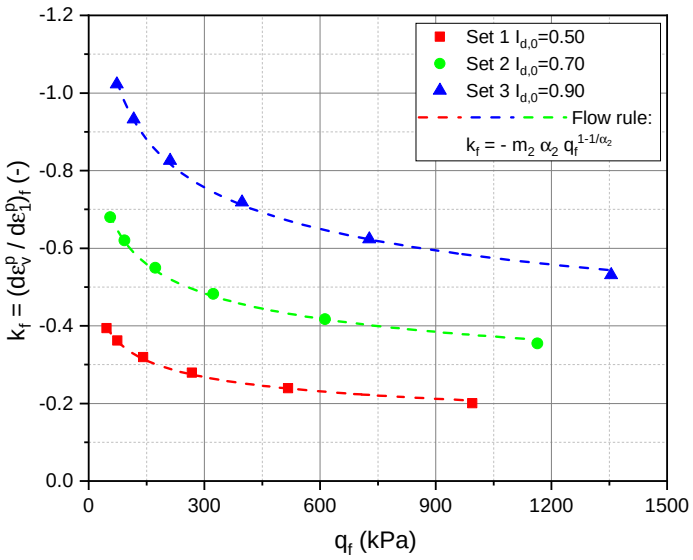

Fig. 6.10.: Dilation rate at failure for different stress levels and different relative density indices of *NE34* sand and the corresponding fitted flow rules obtained based on the modified stress-dilatancy relation

6.2.5 Hardening function

A hardening law should be used to reproduce numerically the pre-peak hardening and the post-peak softening. A new function is proposed to simulate the hardening, while a function already existing in *Cesar-LCPC* packages is adopted to simulate the softening. The global function shows a satisfying performance comparing with the experimental findings. This function is presented in Figure 6.11, and composed of the following two components:

if $x < x_{max}$ (hardening component):

$$H(x) = h_1(x) = h_{max} \frac{\arctan(Bx)}{\arctan(Bx_{max})} \tag{6.19}$$

if $x > x_{max}$ (softening component):

$$H(x) = h_2(x) = h_{res} + (h_{max} - h_{res}) e^{\frac{-(x-x_{max})^2}{\beta^2}} \tag{6.20}$$

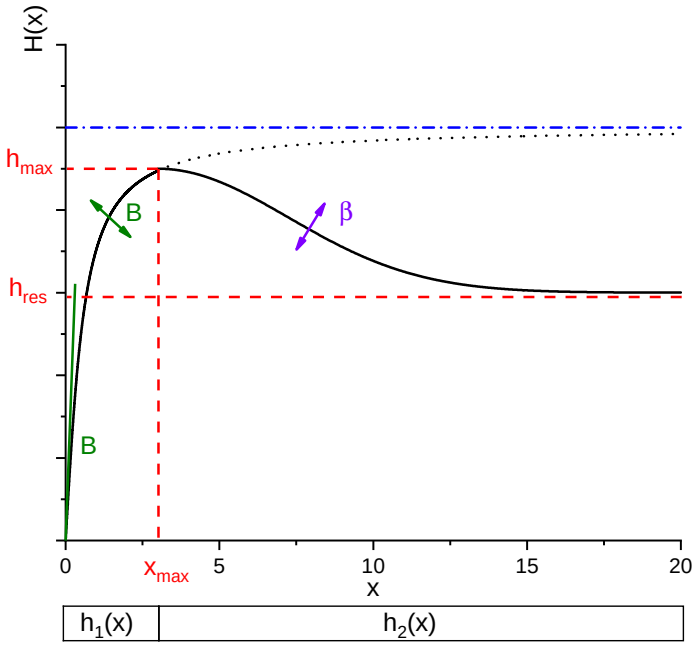

Fig. 6.11.: Hardening function proposed to control the pre-peak hardening and the post-peak softening

where:

h_{max} is the parameter representing the height of the peak.
x_{max} is the parameter controlling the position of the peak ($H(x_{max}) = h_{max}$).
h_{res} is the parameter representing the level of the horizontal asymptote of the hardening function at high values of x.
B and β are the parameters controlling respectively the curvature of the hardening and softening components of the function.

Parameter h_{max}

The hardening function is related to the plastic volumetric strain as a hardening variable. First, the parameter h_{max} defines the limit of the elastic regime by an initial yield surface expressed as:

$$f(\sigma'_1, \sigma'_3) = (\sigma'_1 - \sigma'_3)^{1/\alpha_1} - \frac{m_1}{1 + h_{max}}\sigma'_3 \tag{6.21}$$

After the initial yield surface is reached and further loading in the plastic regime, the plastic components of the strain start to be generated, including the plastic volumetric strain. The yield surface will evolve depending on the hardening variable, which is the plastic volumetric strain (ε_v^p). The equation of the yield surface is then:

$$f(\sigma'_1, \sigma'_3, H(\varepsilon_v^p)) = (\sigma'_1 - \sigma'_3)^{1/\alpha_1} - \frac{m_1}{1 + h_{max}}(1 + H(\varepsilon_v^p))\sigma'_3 \tag{6.22}$$

At $x = x_{max}$, equivalent to $\varepsilon_v^p = (\varepsilon_v^p)_{max}$, the yield surface reaches the maximal yield surface corresponding to the failure state. In this model, h_{max} is fixed at 1, assuming that the elastic limit corresponds to a stress state equal to half of the failure stress state.

Parameter $(\varepsilon_q^p)_{max}$

Referring to Section 6.1.1, the axial strain at which the failure occurs depends on the confining stress. Based on the triaxial findings, a suitable relation is proposed to estimate the plastic deviatoric strain $(\varepsilon_q^p)_{max}$ as a function of the confining stress to control the position of the failure state. In accordance with the relation proposed by Ahmed and Hawlader, 2016, this relation takes a power form:

$$(\varepsilon_q^p)_{max} = C \left(\frac{\sigma'_3}{p_{ref}} \right)^D \tag{6.23}$$

The fitted curves and the corresponding parameters of *NE34* sand at different relative density indices are presented in Figure 6.12 and Table 6.6.

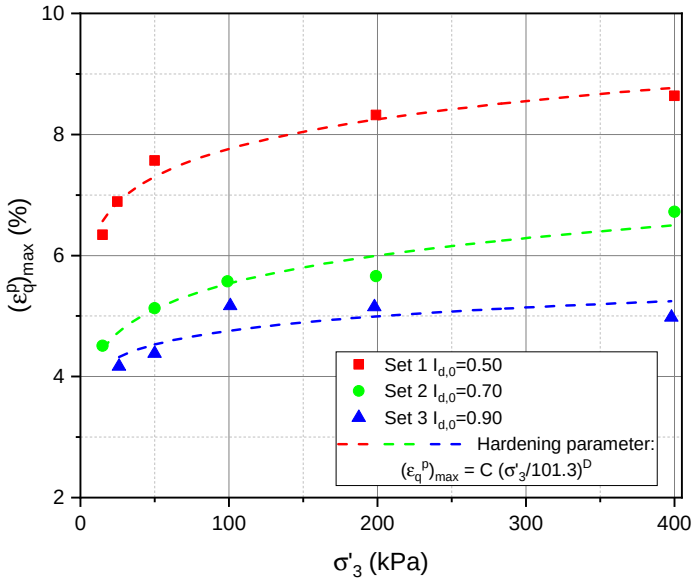

Fig. 6.12.: Plastic deviatoric strain corresponding to the failure state as a function of the confining stress for *NE34* sand

Tab. 6.6.: Parameters of the function related the plastic volumetric strain corresponding to the failure state as a function of the confining stress for *NE34* sand

Set	$I_{d,0}$	C	D	Coef. of correlation r^2
1	0.50	0.0777	0.088	0.96
2	0.70	0.0555	0.116	0.94
3	0.90	0.0476	0.071	0.64

Parameter B

Based on the experimental observations, the decrease of the confining stress leads to a higher failure stress ratio ($q_f/p'_f \propto (\sigma'_1/\sigma'_3)_f$), which causes a stronger curvature on the hardening response. Thus, the parameter B seems to be dependent on the confining stress. A *Python* code is developed to best-fit the parameter in each triaxial test at different relative density indexes and confining stresses. The obtained parameters vary randomly without respecting a clear trend (Figure 6.13), meaning that the effect of the variability of the tests is more dominant than the effect of this parameter. Seeking the simplicity of the model, the possibility to fix this parameter as the average of all experimental values is tested and showed satisfying performance (Section 6.3). The adopted parameter B for all cases is 120, as the average of the fitted values.

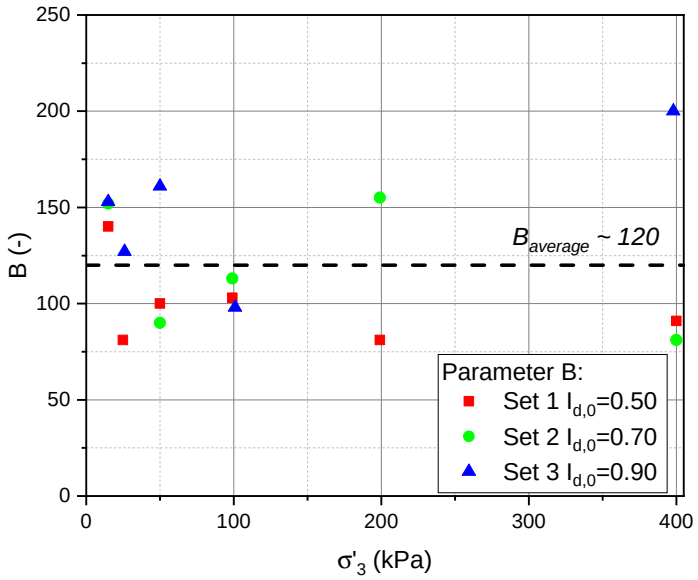

Fig. 6.13.: Parameter B fitted for different triaxial tests

Parameter h_{res}

Referring to Section 6.1.1, the softening of the sand response leads to a unified critical state, corresponding to the critical friction angle (ϕ'_{cr}). In this model, the parameter h_{res} can be determined by a relationship established with the critical friction angle and the confining stress. This equation takes the following form:

$$1 + h_{res} = \frac{1 + h_{max}}{m_1} \left(\frac{2 \sin \phi'_{cr}}{(1 - \sin \phi'_{cr})(\sigma'_3)^{\alpha_1 - 1}} \right)^{\frac{1}{\alpha_1}} \tag{6.24}$$

Parameter $\beta \sim F$

The post-peak softening depends on the failure mode, which makes the numerical fitting of the parameter β almost impossible. An alternative way is proposed, consisting in adjusting values to determine reasonable parameters for each set of triaxial tests. However, fixing the parameter at different confining stress levels leads to an unrealistic intersection of softening responses (Figure 6.14a). To avoid the passage to an additional parameter, imposing a linear relationship between the parameter β and the parameter $(\varepsilon_q^p)_{max}$, which depends on the confining stress, is tested. This relation is:

$$\beta = \frac{-F}{(\varepsilon_q^p)_{max}} \tag{6.25}$$

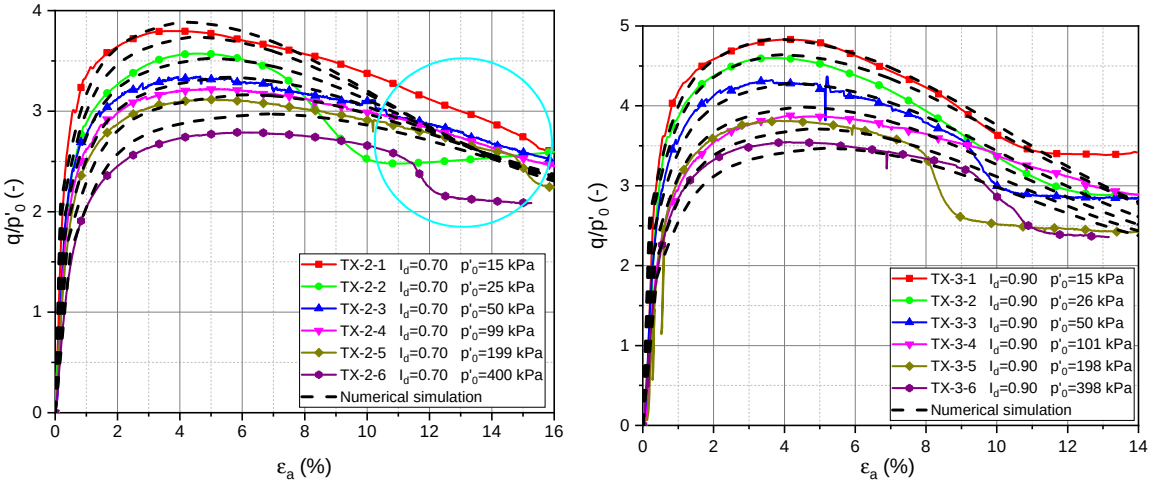

Fig. 6.14.: Numerical simulation of the triaxial tests of *NE34* sand at $I_d = 0.90$: (a) fixed β (b)$\beta \propto (\varepsilon_q^p)_{max}$

Using the *Python* code developed, the parameter F is adjusted to obtain suitable values capable to well-reproduce the softening part of the sand response. This idea seems to ensure a satisfying solution to the challenge encountered (Figure 6.14b). Finally, the values of the parameter F adopted in this study are presented in Table 6.7.

Tab. 6.7.: Softening parameter E adopted for different relative density indices of *NE34* sand

Set	$I_{d,0}$	F
1	0.50	0.010
2	0.70	0.006
3	0.90	0.005

6.3 Numerical simulation of the triaxial tests - *Python* code

After the presentation of the proposed model and the calibration of the corresponding parameters for three sets of the triaxial tests performed in this study (*NE34* sand: $I_d = 0.50$; 0.70; and 0.90). A *Python* code is developed to simulate the response of a set of drained strain-controlled triaxial tests at different confining stress levels, based on this model. The numerical simulations are presented against the experimental findings in terms of the normalized deviatoric stress and the volumetric strain as a function of the axial strain (Figure 3.16). The proposed model shows an excellent ability to reproduce the principal features underlying the medium-dense to dense sand response at different confining stresses.

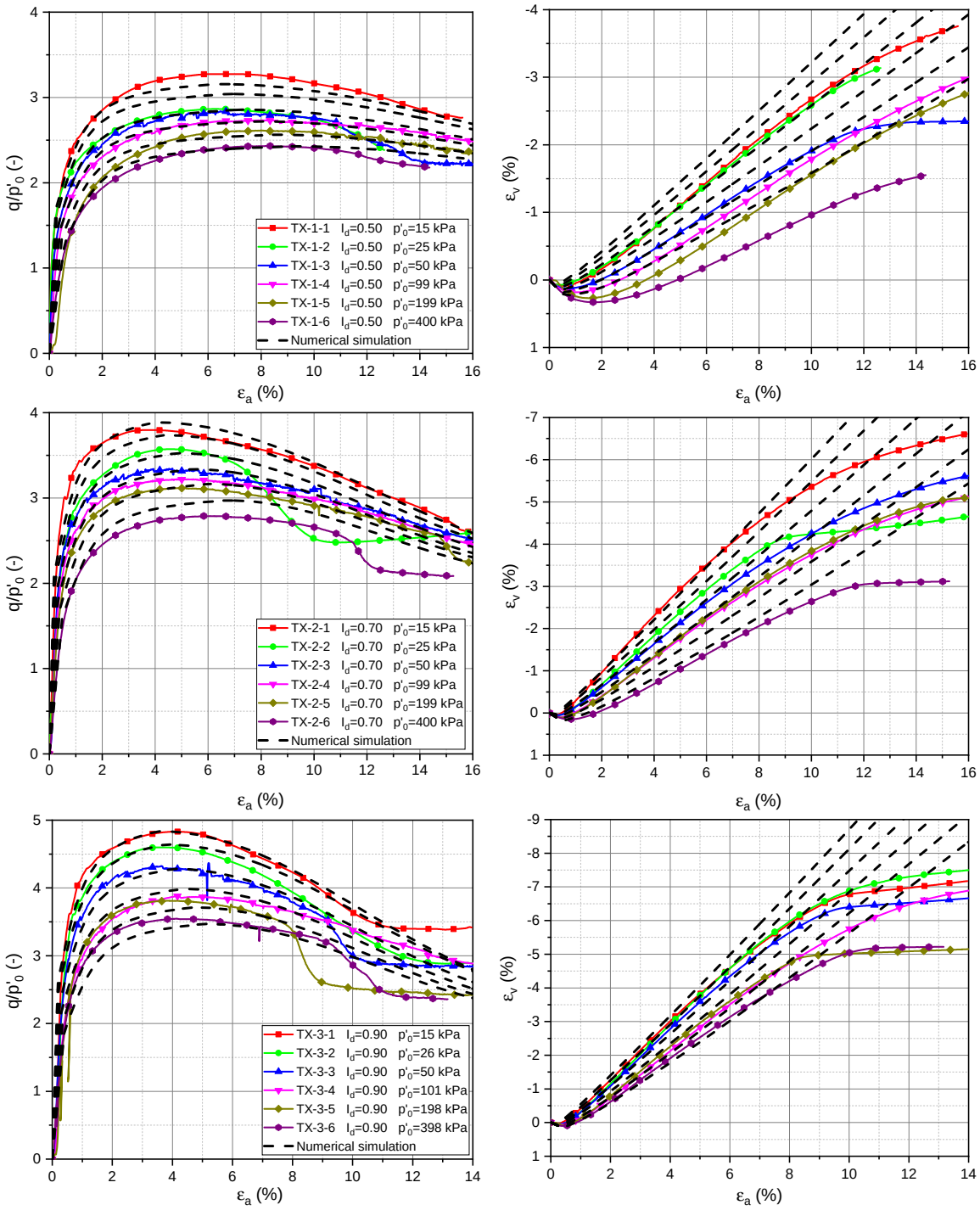

Fig. 6.15.: Experimental triaxial results and numerical simulations for *NE34* sand: (a) $q - \varepsilon_a$ (b) $\varepsilon_v - \varepsilon_a$

6.4 Implementation on *Cesar-LCPC*

The failure criterion and the flow rule adopted (*Hoek-Brown*) already exist in *Cesar-LCPC* packages. The hardening law has been implemented by the development team of *Cesar3D-LCPC* software. Concerning the elastic parameters, the Poisson ratio ν is defined as a constant at all the elements of the *2D* or *3D* model and during the calculation increments, while the Young's modulus is initialized at each element depending on the initial mean effective stress p'_0, and becomes constant during the calculation increments. The hardening parameters h_{max} and B are defined as constants for all the elements of the *2D* or *3D* model and during the calculation increments. The parameter m_1 defined for the yield surface is that corresponding to the elastic limit $m_1/(1+h_{max})$, and the parametersm_1 and α_1 are defined as constants at all the elements of the *2D* or *3D* model and during the calculation increments. The yield surface will be varied depending on the hardening law (plastic volumetric strain ε_v^p) and the evolution of the minor confining stress (σ'_3) at each increment. The flow rule parameters m_2 and α_2 are defined as constants, while the dilation rate depends on the minor confining stress (σ'_3) and will be varied at each element of the *2D* or *3D* model, and after each increment of the calculation.

In order to validate the implementation of the hardening law on *Cesar-LCPC*, an axisymmetric *Cesar2D-LCPC* model is developed to simulate a drained strain-controlled triaxial test. The test conditions and the parameters corresponding to a triaxial test performed experimentally are adopted, and the obtained numerical results are compared to those obtained experimentally and numerically by the *Python* code. The numerical simulations obtained by the *Cesar2D-LCPC* model and the *Python* code are superimposed (Figure 6.16), which validates the implementation of the constitutive model on *Cesar-LCPC* packages.

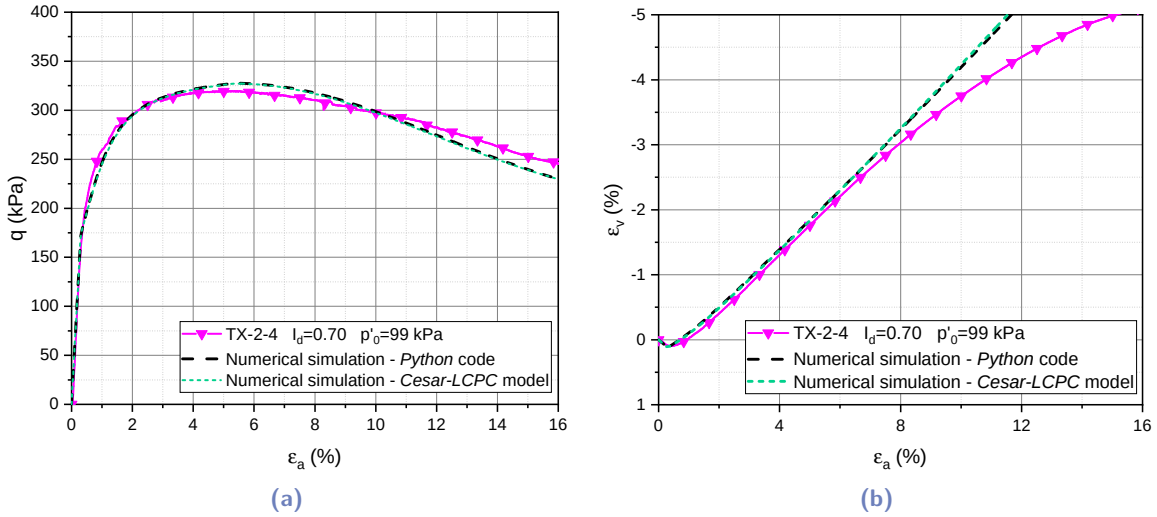

(a) (b)

Fig. 6.16.: Numerical simulation by the *Cesar2D-LCPC* model and the *Python* code of the triaxial tests of *NE34* sand at $I_d = 0.70$ and $p'_0 = 99$ *kPa*: (a) $q - \varepsilon_a$ (b) $\varepsilon_v - \varepsilon_a$

6.5 Advantages and limitations of the proposed model

This section starts by an overview of the proposed model in Table 6.8, presenting the different laws, parameters and methods of calibration.

Tab. 6.8.: Summary of the constitutive model proposed

Description	Equations	Parameters	Calibration methods
Elastic regime	$E = A\left(\frac{p'_0}{101.3}\right)^B$	A; B	Determine from elastic phase of triaxial tests: Linear fitting of $(q-\varepsilon_a)$ as a function of p'_0
	$\varepsilon_{ij} = \frac{1+\nu}{E}\sigma'_{ij} - \frac{\nu}{E}tr(\sigma')\delta_{ij}$	ν	Initial tangent of $(\varepsilon_v - \varepsilon_a)$
Hardening law	$(\varepsilon_q^p)_{max} = C\left(\frac{\sigma'_3}{101.3}\right)^D$	C; D	Determined from triaxial tests: ε_q^p at failure state as a function of σ'_3
	if $\varepsilon_q^p < (\varepsilon_q^p)_{max}$:		
	$H(\varepsilon_q^p) = h_{max}\frac{\arctan(B\varepsilon_q^p)}{\arctan(B(\varepsilon_q^p)_{max})}$	h_{max}	fixed as 1
		B	fixed as 120
	$\beta = \frac{F}{(\varepsilon_q^p)_{max}}$	F	reasonable value adopted based on triaxial tests
	if $\varepsilon_q^p > (\varepsilon_q^p)_{max}$:		
	$H(\varepsilon_q^p) = h_{res} + (h_{max} - h_{res})e^{\frac{-(\varepsilon_q^p - (\varepsilon_q^p)_{max})^2}{\beta^2}}$	h_{res}	Relation established with the ϕ'_{cr} (Eq. 6.24)
Failure criterion	$f(\sigma'_1, \sigma'_3, H(\varepsilon_q^p)) = (\sigma'_1 - \sigma'_3)^{\frac{1}{\alpha_1}}$	m_1; α_1	Determined from triaxial tests: stress
	$-\frac{m_1}{1+h_{max}}(1+H(\varepsilon_q^p))\sigma'_3$		failure state $(\sigma'_1/\sigma'_3)_f$ as a function of σ'_3
Flow rule	$g(\sigma'_1, \sigma'_3) = (\sigma'_1 - \sigma'_3)^{\frac{1}{\alpha_1}} - m_2\sigma'_3$	m_2; α_2	Determined from triaxial tests: dilation rate at failure state $(d\varepsilon_v^p/d\varepsilon_1^p)_f$ as a function of σ'_3
	$d\varepsilon_{ij}^p = d\lambda\frac{\partial g}{\partial \sigma'_{ij}}$		

The idea of this constitutive model is the adoption of a conventional failure criterion, which is generally available on the packages of relevant finite element softwares. This model shows excellent performance to capture the medium-dense to dense sand response at different stress levels by a unique set of parameters. Besides, knowing the range of stresses on any application, the parameters of this model can be calibrated by few triaxial tests (practically three tests).

On another side, this model is unable to simulate the contraction behavior (Figure 6.17a). This issue leads to a relative over-estimation of the dilation rate in the case of medium-dense sands and incapability to reproduce the realistic response in the case of loose sands. For medium-dense sands, the parameter m_2 defined as a controller of the flow rule can be reduced consciously to obtain a more reasonable dilation (Figure 6.17a). This idea is applied in this study for triaxial tests with $I_d = 0.50$, and the dilation rate is reduced by a factor of 0.68 based on the experimental findings (Figure 6.17b). The reflection of this reduction on the numerical simulation is shown in Figure 6.18, showing a notable enhancement in the simulation of the dilation response.

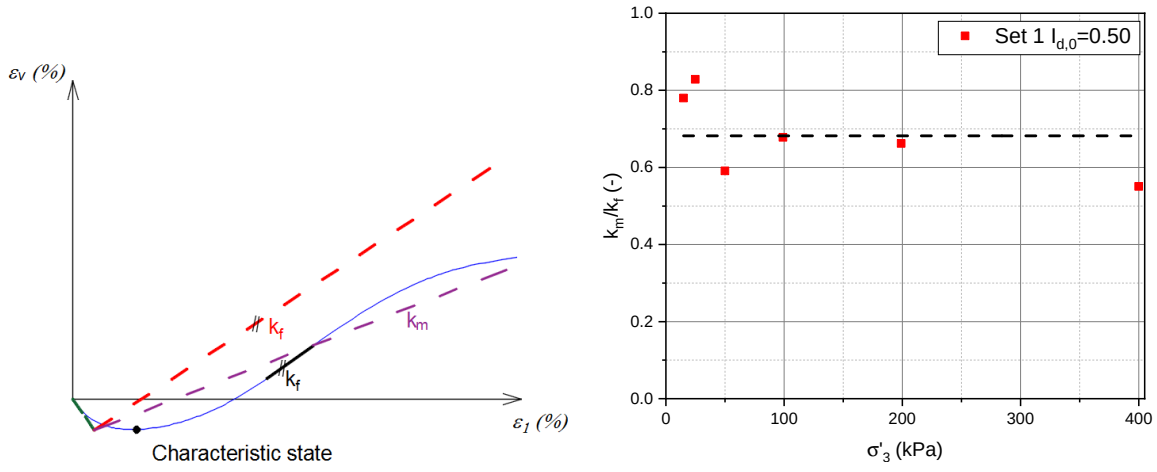

Fig. 6.17.: Idea of the flow rule parameter reduction to enhance the simulation of the dilation response: (a) Concept of the reduction (b) reduction calibrated for triaxial tests with $I_d = 0.50$

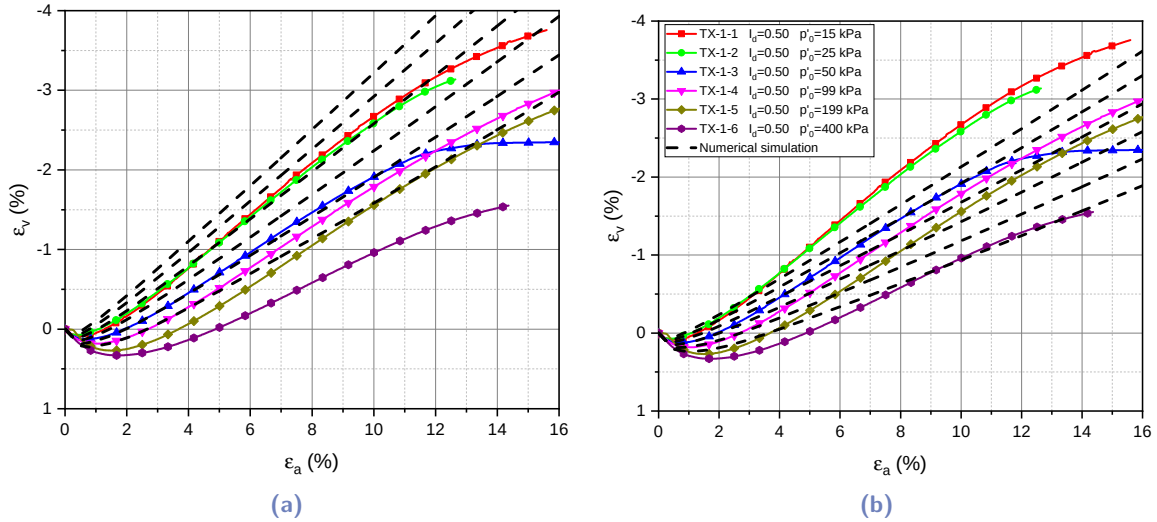

Fig. 6.18.: (a) Dilation response without the reduction of the flow rule parameter and (b)dilation response with the reduction of the flow rule parameter for triaxial tests with $I_d = 0.50$

6.6 Conclusion of the chapter

This chapter presents the development of a new constitutive model capable of capturing the sand behavior at different stress levels during triaxial compression. A calibration method of model parameters is presented and applied to *NE34* sand based on the findings of Chapter 3. Knowing the variation range of stress levels for any geotechnical problem, the model parameters can be calibrated by few triaxial tests (practically three tests).

7

Monotonic laterally loaded monopile: revision of the failure criteria; *FEM* modeling

Based on a parametric study on a monotonic laterally loaded monopile, some purposes are fulfilled: (i) revealing the effect of some variable parameters on the monopile lateral response (length to diameter ratio L/D, sand relative density index I_d, loading eccentricity), (ii) evaluation of the performance of conventional monopile failure criteria against the variation of these parameters, (iii) proposition and validation of a new monopile failure criterion, and (iv) showing the performance of the proposed constitutive model in the *3D* simulation of lateral monopile response.

7.1 Literature review

7.1.1 Relevant failure criteria of laterally loaded rigid monopile

Several criteria are proposed to determine the ultimate lateral capacity of a rigid monopile. In the domain of offshore wind turbines, the determination of the ultimate capacity is a requirement for the design to: (i) verify the satisfaction of the ultimate limit state, and (ii) determine the cyclic magnitude ratio (ζ_b; Section 2.1.1) used in the evaluation of the relative magnitude of cyclic loading. Tens of failure criteria have been proposed in the literature (Section 4.1, Charles et al., 2001, Chen et al., 2011, Aguilar et al., 2019,...), and are mainly based on: a defined limit for the displacement at the ground level (e.g. 300 *mm*; Hu et al., 2006), a defined limit for the rotation (e.g. $2°$, $4°$; Section 4.1), a defined limit for the displacement at the ground level as a percentage of the monopile diameter or embedded length (e.g. $0.1D$, $0.1L$; Section 4.1), a graphical identification (e.g. point at which the curve becomes linear; Meyerhof et al., 1981, intersection between the initial tangent and the tangent when the curve becomes linear; El Haffar, 2018), and mathematical methods to determine the horizontal asymptote which can be reached by the curve (hyperbolic fit; Manoliu et al., 1985). Besides, several simplified theoretical methods are developed to analytically estimate the monopile ultimate capacity (Broms, 1964, Parsad and Chari, 1970, Zhang et al., 2005, Hu et al., 2006, Aguilar et al., 2019,...)

In this study, some criteria are examined based on their performance to identify the ultimate lateral capacity of a rigid monopile subjected to monotonic loading. The following criteria are chosen:

- A displacement of $0.1D$ at the ground level or a rotation of $2°$, which seem to be conventional for rigid monopiles according to Byrne et al., 2017.

- The method proposed by Manoliu et al., 1985, which is based on a hyperbolic function to predict the asymptote to the force-displacement curve at large displacements. This method focuses on the fully mobilized resistance of the monopile and thus constitutes an upper bound to all criteria. The ultimate force is determined as the inverse of the slope of a line obtained with a particular representation of the force-displacement curve (Figure 7.1). In this study, it is found that restricting the determination of the slope to only the linear part of the curve leads to a better prediction of the horizontal asymptote to the force-displacement curve (Figure 7.1). The practical application of this method is simple, and the variation of the range of displacement, at which the slope is determined, has not a considerable effect on the ultimate load obtained.

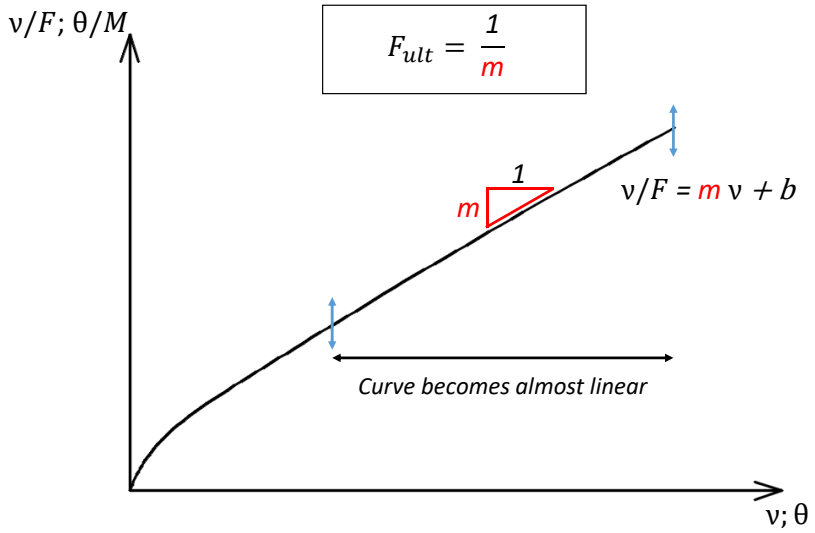

Fig. 7.1.: Failure criteria based on Manoliu et al., 1985

To clarify this idea, the application of this method to a case studied in the present work is presented in Figure 7.2a, and the obtained fitted curves tending to the corresponding ultimate forces are presented in Figure 7.2b.

- The method proposed by Zhang et al., 2005, as a relevant method representing the simplified theoretical methods presented in the literature. This method will be presented in the next section.

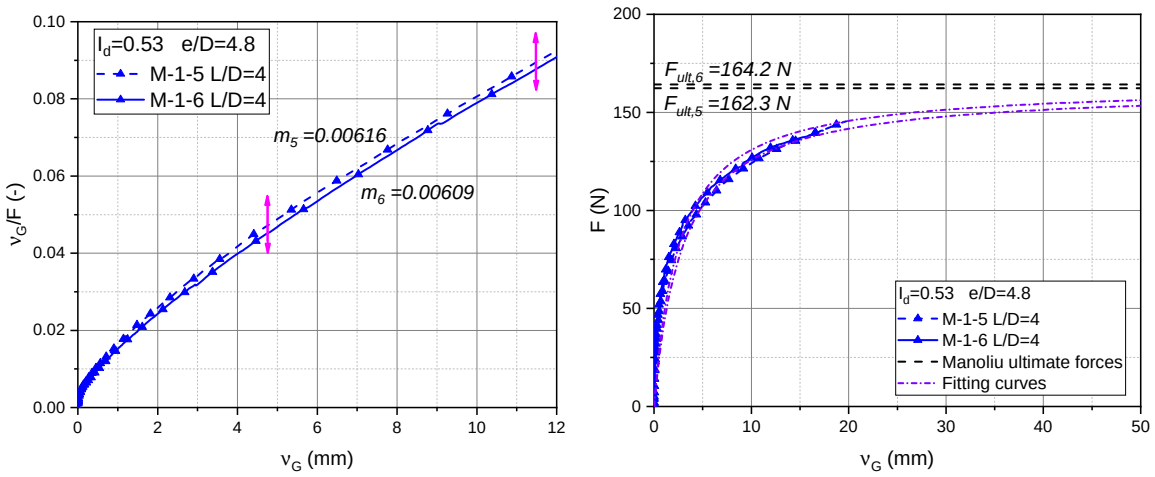

(a) (b)

Fig. 7.2.: Modified application of Manoliu et al., 1985 criterion: (a) linear fitting, (b) obtained fitted curves and ultimate forces

7.1.2 Theoretical method to determine the lateral ultimate capacity (Zhang et al., 2005)

This method starts by defining a theoretical distribution of the earth pressure around the monopile:

- Distribution of front earth pressure and side shear around the monopile subjected to lateral loading (Figure 7.3a; Smith, 1987).

- Distribution of front soil resistance and side shear resistance along the monopile length (Figure 7.3b; Parsad and Chari, 1970).

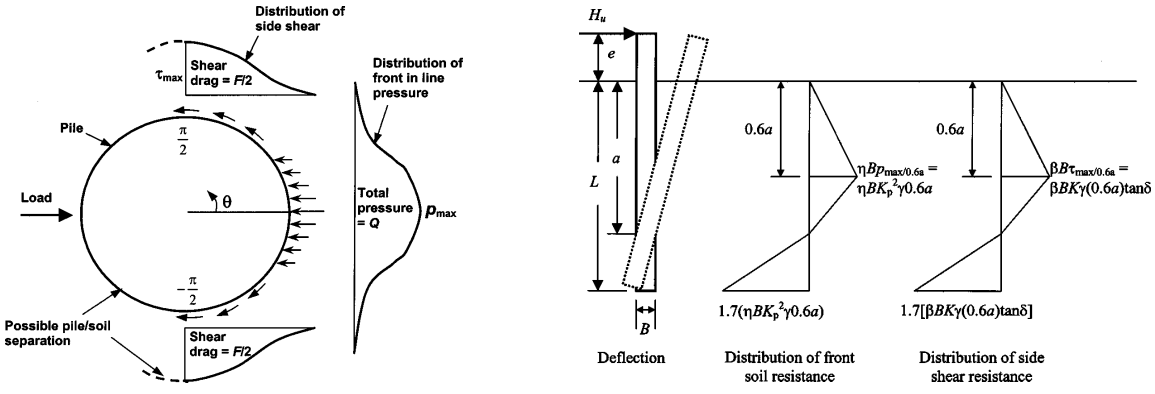

(a) (b)

Fig. 7.3.: Distribution of front earth pressure and side shear (a) around, and (b) along the length of the monopile

The ultimate lateral capacity (F_{ult}) is determined by establishing the equilibrium equation with the resistance earth pressure corresponding to the failure. The obtained equations are:

$$a = [-(0.567L + 2.7e) + (5.307L^2 + 7.29e^2 + 10.541eL)^{0.5}]/2.1996 \quad (7.1)$$

$$F_{ult} = 0.3(\eta K_p^2 + \xi K \tan\delta)\gamma a B(2.7a - 1.7L) \quad (7.2)$$

where B is the monopile diameter, L is the monopile embedded length, a is the depth of the monopile rotation pivot, e is the loading eccentricity, η is a shape factor to account for the non-uniform distribution of earth pressure in front of the monopile: for circular monopiles it is taken as 0.80 (Kulhawy, 1991), K is equal to the lateral earth pressure coefficient at rest K_0 multiplied by a coefficient of 1.5 to account for the effect of the monopile driving (Kulhawy, 1991), δ is the interface friction angle between the monopile and the soil: taken as 80% of the peak friction angle of the soil corresponding to rough steel case (Kulhawy, 1991; the peak friction angle is estimated from the modified stress-dilatancy relation presented in Section 3.2.6), ξ is a shape factor to account for the non-uniform distribution of the side shear: for circular monopiles is taken as 1.0 (Kulhawy, 1991). It should be noted that this method is is meant to predict Meyerhof et al., 1981 failure criterion.

7.2 Background and motivation

Referring to Sections 2.1.2 and 2.2.4, the monopiles supporting the offshore wind turbines tend to have a shorter length to diameter ratio. In addition to the impact of this feature on the design methodologies, the performance of the conventional failure criteria is affected. Figure 7.4 presents the lateral response of three laterally loaded monopiles with three different length to diameter ratios. These curves correspond to some field tests performed in the framework of the *PISA* project (Byrne et al., 2020b). The $0.1D$ failure criterion is applied to determine the ultimate lateral capacity of the three monopiles. It is clearly shown that the monopile with $L/D = 8$ has not fully mobilized resistance, while the monopile with $L/D = 3$ has reached this resistance early with a practical difficulty to achieve the displacement corresponding to the failure criteria. Extending the application of the conventional failure criteria for very short monopiles should then be revised.

On another side, the ultimate force obtained by the application of the failure criteria is used to determine the cyclic magnitude ratio ζ_b, which represents the relative magnitude of the cyclic loading. Then, empirical relations, including this parameter, are proposed to estimate the permanent displacement after a defined number of cycles (Section 4.2). The application of the same relations for monopiles having different length to diameter ratios or subjected to other conditions (e.g. loading eccentricity, sand relative density index) should

be accompanied by the adoption of an appropriate failure criterion, ensuring an equivalent ultimate capacity in different cases.

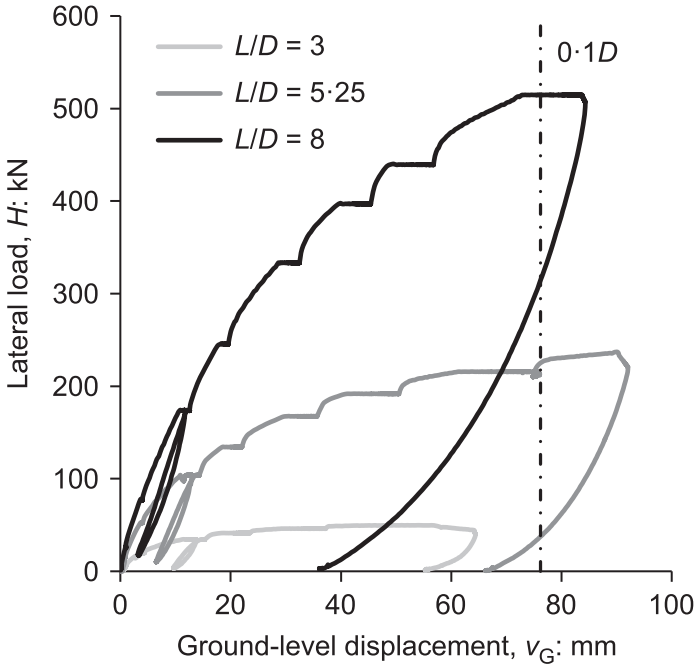

Fig. 7.4.: Field tests performed by *PISA* project (Byrne et al., 2020b)

7.3 Objectives and test program

Based on the testing procedure presented in Section 4.4.1, a parametric study is carried out to determine the effect of the monopile length to diameter ratio, loading eccentricity, and sand relative density index on the performance of some relevant failure criteria. Then, a numerical method is proposed to find the force and the displacement allowing the normalization of each response curve while leading to a unique master curve. This method can be considered as a numerical failure criterion depending on the problem conditions and ensuring an equivalent ultimate capacity for different cases. This method is presented in Section 7.6.1. Based on this numerical development, a new simple failure criterion is proposed.

The test program is performed using a stainless steel tube with a diameter of $80\ mm$ and a thickness of $2\ mm$. Additional test conditions are presented in Table 7.1. The guidance system presented in Section 4.4.1 is not perfectly adapted for this monopile dimensions. However, the repetition of the tests shows satisfying repeatability ensured by the testing set-up.

Tab. 7.1.: Test program to determine the ultimate capacity of laterally loaded rigid monopile at different conditions

Test set	Test identifier	Relative density index I_d $(-)$	length to diameter ratio L/D $(-)$	Loading eccentricity e/D $(-)$
Set 1	M-1-1	0.53	2	4.8
	M-1-2		2	
	M-1-3		3	
	M-1-4		3	
	M-1-5		4	
	M-1-6		4	
	M-1-7		5	
	M-1-8		5	
Set 2	M-2-1	0.53	3	6.0
	M-2-2			7.3
	M-2-3			7.3
Set 3	M-3-1	0.70	3	4.8
	M-3-2	0.70		
	M-3-3	0.90		

7.4 Failure criteria performance

7.4.1 Effect of length to diameter ratio L/D

The monopile embedded length is varied between 160 and 400 *mm*, equivalent to a variation of the length to diameter ratio between 2 and 5. The obtained lateral response for each test is presented in the force-displacement space, where the displacement is deduced at the ground level (Figure 7.5a). The $0.1D$ failure criterion is applied, and the responses are normalized according to the obtained ultimate forces as a function of the corresponding displacements. The normalized responses are presented in Figure 7.5b, showing the effect of the length to diameter ratio on the performance of the $0.1D$ failure criterion. It is shown that the ability of this criterion to define an equivalent ultimate capacity for different cases (i.e. corresponding to a single master curve) is limited, especially for relatively short cases.

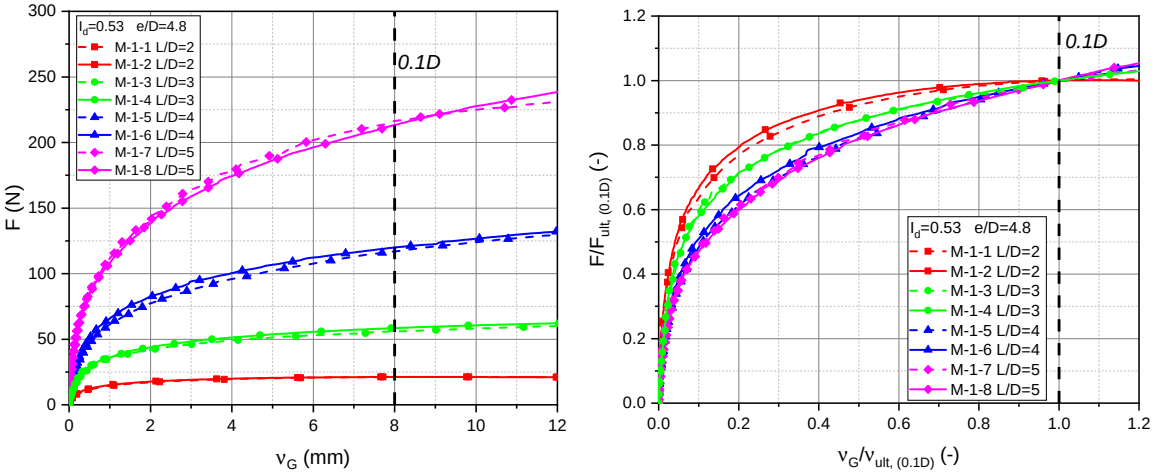

(a) (b)

Fig. 7.5.: (a) Lateral response ($F - \nu$) and (b) normalized lateral response ($F/F_{ult} - \nu/\nu_{ult}$) of rigid monopiles with different length to diameter ratios

The lateral responses of all tests are also presented in the moment-rotation space in Figure 7.6a. The 2° failure criterion is applied, and the responses are normalized according to the obtained ultimate forces and the corresponding rotations. The normalized responses are presented in Figure 7.6b, showing the effect of the length to diameter ratio on the performance of the 2° failure criterion. Based on the comparison between the normalized responses for the two criteria, it is observed that better performance is shown by the 2° criterion, while a notable effect of the length to diameter ratio is still remarked. It should be noted that the outputs of the inclinometer sensor are missed for the two tests with $L/D = 3$. The rotation is deduced based on the outputs of the two laser sensors, which affects the precision of the initial part of the curves. However, these results are not necessary to reach this partial conclusion.

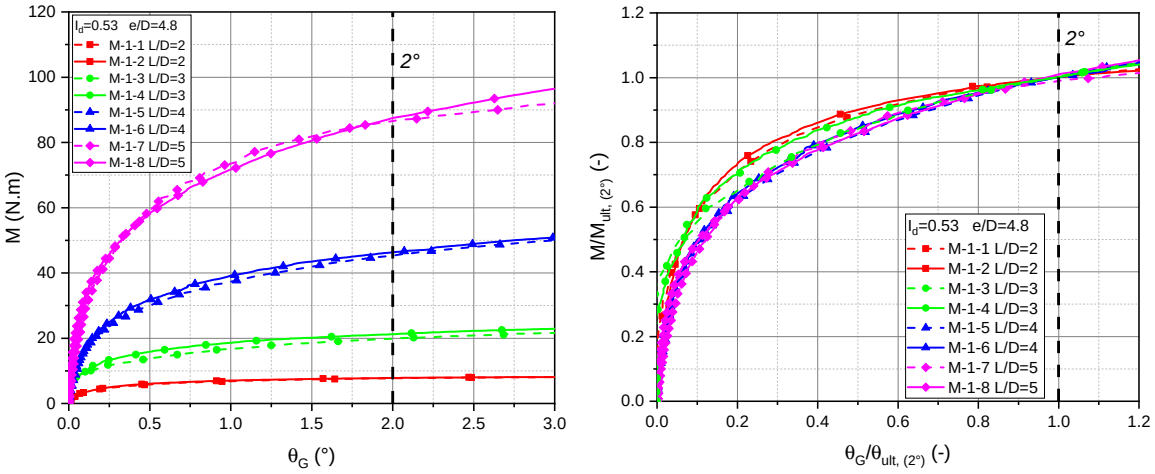

(a) (b)

Fig. 7.6.: (a) Lateral response ($M - \theta$) and (b) normalized lateral response ($M/M_{ult} - \theta/\theta_{ult}$) of rigid monopiles with different length to diameter ratios

7.4.2 Effect of loading eccentricity

The loading eccentricity is varied between 385 and 585 *mm*, equivalent to a variation of the eccentricity in terms of (e/L) between 1.6 and 2.4. The lateral response obtained for each test is presented in the force-displacement space, where the displacement is deduced at the ground level (Figure 7.7a). The $0.1D$ failure criterion is applied, and the responses are normalized according to the obtained ultimate forces and the corresponding displacements. The normalized responses are presented in Figure 7.7b, showing the negligible effect of the loading eccentricity on the performance of the $0.1D$ failure criterion.

The lateral responses of all tests are also presented in the moment-rotation space in Figure 7.8a. The $2°$ failure criterion is applied, and the responses are normalized according to the obtained ultimate forces and the corresponding rotations. The normalized responses are presented in Figure 7.8b, showing also the negligible effect of the loading eccentricity on the performance of the $2°$ failure criterion. The relative enhancement of this criterion is attributed to the accommodation of the $2°$ failure criterion with the length to diameter ratio: the decrease of the embedded length decreases the depth of the monopile rotation pivot, and then a rotation of $2°$ corresponds to a lower displacement at the ground level.

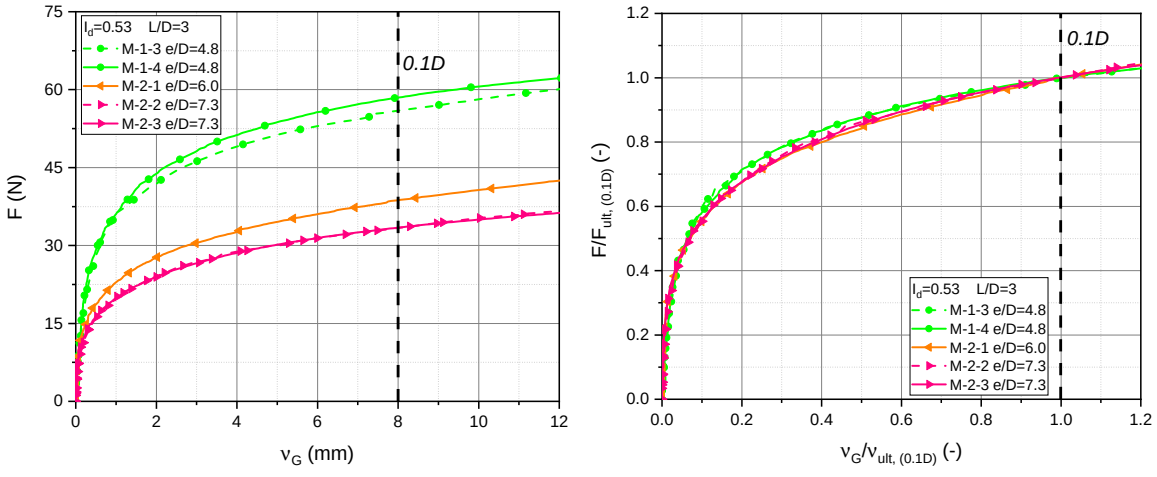

Fig. 7.7.: (a) Lateral response $(F - \nu)$ and (b) normalized lateral response $(F/F_{ult} - \nu/\nu_{ult})$ of rigid monopiles at different loading eccentricities

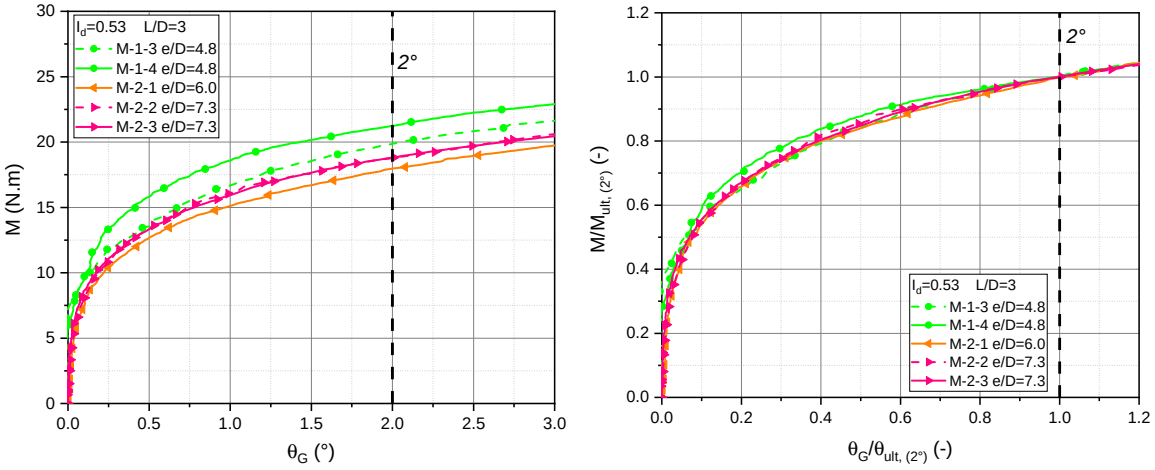

Fig. 7.8.: (a) Lateral response ($M-\theta$) and (b) normalized lateral response ($M/M_{ult}-\theta/\theta_{ult}$) of rigid monopiles at different loading eccentricities

7.4.3 Effect of relative density index I_d

The relative density index of the sand is varied between 0.53 and 0.9. The lateral response obtained for each test is presented in the force-displacement space, where the displacement is deducted at the ground level (Figure 7.9a). The $0.1D$ failure criterion is applied, and the responses are normalized according to the obtained ultimate forces obtained and the corresponding displacements. The normalized responses are presented in Figure 7.9b, showing the negligible effect of the sand relative density index on the performance of the $0.1D$ failure criterion.

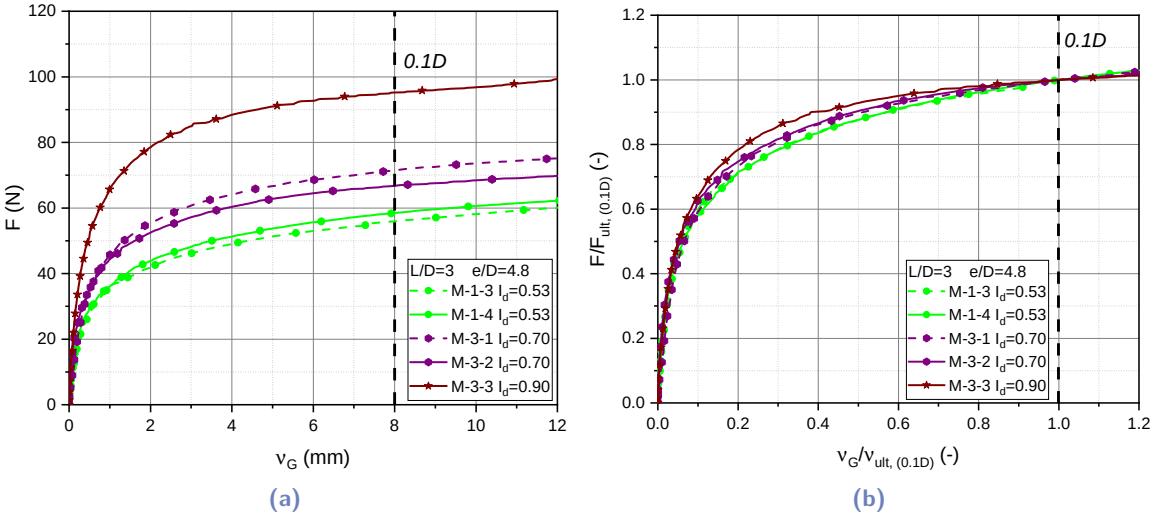

Fig. 7.9.: (a) Lateral response ($F-\nu$) and (b) normalized lateral response ($F/F_{ult}-\nu/\nu_{ult}$) of rigid monopiles at different relative density indexes of the sand

The lateral responses of all tests are also presented in the moment-rotation space in Figure 7.10a. The 2° failure criterion is applied, and the responses are normalized according to the obtained ultimate forces and the corresponding rotations. The normalized responses are presented in Figure 7.10b, showing also the negligible effect of the sand relative density index on the performance of the 2° failure criterion.

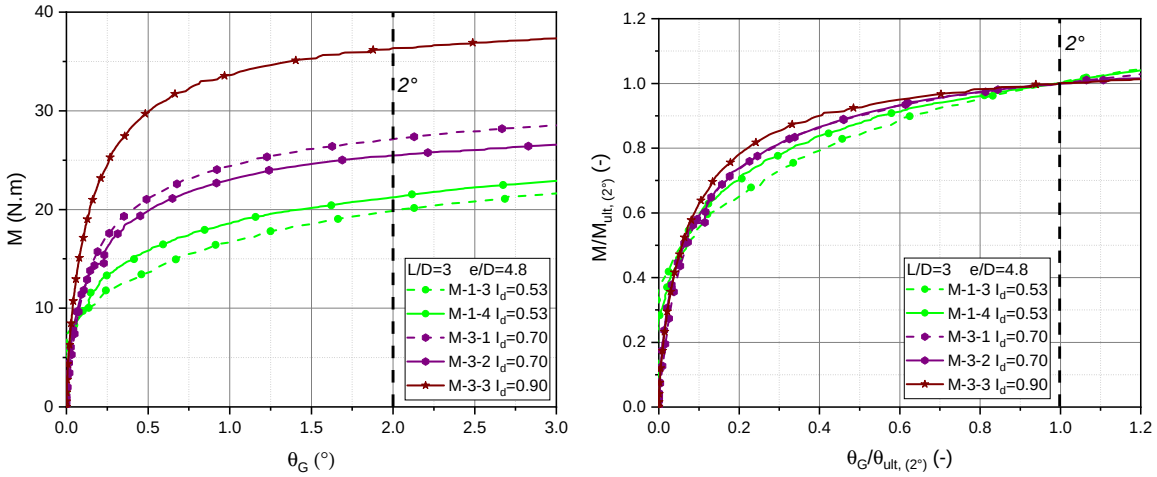

Fig. 7.10.: (a) Lateral response ($M-\theta$) and (b) normalized lateral response ($M/M_{ult}-\theta/\theta_{ult}$) of rigid monopiles at different relative density indexes of the sand

7.4.4 Results validity and partial conclusions

The parametric study conducted in this work leads to the following conclusions:

- The limitation of the conventional failure criteria of rigid monopiles for relatively small length to diameter ratios ($L/D < 4$) has been highlighted.
- The negligible effect of the loading eccentricity and the sand properties on the performance of the failure criteria has been shown.
- A better performance of the 2° criterion compared with the $0.1D$ criterion has been shown.

Conscious of 1g scaling challenges, relevant results of the literature (LeBlanc et al., 2010, Abadie, 2015) are presented with those of the first set of the test program in Figure 7.11. The results of tests with close length to diameter ratios have a very good agreement, showing the good performance of the testing procedure and the validity of the obtained results.

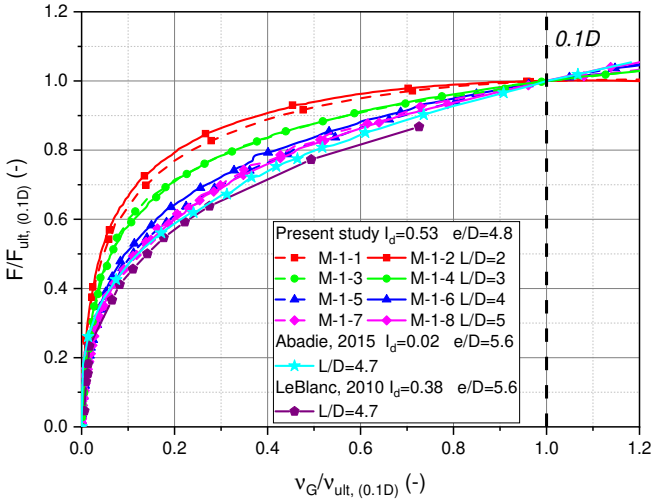

Fig. 7.11.: Consistency between the obtained results and results from the literature

7.5 Ultimate capacity obtained by different methods

The ultimate forces corresponding to the various tests performed are determined by the failure criteria adopted in Section 7.1.1. The obtained results are presented in Table 7.2 and Figure 7.12.

Tab. 7.2.: Ultimate capacity of laterally loaded rigid monopile at different conditions determined by different methods

Test set	Test identifier	Ultimate force (N)			
		$0.1D$	2°	Manoliu et al., 1985	Zhang et al., 2005
Set 1	M-1-1	21.2	20.1	22.9	11.8
	M-1-2	21.2	20.3	22.7	11.8
	M-1-3	56.0	51.5	71.2	35.0
	M-1-4	58.5	55.1	70.7	35.0
	M-1-5	117.0	117.8	162.3	74
	M-1-6	119.9	120.4	164.2	74
	M-1-7	216.4	224.9	299.4	130.4
	M-1-8	213.3	227.2	326.9	130.4
Set 2	M-2-1	38.7	37.0	57.3	29.4
	M-2-2	33.4	32.1	45.3	25.4
	M-2-3	33.4	32.2	47.2	25.4
Set 3	M-3-1	71.5	70.4	85.0	51.6
	M-3-2	66.8	66.2	77.0	51.6
	M-3-3	95.2	94.4	105.8	84.2

Figure 7.12 shows that the ultimate forces obtained by the two conventional criteria ($0.1D$, and $2°$) are close, with slightly higher values obtained by the $0.1D$ criterion for relatively small length to diameter ratios ($L/D = 2; 3$) and by the $2°$ criterion for relatively large length to diameter ratios ($L/D = 5$). The ultimate forces obtained by Manoliu et al., 1985 criterion constitute an upper bound for the other criteria since it is based on the identification of the fully mobilized capacity (horizontal asymptote to the curve). The application of the simplified theoretical method proposed by Zhang et al., 2005 highly underestimates the ultimate capacity for different cases. This underestimation can be justified as a consequence of disregarding the additional components of the soil reaction (e.g. force and moment at the monopile base, vertical shear traction at the soil-pile interface; Byrne et al., 2017) when relatively rigid monopiles are considered.

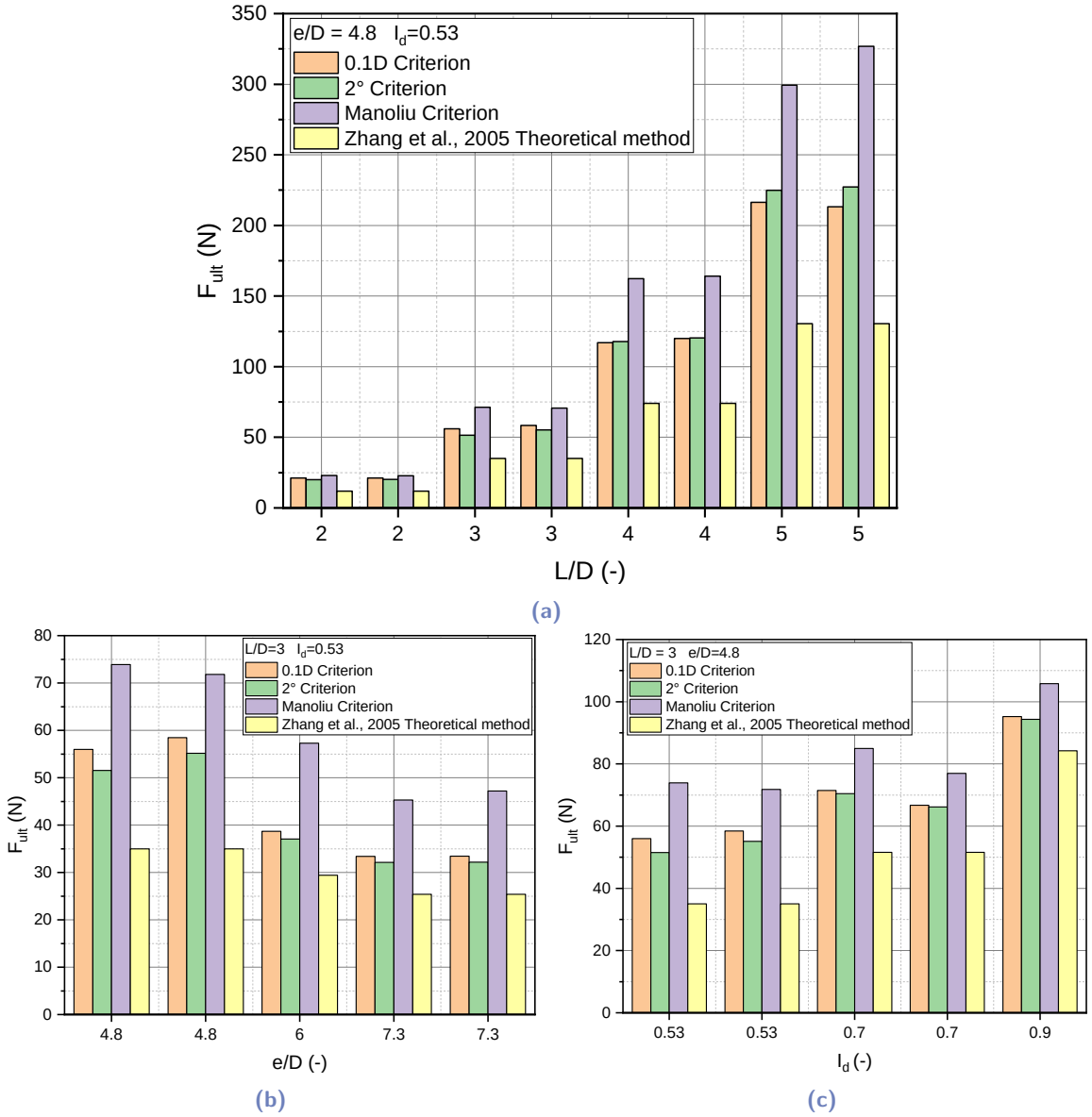

Fig. 7.12.: Effet of various parameters on the ultimate force obtained by different failure criteria: (a) length to diameter ratio, (b) eccentricity, (c) sand relative density index

7.6 New failure criterion

7.6.1 Numerical normalization method

After showing the limitations of the application of the conventional failure criteria at relatively small length to diameter ratios, a numerical idea is proposed to determine an ideal ultimate force and the corresponding displacement leading to a perfect normalization of lateral responses with different length to diameter ratios. This method started by choosing a reference curve and applying the $0.1D$ criterion to normalize it. Then, a *Python* code is developed, which successively normalized the other curves according to their whole range of displacement by increments of 0.1 mm. For each curve and at each step, the normalized curve is compared to the reference normalized curve, and the relative error is calculated. The displacement which led to the minimum error is considered as the failure criterion to the corresponding curve. This numerical method is illustrated in Figure 7.13.

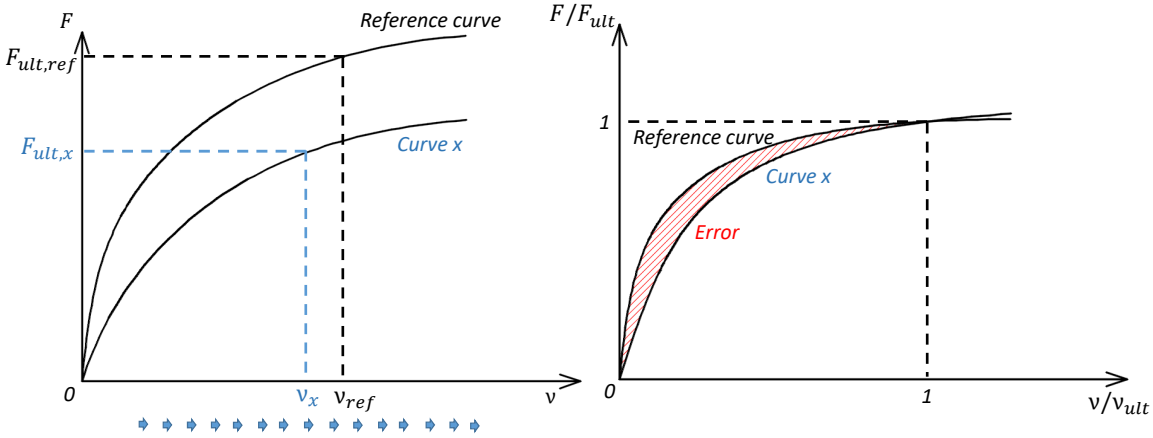

Fig. 7.13.: Schematic illustrating the applied numerical normalization method

In this study, the reference curve is the curve corresponding to the length to diameter equal to 4, at which the conventional failure criteria are commonly adopted. For this case, the two conventional criteria ($0.1D$ and $2°$) gave similar results. The proposed numerical method is applied to the first set of performed tests (L/D effect). The obtained results are presented in Table 7.3, and the corresponding normalized responses are presented in Figure 7.14.

Tab. 7.3.: Displacement at the ground level and ultimate force for rigid monopiles with different length to diameter ratios determined by the numerical method

			Numerical method	
Test set	Test identifier	L/D $(-)$	$\nu_{G,ult}$ (mm)	F_{ult} (N)
Set 1	M-1-1	2	1.9	16.8
	M-1-2	2	1.8	17.2
	M-1-3	3	4.2	50.7
	M-1-4	3	3.7	51.4
	M-1-5	4	12.8	131.5
	M-1-6 (Ref.)	4	8.0	120.8
	M-1-7	5	9.0	219.2
	M-1-8	5	18.5	264.4

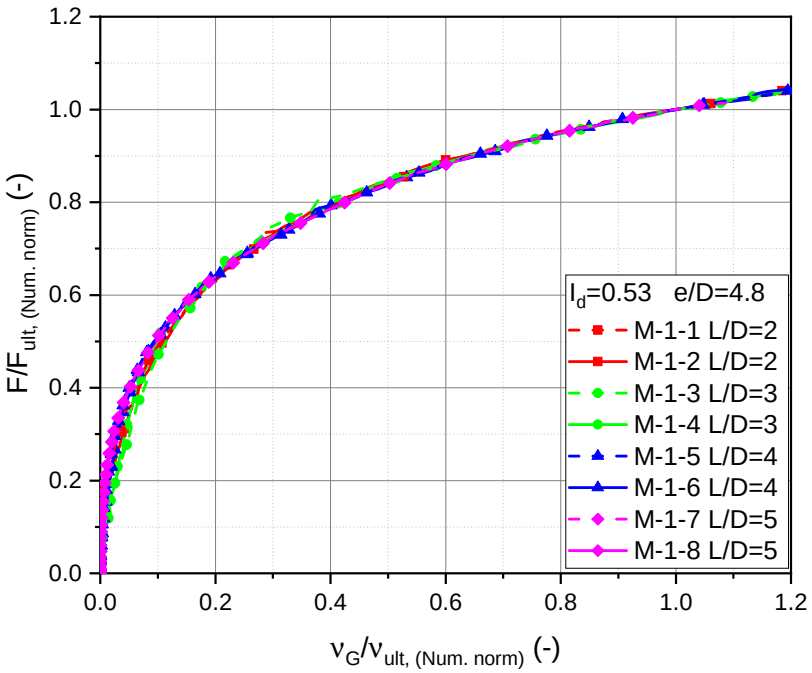

Fig. 7.14.: Normalized lateral responses with different length to diameter ratio by the numerical method

7.6.2 Proposition of a new criterion

As Manoliu et al., 1985 criterion represents the fully mobilized resistance of the monopile, the ultimate forces obtained by all the studied criteria are normalized according to the ultimate forces obtained by this criterion. Figure 7.15 shows that the conventional criteria lead to forces close to the fully mobilized resistance of the monopile for relatively small length to diameter ratio: $\sim 90\%$ of the fully resistance for $L/D = 2$, while these percentages decrease with the increase of the length to diameter ratio to achieve $\sim 65\%$ for $L/D = 5$. This finding is in accordance with the interpretation of the results of *PISA* project presented in Section 7.2. The normalized forces obtained by the numerical method seem to be independent of the length to diameter ratio, with a percentage estimated as 75% of the monopile fully mobilized resistance. This finding is the basis of a new failure criterion proposed as:

$$F_{ult} = 0.75 F_{max} \tag{7.3}$$

where F_{max} is the monopile fully mobilized resistance determined by the simple fit method based on Manoliu et al., 1985 (Figure 7.1).

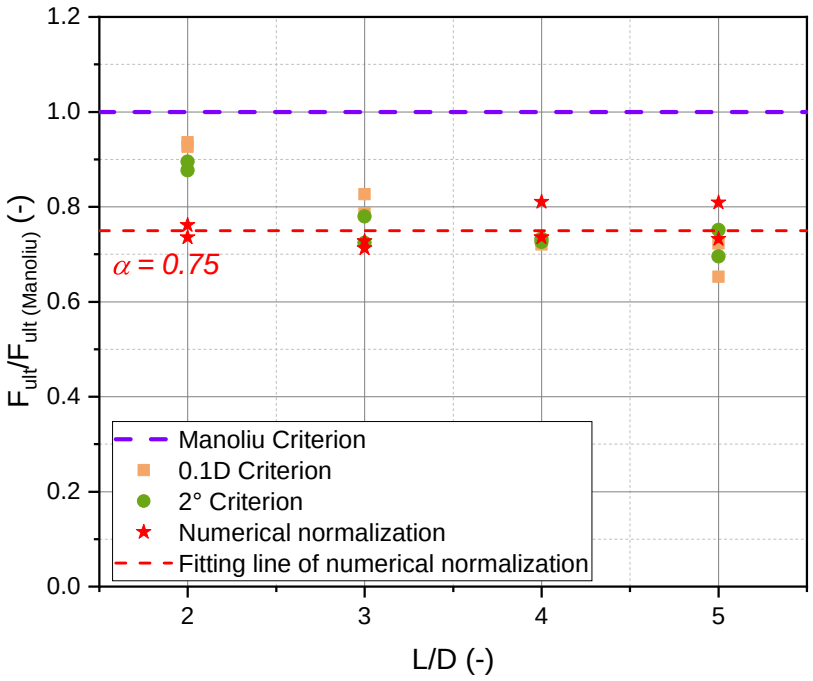

Fig. 7.15.: Normalization of the ultimate forces obtained by different failure criteria according to the monopile fully mobilized resistance at different length to diameter ratios

The proposed criterion is inspired by the failure criterion proposed by Manoliu et al., 1985. It ensures a performance equivalent to that of the conventional criteria for moderate length to diameter ratios of rigid monopiles, while it conserves this performance for smaller length

to diameter ratios, which are expected to become dominant in the domain of offshore wind turbines. Besides, this criterion can be applied for the lateral monopile response in the force-displacement or moment-rotation spaces. Figure 7.16 presents the new failure criterion proposed with different failure criteria adopted in this study.

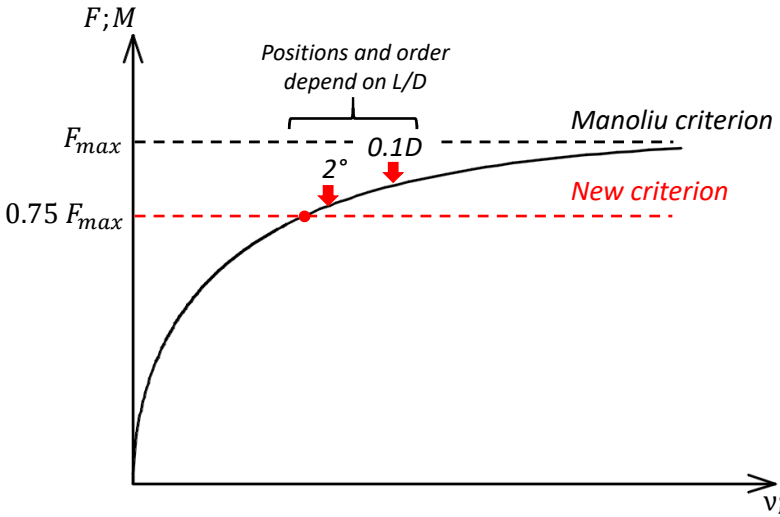

Fig. 7.16.: Schematic of the new failure criterion with different failure criteria adopted in this study

7.6.3 Validation of the new criterion

The new failure criterion is applied to determine the ultimate forces for the set of tests with different length to diameter ratio. Then, the lateral responses are normalized according to the ultimate forces and the corresponding displacements, and presented in Figure 7.17c.

After comparing the normalized curves obtained by the new criterion and the conventional criteria (Figure 7.17), the ability of this criterion to get an equivalent performance (master curve) for different length to diameter ratios is demonstrated.

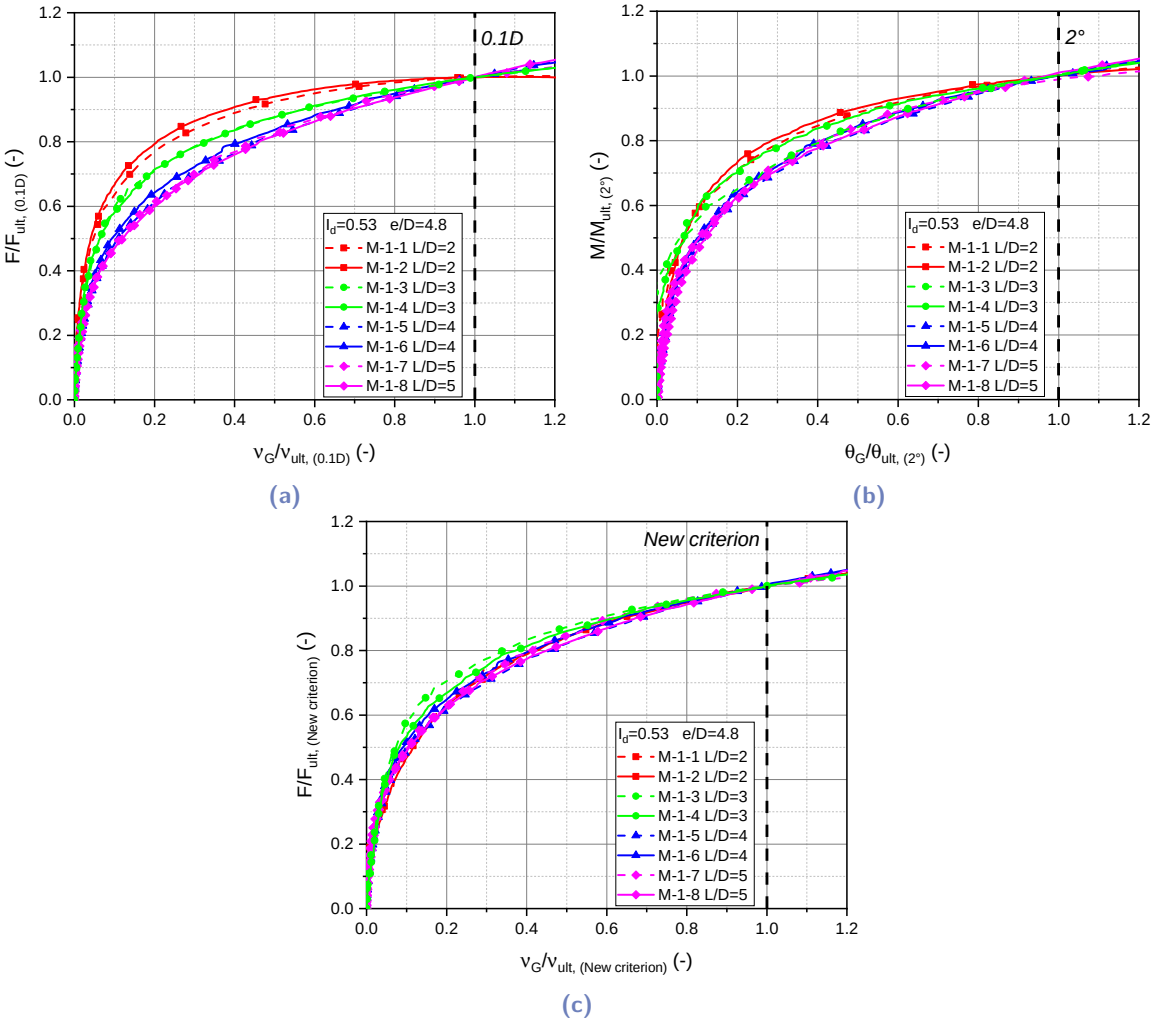

Fig. 7.17.: Normalized lateral responses for tests with different length to diameter ratio by different failure criteria: (a) $0.1D$, (b) $2°$, and (c) the new criterion

7.7 Application of the new criterion on field tests

The new criterion is proposed and validated based on 1g small-scale models of rigid monopiles. It is more reliable to verify the performance of this criterion when applied to large-scale models. The three tests performed by *PISA* project and presented in section 7.2 are used to fulfill this purpose. These tests are large-scale models of rigid monopiles conducted in field conditions in a dense marine sand at *Dunkirk*. The monopiles have a diameter of $0.762\ m$ and large thicknesses, ensuring that yielding of the monopile wall did not occur in any of the tests (perfectly rigid monopiles). Lateral loading is applied at an eccentricity equal to $\sim 10\ m$. The length to diameter ratio is varied as presented in Table 7.4. For more details, refer to Byrne et al., 2020b. In the framework of *PISA* project, the conventional failure criteria $0.1D$ and $2°$ are adopted to identify the ultimate capacity of the monopiles. In this study, the new failure criterion is applied to three field tests, and the results obtained by the three failure criterion are presented in Table 7.4. The findings

are in good agreement with the previous conclusions based on the test program of this study: (i) ultimate forces obtained by the two conventional criteria are very close, (ii) the new criterion is similar to the conventional criteria at a moderate length to diameter ratio ($L/D = 5.25$), and (iii) the new criterion leads to lower ultimate forces at relatively small length to diameter ratio ($L/D = 3$) and higher ultimate forces at relatively large length to diameter ratio ($L/D = 8$).

Tab. 7.4.: Ultimate forces of some field tests, performed by *PISA* project, determined by the $0.1D$, 2°, and the new failure criteria (some data from Byrne et al., 2020b

Test identifier	L/D $(-)$	Ultimate force (kN)			Variation acc. to $0.1D(\%)$
		$0.1D$	2°	New criterion	
DM7	3	49.6	49.2	43.5	-12.3%
DM4	5.25	226.3	227.2	218.6	-3.4%
DM3	8	527.1	522.2	590.5	$+12.0\%$

Then, the lateral responses are normalized according to the $0.1D$ failure criterion (Figure 7.18a) and the new criterion (Figure 7.18b). Again, the capability of the new criterion to get an equivalent normalized response at different length to diameter ratios is demonstrated, but now with field test conditions. This equivalent performance is manifested by a perfect normalization of the lateral response of the three tests, while the normalization according to the $0.1D$ criterion showed a large deviation in the obtained curves, especially at the relatively small length to diameter ratio ($L/D = 3$).

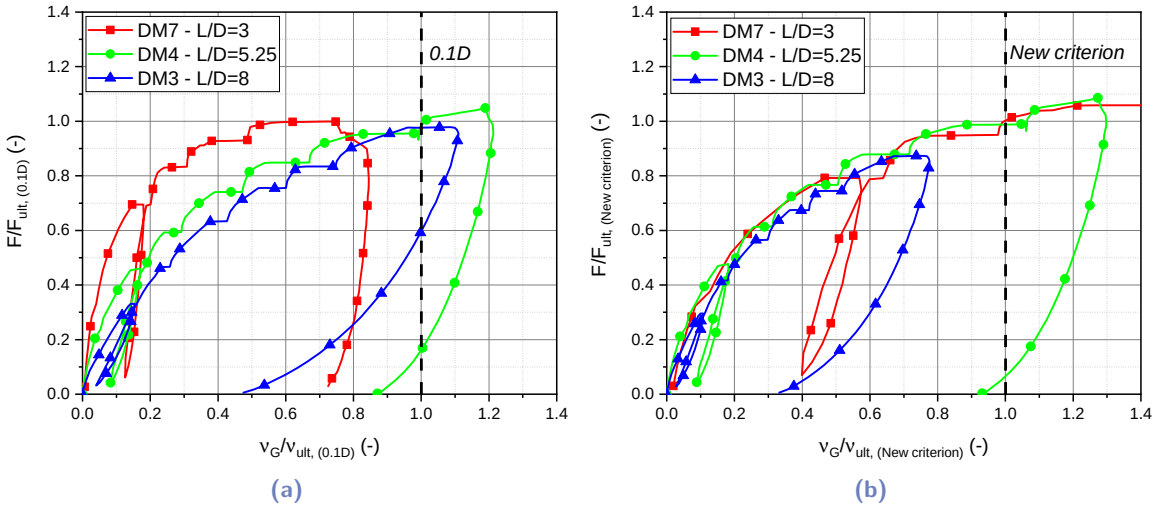

Fig. 7.18.: Normalized lateral responses of three field tests performed by *PISA* project according to (a) the $0.1D$ and (b) the new failure criteria

7.8 Finite element analysis

The constitutive model presented in Chapter 6 has been implemented in the *3D* finite element software (*Cesar-LCPC*) by the software development team. The current parametric study on laterally loaded monopile forms an opportunity to examine the performance of this constitutive model.

7.8.1 Geometry, mesh, and boundary conditions

A *3D* finite element simulation is carried out for the tube representing the monopile and the surrounding sand mass (Figure 7.19a). The stainless steel tube has a diameter of 80 *mm* and a thickness of 2 *mm*, and the modeled sand mass conserves the dimensions of the container used in the experimental procedure ($D = 550$ *mm*). The length of the monopile and the soil mass depends on the test simulated. The symmetry of the problem permits simulating half of the model. A quadratic regular mesh is adopted for the model, where the mesh of the sand mass is refined close to the monopile and at the higher expected strain levels (Figure 7.19c). Similar to Section 4.5.2, the adopted mesh is validated by preliminary calculations. According to the test conditions, suitable boundary conditions are applied (Figure 7.19b).

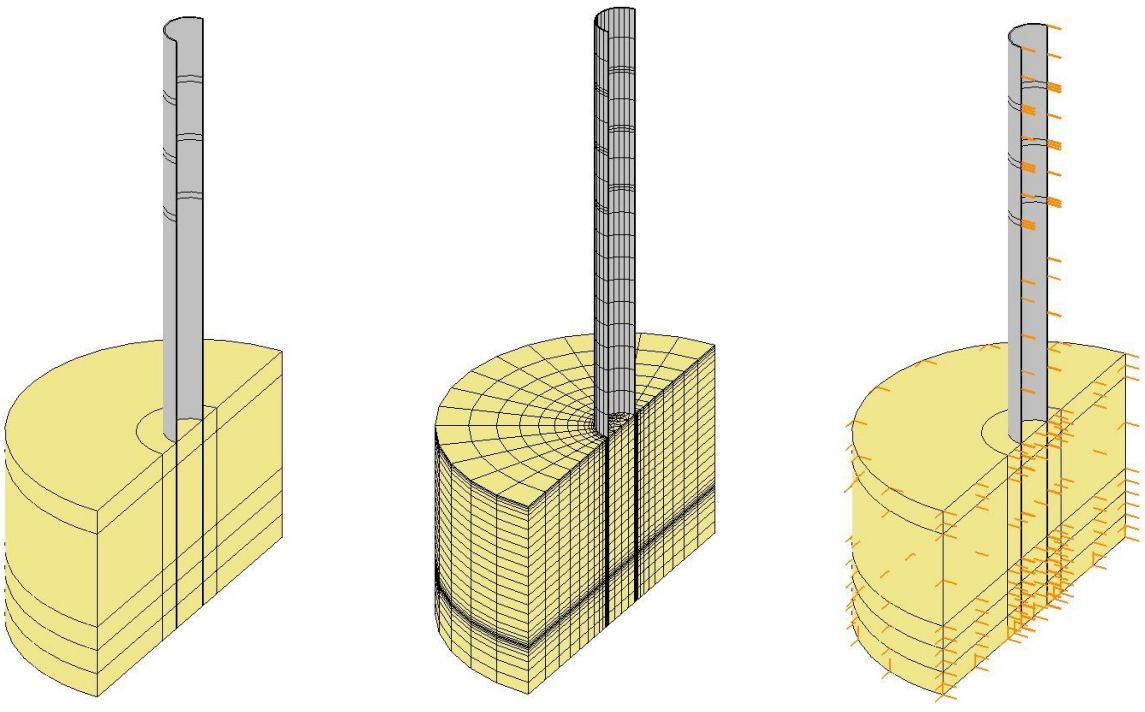

Fig. 7.19.: Presentation of the *3D FEM* model carried out to simulate the lateral response of the monopile with $L/D = 3$: (a) Geometry (b) Mesh (c) Boundary conditions

7.8.2 Material properties

Isotropic linear elastic behavior law is defined for the stainless steel material, whose parameters are presented in Section 4.5.2. The *NE34* sand parameters are initially adopted from the calibration performed in Chapter 6 based on the triaxial findings for the three different relative density indices ($I_d = 0.50$, 0.70, and 0.90; $I_d = 0.50$ being adopted for $I_d = 0.53$). Concerning the interface elements defining the behavior at the soil-monopile interaction, a perfect bond is considered due to their limited effect on the lateral monopile response Brown and Shie, 1991. This assumption is also validated by preliminary tests using *Mohr-Coulomb MC* criterion.

7.8.3 Results and discussions

A staged calculation is applied consisting of three calculation phases:

- Initialization: only the sand mass is activated, and the corresponding weight is applied to generate the initial stress field.
- Activation of the monopile: the geometry representing the monopile is activated, and the corresponding weight is applied.
- Lateral loading: successive increments of loading are applied to obtain the force-displacement curve.

It is decided to start with the simulation of the third set of the monotonic test program (Table 7.1), corresponding to the variation of the relative density index as the most significant case to examine the performance of the model. The obtained results are presented in Figure 7.20 compared with the experimental findings in the force-displacement space. The ultimate forces are defined by the new failure criterion proposed in this study, corresponding to an average ultimate displacement approximately equal to 4 *mm* for this set of tests. The obtained results show an underestimation of the lateral response at relatively small displacement, and an overestimation of the failure state (especially for very dense sand $I_d = 0.90$). The initial underestimation can be related to the driving of the monopile during the installation, which is not simulated by this calculation. The overestimation of the failure state can be justified by various reasons: (i) an overestimation of the failure criterion parameters, supported by the low-stress level characterizing this application; (ii) the distinct stress paths between the current application and the triaxial compression tests from which the parameters are calibrated.

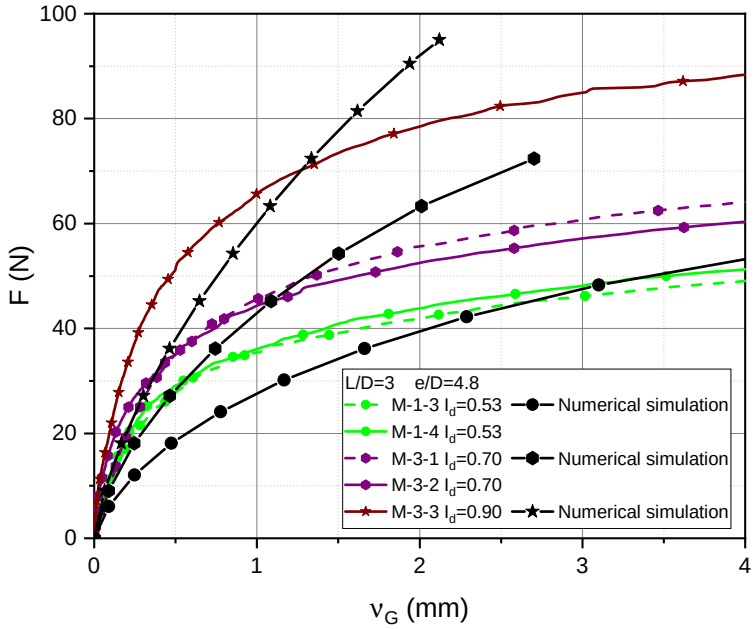

Fig. 7.20.: Simulation of the lateral response of the monopile with $L/D = 3$ at three different relative density indices based on triaxial findings

The following modifications are applied to the parameters, trying to enhance the comprehension of this deviation:

- The dilatancy (flow rule) of the sand is reduced by a factor corresponding to the idea presented in Section 6.5, aiming to consider the contraction phase effect. Factors of 0.68, 0.8, and 0.83 are applied respectively for $I_d = 0.53$, 0.70, and 0.90.

- The elastic modulus is multiplied by a factor of 2 in the three cases, aiming to outcome the initial underestimation of the response.

- The parameters of the failure criterion are manually adjusted, aiming to reach a reasonable failure of the monopile compared with the experimental findings. The proposed parameters are presented in Table 7.5.

Tab. 7.5.: *Hoek-Brown* failure criterion parameters proposed after a back-analysis based on a lateral monopile response for *NE34* sand

Set	$I_{d,0}$	m_1	α_1
1	0.53	3.84	0.94
2	0.70	4.50	0.94
3	0.90	5.50	0.94

After applying these modifications, a good agreement is obtained between numerical and experimental lateral responses. The corresponding failure criterion (from back-analysis) is compared to the triaxial findings including the uncertainties margin evaluated in Section 3.2.4, showing the fall or the proximity of the corrected criterion in the uncertainties margin.

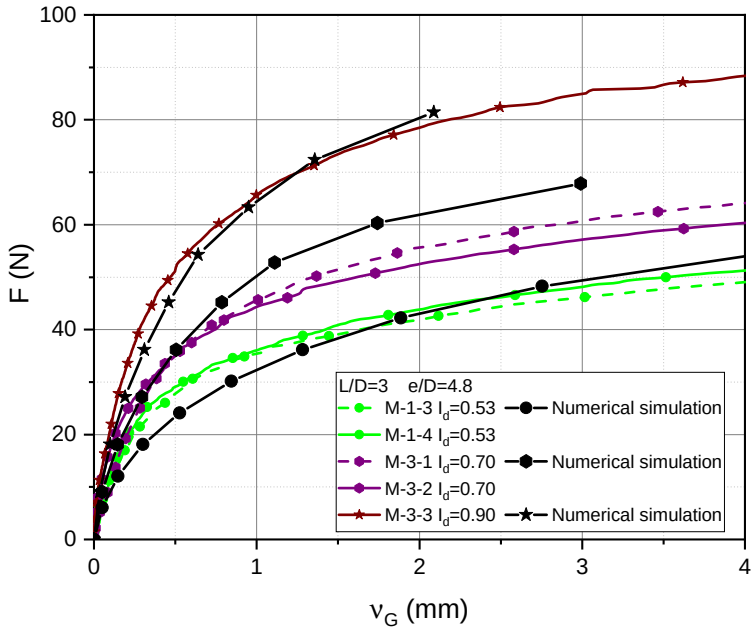

Fig. 7.21.: Simulation of the lateral response of the monopile with $L/D = 3$ at three different relative density indices based on corrected parameters

Then, the corrected parameters corresponding to $I_d = 0.50$ are adopted to simulate the first set of the monotonic test program (Table 7.1), corresponding to the variation of the length to diameter ratio. The four cases are simulated with the same set of parameters, showing a good agreement with the experimental findings (Figure 7.20). The methodology performed can be considered as a partial validation of the model, highlighting its ability to simulate the sand response at different stress levels without changing the parameters. The issue encountered seems to be the determination of suitable parameters at low stress levels. This challenge is extensively discussed in Chapter 3, where the qualitative findings of the tilt method led to similar conclusion.

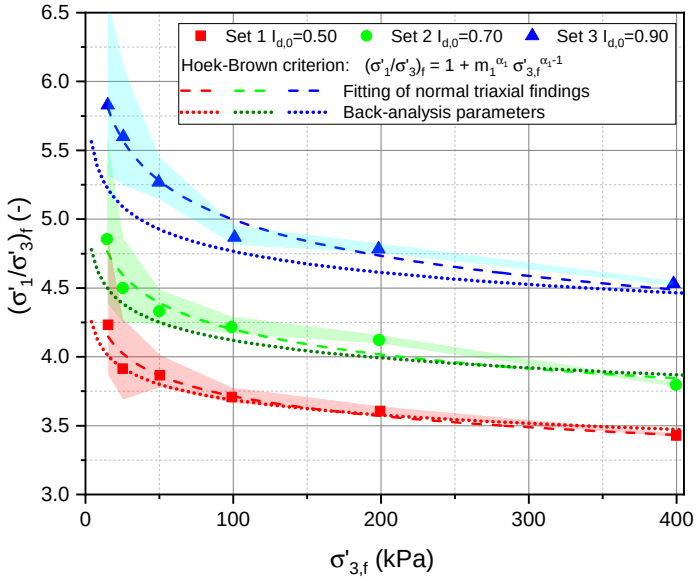

Fig. 7.22.: *Hoek-Brown* failure criterion parameters calibrated against experimental triaxial findings and those corrected after back-analysis of the numerical simulations

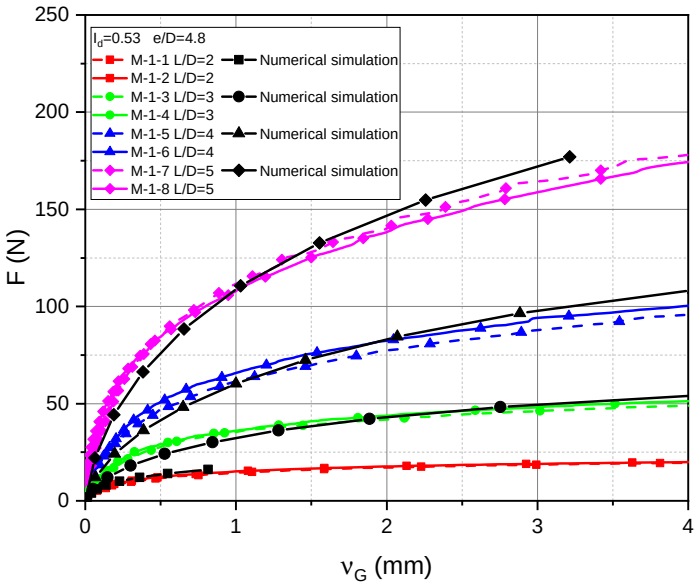

Fig. 7.23.: Simulation of the lateral response of the monopile at different length ratios for a relative density index of 0.53

Finally, some numerical results are presented in Figure 7.24, in terms of lateral displacement, principal stress, and plastic strain fields. These results correspond to a force of approximately $\sim 50\ N$, corresponding to the ultimate capacity of the monopile. These kind of simulations enhance the comprehension of the mechanisms underlying the lateral response, where Figure 7.24 clearly shows the difference between the failure mechanism of the flexible monopiles (wedge failure) and the rigid monopiles (failure occurred also at the base of the monopile, present study). Further efforts can be devoted to enhancing the performance of this model, while the current presentation aims to show its promising capabilities.

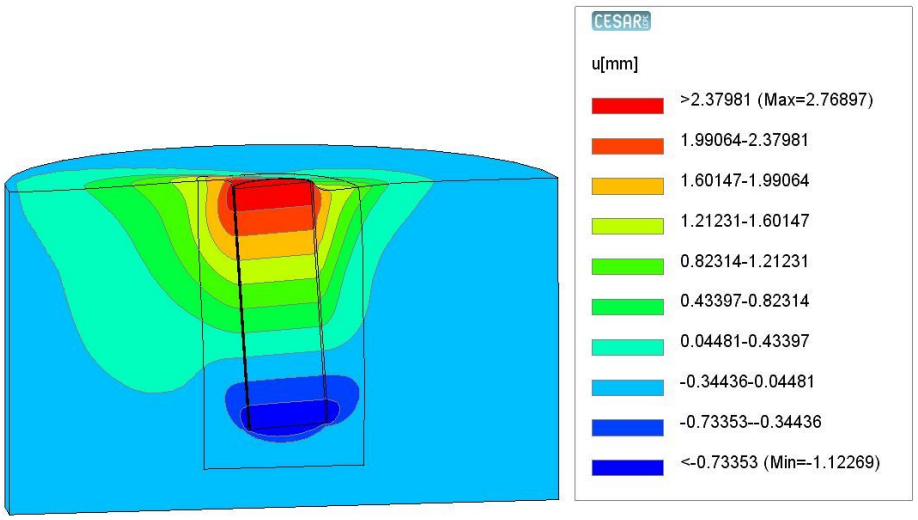

(a)

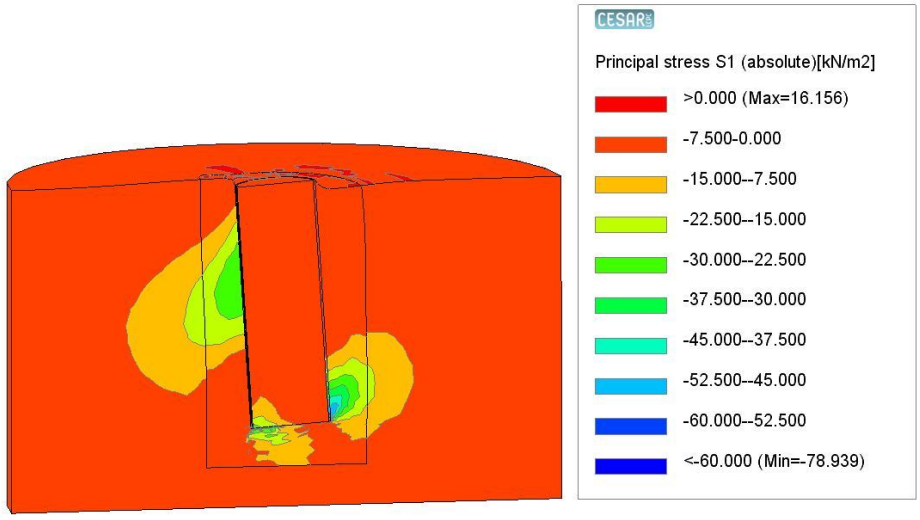

(b)

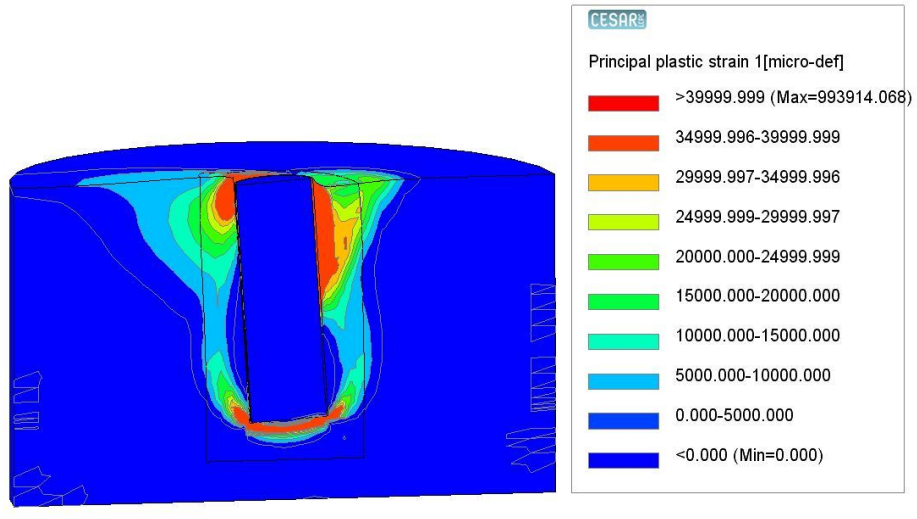

(c)

Fig. 7.24.: Visualization of the sand response under a load of $\sim 50\,N$ around a monopile with $L/D = 3$: (a) Lateral displacement (b) Principal stress (c) Principal plastic strain

7.9 Conclusion of the chapter

This chapter illustrates the findings of an experimental parametric study on a laterally loaded rigid monopile. This study shows the limitation of the conventional failure criteria to define equivalent ultimate capacities for monopiles with different length to diameter ratios. A new failure criterion is proposed, and its capability to fulfill this purpose is proven.

On another side, the findings of this parametric study are used to show the performance of a numerical *FEM* model informed by the constitutive model presented in Chapter 6. The simulations performed show the promising capabilities of this model to simulate the monotonic response of rigid monopiles at different stress levels.

8 Conclusions and perspectives

The conclusions drawn from the different parts of this study are presented below:

- Estimation of load scenarios: the increase of the offshore wind turbines dimensions and their installation at relatively deep water depth affect the characteristics of the environmental loads. Based on wind and wave parameters representing the environmental conditions in the *North sea* and the *North Atlantic ocean*, the relevant load scenarios required for the design of the *DTU 10 MW RWT* are determined. In general, one-way loading can be considered in the case of fatigue and normal operational conditions, while two-way loading is encountered in the case of extreme wind or wave conditions.

- Development of representative 1g scale models: one of the principal aims of this study is the development of representative scale models, leading to significant results in laboratory conditions. The scaling laws proposed and adopted cover all the governing physical quantities involved in the different aspects of the problem: soil-monopile interaction, soil non-linearity, and dynamic sensitivity. Based on a triaxial test program studying the sand behavior at different stress levels, it is found that the dense sand at the prototype scale should be replaced by medium-dense sand in the laboratory to conserve a similar behavior. A dynamic *3D FEM Cesar-LCPC* model is validated based on available experimental findings (kerner, 2017) and used to show the dynamic similarity of the developed scale models. Besides, conscious of the difficulties underlying the 1g modeling, suitable testing procedures are adopted, leading to good repeatability of the obtained results. In parallel, based on the developed scale model, the possibility of the passage of the loading frequency to 1 *Hz* is validated. This passage is beneficial in terms of testing duration and permit to achieve higher numbers of cycles.

- Stress-dilatancy relations: the identification of the properties of the sand used in the scale models is mainly based on the stress-dilatancy theory. The original empirical relation proposed by Bolton, 1986 and the modified form proposed by Giampa and Bradshaw, 2018 are applied to establish the relationship between the excess of friction angle ($\phi'_p - \phi'_{cr}$) and the sand state (relative density index I_d and mean effective stress p'_f or p'_0). The obtained results are in agreement with Giampa and Bradshaw, 2018 and Chakraborty and Salgado, 2010, showing the need to modify the Bolton, 1986 relation to enhance its performance, especially at relatively low stresses. The stress-dilatancy parameters corresponding to *NE34* sand are determined and compared to

similar parameters available in the literature. The effect of grain properties on these parameters is discussed and showed a good agreement with the trends available in the literature. Finally, a tilting test is considered to determine the peak friction angle at extremely low stresses. The experimental difficulties inherent to this tilt method are highlighted, showing the impossibility to obtain quantitative measurements. However, the qualitative interpretation of the findings lets expect an overestimation of the physical quantities obtained by the stress-dilatancy relations at relatively low stresses.

- Numerical tools to estimate the first natural frequency of the offshore wind turbines: the performance of *3D FEM* model and two analytical methods to estimate the first natural frequency is examined based on experimental findings on a scale model obtained by kerner, 2017. The *3D FEM* model shows the best performance with an error smaller than 2% for different conditions. The analytical methods show good capabilities with an error ranging between 5 and 15%.

- Evolution of the first natural frequency: a parametric study is carried out, using the dynamic *3D FEM* model, to evaluate the effect of phenomena underlying the cyclic response on the evolution of the first natural frequency of the system. This study shows that the variation of the first natural frequency is affected by the combination of all these phenomena, depending on the soil, mono-pile, and structure properties. This study also showed that the semi-rigid monopile is more sensitive to subsidence cone formation (caused by the sand densification or hydrodynamic effects induced by waves and currents) than the rigid monopile, leading to a higher decrease in the first natural frequency. This finding can favor the adoption of rigid monopiles, which is the expected trend in the future.

- Elastoplastic constitutive model: this study aimed to provide a numerical tool capable of contributing to the understanding of rigid monopile behavior, which could be used to design this kind of monopiles. A constitutive model has been developed. This model is able to capture the main features of medium-dense to dense sand behavior: the dependence of the strength and the dilatancy on the mean effective stress, the pre-peak hardening, and the post-peak softening. The calibration of this model is based on the triaxial findings and applied in this study to determine the parameters corresponding to *NE34* sand. The obtained results show a good agreement with the experimental findings. This model can be used on different applications with different stress levels: (i) simulations of 1g laboratory tests, soil stability, pipe-soil interaction, and shallow foundations, which are characterized by relatively low-stress levels; (ii) conventional applications (e.g. deep foundations) characterized by relatively high-stress levels.

- Failure criterion for rigid monopiles: after showing the limitation of the conventional failure criteria to identify equivalent ultimate forces at different length to diameter ratios, a new criterion is proposed based on an experimental parametric study on a laterally

loaded rigid monopile. These criteria are applied on available field tests, showing a satisfying performance. The parametric study performed also leads to conclude that the conventional tilt criterion (tilt of $2°$) shows a better performance than the conventional displacement criterion (ground displacement of $0.1D$)

In addition, the work presented in this thesis can be the basis of further works in many directions:

- The 1g scale models are developed, and the testing procedures are validated. Thus, a relatively large testing program can now be launched. This testing program should tackle the conflicting points encountered in the literature. Besides, the findings of this testing program can be used to adopt and validate an empirical law for predicting the monopile response after a high number of cycles; this seems to be a promising method.

- As previously discussed, the state parameter (distance to *CSL*) governs the sand response. This assumption is validated against the monotonic response, while it is adopted on monotonic and cyclic applications (LeBlanc et al., 2010, Richards, 2019, present study...). Based on the stress-dilatancy relation determined for the *NE34* sand, a cyclic triaxial test program can be conducted to check the validity of this assumption during cyclic loading. In parallel, the similarity of sands having the same state parameter involves the secant stiffness (Altaee and Fellenius, 1994), while the validity of this similarity on the initial modulus is unclear. The application of the initial shear modulus profile (Hardin and Richart, 1963) to determine the modulus of sand at low-stress levels leads to relatively high values. Besides, the literature findings show an independence of the relative density index on soil modulus degradation (Kokusho, 1980), which seems to be in contrast with the state parameter approach. The scarce data for low-stress levels is the main cause of these ambiguous issues. Similar to the cyclic response, bender element or resonant column tests can be performed to evaluate the initial shear modulus profile at low-stress levels, and then check the validity of the state parameter approach in terms of initial soil modulus.

- The dynamic *3D FEM* model shows high capability to estimate the first natural frequency of offshore wind turbines. Detailed parametric studies can be conducted to well understand the effect of the monopile cyclic response on the evolution of the first natural frequency, depending on the monopile and soil properties (varying D, L/D, rigidity factor, initial soil modulus...). The findings of this kind of parametric studies can optimize the design of offshore wind turbine monopile.

- Generalize the parametric study tackling the effect of subsidence cone formation in offshore cases to consider the hydrodynamic scouring by adopting reasonable values inspired from realistic published data. These studies quantify the effect of this phenomenon on

the evolution of the system first natural frequency in the case of rigid monopiles and then judge the necessity to add scouring protection.

- In this study, a constitutive model capable of reproducing accurately the sand response is developed and implemented in *3D* finite element software (by the development team of the software). Then, *3D* simulations of lateral monopile response lead to promising findings, with some difficulties in the determination of the suitable parameters expected to be due to the low stresses. Further efforts are required to test the performance of this model on other applications and at different stress levels. The solid validation of this model can ensure an efficient tool contributing to the comprehension of the rigid monopile key mechanisms.

- Most empirical relations widely adopted to predict the cyclic response of monopile depends on the cyclic magnitude ratio (ζ_b). This cyclic ratio depends on the defined failure criterion (Frick and Achmus, 2020, present study,...), which affects the parameters of the obtained law and restrain the possibility to compare the available works. In parallel, this study shows the inability of the conventional failure criteria to identify equivalent ultimate forces at different length to diameter ratios, which affects the reliability of the application of these laws at different conditions. After showing the performance of the new failure criterion proposed in this study, a large database of experimental results is been assembled, whose purpose is to allow the re-evaluation of the empirical design parameters based on the new criterion, leading to an attempt to propose a versatile empirical law.

A

Appendices

A.1 Sensors calibration

Internal force sensor of the triaxial set-up

This sensor is calibrated after loading by known weights and evaluation of the corresponding outputs.

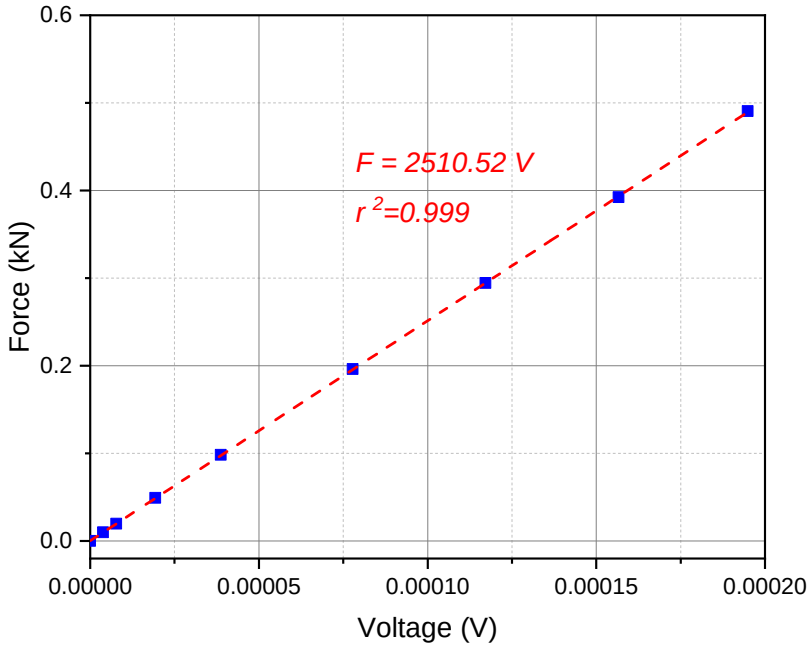

Fig. A.1.: Calibration of the internal force sensor of the triaxial set-up

Force sensor of the monotonic set-up

This sensor is calibrated after loading by known weights and evaluation of the corresponding outputs.

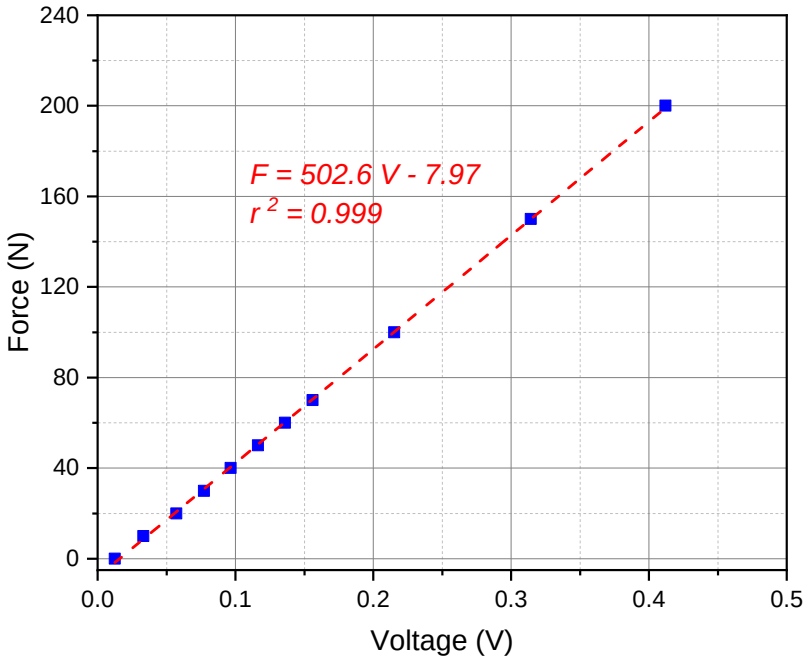

Fig. A.2.: Calibration of the force sensor used in the monotonic test procedure

Force sensor of the cyclic set-up

This sensor is calibrated using a force-controlled loading frame.

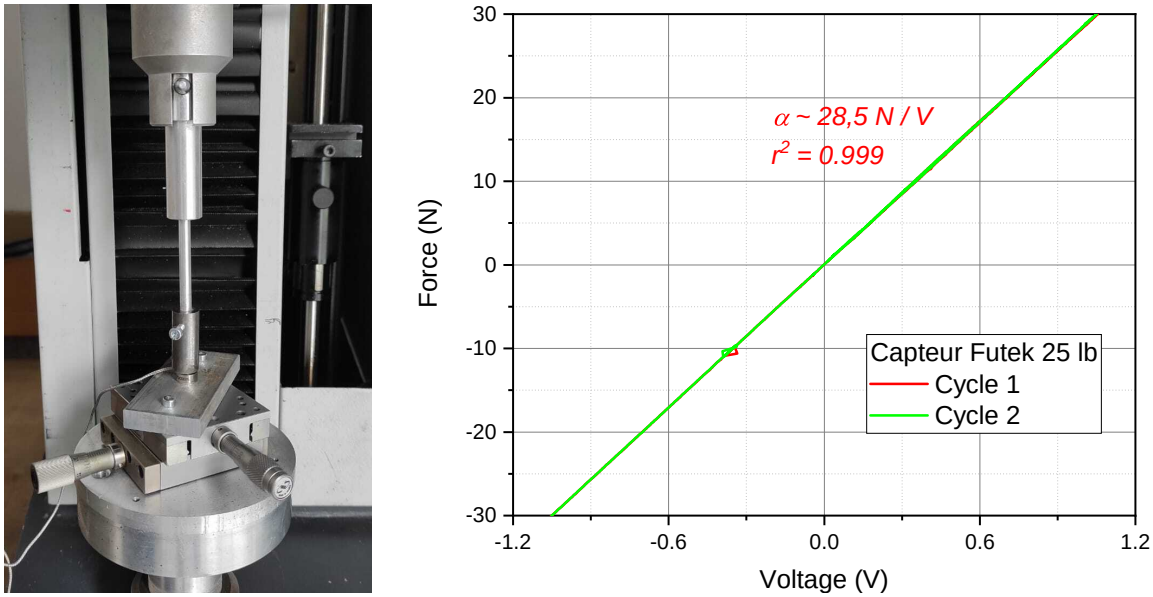

(a) (b)

Fig. A.3.: Calibration of the force sensor used in the cyclic test procedure: (a) photo, (b) results

Inclinometer used in the monotonic and the cyclic set-up

The inclinometer is calibrated by comparing its outputs to the angle deduced by the intervention of an *LVDT* (displacement sensor) after the rotation of long rod.

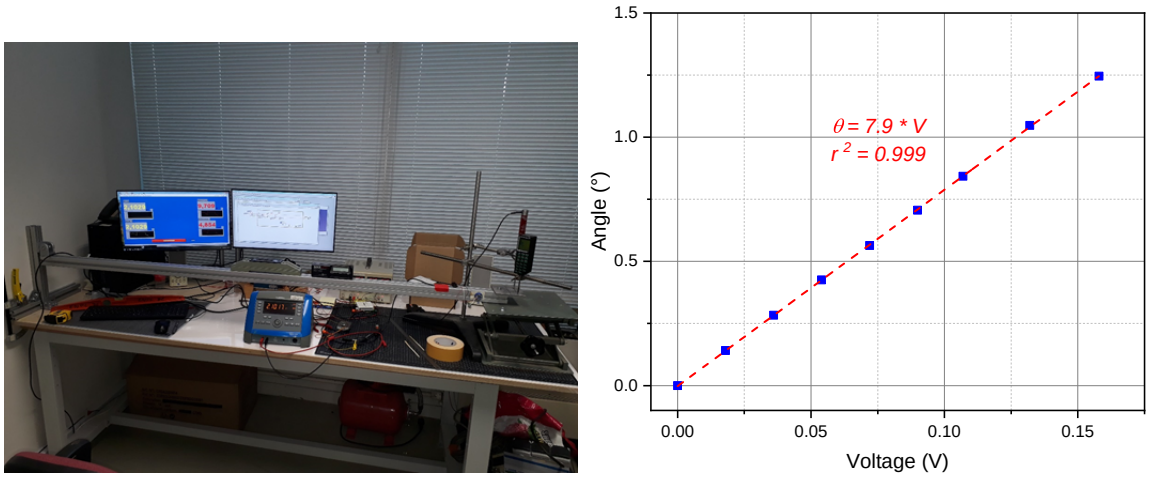

(a) (b)

Fig. A.4.: Calibration of inclinometer used in the monotonic and cyclic test procedures: (a) photo, (b) results

Accelerometer used in the evaluation of the natural frequencies

The calibration of this sensor is available.

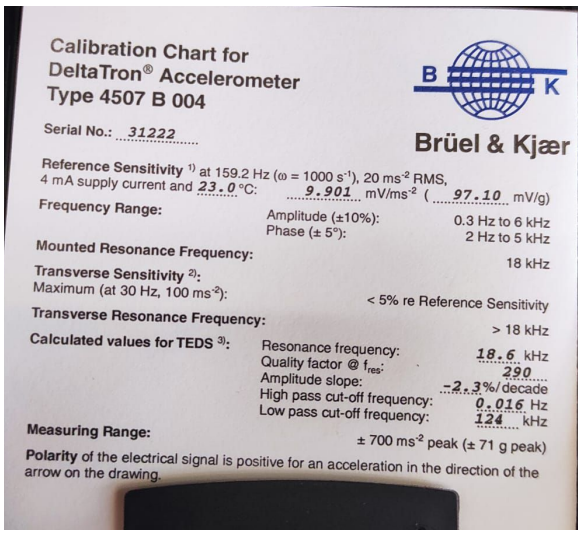
Calibration Chart for
DeltaTron® Accelerometer
Type 4507 B 004

Brüel & Kjær

Serial No.: 31222

Reference Sensitivity 1) at 159.2 Hz (ω = 1000 s-1), 20 ms-2 RMS, 4 mA supply current and 23.0 °C: 9.901 mV/ms-2 (97.10 mV/g)

Frequency Range: Amplitude (±10%): 0.3 Hz to 6 kHz; Phase (± 5°): 2 Hz to 5 kHz

Mounted Resonance Frequency: 18 kHz

Transverse Sensitivity 2): Maximum (at 30 Hz, 100 ms-2): < 5% re Reference Sensitivity

Transverse Resonance Frequency: > 18 kHz

Calculated values for TEDS 3): Resonance frequency: 18.6 kHz; Quality factor @ fres: 290; Amplitude slope: -2.3 %/decade; High pass cut-off frequency: 0.016 Hz; Low pass cut-off frequency: 124 kHz

Measuring Range: ± 700 ms-2 peak (± 71 g peak)

Polarity of the electrical signal is positive for an acceleration in the direction of the arrow on the drawing.

Fig. A.5.: Calibration chart of the accelerometer

A.2 Photos for different equipment of set-up

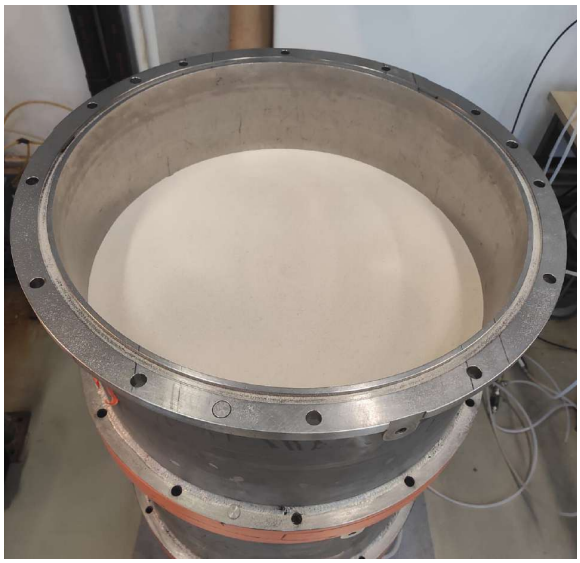

Fig. A.6.: Photo of chamber used to foem the sand mass on monotonic and cyclic tests

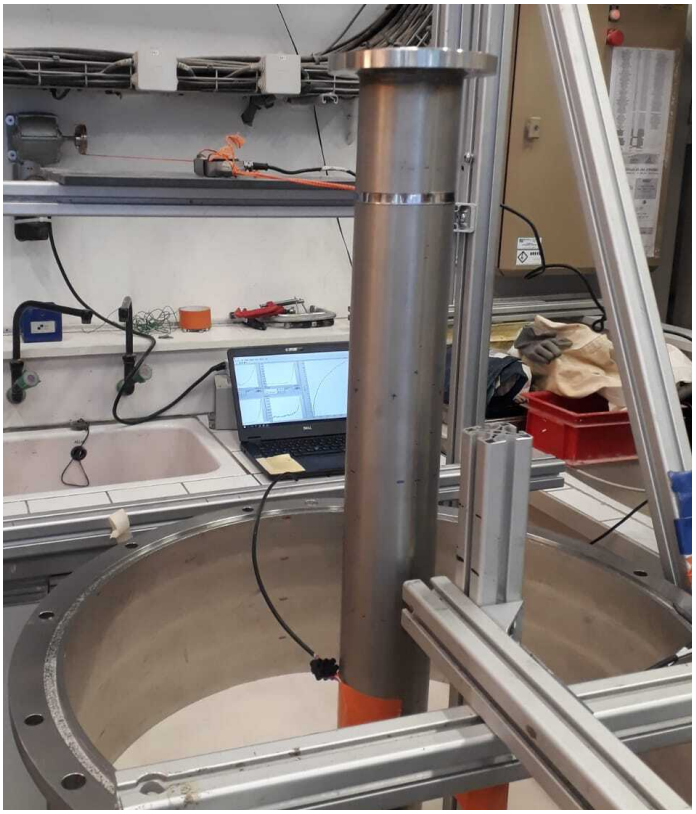

Fig. A.7.: Photo of the monotonic test procedure applied on the monotonic parametric study (Chapter 7)

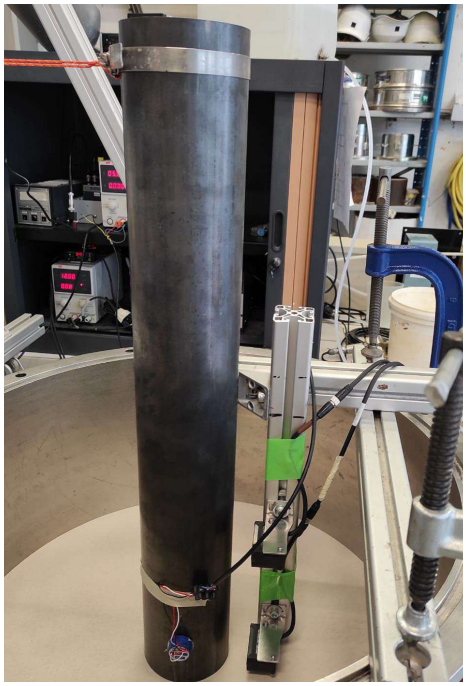

Fig. A.8.: Photo of the monotonic test procedure applied to show the validity (Chapter 4)

Fig. A.9.: Photo of scale models (monopile-substructure) *M1* and *M2*

Fig. A.10.: Photo of the damping device developed

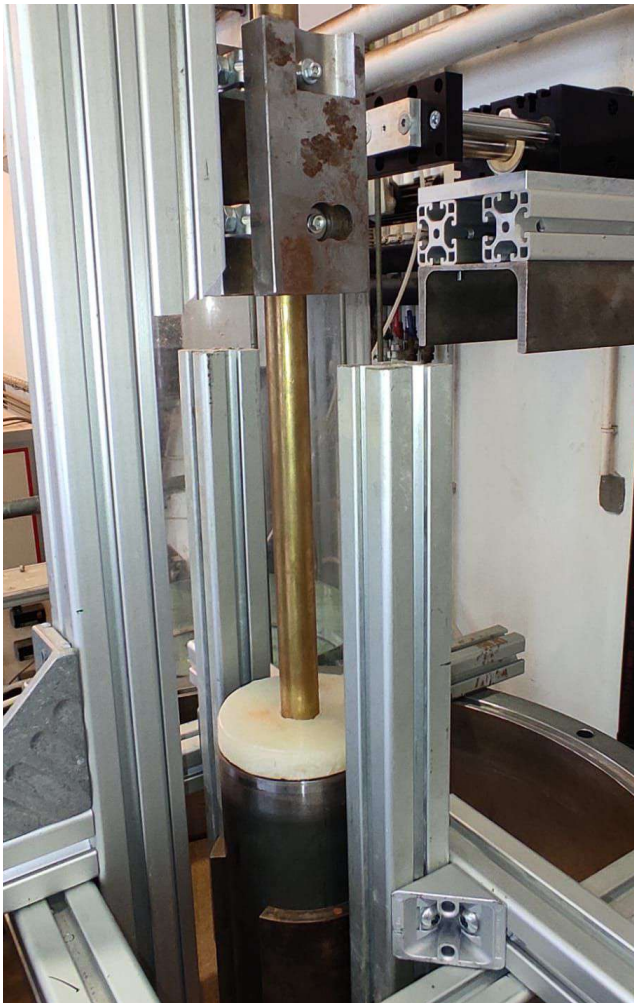

Fig. A.11.: Photo of the driving system

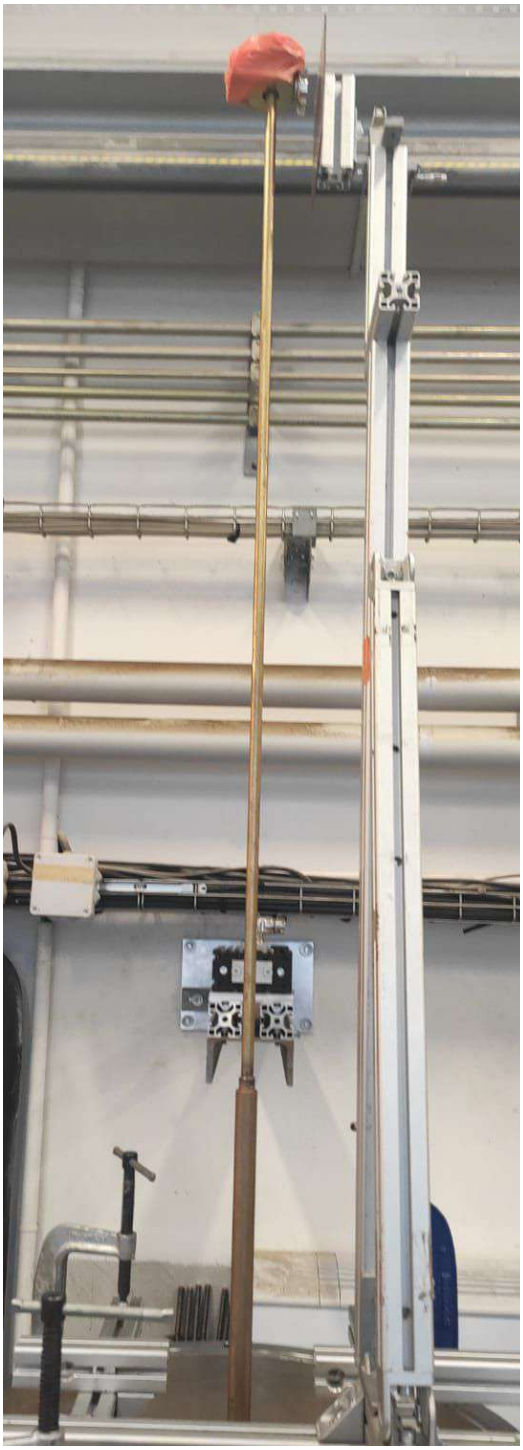

Fig. A.12.: Photo of the cyclic set-up

Bibliography

Abadie, C. (2015). „Cyclic loading response of monopile foundations in cohesionless soils“. PhD thesis. Oxford University (cit. on pp. 38, 89, 123, 142, 194).

Abadie, C. N., B. W. Byrne, and G. T. Houlsby (2019). „Rigid pile response to cyclic lateral loading: Laboratory tests“. *Geotechnique* 69.10, pp. 863–876 (cit. on pp. 25, 28, 39, 49, 147).

Abadie, C. N., B. W. Byrne, G. T. Houlsby, H. J. Burd, R. A. McAdam, and W. J. Beuckelaers (2020). „Modelling of offshore wind monopile lifetime performance“. *4th International Symposium on Frontiers in Offshore Geotechnics (ISFOG)* 6, pp. 1475–1484 (cit. on p. 25).

Abadie, C., B. Byrne, and G. Houlsby (2017). „Modelling of Monopile Response to Cyclic Lateral Loading in Sand“. *Offshore Site Investigation Geotechnics 8th International Conference Proceedings*, pp. 1046–1053 (cit. on p. 25).

Achmus, M., Y. S. Kuo, and K. Abdel-Rahman (2009). „Behavior of monopile foundations under cyclic lateral load“. *Computers and Geotechnics* 36.5, pp. 725–735 (cit. on pp. 24, 25, 162).

Aghakouchak, A., W. W. Sim, and R. J. Jardine (2015). „Stress-path laboratory tests to characterise the cyclic behaviour of piles driven in sands“. *Soils and Foundations* 55.5, pp. 917–928 (cit. on pp. 80, 81, 89, 90).

Aguilar, V., J. M. Stallings, and J. B. Anderson (2019). „Simplified Method for Laterally Loaded Short Piles in Cohesionless Soil“. *Journal of the transportation research record* 2673.2, pp. 605–616 (cit. on p. 185).

Ahmed, S. S. and B. Hawlader (2016). „Numerical Analysis of Large-Diameter Monopiles in Dense Sand Supporting Offshore Wind Turbines“. *International Journal of Geomechanics* 16.5 (cit. on pp. 163, 175).

Albiker, J., M. Achmus, D. Frick, and F. Flindt (2017). „1 G Model Tests on the Displacement Accumulation of Large-Diameter Piles Under Cyclic Lateral Loading“. *Geotechnical Testing Journal* 40.2, pp. 173–184 (cit. on pp. 25, 28, 48, 106).

Alderlieste, E. A., J. Dijkstra, and A. F. Van Tol (2011). „Experimental investigation into pile diameter effects of laterally loaded mono-piles“. *Proceedings of the International Conference on Offshore Mechanics and Arctic Engineering - OMAE* 7.December 2015, pp. 985–990 (cit. on p. 24).

Alkhoury, P., A. H. Soubra, V. Rey, and M. Aït-Ahmed (2021). „A full three-dimensional model for the estimation of the natural frequencies of an offshore wind turbine in sand“. *Wind Energy* 24.7, pp. 699–719 (cit. on p. 133).

Altaee, A. and B. H. Fellenius (1994). „Physical modeling in sand“. *Canadian Geotechnical Journal* (cit. on pp. 42, 43, 63, 64, 67, 213).

Alvarado, J. (2000). „Etude des caractéristiques physiques et granulométriques de sables de reference.“ PhD thesis. Ecole Nationale des Ponts et Chaussées (cit. on pp. 69, 89).

API (American Petroleum Institute) (2010). *RP2A-WSD: Recommended practice for planning, designing and constructing fixed offshore platforms.* (Cit. on pp. 24, 38, 162).

Arany, L., S. Bhattacharya, J. Macdonald, and S. Hogan (2017). „Design of monopiles for offshore wind turbines in 10 steps“. *Soil Dynamics and Earthquake Engineering* 92, pp. 126–152 (cit. on pp. 3, 5, 16, 18, 23, 36, 125, 141, 151).

Arany, L., S. Bhattacharya, J. H. Macdonald, and S. J. Hogan (2016). „Closed form solution of Eigen frequency of monopile supported offshore wind turbines in deeper waters incorporating stiffness of substructure and SSI“. *Soil Dynamics and Earthquake Engineering* 83, pp. 18–32 (cit. on pp. 109, 121, 125).

Arda, C. and O. Cinicioglu (2021). „Influence of grain shape on stress-dilatancy parameters“. *Granular Matter* 23.2, pp. 1–19 (cit. on p. 86).

Arshad, M. and B. C. O'Kelly (2016). „Model Studies on Monopile Behavior under Long-Term Repeated Lateral Loading“. *International Journal of Geomechanics* 17.1 (cit. on pp. 25, 145).

Askarinejad, A., G. Chortis, Q. Li, L. J. Prendergast, R. Brinkgreve, and K. Gavin (2019). „Physical and numerical modelling of the effect of scouring on the lateral behaviour of monopiles“. *The XVII European Conference on Soil Mechanics and Geotechnical EngineeringAt: Reykjavik, Iceland*. September (cit. on p. 156).

ASTM (1996). „Standard Test Method for Consolidated Undrained Triaxial Compression Test for“. 04.April (cit. on pp. 66, 74).

Bak, C., R. Bitsche, T. Kim, Yde, A, L. Henriksen, P. Anderesen, A. Natarajan, and M. Hansen (2013). *Design and performance of a 10 MW wind turbine*. Tech. rep. Delft University of Technology (cit. on p. 32).

Bayton, S. M., J. A. Black, and R. T. Klinkvort (2018). „Centrifuge modelling of long term cyclic lateral loading on monopiles“. *Physical Modelling in Geotechnics* 1.July, pp. 689–694 (cit. on pp. 25, 26).

Been, K. and M. Jefferies (1985). „A state parameter for sands“. *Geotechnique* 35.2, pp. 99–112 (cit. on pp. 62, 63).

Been, K., J. Hachey, and M. G. Jefferies (1991). „The critical state of sands“. *Geotechnique* 41.3, pp. 365–381 (cit. on p. 63).

Benahmed, N. (2001). „Comportement mécanique d 'un sable sous cisaillement monotone et cyclique : application aux phénomènes de liquéfaction et de mobilité cyclique“. PhD thesis. ENPC, Paris, France (cit. on pp. 68, 73, 89).

Bhattacharya, S. and S. Adhikari (2011). „Experimental validation of soil–structure interaction of offshore wind turbines“. *Soil Dynamics and Earthquake Engineering* 31.5-6, pp. 805–816 (cit. on p. 125).

Bhattacharya, S., D. Lombardi, and D. M. Wood (2011). „Similitude relationships for physical modelling of monopile-supported offshore wind turbines“. *International Journal of Physical Modelling in Geotechnics* 11.2, pp. 58–68 (cit. on pp. 29, 30).

Bhattacharya, S., G. Nikitas, L. Arany, and N. Nikitas (2017). „Soil-Structure Interactions (SSI) for Offshore Wind Turbines“. *The Institution of Engineering and Technology*, pp. 1–23 (cit. on p. 10).

Billam, J. (1972). „Some aspects of the behaviour of granular materials at high pressures.“ *Stress strain behaviour of soils* (cit. on p. 64).

Bishop, A. W. (1971). „Shear strength parameters for undisturbed and remolded soil specimens“. *Roscoe Memorial Symp.* Pp. 3–58 (cit. on p. 62).

Bolton, M. D. (1986). „The strength and dilatancy of sands“. I (cit. on pp. 28, 42, 64, 65, 82–85, 88, 163, 211).

Bouzid, D., S. Bhattacharya, and L. Otsmane (2018). „Journal of Rock Mechanics and Geotechnical Engineering Assessment of natural frequency of installed offshore wind turbines using nonlinear fi nite element model considering soil-monopile interaction“. *Journal of Rock Mechanics and Geotechnical Engineering* 10.2, pp. 333–346 (cit. on pp. 121, 125, 127).

Broms, B. B. (1964). „Lateral Resistance of Pile in Cohesionless Soils.“ *Journal of the Soil Mechanics and Foundations Division* 90.3, pp. 123–158 (cit. on p. 185).

Brown, D. A. and C. F. Shie (1991). „Some numerical experiments with a three dimensional finite element model of a laterally loaded pile“. *Computers and Geotechnics* 12.2, pp. 149–162 (cit. on p. 204).

Buckingham, E. (1914). „On physically similar systems; Illustrations of the use of dimensional equations“. *Physical Review* 4.4, pp. 345–376 (cit. on p. 27).

Burton, T., D. Sharpe, N. Jenkins, and E. Bossanyi (2011). *Wind Energy Handbook*, p. 617 (cit. on pp. 12, 15).

Byrne, B. W., R. A. McAdam, H. J. Burd, et al. (2017). „PISA: NEW DESIGN METHODS FOR OFFSHORE WIND TURBINE MONOPILES“. *8th International Conference 12-14 September 2017 Royal Geographical Society*. London, UK (cit. on pp. 3, 24, 162, 186, 196).

Byrne, B. W., H. J. Burd, L. Zdravkovic, et al. (2019). „PISA design methods for offshore wind turbine monopiles“. *Proceedings of the Annual Offshore Technology Conference* 2019-May (cit. on p. 25).

Byrne, B. W., G. T. Houlsby, H. J. Burd, et al. (2020a). „PISA design model for monopiles for offshore wind turbines: Application to a stiff glacial clay till“. *Geotechnique* 70.11, pp. 1030–1047 (cit. on pp. 24, 162, 163).

Byrne, B. W., R. A. McAdam, H. J. Burd, et al. (2020b). „Monotonic laterally loaded pile testing in a dense marine sand at Dunkirk“. *Geotechnique* 70.11, pp. 986–998 (cit. on pp. 188, 189, 201, 202).

Carstensen, A., T. Pucker, and J. Grabe (2018). „Numerical model to predict the displacement of piles under cyclic lateral loading using a new hypoplastic spring element“. *Computers and Geotechnics* 101.September 2017, pp. 217–223 (cit. on pp. 23, 24).

Chakraborty, T. and R. Salgado (2010). „Dilatancy and Shear Strength of Sand at Low“. *JOURNAL OF GEOTECHNICAL AND GEOENVIRONMENTAL ENGINEERING* 136.March, pp. 527–532 (cit. on pp. 65, 84–87, 211).

Charles, W. W., T. L. Y. Yau, J. H. M. Li, and W. H. Tang (2001). „NEW FAILURE LOAD CRITERION FOR LARGE DIAMETER BORED PILES“. *JOURNAL OF GEOTECHNICAL AND GEOENVIRONMENTAL ENGINEERING* 127.June, pp. 488–498 (cit. on p. 185).

Chen, R. P., Y. X. Sun, B. Zhu, and W. D. Guo (2015). „Lateral cyclic pile–soil interaction studies on a rigid model monopile“. *Proceedings of the Institution of Civil Engineers: Geotechnical Engineering* 168.2, pp. 120–130 (cit. on p. 106).

Chen, Y. J., S. W. Lin, and F. H. Kulhawy (2011). „Evaluation of lateral interpretation criteria for rigid drilled shafts“. *Canadian Geotechnical Journal* 48.4, pp. 634–643 (cit. on p. 185).

Coelingh, J. P., A. J. Van Wijk, and A. A. Holtslag (1996). „Analysis of wind speed observations over the North Sea“. *Journal of Wind Engineering and Industrial Aerodynamics* 61.1, pp. 51–69 (cit. on pp. 33, 34).

Comforth, D. (1973). *Prediction of Drained Strength of Sands from Relative Density Measurements* (cit. on p. 66).

Comité Francais de Mecanique des soils et de Géotechnique (2020). „Recommendations for planning and designing foundations of offshore wind turbines“, p. 172 (cit. on p. 38).

Cornforth, D. H. (1964). „Some experiments on the influence of strain conditions on the strength of sand“. *Geotechnique* 14.2, pp. 143–167 (cit. on p. 62).

Correia, A. A., A. Pecker, S. L. Kramer, and R. Pinho (2012). „Nonlinear Pile-Head Macro-Element Model: SSI effects on the Seismic Response of a Monoshaft-Supported“. *15th World Conference on Earthquake Engineering*. Lisbon, Portugal, pp. 1–10 (cit. on p. 23).

Corté, J. (1989). *Model testing - Geotechnical model tests*. Tech. rep., pp. 536–537 (cit. on p. 27).

Cox, W. R., L. C. Reese, U. Texas, and B. R. Grubbs (1974). „Field Testing of Laterally Loaded Piles In Sand“. *OFFSHORE TECHNOLOGY. CONFERENCE 6200 North CentraIExpressway Dallas, Texas 75206* (cit. on p. 24).

Cuéllar, P. (2011). „Pile foundations for offshore wind turbines: numerical and experimental investigations on the behaviour under short-term and long-term cyclic loading“. PhD thesis. Technical university of Berlin (cit. on pp. 4, 29, 30, 41, 42, 142, 145, 149, 151).

Cui, L. and S. Bhattacharya (2016). „Soil–monopile interactions for offshore wind turbines“. *Proceedings of the Institution of Civil Engineers: Engineering and Computational Mechanics* 169.4, pp. 171–182 (cit. on p. 154).

Darendeli, B. M. (2001). „Development of a new family of normalized modulus reduction and material damping curves“. PhD thesis. University of Texas at Austin, TX, USA, pp. 148–162 (cit. on p. 59).

De Josselin De Jong, G. (1976). „Rowe's Stress-Dilatancy Relation Based on Friction“. *Geotechnique* 26.3, pp. 527–534 (cit. on p. 62).

Delfosse-Ribay, E., I. Djeran-Maigre, R. Cabrillac, and D. Gouvenot (2004). „Shear modulus and damping ratio of grouted sand“. *Soil Dynamics and Earthquake Engineering* 24.6, pp. 461–471 (cit. on pp. 57, 58).

Diederich, W., B. Franklin, and L. Field (1957). *Effect of spanwise variations in gust intensity of the lift due to atmospheric turbulence*. Tech. rep. (cit. on p. 12).

Dietrich, T. (1982). „Incremental parabolic hardening of psammic material; application to laterally loaded piles in sand.“ *Proceedings of IUATAM conference on deformation and failure of granular materials* (cit. on pp. 3, 21).

DNV GL (2014). „DNV-RP-C205: Environmental Conditions and Environmental Loads - Recommended Practice“. *Dnv Gl* April (cit. on pp. 13, 17).

DNV GL AS (2016). *DNVGL-ST-0437: Loads and site conditions for wind turbines*. November, p. 108 (cit. on pp. 14, 33).

DNV-OS-J101 (2014). „Design of Offshore Wind Turbine Structures“. *May* May, pp. 212–214 (cit. on pp. 4, 11, 12, 15, 21–24, 33, 36, 141).

DNVGL-ST-0126 (2016). *Support structures for wind turbines*. Tech. rep. April (cit. on p. 114).

Doherty, P. and K. Gavin (2012). „Laterally loaded monopole design for offshore wind farms“. *Proceedings of Institution of Civil Engineers: Energy* 165.1, pp. 7–17 (cit. on p. 24).

Duncan, J. M. and S. Wright (2005). *Soil Strength and Slope Stability, 1st edition* (cit. on p. 67).

Dupla, J.-C., E. Palix, G. Damblans, et al. (2019). „Le projet ANR SOLCYP+ pour améliorer le dimensionnement des monopieux utilisés comme fondations d'éoliennes marines“. *Revue Francaise de Géotechnique* (cit. on p. 3).

El Haffar, I. (2018). „Physical modeling and study of the behavior of deep foundations of offshore wind turbines“. PhD thesis. Ecole centrale de Nantes, p. 298 (cit. on p. 185).

Fahey, M. and J. P. Carter (1993). „A finite element study of the pressuremeter test in sand using a nonlinear elastic plastic model“. *Canadian Geotechnical Journal* 30.2, pp. 348–362 (cit. on p. 59).

Fan, S. (2020). „Effect of the installation process on the subsequent response of monopiles under lateral loading in sand by“. PhD thesis. Western Australia (cit. on p. 115).

Feia, S., J. Sulem, J. Canou, S. Ghabezloo, and X. Clain (2016). „Changes in permeability of sand during triaxial loading: effect of fine particles production“. *Acta Geotechnica* 11.1, pp. 1–19 (cit. on pp. 69, 89).

Frick, D. and M. Achmus (2020). „An experimental study on the parameters affecting the cyclic lateral response of monopiles for offshore wind turbines in sand“. *Soils and Foundations* 60.6, pp. 1570–1587 (cit. on pp. 25, 28, 107, 214).

Futai, M. M., J. Dong, S. K. Haigh, and S. P. Madabhushi (2018). „Dynamic response of monopiles in sand using centrifuge modelling“. *Soil Dynamics and Earthquake Engineering* 115.July, pp. 90–103 (cit. on p. 131).

Galanis, G., P. C. Chu, G. Kallos, Y. H. Kuo, and C. T. Dodson (2012). „Wave height characteristics in the north Atlantic ocean: A new approach based on statistical and geometrical techniques“. *Stochastic Environmental Research and Risk Assessment* 26.1, pp. 83–103 (cit. on pp. 34, 35).

Garnier, J., C. Gaudin, S. Springman, P. Culligan, D. Goodings, D. Konig, B. Kutter, R. Phillips, M. Randolph, and L. Thorel (2007). „Cataloque of scaling laws and similutude questions in geotechnical centrifuge modelling“. *IJPMG-International Journal of Physical Modelling in Geotechnics*, pp. 01–23 (cit. on p. 27).

Giampa, J. R. and A. S. Bradshaw (2018). „A Simple Method for Assessing the Peak Friction Angle of Sand at Very Low Confining Pressures“. *Geotechnical Testing Journal* 41, pp. 639–647 (cit. on pp. 65, 67, 84, 85, 87, 90, 92–95, 211).

Gotschol, A. (2002). *Veränderlich elastisches und plastisches Verhalten nichtbindiger Böden und Schotter unter zyklisch-dynamischer Beanspruchung*. April, p. 196 (cit. on pp. 41, 138).

Hameury, O. (1995). „Quelques aspects du comportement des sables avec et sans rotation des axes principaux: des petites aux grandes déformations“. PhD thesis (cit. on p. 57).

Hamidi, A., E. Azini, and B. Masoudi (2012). „Impact of gradation on the shear strength-dilation behavior of well graded sand-gravel mixtures“. *Scientia Iranica* 19.3, pp. 393–402 (cit. on p. 86).

Hardin, B., V. Drnevich, J. Wang, and C. Sams (1994). „Resonant column testing at pressures up to 3.5 Mpa (500 psi).“ (cit. on p. 61).

Hardin, B. (1978). „THE NATURE OF STRESS-STRAIN BEHAVIOR FOR SOILS“ (cit. on p. 57).

Hardin, B. O. and V. P. Drnevich (1972a). „Shear Modulus and Damping in Soils: Design Equations and Curves“. *Journal of the Soil Mechanics and Foundations Division* 98.7, pp. 667–692 (cit. on p. 59).

Hardin, B. O. and V. P. Drnevich (1972b). „Shear Modulus and Damping in Soils: Measurement and Parameter Effects (Terzaghi Leture)“. *Journal of the Soil Mechanics and Foundations Division* 98.6, pp. 603–624 (cit. on pp. 56, 59).

Hardin, B. O. and F. Richart (1963). „Elastic wave velocities in granular soils.“ *Journal of the Soil Mechanics and Foundations Division* (cit. on pp. 56, 57, 213).

Harehdasht, S. A., M. N. Hussien, M. Karray, V. Roubtsova, and M. Chekired (2019). „Influence of particle size and gradation on shear strength–dilation relation of granular materials“. *Canadian Geotechnical Journal* 56.2, pp. 208–227 (cit. on p. 86).

Hasselmann, K., T. P. Barnett, E. Bouws, et al. (1973). „Measurements of wind-wave growth and swell decay during the joint North Sea wave project (JONSWAP).“ (cit. on p. 14).

Hoek, E., D. Wood, and S. Shah (1992). „A modified Hoek–Brown criterion for jointed rock masses.“ *Hudson JA (ed) Proc. Rock Characterization Symp. ISRM, Eurock'92* (cit. on p. 163).

Hoek, E. and E. T. Brown (1980). *Underground Excavations in Rock*. (Cit. on p. 163).

Hoek, E. and E. Brown (1988). „The Hoek-Brown failure criterion-a 1988 update“. *Proc. 15th Canadian Rock Mech. Symp* February, pp. 31–38 (cit. on p. 163).

HOR, B. (2012). „Evaluation et Réduction des Conséquences des Mouvements de Terrains sur le Bâti : Approches Expérimentale et Numérique“. PhD thesis (cit. on p. 62).

Houlsby, G. T., C. N. Abadie, W. J. Beuckelaers, and B. W. Byrne (2017). „A model for nonlinear hysteretic and ratcheting behaviour“. *International Journal of Solids and Structures* 120, pp. 67–80 (cit. on pp. 24, 25).

Hsu, S. and H. Liao (1998). „Uplift behaviour of cylindrical anchors in sand“. *Canadian Geotechnical Journal* 35.1, pp. 70–80 (cit. on p. 62).

Hu, Z., M. McVay, D. Bloomquist, R. Herrera, and P. Lai (2006). „Influence of Torque on Lateral Capacity of Drilled Shafts in Sands“. *Journal of Geotechnical and Geoenvironmental Engineering* 132.4, pp. 456–464 (cit. on p. 185).

Huang, Y., H. L. Cheng, T. Osada, A. Hosoya, and F. Zhang (2015). „Mechanical Behavior of Clean Sand at Low Confining Pressure : Verification with Element and Model Tests“. *Journal of Geotechnical and Geoenvironmental Engineering* 141.8, pp. 1–6 (cit. on pp. 62, 66–68).

IEC-61400-1 (2005). *IEC 61400 -1Wind turbines – Part 1: Design requirements*, p. 88 (cit. on pp. 15, 16, 21).

Igoe, P., B. Fitzgerald, D. John, and S. Sarkar (2018). „Monopile soil-structure interaction for estimating the dynamic response of an offshore wind turbine Monopile soil-structure interaction for estimating the dynamic response of an offshore wind turbine“. *Civil Engineering Research*. August. Dublin, Ireland, pp. 1–6 (cit. on p. 24).

Irina AndriaNtoanina (2011). *Caractérisation dynamique de sables de référence en laboratoire - Application à la réponse sismique de massifs sableux en centrifugeuse Institut*. Tech. rep. (cit. on pp. 57, 89, 91).

Ishibashi, I. and X. Zhang (1993). „Unified dynamic shear moduli and damping ratios of sand and clay.“ *Chemical Pharmaceutical Bulletin* 33, pp. 182–191 (cit. on pp. 60, 61).

Iwasaki, T., F. Tatsuoka, and Y. Takagi (1978). „Shear Moduli of Sands Under Cyclic Torsional Shear Loading.“ *Soils and Foundations* 18.1, pp. 39–56 (cit. on pp. 56–59, 61).

Jalbi, S., L. Arany, A. R. Salem, L. Cui, and S. Bhattacharya (2019). „A method to predict the cyclic loading profiles (one-way or two-way) for monopile supported offshore wind turbines“. *Marine Structures* 63.September 2018, pp. 65–83 (cit. on pp. 3, 19, 22, 23, 36).

Jardine, R. J., D. M. Potts, J. B. Burland, and A. B. Fourie (1986). „Studies of the influence of non-linear stress–strain characteristics in soil–structure interaction“. *Geotechnique* 36.3, pp. 377–396 (cit. on p. 43).

Jefferies, M. G. and K. Been (2006). *Soil liquefaction: a critical state approach.* (Cit. on p. 79).

Kaimal, J. C., J. C. Wyngaard, Y. Izumi, and O. R. Coté (1972). „Spectral characteristics of surface-layer turbulence“. *Quarterly Journal of the Royal Meteorological Society* 98.417, pp. 563–589 (cit. on p. 12).

Kallehave, D., C. LeBlanc, and M. Liingaard (2012). „Modification of the API p-y formulation of initial stiffness of sand“. *Offshore site investigation and geotechnics: integrated technologies - present and future* (cit. on p. 162).

Kelly, R. B., G. T. Houlsby, and B. W. Byrne (2006). „A comparison of field and laboratory tests of caisson foundations in sand and clay“. *Geotechnique* 56.9, pp. 617–626 (cit. on p. 28).

Kempfert, H., A. Gotschol, and T. S. Ocker (2000). *Kombiniert zyklische und dynamische Elementversuche zur Beschreibung des Kurz- und Langzeitverhaltens von Schotter und granularen Boden.* Tech. rep., pp. 241–254 (cit. on p. 138).

kerner, L. (2017). „Interaction sol-structure sous sollicitations cycliques dynamiques : Application aux éoliennes offshore fondées sur monopieu“. PhD thesis. ENPC, Paris, France (cit. on pp. 18, 24, 30, 31, 89, 113, 116, 117, 121–124, 128, 129, 131, 211, 212).

Kirkwood, P. B. and S. K. Haigh (2014). „Centrifuge testing of monopiles subject to cyclic lateral loading“. *8th International Conference on Physical Modelling in GeotechnicsAt: Perth*.

Kirkwood, P. and S. Haigh (2013). „Centrifuge Testing of Monopiles for Offshore Wind Turbines predicting the behaviour of monopiles“. *Proceedings of the Twenty-third 2013 International Offshore and Polar Engineering Anchorage, Alaska, USA*, pp. 126–130.

Klinkvort, R. T. and O. Hededal (2013). „Lateral response of monopile supporting an offshore wind turbine“. *Proceedings of the Institution of Civil Engineers - Geotechnical Engineering* 166.2, pp. 147–158 (cit. on pp. 25, 104–106).

Klotz, E. U. and M. R. Coop (2002). „On the identification of critical state lines for sands.“ *Geotech. Testing J* 25.3, pp. 289–302 (cit. on p. 79).

Kokusho, T. (1980). „Cyclic Triaxial Test of Dynamic Soil Properties for Wide Strain Range.“ *Soils and Foundations* 3.2, pp. 305–312 (cit. on pp. 58, 59, 213).

Kolymbas, D. and W. Wu (1990). „Recent results of triaxial tests with granular materials“. *Powder Technology* 60.2, pp. 99–119 (cit. on p. 62).

Kulhawy, F. H. (1991). *“Drilled shaft foundations.” Foundation engineering handbook.* (Cit. on p. 188).

Kuo, Y. S., M. Achmus, and K. Abdel-Rahman (2011). „Minimum embedded length of cyclic horizontally loaded monopiles“. *J. Geotech. Geoenviron. Eng* (cit. on p. 162).

Lancelot, Laurent Shahrour, I. and M. A. Mahmoud (1996). „Comportement du sable d'Hostun sous faibles contraintes“, pp. 63–74 (cit. on p. 62).

LeBlanc, C., G. T. Houlsby, and B. W. Byrne (2010). „Response of stiff piles in sand to long-term cyclic lateral loading“. *Geotechnique* 60.2, pp. 79–90 (cit. on pp. 18, 25, 28, 42, 67, 99, 100, 102, 105, 106, 145, 194, 213).

Lee, K. and H. Seed (1967). „Drained Strength Characteristics of Sands“. *Journal of the Soil Mechanics and Foundations Division* 93.6, pp. 117–141 (cit. on p. 62).

Li, Q., A. Askarinejad, and K. Gavin (2020). „Lateral response of rigid monopiles subjected to cyclic loading: centrifuge modelling“. *Proceedings of the Institution of Civil Engineers - Geotechnical Engineering*, pp. 1–35 (cit. on pp. 152, 156).

Li, S., Y. Zhang, and H. P. Jostad (2019). „Drainage conditions around monopiles in sand“. *Applied Ocean Research* 86.September 2018, pp. 111–116 (cit. on p. 41).

Li, X. S. and Y. F. Dafalias (2000). „Dilatancy for cohesionless soils“. *Geotechnique* 50.4, pp. 449–460 (cit. on p. 63).

Li, X. S. and Y. Wang (1998). „Linear Representation of Steady-State Line for Sand“. *Journal of Geotechnical and Geoenvironmental Engineering* 124.12, pp. 1215–1217 (cit. on pp. 63, 79).

Li, Z., S. K. Haigh, and M. D. Bolton (2010). „Centrifuge modelling of mono-pile under cyclic lateral loads“. *7th International Conference on Physical Modelling in Geotechnics, Zurich, Vol. 2, 965-970*, pp. 963–968 (cit. on p. 142).

Li, Z., S. Escoffier, P. Kotronis, Z. Li, S. Escoffier, P. Kotronis, Z. Li, S. Escof, and P. Kotronis (2013). „Using centrifuge tests data to identify the dynamic soil properties : Application to Fontainebleau sand“ (cit. on pp. 60, 61).

Li, Z., P. Kotronis, S. Escoffier, and C. Tamagnini (2016). „A hypoplastic macroelement for single vertical piles in sand subject to three-dimensional loading conditions“. *Acta Geotechnica* 11.2, pp. 373–390 (cit. on p. 23).

Liang, R., Y. Yuan, D. Fu, and R. Liu (2020). „Cyclic response of monopile-supported offshore wind turbines under wind and wave loading in sand“. *Marine Georesources and Geotechnology* 0.0, pp. 1–14 (cit. on pp. 5, 29, 106, 146, 149, 150, 154, 156).

Liu, H. Y., J. A. Abell, A. Diambra, and F. Pisanò (2019a). „Modelling the cyclic ratcheting of sands through memory-enhanced bounding surface plasticity“. *Geotechnique* 69.9, pp. 783–800 (cit. on p. 25).

Liu, J., Z. Guo, N. Zhu, H. Zhao, A. Garg, L. Xu, T. Liu, and C. Fu (2019b). „Dynamic Response of Offshore Open-Ended Pile under Lateral Cyclic Loadings“. *Journal of Marine Science and Engineering* 7.5, p. 128.

Loukidis, D. and R. Salgado (2009). „Modeling sand response using two-surface plasticity“. *Computers and Geotechnics* 36.1-2, pp. 166–186 (cit. on p. 163).

M. Abdel-Rahman, K. A. (2006). „Behaviour of monopile and suction bucket foundation systems for offshore wind energy plants“. *Proc., 5th Int. Engineering Conf.* (Cit. on p. 162).

Mahmoud, M. A. (1997). „ETUDE EN LABORATOIRE DU COMPORTEMENT DES SABLES SOUS FAIBLES CONTRAINTES“. PhD thesis. Ecole centrale de Lille (cit. on p. 66).

Mair, R. (1992). „Developments in geotechnical engineering research: application to tunnels and deep excavation“ (cit. on p. 43).

Manoliu, I., D. Dimitriu, N. Radulescu, and G. Dobrescu (1985). „Load–deflection characteristics of drilled piers.“ *n Proceedings of 11th International Conference on Soil Mechanics and Foundation Engineering, San Francisco, Calif., 12–16* (cit. on pp. 185–187, 195, 196, 199).

Manzari, M. and Y. Dafalias (1997). „A critical state two-surface plasticity model for sands“. *Geotechnique* 2, pp. 255–272 (cit. on p. 163).

Mayall, R. O., R. A. McAdam, R. J. S. Whitehouse, H. J. Burd, B. W. Byrne, S. G. Heald, B. B. Sheil, and P. L. Slater (2020). „Flume Tank Testing of Offshore Wind Turbine Dynamics with Foundation Scour and Scour Protection“. *Journal of Waterway, Port, Coastal, and Ocean Engineering* 146.5, p. 04020033 (cit. on p. 156).

McNamara, A. and R. Klinkvort (2018). „A review of modelling effects in centrifuge monopile testing in sand“. *Physical Modelling in Geotechnics*, pp. 720–723 (cit. on p. 27).

Meyerhof, G. G., S. K. Mathur, and A. J. Valsangkar (1981). „Lateral Resistance and Deflection of Rigid Walls and Piles in Layered Soils.“ *Canadian geotechnical journal* 18.2, pp. 159–170 (cit. on pp. 185, 188).

Morison, J., J. Johnson, and S. Schaaf (1950). „The Force Exerted by Surface Waves on Piles“. *Journal of Petroleum Technology* 2.05, pp. 149–154 (cit. on p. 17).

Mostefa Kara, E., M. Meghachou, and N. Aboubekr (2013). „Contribution of Particles Size Ranges to Sand Friction“. *Engineering, Technology & Applied Science Research* 3.4, pp. 497–501 (cit. on p. 86).

Mulilis, J., C. Chan, and S. HB. (1975). *The effects of method of sample preparation on the cyclic stress-strain behavior of sands*. Tech. rep. University of California (cit. on p. 138).

NF P94-074 (1994). „Essais à l'appaeil triaxial de révolution“. *AFNOR* (cit. on p. 71).

Nicolai, G., L. B. Ibsen, C. D. O. Loughlin, and D. J. White (2017). „Quantifying the increase in lateral capacity of monopiles in sand due to cyclic loading“. *Géotechnique Letters 7*, pp. 245–252.

Niemunis, A., T. Wichtmann, and T. Triantafyllidis (2005). „A high-cycle accumulation model for sand“. *Computers and Geotechnics* 32.4, pp. 245–263 (cit. on p. 25).

Nova, R. and L. Montrasio (1991). „Settlements of shallow foundations on cohesionless soils“. *Géotechnique* 41.2, pp. 243–256 (cit. on p. 23).

Obrzud, R. F. (2010). „On the use of the Hardening Soil Small Strain model in geotechnical practice“. *Numerics in Geotechnics and Structures*, p. 16 (cit. on p. 56).

OE5665 (2015). *Monopile Design - Part I, in Lecture Notes on Offshore Wind Support Structures (OE5665)*. Tech. rep. Delft University of Technology (cit. on p. 38).

Ovesen, N. K. (1980). „The use of physical models in design - The scaling law relationships“. *Design Parameters in Geotechnical Engineering* (cit. on p. 42).

OZTOPRAK, S. and M. BOLTON (2013). „Stiffness of sands through a laboratory test database“. *Geotechnique* 1, pp. 54–70 (cit. on pp. 59, 60).

Page, A. M., G. Grimstad, G. R. Eiksund, and H. P. Jostad (2018). „A macro-element pile foundation model for integrated analyses of monopile-based offshore wind turbines“. *Ocean Engineering* 167.January, pp. 23–35 (cit. on p. 23).

Parsad, V. and T. Chari (1970). „Lateral capacity of model rigid piles in cohesionless soils“. *Chemical Pharmaceutical Bulletin* 43, p. 2091 (cit. on pp. 23, 185, 187).

Peng, J., B. G. Clarke, and M. Rouainia (2011). „Increasing the Resistance of Piles Subject to Cyclic Lateral Loading“. October, pp. 977–982.

Peralta, P. (2010). „Investigations on the Behavior of Large Diameter Piles under Long-Term Lateral Cyclic Loading in Cohesionless Soil“. PhD thesis. University of Hannover (cit. on pp. 41, 138).

Peralta, P. and M. Achmus (2010). „An experimental investigation of piles in sand subjected to lateral cyclic loads“. *Physical Modelling in Geotechnics - Proceedings of the 7th International Conference on Physical Modelling in Geotechnics 2010, ICPMG 2010* 2, pp. 985–990 (cit. on pp. 3, 21, 27, 28, 42).

Pierson, W. J. and L. Moskowitz (1964). „A Proposed Spectral Form for Fully Developed Wind Seas Based on the Similarity Theory of S . A . Kitaigorodskii“. 69.24 (cit. on p. 14).

Pisanò, F. (2019). „Input of advanced geotechnical modelling to the design of offshore wind turbine foundations“. *Proceedings of the XVII ECSMGE-2019* September, p. 27 (cit. on p. 25).

Ponce, V. and J. Bell (1971). „Shear Strength of Sand at Extremely Low Pressures“. *Journal of the Soil Mechanics and Foundations Division* 97.4 (cit. on pp. 62, 66).

Pöschel, T., C. Saluena, and T. Schwager (2001). „Can we scale granular systems?“ *Powders and Grains 2001* 2, pp. 439–442 (cit. on p. 46).

Poulos, H. G. and T. S. Hull (1989). „Role of analytical geomechanics in foundation engineering“. January 1989, pp. 1578–1606 (cit. on pp. 21, 28).

Poulos, S. J. (1981). „The Steady State of Deformation“. *Journal of the Geotechnical Engineering Division* 107.5 (cit. on p. 63).

Prendergast, L. J., K. Gavin, and P. Doherty (2015). „An investigation into the effect of scour on the natural frequency of an offshore wind turbine“. *Ocean Engineering* 101, pp. 1–11 (cit. on pp. 5, 156).

Puech, A. and J. Garnier (2017). *Design of Piles Under Cyclic Loading* (cit. on pp. 3, 24).

Qian, H. U., F. Han, M. Prezzi, R. Salgado, and M. Z. Ã (2021). „Lateral load response of large-diameter monopiles in sand“. *Géotechnique* (cit. on p. 163).

Rathod, D., D. Nigitha, and K. T. Krishnanunni (2021). „Experimental Investigation of the Behavior of Monopile under Asymmetric Two-Way Cyclic Lateral Loads“. *International Journal of Geomechanics* 21.3, pp. 1–14 (cit. on p. 107).

Reese, L. C. (1974). *Analysis of Laterally Loaded Piles in Sand* (cit. on p. 24).

Remaud, D. (1999). „Pieux sous charges laterales: Etude experimentale de l’effet de groupe“. PhD thesis (cit. on p. 42).

Richards, I. (2019). „Monopile foundations under cyclic lateral loading“. PhD thesis. Oxford University, p. 239 (cit. on pp. 3, 4, 28, 213).

Riemer, M. F., R. B. Seed, P. G. Nicholson, and H.-L. J. Jong (1990). „STEADY STATE TESTING OF LOOSE SANDS: LIMITING MINIMUM DENSITY“. *Journal of Geotechnical Engineering* 116.2, pp. 332–337 (cit. on p. 63).

Roesen, H. R., L. B. Ibsen, and L. V. Andersen (2013). „Experimental testing of monopiles in sand subjected to one-way long-term cyclic lateral loading“. *18th International Conference on Soil Mechanics and Geotechnical Engineering: Challenges and Innovations in Geotechnics, ICSMGE 2013* 3, pp. 2391–2394 (cit. on p. 28).

Roscoe, K. H., A. N. Schofield, and C. P. Wroth (1958). „On the yielding of soils“. *Geotechnique* 8.1, pp. 22–53 (cit. on p. 63).

Rowe, P. (1962). „The stress-dilatancy relation for static equilibrium of an assembly of particles in contact“. *Proceedings of the Royal Society of London. Series A. Mathematical and Physical Sciences* 269.1339, pp. 500–527 (cit. on p. 62).

Roy, K., B. Hawlader, S. Kenny, and I. Moore (2016). „Finite element modeling of lateral pipeline-soil interactions in dense sand“. *Canadian Geotechnical Journal* 53.3, pp. 490–504 (cit. on p. 163).

Sadrekarimi, A. and S. M. Olson (2011). „Critical state friction angle of sands“. *Geotechnique* 61.9, pp. 771–783 (cit. on p. 67).

Santamarina, J. C. and G. C. Cho (2001). „Determination of Critical State Parameters inSandy Soils - Simple Procedure“. *Geotechnical Testing Journal* 24.2, pp. 185–192 (cit. on p. 67).

Schofeld, A. and C. Wroth (1968). *Critical state soil mechanics* (cit. on p. 63).

Schroeder, F., A. Merritt, K. Sorensen, A. M. Wood, C. Thilsted, and D. Potts (2015). „Predicting monopile behaviour for the Gode Wind offshore wind farm“. *Frontiers in Offshore Geotechnics III* (cit. on pp. 3, 20).

Sedran, G., D. F. E. Stolle, and R. G. Horvath (2001). „An investigation of scaling and dimensional analysis of axially loaded piles“. *Canadian Geotechnical Journal* (cit. on p. 42).

Seed, H. B., R. T. Wong, I. M. Idriss, and K. Tokimatsu (1986). „MODULI AND DAMPING FACTORS FOR DYNAMIC ANALYSES OF COHESIONLESS SOILS“. *J. Geotech. Engrg* 112.11, pp. 1016–1032 (cit. on pp. 56, 58, 59).

Shadlou, M. and S. Bhattacharya (2016). „Dynamic stiffness of monopiles supporting offshore wind turbine generators“. *Soil Dynamics and Earthquake Engineering* 88, pp. 15–32 (cit. on p. 130).

Shariff, A. A. and M. Hadi Hafezi (2012). „Modelling significant wave height data of North Sea: Rayleigh vs Weibull distribution“. *Applied Mechanics and Materials* 157-158, pp. 652–657 (cit. on pp. 34, 35).

Sheil, B. B. and B. A. McCabe (2017). „Biaxial Loading of Offshore Monopiles: Numerical Modeling“. *International Journal of Geomechanics* 17.2, p. 04016050 (cit. on p. 25).

Sibuya, S., F. Tatsuoka, S. Teachavorasinskun, X. Kong, F. Abe, Y. Kim, and C. Park (1992). „Elastic Deformation properties of Geomaterials“. *Soils and Foundations* (cit. on p. 56).

Sladen, J. A. and J. M. Oswell (1989). „The behavior of very loose sand in the triaxial compression test“. *Can. Geotech. J.* 26.1, pp. 103–113 (cit. on p. 62).

Sladen, J., R. D. D. Hollander, and J. Krahn (1985). „Liquefaction of sands, a collapse surface approach“. *International Journal of Rock Mechanics and Mining Sciences & Geomechanics Abstracts* 22, pp. 564–578 (cit. on p. 62).

Smith, T. D. (1987). „Pile horizontal soil modulus values“. *J. Geotech. Engrg* 113.9, pp. 1040–1044 (cit. on pp. 23, 187).

Sorensen, S. P. H., K. T. Brodbik, M. Moller, A. H. B. Augustesen, and L. Ibsen (2009). „Evaluation of the load-displacement relationships for large-diameter piles in sand.“ *2th Int. Conf. on Civil, Structural and Environmental Engineering Computing* (cit. on p. 162).

Sorenson, S., A. Augustesen, C. Lrth, M. Ostergaard, and M. Moller (2017). „Consequences of p-y curve selection for mono-pile design for offshore wind turbines“. *Smarter Solutions for Future Off shore Developments* 216.6 2 (cit. on pp. 3, 20).

Stewart, R. H. (1987). „Physical oceanography“. *Deep Sea Research Part B. Oceanographic Literature Review* 34.8, pp. 629–645 (cit. on p. 15).

Taborda, D., L. Zdravkovic, S. Kontoe, and D. M. Potts (2014). „Computational study on the modification of a bounding surface plasticity model for sands Computers and Geotechnics Computational study on the modification of a bounding surface plasticity model for sands“. June (cit. on p. 163).

Tatsuoka, F. (1987). „Discussion on 'The strength and dilatancy of sands' by Bolton, 1986.“ *Geotechnique* 37.2, pp. 219–226 (cit. on p. 65).

Tatsuoka, F. and (1984). „Strength and deformation characterisatics of saturated sand at extremely low pressures“. *Soils and Foundations* (cit. on pp. 62, 65, 66).

Tatsuoka, F., S. Goto, and M. Sakamoto (1986). „Effects of Some Factors on Strength and Deformation Characteristics of Sand At Low Pressures.“ *Soils and Foundations* 26.1, pp. 105–114 (cit. on p. 65).

TheGuardian (2021). „https://www.theguardian.com/us-news/2021/oct/13/biden-wind-farms-environment-climate-crisis“ (cit. on p. 1).

Thieken, K., M. Achmus, and K. Lemke (2015). „A new static p-y approach for piles with arbitrary dimensions in sand“. *Geotechnik* (cit. on p. 162).

Truong, P., B. M. Lehane, V. Zania, and R. T. Klinkvort (2018). „Empirical approach based on centrifuge testing for cyclic deformations of laterally loaded piles in sand“. *Géotechnique* 69.2, pp. 133–145 (cit. on pp. 18, 106, 145).

Van der Hoven, I. (1957). „Power spectrum of horizontal wind speed in the frequency range from 0.0007 to 900 cycles per hour“ (cit. on p. 12).

Van der Tempel, J. (2006). *Design of support structure for offshore wind turbines*. april, p. 223 (cit. on pp. 11, 15, 34).

Velarde, J. (2016). „Master thesis: Design of monopile foundations to support the DTU 10MW wind turbine“ (cit. on p. 32).

Velarde, J. and E. E. Bachynski (2017). „Design and fatigue analysis of monopile foundations to support the DTU 10 MW offshore wind turbine“. *Energy Procedia* 137, pp. 3–13 (cit. on p. 38).

Verdure, L., J. Garnier, and D. Levacher (2003). „Lateral cyclic loading of single piles in sand“. *International Journal of Physical Modelling in Geotechnics* (cit. on p. 42).

Vesic, A. S. and G. W. Clough (1968). „Behaviour of granular materials under high stresses.“ *J. Soil Mech. Fdns* 94, pp. 661–688 (cit. on p. 64).

Vucetic, M., G. Lanzo, and M. Doroudian (1998). „DAMPING AT SMALL STRAINS IN CYCLIC SIMPLE SHEAR TEST“. *Journal of Geotechnical and Geoenvironmental Engineering* 124.July, pp. 585–594 (cit. on p. 59).

Wang, H., L. Wang, Y. Hong, A. Askarinejad, B. He, and H. Pan (2021). „Influence of pile diameter and aspect ratio on the lateral response of monopiles in sand with different relative densties“. *Journal of Marine Science and Engineering* 9.6 (cit. on p. 162).

Wichtmann, T. and T. Triantafyllidis (2004). „Influence of a cyclic and dynamic loading history on dynamic properties of dry sand, part II: Cyclic axial preloading“. *Soil Dynamics and Earthquake Engineering* 24.11, pp. 789–803 (cit. on pp. 58, 59).

Wichtmann, T. (2005). „Explicit accumulation model for non-cohesive soils under cyclic loading by“. PhD thesis. Ruhr-Universitat Bochum (cit. on p. 138).

Wichtmann, T., T. Triantafyllidis, and S. Chrisopoulos (2017). „Prediction of Long-Term Deformations of Offshore Wind Power Plant Foundations Using HCA-Based Engineer-Oriented Models Prediction of Long-Term Deformations of Offshore Wind Power Plant Foundations Using HCA-Based Engineer-Oriented Models“. *International Journal of Offshore and Polar Engineering* December (cit. on p. 25).

Wiemann, J., K. Lesny, and W. Richwien (2004). „Evaluation of pile diameter effects on soil-pile stiffness“. *DEWEK* (cit. on p. 162).

Williams, M. (2008). *Wave mapping in UK waters Supporting document*. Tech. rep. (cit. on p. 35).

Wind Europe (2020). *https://windeurope.org/* (cit. on pp. 1, 2, 20).

Windindustrie in Deutschland (2016). *1300 tonnes – world ´s largest monopile moved on self-propelled transporters* (cit. on p. 20).

Winkler, E. (1867). *Die Lehre von der Elasticität und Festigkeit* (cit. on p. 23).

Wolf, T. K., K. L. Rasmussen, M. Hansen, L. B. Ibsen, and H. R. Roesen (2013). *Assessment of p–y curves from numerical methods for a non-slender monopile in cohesionless soil*. Tech. rep. Aalborg University (cit. on p. 162).

Wood, D. M. (2006). *Geotechnical modelling*, pp. 1–488 (cit. on pp. 27, 29).

Wroth, C. P. and R. H. Bassett (1965). „A stress-strain relationship for the shearing behaviour of a sand“. *Geotechnique* 15.1, pp. 32–56 (cit. on p. 62).

Xiao, Y., L. Long, T. Matthew Evans, H. Zhou, H. Liu, and A. W. Stuedlein (2019). „Effect of Particle Shape on Stress-Dilatancy Responses of Medium-Dense Sands“. *Journal of Geotechnical and Geoenvironmental Engineering* 145.2, p. 04018105 (cit. on p. 86).

Yang, J. and X. S. Li (2004). „State-Dependent Strength of Sands from the Perspective of Unified Modeling“. *Journal of Geotechnical and Geoenvironmental Engineering* 130.2, pp. 186–198 (cit. on p. 64).

Yang, J. and X. D. Luo (2018). „The critical state friction angle of granular materials: does it depend on grading?“ *Acta Geotechnica* 13.3, pp. 535–547 (cit. on p. 86).

Yu, L. Q., L. Z. Wang, Z. Guo, S. Bhattacharya, G. Nikitas, L. L. Li, and Y. L. Xing (2015). „Long-term dynamic behavior of monopile supported offshore wind turbines in sand“. *Theoretical and Applied Mechanics Letters* 5.2, pp. 80–84 (cit. on pp. 5, 29, 149, 150, 154, 156).

Zdravkovic, L., R. J. Jardine, D. M. Taborda, et al. (2020). „Ground characterisation for PISA pile testing and analysis“. *Geotechnique* 70.11, pp. 945–960 (cit. on pp. 56, 57, 79–81).

Zhang, L., F. Silva, and R. Grismala (2005). „Ultimate Lateral Resistance to Piles in Cohesionless Soils“. *Journal of Geotechnical and Geoenvironmental Engineering* 131.1, pp. 78–83 (cit. on pp. 185–187, 195, 196).

Zhang, X., C. Zhang, Y. Liu, and Z. Hu (2020). „Nondimensional parametric method for studying lateral cyclic response of offshore monopiles in sand“. *Marine Georesources and Geotechnology* 0.0, pp. 1–12 (cit. on pp. 106, 142).

Zhu, Z., F. Zhang, J. C. Peng Qingyun and, J. Canou, G. Cumunel, and E. Foerster (2021). „Effect of the loading frequency on the sand liquefaction behaviour in cyclic triaxial tests“. *Soil Dynamics and Earthquake Engineering* (cit. on p. 138).

List of Figures

List of Tables